UNIVERSITÀ DEGLI STUDI
DI GENOVA
UNIVERSITY OF GENOVA
Ph.D. Course in Mechanical, Energy and Management Engineering
Curriculum: Technical Physics

Lattice Boltzmann Method: applications to thermal fluid dynamics and energy systems

By

JOHAN AUGUSTO BOCANEGRA CIFUENTES

Thesis submitted for the degree of

Doctor of Philosophy (XXXIV cycle)

October 2021

Prof. Ing. Mario Misale — Supervisor

Prof. Ing. Giovanni Berselli — Head of the PhD program

Department: of Mechanical, Energy, Management and Transport Engineering (DIME)

I would like to dedicate this work to my whole family, my beloved wife Francy, and my son Leon… all my achievements are yours

Declaration

I hereby declare that except where specific reference is made to the work of others, the contents of this dissertation are original and have not been submitted in whole or in part for consideration for any other degree or qualification in this, or any other university. This dissertation is my own work. The outcome of work done in collaboration with others is specified in the text and Acknowledgements.

This dissertation contains fewer than 65,000 words including appendices, bibliography, footnotes, tables and equations and has fewer than 150 figures.

Johan Augusto Bocanegra Cifuentes

October, 2021

Acknowledgements

I would like to acknowledge the scientific support during the Ph.D. course, especially to my tutor, prof. Mario Misale, who made me part of his research team and allowed me to work on interesting projects. I had the opportunity to perform fascinating experiments under his guidance. He gave me an invaluable direction into the Thermo Fluid Dynamics field.

To prof. Davide Borelli, who gave me support throughout my Ph.D. studies, I appreciate his contributions to the development of this thesis. He gave me scientific direction in Acoustics and Computational Physics field and generously shared his knowledge.

I would like to acknowledge my dear co-authors for the opportunity to work together: prof. Annalisa Marchitto, prof. Guglielmo Lomonaco, prof. Tomaso Gaggero, prof. Antonio Cammi, prof. Enrico Rizzuto, prof. Giorgio Tani, prof. Ruben Pico, and prof. Corrado Schenone who involved me in the Applied Acoustics Laboratory.

To all the DIME-TEC team that supported me during this scientific travel, especially to prof. Francesco Devia who was always available.

Finally, I would like to thank prof. Luca Tagliafico and prof. Federico Scarpa for the opportunity to apply my knowledge beyond my own expectations, introducing me to the Magnetic Refrigeration field.

Abstract

In many energy systems fluids play a fundamental role, and computational simulations are a valuable tool to study their complex dynamics. The Lattice Boltzmann Method (LBM) is a relatively new numerical method for computational fluid dynamics, but its applications can be extended to physical phenomena beyond fluid flows. This thesis presents applications of the LBM to thermal fluid dynamics and energy systems. Specific applications considered are: application to nuclear reactor engineering problems; thermal fluid dynamic behavior of a Natural Circulation Loop; nanoparticles gravitational sedimentation; acoustical problems.

The main original contributions derived from this work are: first, the systematic description of the current status of LBM applications to nuclear reactors problems, including test cases and benchmark simulations; second, the development and validation of a LBM model for a single-phase natural circulation loop; third, the development and validation of a LBM model for gravitational sedimentation of nanoparticles, and fourth, the systematic description of the current status of LBM applications to acoustics, including simulations of test cases. The development of this thesis was not limited to simulations; experimental studies in parallel connected natural circulation loops of small inner diameter were conducted, showing the wide applicability of the one-dimensional theoretical models used to validate the LBM results. Additional contributions derived from this work: 1. the applicability of the method to study neutron transport and nuclear waste disposal using porous materials was shown. 2. changes in the thermophysical performance of the natural circulation loop when the loop reached a non-laminar (transition) regime were found at a Reynolds number lower than the typical range. 3. variable diffusion and sedimentation parameters were effective to model the experimental sedimentation curves. In conclusion, this work shows that the LBM is a versatile and powerful computational tool that can be used beyond the common Computational Fluid Dynamics applications.

TABLE OF CONTENTS

LIST OF FIGURES

LIST OF TABLES

ABBREVIATIONS AND NOMENCLATURE

Abbreviations

ABC	absorbing boundary condition
AMR	Adaptive Mesh Refinement
BB	bounce back
BC	Boundary conditions
BEM	Boundary Element Method
BF	Base flow
BGK	Bhatnagar–Gross–Krook
BIM	Boundary Immersed Method
BTE	Boltzmann Transport Equation
BWR	Boiling Water Reactor
CBC	Characteristic Boundary Conditions
CFD	Computational Fluid Dynamics
CPU	Computer processor unit
DAS	Direct Absorber Systems
DDF	Double distribution function
DEM	Discrete Element Method
DLS	Direct Light Scattering
DLVO	Derjaguin–Landau–Verwey–Overbeek
DNS	Direct Numerical Simulation
DOF	degree of freedom
DOM	Discrete Ordinate Method
DRT	Double Relaxation Time
DWG	Digital wave guide
E	Entropic
EM	Extrapolation Method
FBR	Fast Breeder Reactor
FD	Finite Differences
FEM	Finite Element Method
FV	Finite Volume
FVM	Finite Volume Method
FWH	Ffowcs Williams and Hawkings
GPU	graphic processing unit
HHHC	horizontal heater horizontal cooler
HHVC	horizontal heater vertical cooler
HLBM	high-order, hybrid
HPI	High-Pressure Injection
HT	hybrid thermal
HTGR	High-Temperature Gas Reactor
HVAC	Heating, Ventilation, and Air Conditioning
IC	Initial Condition
IDM	impurity deposition model
LBE	Lattice Boltzmann Equation
LBM	Lattice Boltzmann Method
LES	Large Eddy Simulation
LGA	Lattice Gas Automata
LGK	Gas Kinetic Algorithm
LM	Liquid Metal
LOCA	Loss of Coolant Accident
LODI	local one-dimensional inviscid
LR	low Reynolds number
LWR	Light Water Reactor
MB	Multiblock
MC	Monte Carlo
mfp	mean free path
MLS	Multiple Light Scattering
MOX	mixed-oxide
MRI	Magnetic Resonance Imaging
MRT	Multiple Relaxation Time
MRT	multiple relaxation time
MSUPS	Mega Site Updates per Second
MWCNT	Multi-walled carbon nanotubes
NCL	Natural Circulation Loop
NCL	Natural Circulation Loop
ND	Neutron Diffusion
NFV	neutron finite volume
NRBC	non reflective boundary conditions
NS	Navier-Stokes
NT	Neutron Transport
NTE	Neutron Transport Equation
NZVI	nanoscale zero-valent iron
ODE	Ordinary differential equation
OGV	outlet guide vane
PIV	particle image velocimetry
PML	Perfectly match layer
Pn	Spherical Harmonics Method
PV	Photo-Voltaic
PWR	pressurized water reactor
R	Regularized
RANS	Reynolds-averaged Navier–Stokes
RLC	rod linear cascade
RNG	Renormalization Group
RT	transport
SAMR	Structured Radiation Adaptive Mesh Refinement
SAMR	Structured Adaptive Mesh Refinement
SAXRS	Small-angle X-ray scattering
SB	Small Break
SEM	Scanning Electron Microscopy
SHM	Spherical Harmonics Method
Sn	Discrete Ordinate Method
SRT	Single Relaxation Time
SSAMR	Streaming-based block Structured Adaptive Mesh Refinement
T	Thermal
TEM	Transmission Electron Microscopy
UNIGE	Genoa University
UV	Ultraviolet
VHHC	vertical heater horizontal cooler
VHTR	Very High-Temperature Reactor
VHVC	vertical heater vertical cooler
Vis	Visible
VLES	Very-Large Eddies Simulation
VR	Variable resolution
WALE	wall adapting local eddy viscosity
ZG	zero gradient

Symbols

a	acceleration (m s-^{2})
A	area (m^2)
B	distribution parameter (-)
$\boldsymbol{c}$	velocity vector (m/s)
C	volumetric concentration (-)
c_p	isobaric specific heat (J kg^{-1}K^{-1})
c_v	isochoric specific heat (J kg^{-1}K^{-1})
c_s	sound speed (m s^{-1})
d	nanoparticle diameter (m)
D	diffusion coefficient (m^2 s^{-1})
E	energy (J)
f	density distribution function (s m^{-1})
F	body force (N kg^{-1})
ff	friction factor (-)
g	temperature distribution function (s m^{-1})
G	dimensionless sedimentation group (-)
Gr_m	modified Grashof number (-)
H	height (m)
ID	inner diameter of the tube (m)
$\boldsymbol{i}$	x unitary vector (-)
$\boldsymbol{j}$	y unitary vector (-)
$\boldsymbol{k}$	z unitary vector (-)
Kr	dissolution rate (-)
K	local pressure loss (-)
k	wave number (m^{-1})
k_b	Boltzmann constant (J K^{-1})
K_{eff}	multiplication factor (-)
Kn	Knudsen number (-)
l	characteristic length (m)
L	total length (m)
M	cells number (-)
M	mass (kg)
Ma	Mach number (-)
n	number (-)
N	cells number (-)
N_G	geometric factor (-)
$Nppw$	number of points per wavelength (-)
Nu	Nusselt number (-)
O	order (-)
P	pressure (Pa)
Pr	Prandtl number (-)
Q	collision operator (-)
q	heating power (W)
$\boldsymbol{r}$	position (m)
Ra	Rayleigh number (-)
Re	Reynolds number (-)
s	Source (-)
S	sedimentation coefficient (m s^{-1})
T	temperature (K)
T	period (s)
t	time (s)
U	overall heat transfer (W m^{-2} C^{-1})
v	speed (m s^{-1})
v_p	volumetric concentration (-)
W	width (m)
w_i	velocity quadrature weights (-)
x	spatial coordinate (m)
y	spatial coordinate (m)
z	spatial coordinate (m)

Greek symbols

Δ	difference (-)
Σ	macroscopic cross section (cm^{-1})
Φ	neutron flux (cm^{-2}s^{-1})
Ψ	neutron distribution function (s m^{-1})
ω	relaxation frequency (s^{-1})
Ω	solid angle (-)
v	neutron velocity (m s^{-1})
Γ	absorption coefficients matrix (-)
Λ	relaxation matrix (s^{-1})
α	thermal diffusivity (m^2 s^{-1})
β	volumetric expansion coefficient (k^{-1})
ν	kinematic viscosity (m^2 s^{-1})
γ	specific heat ratio (-)
ε	effectiveness (-)
λ	molecular mean free path (m)
λ	wavelength (nm)
μ	dynamic viscosity (Pa s)
ρ	density (kg m^{-3})
σ	cross section operator (-)
ϕ	sponge profile (-)
τ	relaxation time (s)

Subscripts and superscripts

$\bar{}$ *avg*	average
‘ *	modified
BGK	Bhatnagar–Gross–Krook
C	cool
eq	equilibrium
exp	experimental
f	fluid
g	neutron group
H	heater
i	grid direction
0 ini	initial
max	maximum
N	neutron
neq	non equilibrium
p	particles
ref	reference
res	residual
rms	root main square
sed	sedimentation
sink	sink
ss	steady state
t	total
theo	theoretical
W	wall node
α	angular direction
x	*x* direction
y	*y* direction
z	*z* direction

1. INTRODUCTION

1.1 Motivation

Computers and numerical methods are nowadays widely spread in engineering and science. A relatively new numerical method called Lattice Boltzmann Method (LBM) is a development that combines both statistical mechanics (physical principles) and *cellular automata* (computational algorithms) and can be a very useful tool in research, engineering, and design. This numerical method has been becoming popular by its application as a computational fluid dynamics (CFD) solver. The alternative approach of the LBM differs from the more common approach followed by numerical methods based in the solution of the Navier-Stokes (NS) equations, e.g., Finite Element Method (FEM) or Finite Volume Method (FVM). Table 1.1 presents a brief comparison of the LBM with those NS based methods and highlights some differences and possible advantages of using this numerical method. A critical point of view must consider LBM as some other tool, not a competitor of the NS-based methods.

Table 1.1 Comparison between the LBM and NS based methods (adapted from [1,2]).

Feature	NS based methods	LBM
Equation	Integral or differential Navier Stokes equations	Discretized Boltzmann equation
Partial Differential Equation	2nd order	Set of 1st order
Convective term	No-linear	Linear
Coordinates	Independent of the mesh	Dependent on the grid (mesh)
Convergence	Iterative to obtain convergence	Explicit, do not need iterative procedures
Boundary Conditions	Macroscopic conditions can be implemented using the NS equations	Macroscopic boundary conditions must be translated to mesoscopic distribution functions Special treatment for complex geometries including corners and curvature (off-lattice positions).
Molecular interactions	Continuum assumption. Is not easy to include molecular physics	No continuum assumption. Relatively easy to include molecular physics

The LBM is based in the propagation and evolution of probability functions in a uniform grid or lattice, and the recovery of the macroscopic physical properties by calculations over those probabilities. In Fig. 1.1 a typical two-dimensional lattice is represented with different cells in a square lattice, and vectors representing the probabilities that become propagated to the neighbour nodes in the grid.

The LBM algorithm is relatively simple, is highly parallelizable. In comparison with FEM or FVM the preprocessing of the geometry in LBM is simpler and more efficient (in computational terms). Some limitations that have slow down their popularity are related to the necessary physical background (relatively less intuitive than in NS solvers) and the lack of commercial tools (if even some solutions exist in the market), that implies a programming culture background for the interested user, however it is not much different to the common knowledge necessary to develop a Finite Differences model.

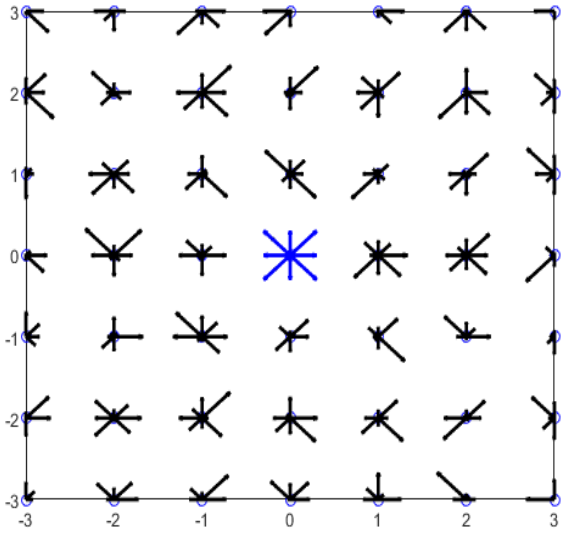

Figure 1.1 Two-dimensional geometrical model used in LBM.

1.2 Objective

The main objective of this thesis is to present Lattice Boltzmann Method applications to thermal fluid dynamics and energy systems, showing that this numerical method is a versatile and powerful computational tool not limited to common Computational Fluid Dynamics applications.

Specifically, the aim is to present LBM applications to:

- Nuclear reactor problems, subdivided into fluid dynamics and radiation transport;
- Thermal fluid dynamics, in the simulation of a Natural Circulation Loop;
- Advection diffusion problems, to model the nanoparticles gravitational sedimentation;
- Wave phenomena focused on acoustical problems.

1.3 Prolegomena to Statistical Mechanics

The LBM adopts a mesoscopic approach linking the microscopic molecular dynamics and the macroscopic physical variables: is a numerical method based on statistical mechanics. This section introduces the main concepts used for the LBM formulation. During the rest of this thesis, a given fluid (in liquid or gaseous phase) is considered, and the term "particle" refers to the molecules or the single atoms that compose the fluid, in the case of a monoatomic substance.

1.3.1 Maxwell-Boltzmann distribution

The Maxwell-Boltzmann distribution represents the probability to finding a particle with a given velocity in an idealized gas. The particles move freely and no interactions between the particles are considered except for collisions (with energy and momentum exchange). The thermodynamic equilibrium of the whole system is considered. This velocity distribution maximizes the entropy and conserves the average energy.

$$f(c) = \left(\frac{m}{2\pi k_B T}\right)^{\frac{3}{2}} 4\pi c^2 \, e^{-mc^2/2k_B T} \tag{1.1}$$

The Eq. (1.1) represents the normalized Maxwell-Boltzmann distribution, where *f* is the probability, per unit speed, to find a particle with a given speed $c = ({c_x}^2 + {c_y}^2 + {c_z}^2)^{1/2}$. Additionally, the parameters that determine the dispersion of the distribution are the temperature T and the mass m. The Boltzmann constant is k_B. The ratio $\sqrt{T/m}$ controls the distribution. Incrementing the temperature T leads the peak (most probably speed $\sqrt{2\,k_B T/m}$) of the distribution move to high velocities but also the probability distribution spreads.

The Boltzmann distribution stablish that the probability of being in a state with energy E is proportional to $e^{-E/k_B T}$, considering only the kinetic energy in one direction the Boltzmann distribution can be written as $f(\mathrm{c}_x) = (m/(2\pi k_B\, T))^{1/2} e^{-m{c_x}^2/2k_B T}$. The term $4\pi \mathrm{c}^2$ in the Maxwell-Boltzmann distribution (Eq. 1.1) accounts for the integration over the solid angle in the phase space of $f(\mathrm{c}_x) f(\mathrm{c}_y) f(\mathrm{c}_z)$.

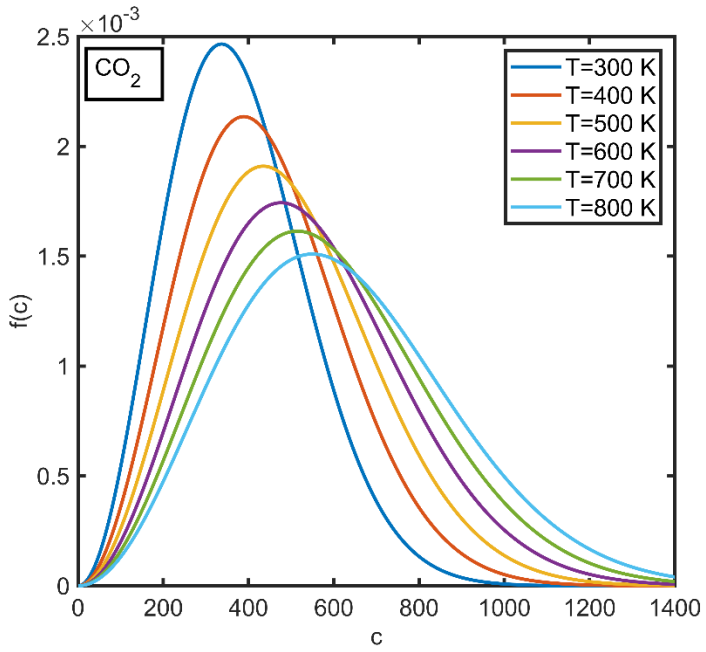

Figure 1.2 Maxwell-Boltzmann distribution with different temperatures. If the temperature increases, the average velocity increases as the dispersion of the distribution. CO_2 properties are considered to calculate this example.

Figure 1.2 represents the Boltzmann distribution calculated for carbon dioxide at different temperatures. Considering a gas in a volume in thermodynamic equilibrium, the distribution shape in each possible location and time must be similar, and it is possible to represent the probability in function of the velocity. Note that *f* has a bell shape, specifically a *chi* distribution. Given the probabilistic nature of the collisions between the molecules and the associated momentum transfer, it is expected that not all the particles have the same velocity. Instead, some particles have lower velocities, and some others have higher ones. Of course, if the temperature increases, the probability of finding a particle with higher velocities increases.

The exponential function in the Eq. 1.1 can be expanded in a Taylor series and truncated to obtain a polynomial approximation of the function. Moreover, some other function spaces can be used for the series expansion, in particular is of interest the Hermite polynomial base (conformed by the polynomials solution of the Hermite differential equation).

The collision process goes on in thermodynamic equilibrium, and momentum exchange is yet possible, but the statistical ensemble holds their distribution function.

1.3.2 **The Boltzmann equation**

The Boltzmann equation (also known as Boltzmann Transport Equation, BTE) describes the statistical evolution of a thermodynamic system that is not in equilibrium.

The statistical distribution of particles (or density distribution function) is represented by $f(\boldsymbol{r}, \boldsymbol{c}, t)$ which shows, for a given time t, the probability of finding a particle in a position $\boldsymbol{r} + d\boldsymbol{r}$ with a velocity $\boldsymbol{c} + d\boldsymbol{c}$; considering $\boldsymbol{r} = x\boldsymbol{i} + y\boldsymbol{j} + z\boldsymbol{k}$ and $\boldsymbol{c} = \mathrm{c}_x\boldsymbol{i} + \mathrm{c}_y\boldsymbol{j} + \mathrm{c}_z\boldsymbol{k}$. The density distribution function considers the probability to occupy an infinitesimal region in the space phase, i.e., an infinitesimal region d^3r and d^3c. The number of particles in a given time occupying this phase space can be obtained by integration of f over d^3r and d^3c. The total differential of f can be written as Eq. 1.2:

$$df = \left(\frac{\partial f}{\partial x}\right)dx + \left(\frac{\partial f}{\partial y}\right)dy + \left(\frac{\partial f}{\partial z}\right)dz + \left(\frac{\partial f}{\partial c_x}\right)du + \left(\frac{\partial f}{\partial c_y}\right)dv + \left(\frac{\partial f}{\partial c_z}\right)dw + \left(\frac{\partial f}{\partial t}\right)dt \qquad (1.2)$$

Using the gradient operator $\nabla = \left(\frac{\partial}{\partial x}\right)\boldsymbol{i} + \left(\frac{\partial}{\partial y}\right)\boldsymbol{j} + \left(\frac{\partial}{\partial z}\right)\boldsymbol{k}$ and $\nabla_c = \left(\frac{\partial}{\partial \mathrm{c}_x}\right)\boldsymbol{i} + \left(\frac{\partial}{\partial \mathrm{c}_y}\right)\boldsymbol{j} + \left(\frac{\partial}{\partial \mathrm{c}_z}\right)\boldsymbol{k}$ the velocity analogous operator, Eq.1.2 can be written as Eq.1.3:

$$df = \nabla f \cdot d\boldsymbol{r} + \nabla_c f \cdot d\boldsymbol{c} + \left(\frac{\partial f}{\partial t}\right)dt \qquad (1.3)$$

Using the body force $\boldsymbol{F}$ and the velocity $\boldsymbol{c}$ to rewrite the first two terms of the right side the Eq.1.4 is obtained:

$$df = \nabla f \cdot \boldsymbol{c}dt + \nabla_c f \cdot \boldsymbol{F}dt + \left(\frac{\partial f}{\partial t}\right)dt \qquad (1.4)$$

Considering that the number of particles in the considered infinitesimal space phase at given time changes by an inter-particle collision altering the particles that are scattered in and out of the considered volume, the total rate of change can be equaled to the collision operator *Q(f)*, Eq. 1.5.

$$\frac{df}{dt} = Q(f) \qquad (1.5)$$

In this way the total rate of change of f can be written as Eq.1.6. Known as the Boltzmann Transport Equation (BTE). This equation represents the equilibrium between the transport (left side) and the collision process (right side), and takes the integral-differential form:

$$\frac{\delta f}{\delta t} + \boldsymbol{c} \cdot \frac{\delta f}{\delta \boldsymbol{r}} + \boldsymbol{F}\frac{\delta f}{\delta \boldsymbol{c}} = Q(f) \qquad (1.6)$$

where the first term represents the local time derivative of *f*, the second the convective derivative or diffusion of *f* by its spatial gradient, and the third terms represents the transport by $\boldsymbol{F}$, the body force.

The collision operator $Q(f)$ can be approximated by considering only two colliding populations or "molecular chaos assumption". The two colliding particles are considered uncorrelated prior to the interaction and the velocities does not depends on their position, moreover the probability to occur a collision can be calculated by considering each particle separately. The molecular chaos assumption is known as the *Stosszahl ansantz*, recent works show the possibility to go beyond this assumption if two or more particles are considered deriving a new hydrodynamical treatment [3]. For two colliding distribution functions (f_1, f_2) the collision operator $Q(f)$ can be described in an integral form (over the solid angle Ω and the velocity

space $\boldsymbol{c}$) considering the cross-section of the collision $\sigma(\Omega)$ and transforms the incoming distributions into the outcoming distributions (f_1', f_2'), as it is showed in Eq.1.7:

$$Q(f_1, f_2) = \int\int \sigma(\Omega)|\boldsymbol{c_2} - \boldsymbol{c_1}|[f_1' f_2' - f_1 f_2] d\Omega d\boldsymbol{c} \tag{1.7}$$

A relevant consequence of the BTE and the *Stosszahl ansantz* is the H-teorem [4]: the H function is at a minimum when the particles follow a Maxwell-Boltzmann distribution ($H(t) = \int f \ln(f)\, d\boldsymbol{c}$), (isolated ideal gas with a total number of particles and energy fixed), if the distribution is different to the Maxwell-Boltzmann distribution the system is unstable and (trough the collisions) trends to the Maxwell-Boltzmann distribution, and trends to minimize H [5]. The H statistical function can be understood as a measure of information entropy, that can provide a base to interpretate the thermodynamic entropy [6]. Boltzmann results point to a microscopical probe of the second law of thermodynamics. However, in mechanical statistics this must be considered carefully, and subsequent works of Gibbs and Tolman highlight weaknesses in this approach: among others, by the implicit assumption that if collisions between some particles occur, some initial conditions that correlate the particles exist, driving to a contradiction with the uncorrelation assumption. This deep theoretical discussion is out of the scope of this work that deals with a numerical approximation based on statistical mechanics principles. Moreover, here quantum effects (that violates conservation of number of particles) are not considered.

The collision operator $Q(f_1, f_2)$ described in Eq.1.7 is very difficult to calculate directly, and the LBM is based on a further simplification described in the next section. Moreover, the BTE described in Eq. 1.6 is discretized in time, space, and velocity. The BTE, or Boltzmann kinetic equation is applicable for other macroscopic quantities as momentum, energy, or particle number for radiation problems.

1.4 LBM basic formulation

In this section, a basic description of the LBM is presented, not aiming to be a rigorous deduction of the method, but just to serve as an introduction to it. A more detailed overview of the method can be found in [7] and [8]. If interested, the reader can find parallel-computing optimized LBM open-source libraries such as Palabos [9,10] and OpenLB [11,12].

A novel way to solve the mechanics of a fluid emerged with the Lattice Gas Automata (LGA) method, which solves the fluid dynamics by applying a local interaction rule among a discrete number of molecules that move with a discrete set of velocities in a grid (or lattice). In 1974 was published a novel collision rule for the LGA on a square grid by Hardy, Pomeau and de Pazzis [13]; after that, in 1986, a new isotropic rule for a hexagonal grid was published by Frisch, Hasslacher and Pomeau [14]: this last model recovers the Navier-Stokes equations. These two models are considered the base of the LGA method. Some drawbacks of this approach such as statistical molecular noise, the non-physical meaning of some relations (as pressure dependance to velocity), and lack of Galilean invariance were found. The LBM overcomes the LGA drawbacks, taking also a restricted set of velocities for the molecules in a grid, but using a linearized form of the collision operator known as BGK (Bhatnagar–Gross–Krook, 1954 [15]), and using a probabilistic distribution of molecules instead of single molecules in the grid [16].

The first paper related to the method comes from 1988 McNamara and Zanneti [17] and the first viable computational implementation is from 1989 Higuera et al. [18]: the idea behind is that the macroscopic fluid properties emerge from the microscopic interactions of many particles but the details of the interaction of a single molecule do not affect the statistical macroscopic behavior of the fluid. The statistical distribution of particles (or density distribution) is represented by $f(\boldsymbol{r}, \boldsymbol{c}, t)$ as previously described.

To solve the Boltzmann equation, in addition to the BGK operator, the discretization of the velocity and the position space in the lattice denoted as *DxQy* is used (where *x* is the number of dimensions *D* (1, 2 or 3) and *y* is the number of possible velocities or velocity quadrature *Q:* a graphic reference is depicted in Fig. 1.3. In each position of the grid (or node), some *y* degrees of freedom allow the streaming and interaction between the density functions. Each one of the *y* degrees of freedom has a discrete velocity vector $\boldsymbol{c_i}$ and a distribution function $f_i(\boldsymbol{r},t)$ is directly associated: in this way the collision and transport between neighbor distribution functions is calculated individually with the following discrete lattice Boltzmann equation (LBE) for a given time step Δt, Eq.1.8:

$$f_i(\boldsymbol{r}+\boldsymbol{c_i}\Delta t, t+\Delta t) - f_i(\boldsymbol{r},t) = -\frac{\Delta t}{\tau}\left(f_i(\boldsymbol{r},t) - f_i^{eq}(\boldsymbol{r},t)\right) + s_i(\boldsymbol{r},t) \tag{1.8}$$

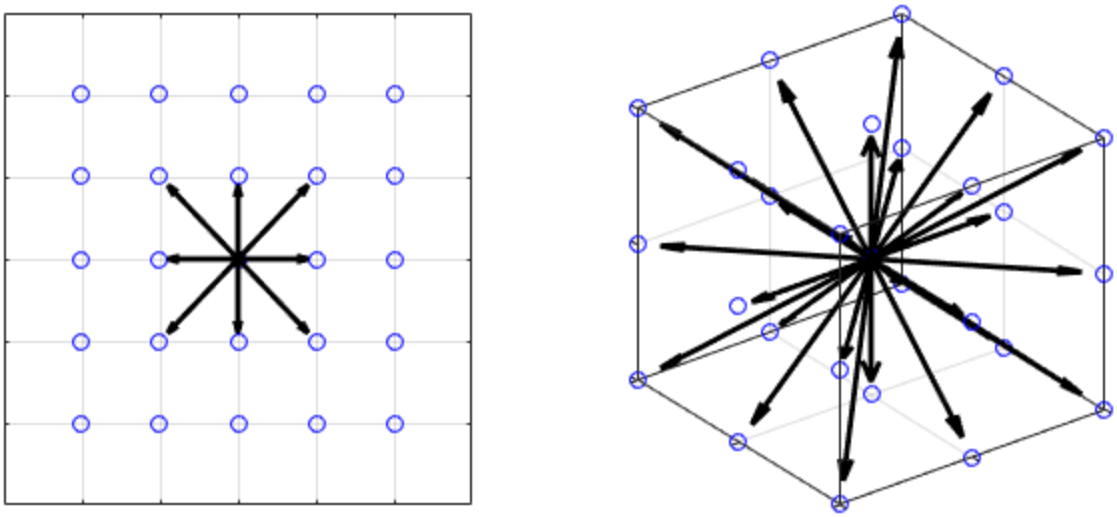

(**a**) (**b**)

Figure 1.3 Common grids used in the LBM (a) D2Q9; (b) D3Q27.

In the LBM algorithm, this discretized Boltzmann equation is divided into two steps, called stream-step and collision-step. In the collision-step, the first term in the right side of the equation represents the BGK collision operator and is used to calculate from the incoming population $f_i(\boldsymbol{r},t)$ an outcoming $f_i'(\boldsymbol{r},t)$ population relaxed to the equilibrium $f_i^{eq}(\boldsymbol{r},t)$ (τ represents the Single Relaxation Time SRT of this process), while in the streaming-step the left side of the equation is used for a single step of time Δt to transport the value of a particular density function $f_i'(\boldsymbol{r},t)$ to the next grid position $f_i(\boldsymbol{r}+\boldsymbol{c_i}\Delta t, t+\Delta t)$. The external source term $s_i(\boldsymbol{r},t)$ describes the coupling of the fluid with the environment and is the key to include external forces or potential energy interactions.

The equilibrium distribution function $f_i^{eq}(\boldsymbol{r},t)$ is approximated in the LBM as a Taylor expansion of the Boltzmann distribution. The exponential function in the Boltzmann distribution can be approximated as $e\text{^}(-x) = 1 - x + x\text{^}2/2 - x\text{^}3/3!$ ... Truncating this series holding the second order terms the equilibrium distribution can be calculated from the following equation, Eq. 1.9, that only depends on the macroscopic quantities density ρ and velocity $\boldsymbol{u}$ of the fluid:

$$f_i^{eq}(\boldsymbol{r},t) = w_i\rho\left(1 + \frac{\boldsymbol{c_i}\cdot\boldsymbol{u}}{c_s} + \frac{(\boldsymbol{c_i}\cdot\boldsymbol{u})^2}{c_s^4} - \frac{\boldsymbol{u^2}}{c_s^2}\right) \tag{1.9}$$

The sound speed c_s is a propagation constant in the computational domain that depends on the selected quadrature model: in the simplest case of *D2Q9* $c_s = 1/\sqrt{3}$; the discrete set of velocities $\boldsymbol{c}_i$ and the correlated weights w_i are also fixed in each quadrature model.

The macroscopic physical quantities can be calculated from the populations $f_i(\boldsymbol{r}, t)$ in each grid point, using the different integral *moments* of $f_i(\boldsymbol{r}, t)$ (integration of the probability density function over the quadrature space). The integration process leads to macroscopic variables as density $\rho(\boldsymbol{r}, t)$, velocity $\boldsymbol{u}(\boldsymbol{r}, t)$, momentum flux, or stresses. The calculation is relatively simple and only requires a simple summation over the y degrees of freedom in each position, i.e., for local density $\rho(\boldsymbol{r}, t)$ the zero-order integral *moment*, Eq.1.10:

$$\rho(\boldsymbol{r}, t) = \int f(\boldsymbol{r}, \boldsymbol{c}, t) d^3c = \sum_{i=1}^{y} f_i(\boldsymbol{r}, t) \tag{1.10}$$

and for the fluid velocity the *first-order moment, Eq.1.11*:

$$\boldsymbol{u}(\boldsymbol{r}, t) = \frac{1}{\rho} \int |\boldsymbol{c}| f(\boldsymbol{r}, \boldsymbol{c}, t) d^3c = \frac{1}{\rho} \sum_{i=1}^{y} \boldsymbol{c_i} f_i(\boldsymbol{r}, t) \tag{1.11}$$

The pressure $P(\boldsymbol{r}, t)$ can be obtained by the simple state equation, Eq.1.12:

$$P(\boldsymbol{r}, t) = c_s^2 \, \rho(\boldsymbol{r}, t) \tag{1.12}$$

The *Chapman-Enskog expansion* is an analytical method that allows the recovering of the Navier Stokes equations from the Lattice Boltzmann equation (Eq.1.8). The solution of the BTE is approximated by a series expansion in terms of the Knudsen number, ($Kn = \lambda / l$, i.e., the ratio between the molecular mean free path and the significant physical length); ref. [19] presents two ways to recover the macroscopic equations by the *Chapman-Enskog expansion* or a Taylor expansion. Following the *Chapman-Enskog expansion* is possible to obtain the value of the relaxation time τ and its dependence on macroscopic physical properties. In the described BGK-SRT model the relaxation time is related to the kinematic viscosity ν of the fluid by the Eq.1.13:

$$\nu = \frac{1}{c_s^2} (\tau - \frac{1}{2}) \tag{1.13}$$

The basic LBM-BGK (SRT) approximation is valid for relatively low Mach numbers ($Ma < 0.3$) to be within the incompressible limit (small density variations), but the model has evolved to be applicable to compressible flow and to enhance the Mach number limit. Some relevant modifications are called the regularized model or the entropic compressible LBM; a review of the progress in the development of the LBM for a high Mach number can be found in [20]. The Boltzmann equation has no limit for Kn and, for this reason, the LBM can be applied to study microfluidics problems. Regarding the Reynolds number Re, LBM can handle high values in the turbulent regime and can converge to a solution if a high dimensional discretization scheme is applied or some turbulence model is adopted.

To enhance the stability of the BGK model D'Humieres et al. [21] introduced a Multiple Relaxation Time (MRT) approach writing the collision operator using the moments space instead of the velocity space: this drives to multiple equilibrium equations and multiple relaxation times. In this way the model remains stable at high Reynolds numbers, but the computational time increases. The entropic model also enhances the stability of the LBM; modified relaxation time is calculated after each time step. If the solution begins to diverge from a stable condition the modified relaxation time should control the divergency. To know which modified relaxation time will correct the instability an entropy function is determined. The first entropic model was proposed in 1998 Karlin and Succi [22], and in 1999 by Karlin et al. [23], using a discretized form of the continuum Boltzmann entropy function; in 2001 Boghosian et al. [24] used the Tsallis entropy

function. Entropic LBM is stable at very high velocities without the computational drawback of the MRT model. An alternative attempt to give more stability to the LBM was developed in 2006 by Latt and Chopard [25]: The model is known as regularized LBM. In this model the density distribution function is separated into an equilibrium part and a non-equilibrium part, the collision operator is modified to operate only in the non-equilibrium part, and the enhancement of the stability is lower than in the entropic method but has no impact on the computational time and can be combined with the MRT. A common framework and a comprehensive analysis of the different collision models can be found in [26].

Implementation of the Boundary Conditions (BC) in LBM is still an open field of research. Some early works as Zou and He, 1997 [27] expand the Bounce back boundary conditions to include conservation of mass and momentum; in 2002 Zhao et al. [28] proposed an improvement of the BC based on extrapolation schemes; in 2003 Yu et al. [29] proposed a treatment for the curved boundaries based on a single interpolation scheme. An overview of the Boundary Conditions for the LBM with special attention to heat and mass transfer can be found in [30].

Figure 1.4(a) shows a *D2Q9* lattice with some boundary nodes (red line with empty circles) on the right side; the problem is to obtain the unknown incoming populations depicted as red arrows in the Figure 1.4(b), because there are no nodes on the right side of the boundary to propagate this information, The unknow populations are arbitrarily numbered as (f_4, f_5, f_6). One solution is to obtain this information is imposing an extrapolation scheme from the neighbour fluid nodes. In this way, the BC acts as an outflow pressure release. Some other proposals were developed to assign a value to the unknow populations, i.e., imposing the equilibrium value $f_4^{eq}, f_5^{eq}, f_6^{eq}$, or reflecting the incoming populations to obtain bounce back boundary conditions.

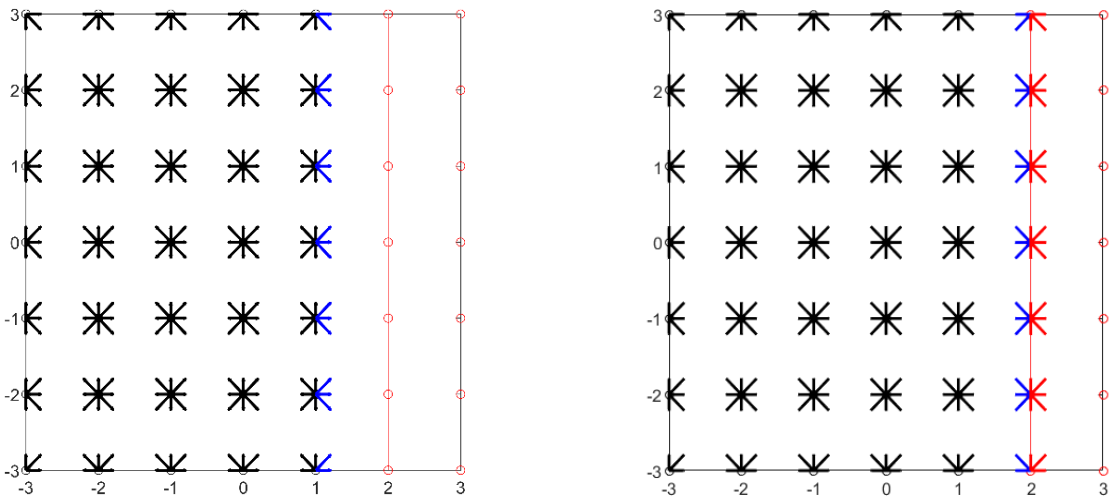

(a) (b)

Figure 1.4 Right side boundary nodes in a D2Q9 lattice with unknown populations (a) before the propagation of the populations to the boundary (blue arrows); (b) before the collision step the unknown populations (red arrows) must be calculated.

Some other interesting developments come from the classic work of Shan and Chen, 1993 [31], that introduces a model for multiphase fluids based on adding an interaction force between the phases into the equilibrium function. The current status of the Lattice Boltzmann Method applied to aerodynamics, aeroacoustics, and thermal flows was presented in [32]. The amount of literature concerning LBM is increasing and its theoretical development does not diminishes [33]; moreover, the future perspective of the method is supported on intensive research by LBM enthusiasts.

REFERENCES

[1] D. Arumuga Perumal, A.K. Dass, A Review on the development of lattice Boltzmann computation of macro fluid flows and heat transfer, Alexandria Engineering Journal. 54 (2015) 955–971. https://doi.org/10.1016/j.aej.2015.07.015.

[2] J.A. Bocanegra Cifuentes, D. Borelli, A. Cammi, G. Lomonaco, M. Misale, Lattice Boltzmann Method Applied to Nuclear Reactors—A Systematic Literature Review, Sustainability. 12 (2020) 7835. https://doi.org/10.3390/su12187835.

[3] G. Chliamovitch, O. Malaspinas, B. Chopard, Kinetic Theory beyond the Stosszahlansatz, Entropy. 19 (2017) 381. https://doi.org/10.3390/e19080381.

[4] C. Medel-Portugal, J.M. Solano-Altamirano, J.L.E. Carrillo-Estrada, Classical and Quantum H-Theorem Revisited: Variational Entropy and Relaxation Processes, Entropy. 23 (2021) 366. https://doi.org/10.3390/e23030366.

[5] H. Grad, On Boltzmann's H-Theorem, Journal of the Society for Industrial and Applied Mathematics. 13 (1965) 259–277. https://doi.org/10.1137/0113016.

[6] A. Ben-Naim, Entropy, Shannon's Measure of Information and Boltzmann's H-Theorem, Entropy. 19 (2017) 48. https://doi.org/10.3390/e19020048.

[7] S. Succi, The Lattice Boltzmann Equation for Fluid Dynamics and Beyond, Clarendon Press, Oxford, England, 2001.

[8] Z. Guo, C. Shu, Lattice Boltzmann method and its applications in engineering, World Scientfic Publishing co., Toh Tuck Link, Singapore, 2013.

[9] Home - Palabos - UNIGE, Home - Palabos - UNIGE. (2020). https://palabos.unige.ch/ (accessed June 2, 2020).

[10] J. Latt, O. Malaspinas, D. Kontaxakis, A. Parmigiani, D. Lagrava, F. Brogi, M.B. Belgacem, Y. Thorimbert, S. Leclaire, S. Li, F. Marson, J. Lemus, C. Kotsalos, R. Conradin, C. Coreixas, R. Petkantchin, F. Raynaud, J. Beny, B. Chopard, Palabos: Parallel Lattice Boltzmann Solver, Computers & Mathematics with Applications. (2020) S0898122120301267. https://doi.org/10.1016/j.camwa.2020.03.022.

[11] OpenLB – Open Source Lattice Boltzmann Code, OpenLB – Open Source Lattice Boltzmann Code. (2020). https://www.openlb.net/ (accessed June 2, 2020).

[12] M.J. Krause, A. Kummerländer, S.J. Avis, H. Kusumaatmaja, D. Dapelo, F. Klemens, M. Gaedtke, N. Hafen, A. Mink, R. Trunk, J.E. Marquardt, M.-L. Maier, M. Haussmann, S. Simonis, OpenLB—Open source lattice Boltzmann code, Computers & Mathematics with Applications. (2020) S0898122120301875. https://doi.org/10.1016/j.camwa.2020.04.033.

[13] J. Hardy, O. de Pazzis, Y. Pomeau, Molecular dynamics of a classical lattice gas: Transport properties and time correlation functions, Phys. Rev. A. 13 (1976) 1949–1961. https://doi.org/10.1103/PhysRevA.13.1949.

[14] U. Frisch, B. Hasslacher, Y. Pomeau, Lattice-Gas Automata for the Navier-Stokes Equation, Phys. Rev. Lett. 56 (1986) 1505–1508. https://doi.org/10.1103/PhysRevLett.56.1505.

[15] P.L. Bhatnagar, E.P. Gross, M. Krook, A Model for Collision Processes in Gases. I. Small Amplitude Processes in Charged and Neutral One-Component Systems, Phys. Rev. 94 (1954) 511–525. https://doi.org/10.1103/PhysRev.94.511.

[16] S. Succi, R. Benzi, F. Massaioli, A Review of the Lattice Boltzmann Method, International Journal of Modern Physics C. 4 (1993) 409–415.

[17] G.R. McNamara, G. Zanetti, Use of the Boltzmann Equation to Simulate Lattice-Gas Automata, Phys. Rev. Lett. 61 (1988) 2332–2335. https://doi.org/10.1103/PhysRevLett.61.2332.

[18] F.J. Higuera, S. Succi, R. Benzi, Lattice Gas Dynamics with Enhanced Collisions, Europhysics Letters (EPL). 9 (1989) 345–349. https://doi.org/10.1209/0295-5075/9/4/008.

[19] J. Lu, H. Lei, C. Shu, C. Dai, The more actual macroscopic equations recovered from lattice Boltzmann equation and their applications, Journal of Computational Physics. 415 (2020) 109546. https://doi.org/10.1016/j.jcp.2020.109546.

[20] R.M.C. So, R.C.K. Leung, E.W.S. Kam, S.C. Fu, Progress in the development of a new lattice Boltzmann method, Computers & Fluids. 190 (2019) 440–469. https://doi.org/10.1016/j.compfluid.2019.04.009.

[21] D. d'Humières, Multiple–relaxation–time lattice Boltzmann models in three dimensions, Philosophical Transactions of the Royal Society of London. Series A: Mathematical, Physical and Engineering Sciences. 360 (2002) 437–451. https://doi.org/10.1098/rsta.2001.0955.
[22] I.V. Karlin, S. Succi, Equilibria for discrete kinetic equations, Phys. Rev. E. 58 (1998) R4053–R4056. https://doi.org/10.1103/PhysRevE.58.R4053.
[23] I.V. Karlin, A. Ferrante, H.C. Öttinger, Perfect entropy functions of the Lattice Boltzmann method, Europhys. Lett. 47 (1999) 182–188. https://doi.org/10.1209/epl/i1999-00370-1.
[24] B.M. Boghosian, J. Yepez, P.V. Coveney, A. Wager, Entropic lattice Boltzmann methods, Proc. R. Soc. Lond. A. 457 (2001) 717–766. https://doi.org/10.1098/rspa.2000.0689.
[25] J. Latt, B. Chopard, Lattice Boltzmann method with regularized pre-collision distribution functions, Mathematics and Computers in Simulation. 72 (2006) 165–168. https://doi.org/10.1016/j.matcom.2006.05.017.
[26] C. Coreixas, B. Chopard, J. Latt, Comprehensive comparison of collision models in the lattice Boltzmann framework: Theoretical investigations, Phys. Rev. E. 100 (2019) 033305. https://doi.org/10.1103/PhysRevE.100.033305.
[27] Q. Zou, X. He, On pressure and velocity boundary conditions for the lattice Boltzmann BGK model, Physics of Fluids. 9 (1997) 1591–1598. https://doi.org/10.1063/1.869307.
[28] G. Zhao-Li, Z. Chu-Guang, S. Bao-Chang, Non-equilibrium extrapolation method for velocity and pressure boundary conditions in the lattice Boltzmann method, Chinese Physics. 11 (2002) 366–374. https://doi.org/10.1088/1009-1963/11/4/310.
[29] D. Yu, R. Mei, W. Shyy, A Unified Boundary Treatment in Lattice Boltzmann Method, in: 41st Aerospace Sciences Meeting and Exhibit, Reno, Nevada, US, 2003. https://doi.org/10.2514/6.2003-953.
[30] L. Jahanshaloo, N.A.C. Sidik, A. Fazeli, M.P. H.A., An overview of boundary implementation in lattice Boltzmann method for computational heat and mass transfer, International Communications in Heat and Mass Transfer. 78 (2016) 1–12. https://doi.org/10.1016/j.icheatmasstransfer.2016.08.014.
[31] X. Shan, H. Chen, Lattice Boltzmann model for simulating flows with multiple phases and components, Phys. Rev. E. 47 (1993) 1815–1819. https://doi.org/10.1103/PhysRevE.47.1815.
[32] K.V. Sharma, R. Straka, F.W. Tavares, Current status of Lattice Boltzmann Methods applied to aerodynamic, aeroacoustic, and thermal flows, Progress in Aerospace Sciences. 115 (2020) 100616. https://doi.org/10.1016/j.paerosci.2020.100616.
[33] S. Succi, Lattice Boltzmann 2038, EPL. 109 (2015) 50001. https://doi.org/10.1209/0295-5075/109/50001.

2. THERMAL FLUID MECHANICS AND ENERGY SYSTEMS

The term *energy systems* groups together different technological applications based on the physical principles of energy transformation and the interaction between energy and matter. Energy production and distribution are common examples of this kind of systems, e.g., solar cells, nuclear reactors, burners, and thermosyphons.

In many energy systems, fluids play a relevant role as the medium used to carry the bulk energy (main working fluid) or as secondary working fluid, for example, to couple two parts or cool down a sub-system. Fluids are of interest by their dynamics and the associated heat transfer mechanisms. The fluid mechanics is complex and includes different flow regimes that are often difficult to describe (turbulent regime). Moreover, the interaction between the fluid and solid gives origin to a particular heat transfer mechanism, convection. Although not all the energy systems use heat as the main energy form (for example, PV solar cells transform radiation into electricity), heat is generated in all those systems and must be removed and, if possible, profitably used. Thus, in this field, the thermal fluid dynamics behavior is of great interest.

Some specific topics in the energy systems were selected to show the applicability of the Lattice Boltzmann Method. The selection of those topics was based on their relevance in current technical and scientific research, the wide coverage of applied physics topics, the possibility to extrapolate the results to other energy systems, and the development of experimental activity at the DIME-UNIGE facilities.

The considered topics are nuclear reactors, natural circulation loops, nanofluid sedimentation, and acoustics.

2.1 Nuclear Reactors

The need for achieving energy sustainability and reliability, as well as cutting air pollutants, greenhouse gases, and ozone-depleting substances, could require nuclear energy to be part of the energy mix since renewable energies (such solar, wind, etc.) are inherently intermittent [1-3]. The penetration of the intermittent renewable energies in the power system demands increased flexibility, and since the nuclear operation may be flexible, it can help achieve a higher renewable energy penetration [4]. Moreover, with the advent of modern and foreseeable technologies such as fast reactors and seawater uranium extraction, nuclear energy could also be considered substantially *"renewable"* and potentially inexhaustible [5]. It has been even suggested that *"The support of a thermal reactor fleet in the mix will in all cases be needed until the end of the present century an even beyond, independently of the reactor type and global or regional plutonium mass availability"* [6]. However, the future scenario concerning nuclear fuel availability must be evaluated considering particular regional characteristics regarding possible energy demand growth, uranium availability, fuel cycle facilities and different type of reactors instead of considering only idealized *homogeneous* global trends [6]. Thereby, the relevance of the nuclear power plants on the energy production for different developed countries as the UK [7], France [8], or the US [9] (with nuclear power plants in function) is strongly contrasted between them and with those countries with fast economic growth as Brazil, Russia, India [10], China [11] or Pakistan [12], or some other regions without nuclear power plants as Italy [13], Turkey [14] or Ghana [15], with local context involving different variables that cannot be reduced only to economic viability or reduction of CO_2 emission. For now, could be expected that nuclear reactors

play a relevant and different role in the energy production in each world region, by which the research around Nuclear Reactors at different levels (fundamental physics, design, control, training, etc.) continues to be needed.

A nuclear (fission) reactor is a thermodynamic system that uses the great amount of energy generated by nuclear reactions of heavy radioactive materials as uranium in a controlled and self-sustained nuclear chain reaction. One of the common uses is electricity generation in nuclear power plants. In most of these plants, the energy emitted by the nuclear chain reactions can heat a working fluid and, typically, can generate electricity by means of steam turbine generators.

The heat removal from the core of the nuclear reactor, where the nuclear fuel is *"burned"*, is not only the main operating principle of the circuit but also the most relevant safety issue in this kind of systems in which the core temperature can typically rise to hundreds of degrees (°C) and the capability to predict the behavior of the system is fundamental [16]. Heat extraction from the core uses the working fluid as a coolant which can be either single-phase or multi-phase, where phenomena as boiling and nucleation occur. Some commonly used working fluids are water, helium, or in the next generation of nuclear reactors such as liquid metals like sodium, lead, or lead-bismuth eutectic. The working fluid removes heat from the core mainly by convection, natural or forced. In some cases, conduction is also relevant, e.g., if a liquid metal is used as the coolant. Commonly, the fluid is in a turbulent regime to enhance heat transfer coefficients, which means a flow characterized by a high Reynolds number (Re). The interaction between the fluid and the nuclear fuel in such complex geometries (e.g., arrays of fuel bars in a coaxial cylindrical vessel or fuel spheres in a pebble bed) determines the temperature gradients in the system.

Neutrons emission from the atomic nuclei and the subsequent kinetics in the surrounding medium is a fundamental part of a nuclear reactor system. Neutron transport is a complex process that includes the emission, scattering, and absorption, leading to flux patterns in space which determines the probability to find a neutron in a certain place and with a specific energy. As known, neutron kinetic can be (at least in principle) characterized by solving the neutron transport equations or by the simplified neutron diffusion approximation.

Computer modeling and simulation plays an important role in researching nuclear power with several applications as *"nuclear safety research, optimization of technical and economic parameters, planning and support of reactor experiments, research and design of new devices and technologies, design and development of simulators for operating personnel training"* [17]. for this reason, modern, accurate and efficient numerical techniques are required to design, study and simulate the physical phenomena that occur in complicate environments such as nuclear power plants, reducing the need of expensive and time-consuming experimental investigations: *"one important part of nuclear reactor simulation is the benchmarking process is used to demonstrate reliability and repeatability in the simulation of real cases, for which data are well documented (from reactor operation or experiments)"* [18].

The growing interest in Numerical Methods applied to physics and engineering fields, particularly to fluid dynamics problems, is related to the increment of the computing capabilities in modern devices [19]. This trend positively impacts the nuclear engineering field, where the possibility to predict the behavior of the systems in a nuclear power plant using high-fidelity simulation can help increase confidence concerning safety from stakeholders. The validation of computer codes and calculation methods in nuclear power plants must to fulfilled a series of criteria required by a framework of international organizations (Committee on the Safety of Nuclear Installations of Nuclear Energy Agency of The Organization for Economic Cooperation and Development and the International Atomic Energy Agency, with the support of institutions from different countries)[16,20], as will be shown in the chapter 3 the Lattice Boltzmann Method has great potential. However, more studies are required to accomplish the formal validation.

2.2 Natural Circulation Loops

Thermal energy is dissipated from several systems such as electronics, computers, and mechanical machinery. This dissipated energy can be considered as waste heat. On the other hand, several energy production systems use heat as the primary source, e.g., geothermal generators or nuclear power plants. The heat involved in those systems can be used *efficiently* if an optimized technology is used to transport this heat from the source to the desired heat sink. This *efficiency* must consider different thermodynamic factors (as heat transfer effectiveness), environmental factors (as the use of non-toxic substances and reduced energy consumption), and economic factors (as implementation cost and maintenance costs).

Natural Circulation Loops (NCL) are engineering systems used to transport heat from a source to a sink by the motion of a working fluid induced by the thermal expansion. It is interesting because this kind of thermal circuit can work without a pump or a recirculation system [21]. NCL finds application in several fields such as electronic cooling [22], solar systems [23], or nuclear power plants [24,25].

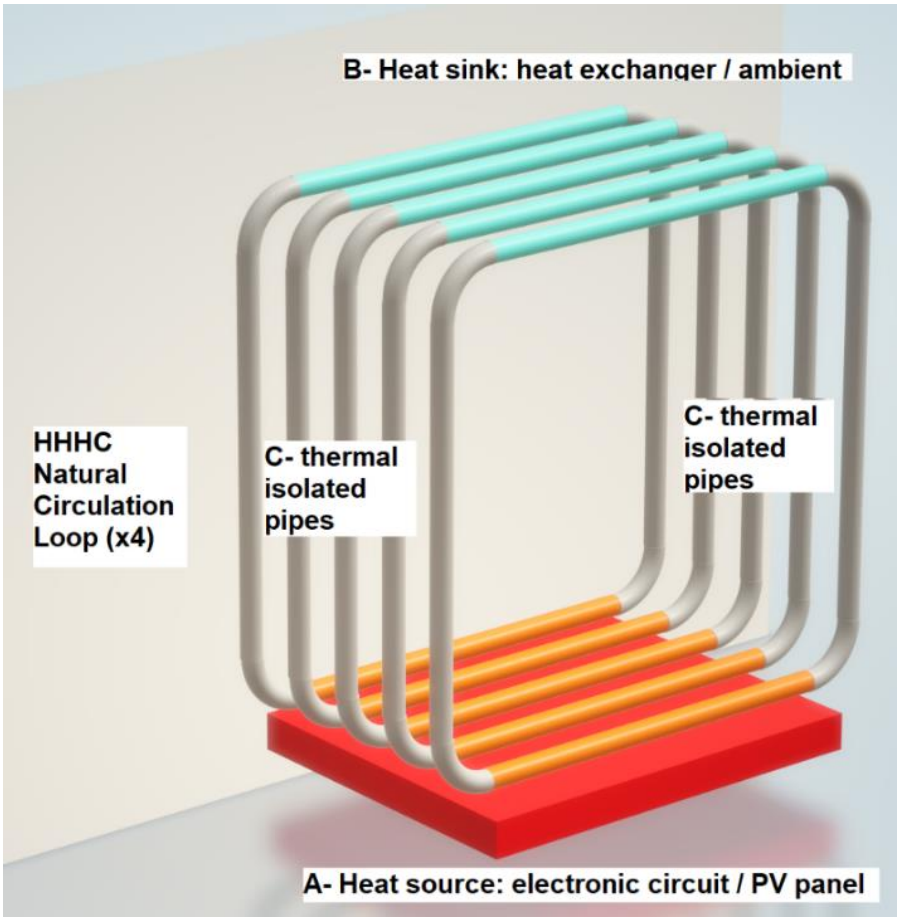

Figure 2.1 Application example: four NCL in horizontal heater horizontal cooler (HHHC) configuration transports the heat from A (circuit or PV panel, hot temperature) to B (heat sink, cold temperature). The number of loops can vary for each application.

Among the systems that need an effective cooling system in a mini-scale (under-meter systems) are common electronics and solar collectors. For example, in electronics and computation, the new trend of mining cryptocurrencies [26,27] and the use of massive computation clusters and data centers [28] lead to a constant heat production that must be efficiently transported to a convenient sink (in many applications this can be simply the ambient). On the other hand, a very interesting application can be found in the solar energy field: the PV panels work better at low temperatures, then the solar energy can be exploited implementing thermal-

voltage hybrid systems (PV-T): the heat can be stored and used for water heating [29] or can be used directly for other applications as dryer systems [30]. Fig. 2.1 presents a possible application of NCL.

As will be shown in chapter 4 the Lattice Boltzmann Method can be applied to simulate the thermohydraulic behavior of single-phase natural circulation loops under different operational regimes, including non-laminar (transition) regimes, and reproduce interesting experimental and analytical findings.

2.3 Nanofluids

Nanofluids are colloids consisting of a solid phase (nanoparticles) suspended into a liquid phase (base fluid), Choi [31]. The suspended nanoparticles change the physical properties of the base fluid; for example, they increment the thermal conductivity, and this effect depends on several conditions such as the nanoparticles volumetric concentration, nanoparticle dimensions, pH, and temperature ([32-38]).

The energy industry can be positively impacted by using fluids with superior thermal performance as nanofluids [37]. The employment of nanofluid as working fluid has been studied in geothermics [39-42], and some other heat transfer technologies as Natural Circulation Loops (NCL) [43], or solar flat collectors [44], showing an increase of the thermal efficiency. On the other hand, some solar energy systems make use of the altered optical properties of nanofluids, mainly by the enhancement of the radiation absorbance, to use the working fluid as a direct absorber [45-49].

The cost of the nanofluid preparation, the possible toxicity, the induced erosion (mechanical), and the corrosion (chemical), as the augmented viscosity, with consequent pressure drops and increased pumping power, are some of the problems observed during their employment in an energy system. In particular, the long-term stability of the nanofluids limits their use in real-life applications, i.e., when the gravitational sedimentation takes place, the uniform distribution of the solid phase is disrupted, and a higher concentration of nanoparticles at the bottom of the containers is noticed. Several operative conditions such as the storage time, rest time, high temperatures and thermal cycling, possible phase change, and cycling with high UV radiation (in solar applications) affect the nanofluid stability [50-56].

As will be shown later, in chapter 5, the Lattice Boltzmann Method can be applied to simulate the nanofluid sedimentation. It is possible to include different sub-models for the nanoparticle’s sedimentation velocity and diffusive behavior, reproducing long-term experimental results.

2.4 Acoustics

In energy systems, a particular phenomenon occurs, i.e., a fluid flow can induce noise. If the system is composed of pipes, as the nuclear reactors or the NCL, the noise can cause fatigue by acoustic-induced vibrations and compromise the system's safety [57]. Closed side branches are present in nuclear plants by the presence of safety relief valves of secondary emergency systems. It was found experimentally that for a specific flow rate, the cavity formed by a side branch can act as a Helmholtz resonator, generating high noise levels and excessive vibration that travels and affects the pipelines [58]. The possible origin of this kind of noise is related to the vortex shedding at the upstream edge of the resonant cavity and the successive impact of the traveling vortex with the downstream edge [59]. Corrugated tubes also have flow-induced noise [60], the mechanism seems similar, and the corrugated surface acts as a series of many resonant cavities. Some researchers studied the influence of the edge shape in the induced noise and tried different geometries to attempt a mitigation [61].

Many other flow-induced noises can be found, as turbulent jets at pipe outlets or edge noise (generated by the impact of a jet on edge) [62]. Visualizing the exact mechanisms experimentally in flow-induced noise is complex. Numerical methods are a valuable tool to understand the generation and mitigation mechanisms. All the mentioned cases (jet, edge, cavities) imply the simulation of complex fluid patterns with traveling

vortices and normally a mean fluid flow; then, the applicable numerical method must simulate complex transient flow patterns, vortices, and simultaneously the main flow and the acoustic field. Other acoustic applications of interest are related to sound absorption by porous materials or perforated plates [63,64].

The Lattice Boltzmann Method can be a useful tool to simulate different acoustic problems, including absorption by porous materials and flow-induced noises, as will be shown in chapter 6.

REFERENCES

[1] B.W. Brook, A. Alonso, D.A. Meneley, J. Misak, T. Blees, J.B. van Erp, Why nuclear energy is sustainable and has to be part of the energy mix, Sustainable Materials and Technologies. 1–2 (2014) 8–16. https://doi.org/10.1016/j.susmat.2014.11.001.

[2] K. Matsui, H. Ujita, M. Tashimo, Role of Nuclear Energy in Environment, Economy and Energy Issues of the 21st century Green House Gas Emission Constraint Effects, Progress in Nuclear Energy. 50 (2008) 97–102. https://doi.org/10.1016/j.pnucene.2007.10.010.

[3] A. Mezősi, B. Felsmann, L. Kerekes, L. Szabó, Coexistence of nuclear and renewables in the V4 electricity system: Friends or enemies?, Energy Policy. 140 (2020) 111449. https://doi.org/10.1016/j.enpol.2020.111449.

[4] J. Zhang, R. Leng, M. Chen, X. Tian, N. Zhang, The future role of nuclear power in the coal dominated power system: The case of Shandong, Journal of Cleaner Production. 256 (2020) 120744. https://doi.org/10.1016/j.jclepro.2020.120744.

[5] H.D. Lightfoot, W. Manheimer, D.A. Meneley, D. Pendergast, G.S. Stanford, Nuclear fission fuel is inexhaustible, in: 2006 IEEE EIC Climate Change Technology Conference, EICCCC 2006, Ottawa, ON, Canada, 10-12 May 2006, 2006: pp. 1–8. https://doi.org/10.1109/EICCCC.2006.277268.

[6] V. Romanello, M. Salvatores, A. Schwenk-Ferrero, F. Gabrielli, B. Vezzoni, A. Rineiski, C. Fazio, Sustainable Nuclear Fuel Cycles and World Regional Issues, Sustainability. 4 (2012) 1214–1238. https://doi.org/10.3390/su4061214.

[7] R.E. McKie, An environmental harm perspective to examine our understanding of UK nuclear energy expansion, The Extractive Industries and Society. 7 (2020) 556–564. https://doi.org/10.1016/j.exis.2019.10.011.

[8] J. Percebois, S. Pommeret, Storage cost induced by a large substitution of nuclear by intermittent renewable energies: The French case, Energy Policy. 135 (2019) 111067. https://doi.org/10.1016/j.enpol.2019.111067.

[9] A. Epiney, C. Rabiti, P. Talbot, A. Alfonsi, Economic analysis of a nuclear hybrid energy system in a stochastic environment including wind turbines in an electricity grid, Applied Energy. 260 (2020) 114227. https://doi.org/10.1016/j.apenergy.2019.114227.

[10] R.B. Grover, Green growth and role of nuclear power: A perspective from India, Energy Strategy Reviews. 1 (2013) 255–260. https://doi.org/10.1016/j.esr.2012.12.010.

[11] S.T. Hassan, Danish, Salah-Ud-Din khan, M. Awais baloch, Z.H. Tarar, Is nuclear energy a better alternative for mitigating CO2 emissions in BRICS countries? An empirical analysis, Nuclear Engineering and Technology. (2020) S1738573320302564. https://doi.org/10.1016/j.net.2020.05.016.

[12] M. Luqman, N. Ahmad, K. Bakhsh, Nuclear energy, renewable energy and economic growth in Pakistan: Evidence from non-linear autoregressive distributed lag model, Renewable Energy. 139 (2019) 1299–1309. https://doi.org/10.1016/j.renene.2019.03.008.

[13] A. Bersano, S. Segantin, N. Falcone, B. Panella, R. Testoni, Evaluation of a potential reintroduction of nuclear energy in Italy to accelerate the energy transition, The Electricity Journal. 33 (2020) 106813. https://doi.org/10.1016/j.tej.2020.106813.

[14] C.İ. Aydın, Nuclear energy debate in Turkey: Stakeholders, policy alternatives, and governance issues, Energy Policy. 136 (2020) 111041. https://doi.org/10.1016/j.enpol.2019.111041.

[15] E.B. Agyekum, M.N.S. Ansah, K.B. Afornu, Nuclear energy for sustainable development: SWOT analysis on Ghana's nuclear agenda, Energy Reports. 6 (2020) 107–115. https://doi.org/10.1016/j.egyr.2019.11.163.

[16] N. Aksan, An overview on thermal-hydraulic phenomena for water cooled nuclear reactors; part I: SETs, and ITFs of PWRs, BWRs, VVERs, Nuclear Engineering and Design. 354 (2019) 110212. https://doi.org/10.1016/j.nucengdes.2019.110212.

[17] M.Y. Tikhonchev, G.A. Shimansky, E.E. Lebedeva, V.V. Lichadeev, D.K. Ryazanov, A.I. Tellin, The role of computer simulation in nuclear technologies development, in: International Youth Nuclear Congress 2000: Youth, Future, Nuclear. Proceedings and Multimedia Presentation, Bratislava (Slovakia), 2000: p. 4. https://www.osti.gov/etdeweb/biblio/20236667.

[18] A. Rodríguez Hernández, A. Miguel Gómez-Torres, E. del Valle-Gallegos, Nuclear Reactor Simulation, in: N. Sayed Awwad, S. A. AlFaify (Eds.), New Trends in Nuclear Science, IntechOpen, 2018. https://doi.org/10.5772/intechopen.79723.

[19] M.L. Hosain, R.B. Fdhila, Literature Review of Accelerated CFD Simulation Methods towards Online Application, Energy Procedia. 75 (2015) 3307–3314. https://doi.org/10.1016/j.egypro.2015.07.714.
[20] Validation of Computer Codes and Calculation Methods, Office for Nuclear Regulation, UK, 2019. http://www.onr.org.uk/operational/tech_asst_guides/ns-tast-gd-042.pdf.
[21] M. Misale, Overview on single-phase natural circulation loops, in: International Conference on Advances in Mechanical & Automation Engineering, Rome (Italy), 2014: p. 13.
[22] J. Gu, D. Han, Y. Liu, Y. Li, C. Jin, W. Yu, Performance analysis of a thermoelectric generator with closed and flooded passive cooling in small-scale space, Energy for Sustainable Development. 51 (2019) 21–31. https://doi.org/10.1016/j.esd.2019.05.002.
[23] A. Rahmani, A. Boutriaa, A. Hadef, An experimental approach to improve the basin type solar still using an integrated natural circulation loop, Energy Conversion and Management. 93 (2015) 298–308. https://doi.org/10.1016/j.enconman.2015.01.026.
[24] M.K.S. Sarkar, A.K. Tilak, D.N. Basu, A state-of-the-art review of recent advances in supercritical natural circulation loops for nuclear applications, Annals of Nuclear Energy. 73 (2014) 250–263. https://doi.org/10.1016/j.anucene.2014.06.035.
[25] D.N. Basu, S. Bhattacharyya, P.K. Das, A review of modern advances in analyses and applications of single-phase natural circulation loop in nuclear thermal hydraulics, Nuclear Engineering and Design. 280 (2014) 326–348. https://doi.org/10.1016/j.nucengdes.2014.09.011.
[26] S.L. Náñez Alonso, J. Jorge-Vázquez, M.Á. Echarte Fernández, R.F. Reier Forradellas, Cryptocurrency Mining from an Economic and Environmental Perspective. Analysis of the Most and Least Sustainable Countries, Energies. 14 (2021) 4254. https://doi.org/10.3390/en14144254.
[27] A. de Vries, Bitcoin's Growing Energy Problem, Joule. 2 (2018) 801–805. https://doi.org/10.1016/j.joule.2018.04.016.
[28] P. Huang, B. Copertaro, X. Zhang, J. Shen, I. Löfgren, M. Rönnelid, J. Fahlen, D. Andersson, M. Svanfeldt, A review of data centers as prosumers in district energy systems: Renewable energy integration and waste heat reuse for district heating, Applied Energy. 258 (2020) 114109. https://doi.org/10.1016/j.apenergy.2019.114109.
[29] X. Ju, C. Xu, Z. Liao, X. Du, G. Wei, Z. Wang, Y. Yang, A review of concentrated photovoltaic-thermal (CPVT) hybrid solar systems with waste heat recovery (WHR), Science Bulletin. 62 (2017) 1388–1426. https://doi.org/10.1016/j.scib.2017.10.002.
[30] H.H. Al-Kayiem, Hybrid techniques to enhance solar thermal: the way forward, Int. J. EQ. 1 (2015) 50–60. https://doi.org/10.2495/EQ-V1-N1-50-60.
[31] S.U.S. Choi, J.A. Eastman, Enhancing thermal conductivity of fluids with nanoparticles, in: ASME International Mechanical Engineering Congress & Exposition, ASME, San Francisco, California, US., 1995: p. 9.
[32] S.K. Das, N. Putra, P. Thiesen, W. Roetzel, Temperature Dependence of Thermal Conductivity Enhancement for Nanofluids, Journal of Heat Transfer. 125 (2003) 567–574. https://doi.org/10.1115/1.1571080.
[33] H.U. Kang, S.H. Kim, J.M. Oh, Estimation of Thermal Conductivity of Nanofluid Using Experimental Effective Particle Volume, Experimental Heat Transfer. 19 (2006) 181–191. https://doi.org/10.1080/08916150600619281.
[34] H. Masuda, A. Ebata, K. Teramae, N. Hishinuma, Alteration of Thermal Conductivity and Viscosity of Liquid by Dispersing Ultra-Fine Particles, Netsu Bussei. 7 (1993) 227–233. https://doi.org/10.2963/jjtp.7.227.
[35] X. Wang, X. Xu, S.U.S. Choi, Thermal Conductivity of Nanoparticle - Fluid Mixture, Journal of Thermophysics and Heat Transfer. 13 (1999) 474–480. https://doi.org/10.2514/2.6486.
[36] W. Yu, D.M. France, J.L. Routbort, S.U.S. Choi, Review and Comparison of Nanofluid Thermal Conductivity and Heat Transfer Enhancements, Heat Transfer Engineering. 29 (2008) 432–460. https://doi.org/10.1080/01457630701850851.
[37] T. Ambreen, M.-H. Kim, Influence of particle size on the effective thermal conductivity of nanofluids: A critical review, Applied Energy. 264 (2020) 114684. https://doi.org/10.1016/j.apenergy.2020.114684.
[38] M.M. Tawfik, Experimental studies of nanofluid thermal conductivity enhancement and applications: A review, Renewable and Sustainable Energy Reviews. 75 (2017) 1239–1253. https://doi.org/10.1016/j.rser.2016.11.111.

[39] R. Du, D. Jiang, Y. Wang, K. Wei Shah, An experimental investigation of CuO/water nanofluid heat transfer in geothermal heat exchanger, Energy and Buildings. 227 (2020) 110402. https://doi.org/10.1016/j.enbuild.2020.110402.
[40] M. Daneshipour, R. Rafee, Nanofluids as the circuit fluids of the geothermal borehole heat exchangers, International Communications in Heat and Mass Transfer. 81 (2017) 34–41. https://doi.org/10.1016/j.icheatmasstransfer.2016.12.002.
[41] D. Sui, Investigation of Thermophysical Properties of Nanofluids for Application in Geothermal Energy, Energy Procedia. (2017) 6.
[42] F.A. Boyaghchi, M. Chavoshi, V. Sabeti, Optimization of a novel combined cooling, heating and power cycle driven by geothermal and solar energies using the water/CuO (copper oxide) nanofluid, Energy. 91 (2015) 685–699. https://doi.org/10.1016/j.energy.2015.08.082.
[43] M. Misale, F. Devia, P. Garibaldi, Experiments with Al2O3 nanofluid in a single-phase natural circulation mini-loop: Preliminary results, Applied Thermal Engineering. 40 (2012) 64–70. https://doi.org/10.1016/j.applthermaleng.2012.01.053.
[44] R. Mondragón, D. Sánchez, R. Cabello, R. Llopis, J.E. Juliá, Flat plate solar collector performance using alumina nanofluids: Experimental characterization and efficiency tests, PLoS ONE. 14 (2019) e0212260. https://doi.org/10.1371/journal.pone.0212260.
[45] S.K. Verma, Performance augmentation in flat plate solar collector using MgO/water nanofluid, Energy Conversion and Management. (2016) 11.
[46] O. Mahian, A. Kianifar, A.Z. Sahin, S. Wongwises, Performance analysis of a minichannel-based solar collector using different nanofluids, Energy Conversion and Management. 88 (2014) 129–138. https://doi.org/10.1016/j.enconman.2014.08.021.
[47] M.T. Jamal-Abad, A. Zamzamian, E. Imani, M. Mansouri, Experimental Study of the Performance of a Flat-Plate Collector Using Cu–Water Nanofluid, Journal of Thermophysics and Heat Transfer. 27 (2013) 756–760. https://doi.org/10.2514/1.T4074.
[48] T. Yousefi, F. Veysi, E. Shojaeizadeh, S. Zinadini, An experimental investigation on the effect of Al2O3–H2O nanofluid on the efficiency of flat-plate solar collectors, Renewable Energy. 39 (2012) 293–298. https://doi.org/10.1016/j.renene.2011.08.056.
[49] T.P. Otanicar, P.E. Phelan, R.S. Prasher, G. Rosengarten, R.A. Taylor, Nanofluid-based direct absorption solar collector, Journal of Renewable and Sustainable Energy. 2 (2010) 033102. https://doi.org/10.1063/1.3429737.
[50] T.B. Gorji, A review on optical properties and application of nanofluids in direct absorption solar collectors (DASCs), Renewable and Sustainable Energy Reviews. (2017) 23.
[51] A.K. Hussein, D. Li, L. Kolsi, S. Kata, B. Sahoo, A Review of Nano Fluid Role to Improve the Performance of the Heat Pipe Solar Collectors, Energy Procedia. 109 (2017) 417–424. https://doi.org/10.1016/j.egypro.2017.03.044.
[52] S.K. Verma, A.K. Tiwari, Progress of nanofluid application in solar collectors: A review, Energy Conversion and Management. 100 (2015) 324–346. https://doi.org/10.1016/j.enconman.2015.04.071.
[53] K Sopain, A.N. Al-Shamani, Sohif Mat, M H Ruslan, Azher M Abed, Effect of Using Nanofluids in Solar Collector: A Review, (2015). https://doi.org/10.13140/RG.2.1.3660.3603.
[54] P.K. Nagarajan, J. Subramani, S. Suyambazhahan, R. Sathyamurthy, Nanofluids for Solar Collector Applications: A Review, Energy Procedia. 61 (2014) 2416–2434. https://doi.org/10.1016/j.egypro.2014.12.017.
[55] F.S. Javadi, R. Saidur, M. Kamalisarvestani, Investigating performance improvement of solar collectors by using nanofluids, Renewable and Sustainable Energy Reviews. 28 (2013) 232–245. https://doi.org/10.1016/j.rser.2013.06.053.
[56] O.Z. Sharaf, R.A. Taylor, E. Abu-Nada, On the colloidal and chemical stability of solar nanofluids: From nanoscale interactions to recent advances, Physics Reports. 867 (2020) 1–84. https://doi.org/10.1016/j.physrep.2020.04.005.
[57] S. Takahashi, M. Ohtsuka, K. Okuyama, T. Ito, K. Yoshikawa, Experimental Study of Acoustic and Flow-Induced Vibrations in BWR Main Steam Lines and Steam Dryers, in: 2008: pp. 41–47. https://doi.org/10.1115/PVP2008-61318.
[58] S. Takahashi, K. Okuyama, A. Tamura, Y. Mabuchi, T. Kubota, K. Yoshikawa, Development of BWR Steam Dryer Loading Evaluation Methods Through Scale Model Tests Under Actual Steam Conditions, in: 2013. https://doi.org/10.1115/PVP2013-97564.

[59] K. Okuyama, S. Takahashi, A. Tamura, K. Nishida, M. Ohtsuka, M. Tsubaki, Flow Visualization of Acoustic Resonance for Safety Relief Valves in Power Uprated BWRs, in: 2009: pp. 11–18. https://doi.org/10.1115/ICONE17-75035.
[60] Y. Nakamura, N. Fukamachi, Sound generation in corrugated tubes, Fluid Dynamics Research. 7 (1991) 255–261. https://doi.org/10.1016/0169-5983(91)90018-E.
[61] Y. Xiao, W. Zhang, J. Li, X. Gao, C. Huang, H. Gu, Effects of edge geometry on the flow-induced acoustic resonances in closed side branches, Annals of Nuclear Energy. 160 (2021) 108372. https://doi.org/10.1016/j.anucene.2021.108372.
[62] W.C.P. van der Velden, S. Pröbsting, A.H. van Zuijlen, A.T. de Jong, Y. Guan, S.C. Morris, Numerical and experimental investigation of a beveled trailing-edge flow field and noise emission, Journal of Sound and Vibration. 384 (2016) 113–129. https://doi.org/10.1016/j.jsv.2016.08.005.
[63] K. Habibi, L. Mongeau, Prediction of sound absorption by a circular orifice termination in a turbulent pipe flow using the Lattice-Boltzmann method, Applied Acoustics. 87 (2015) 153–161. https://doi.org/10.1016/j.apacoust.2014.07.008.
[64] M. Ayub, A.C. Zander, C.Q. Howard, B.S. Cazzolato, D.M. Huang, A Review of MD Simulations of Acoustic Absorption Mechanisms at the Nanoscale, in: Proceedings of Acoustics 2013–Victor Harbor, Victor Harbor, Australia, 2013: p. 8.

3. APPLICATIONS TO NUCLEAR REACTORS ENGINEERING

The applicability of the Lattice Boltzmann Method in the Nuclear Reactor engineering field is important for several reasons, which do not only concern the relevance of nuclear energy in the sustainability development and the necessity to implement simulations to approach problems in a safe and effective way, but also by the inner capabilities of the LBM such as the easy handling of complex geometries, the inherently parallelizable algorithm, and the possible multi-physics application of the method. No literature item entirely summarizes the research works that implement the Lattice Boltzmann Methodology in the nuclear engineering field. A review on simulation methods coupling neutronic and thermal hydraulics for nuclear reactor analysis can be found in [1] without mentioning LBM.

Along with the results from a Systematic Literature Review concerning the "Lattice Boltzmann Method Applied to Nuclear Reactors" [2] some simulations are presented in this chapter showing the applicability of the LBM in this context.

In this chapter is given an overview of the framework and the application of the LBM in a wide range of nuclear engineering fields:

1. which problems in the nuclear engineering field have been addressed with the LBM;
2. how the LBM has been adapted to be applied in nuclear engineering problems;
3. how were validated the results;
4. explore some trends in the research of LBM applied to nuclear engineering problems;
5. test the nuclear variants of the LBM algorithm with benchmark simulations

The methodology adopted to accomplish the first four objectives is known as a Systematic Literature Review. We have identified the relevant literature items in the scientific databases through this methodology, following the general recommendations from [3,4].

The analysis is focused on the two general application fields:

Chapter 3.1 Computational Fluid Dynamics (including isothermal and thermal flow)

Chapter 3.2 Neutronics (including transport and diffusion).

Briefly, the data extraction was performed as described below:

- The specific nuclear engineering problem was identified, and the included items were classified into two categories (CFD applications and Neutronics applications);
- the adaptation of the LBM to solve the nuclear engineering problem was individuated (such as grid type, collision model, turbulence model);
- the validation techniques were subdivided into experimental, numerical, or analytic;
- the literature was sorted by date to provide an overview of the research trends;
- some special features or conclusions emerging from each study were extracted.

3.1 Computational Fluid Dynamics

The wide field of applications of the LBM as a CFD tool in nuclear engineering problems includes:

- Mixing of the coolant in the reactor vessel helps to understand if a thermocouple in the top head of the vessel can measure the mean temperature of the coolant at the exit knowing the mixing conditions. The isothermal flux around fuel rods is presented in [5-14]. A thermal approach to flow is explored in [15-17]. It is of great interest the investigation of the flux in the turbulent regime around the fuel rods, including geometric details of the nuclear implant as the grid separators.
- Pebbles recirculation associated with gas coolant circulation in an High Temperature Gas Reactor [18].
- Simulation of liquid metals used in recent reactors, [12,16,19].
- Corrosion mitigation mechanisms like Oxygen Active Controls [20-21] or mesh wires traps [22-23]. Crud formation mechanism and deposition schemes, [24], all applicable to liquid-metal reactors.
- Possible fractures in the reactor after a Small Break-Loss of Coolant Accident (SB-LOCA), by a high-temperature gradient following the emergency cold injection by a High-Pressure Injection system [25,26].
- After a Loss Of Coolant Accident (LOCA), how the debris (contaminant particulate material) can be trapped in weir traps under a wire floor [27,28].
- How flow acoustic resonances in steam dyer pipe are generated and can cause problems related to fatigue [29].

Some works in the CFD field related to nuclear engineering do not need a relevant modification of the traditional LBM scheme (i.e. [9,27,28]), but it is common to adapt the LBM with high discretization schemes in 3d as *D3Q27,* and with turbulence models, being the large eddy simulation (LES) the most basic turbulence model [5-7,11,15,29]. More sophisticated turbulence models as very large eddy simulation VLES or LES-WALE (Wall-Adapting Local Eddy viscosity) [8,12-14,16] are also used, leading to better results than LES and that the use of the LBM only without taking into account turbulence. It is relevant the inclusion of thermal field models [15-17,25,26] to upgrade the classical isothermal LBM to a numerical method capable of simulating the heat transfer mechanisms present in the reactor (in particular the convective heat transfer): the most commonly used is based in the secondary distribution approach. The inclusion of species transport is used to simulate chemical reactions such as corrosion and deposition [20], [21-24]. For what concerns CFD, is remarkable the work of the research group of Tiftikci, Kocar et al. [9,12-16].

3.1.1 Coolant mixing: Turbulent flow

Rod bundle flow in a Pressurized Water Reactor (PWR) (with a triangular array of fuel rods) was simulated by Hazi & Mayer in 2005 [5] using an isothermal LBM. Pulsation in the main flux was observed. The secondary flow pattern strongly depends on the exact geometry and the Reynolds number value. In subsequent work, Mayer & Házi in 2006 [6] simulate the flux around the fuel rods in a similar triangular symmetry and compare the performance in laminar and turbulent regimes for two lattices (*D3Q19* and *D3Q27*), finding that in a turbulent regime, only *D3Q27* reproduces the expected flux characteristics. Mayer et al. in 2007 [7] have simulated a similar geometry in the turbulent regime, using only *D3Q27* and LES turbulence model with an isothermal LBM framework to test the grid size independence of the solution. Specifically, the mean axial velocity agrees with the reference values, and the secondary flow is obtained with some recirculation cells. In conclusion, they validated the use of LES-LBM *D3Q27* to study the turbulent regime in bundle rods geometries.

Park in 2011 [8] developed a three-dimensional LBM simulation of a Very High-Temperature Reactor (VHTR) lower plenum. The turbulent flow phenomena in a scale model of the lower plenum of a typical prismatic VHTR were performed by two turbulent models: WALE (wall adapting local eddy viscosity) and a Smagorinsky-based LES. The velocity contours for turbulence flows and streamlines were compared qualitatively with benchmark data and results from a commercial CFD tool (Ansys Fluent).

Tiftikçi et al. in 2013 [9] developed a study concerning a 3D simulation of flux in a 2x2 rod bundle array of a PWR including some geometrical details as mixing vanes, in laminar regime, with no turbulent or thermal model, showing the capability of the LBM to handle velocity and pressure calculations in complex geometries. Carrasco in 2013 [10] applied the LBM to a coolant flow in a nuclear plant lower plenum of a PWR core: a simplified 3D coaxial geometry was simulated, and a successive grid refinement was applied to search complex flow phenomena and instabilities. A multiscale grid approach was developed to increase resolution by interpolating results only in the interesting zones, while a coarser grid was used in the relatively less complex geometry to overcome the computational effort for the calculations of high Reynolds number flows.

Park in 2015 [11] presented the simulation of flow on stage rod bundles in turbulent regime (2D geometry, using primitive cells and periodic boundary conditions) applying a Multiple Relaxation time (MRT) LBM, with an LES-Smagorinsky turbulence model. Comparing its results with experimental and CFD benchmark data showed a good agreement in velocity profiles and reproduced some phenomena as flow oscillations. The computational time reduction compared to other CFD techniques was highlighted.

Tiftikci and Kocar in 2015 [12] simulated a three-dimensional isothermal flux around the fuel rods, using hexagonal primitive domains with 7 rods with a helicoidal wire bundle separator enhancing the turbulence and the mixing process. They compare two turbulence models, i.e., LES (Smagorinsky) and Very-Large Eddies Simulation VLES (k-ε). Tiftikci and Kocar in 2016 [15] continued their research comparing thermal LBM with Finite Volume Method (FVM) in a triangular rod array geometry. They simulated the thermo fluid dynamic flow around the rods with and without rod spacers. The same authors presented in [13] the application of the isothermal regularized LBM to calculate the turbulent flux around a triangular array of rods. In this paper, a wide set of turbulence models was compared with FVM simulations and with experimental results. The authors conducted a sensitivity analysis of the results: testing grid size and turbulence model parameters (Smagorinsky constant, filter size) and testing the performance of the grid types *D3Q15*, *D3Q19,* and *D3Q27.* They found that the VLES turbulent model has a consistent performance in *D3Q19* and *D3Q27*, while *D3Q15* fails to reproduce the main turbulent characteristics. In 2016 Tiftikci & Kocar [16] presented a thermal turbulent flow simulation in a Prototype Fast Breeder Reactor (FBR) geometry, with uniform heat flux conditions and a hexagonal 7-wire rod primitive cell. The use of metal-liquid as a coolant (sodium) implies a low Prandtl number and a relevant role of conduction in the heat transfer process. The study compares two turbulence models, i.e., LES-WALE and VLES. This study made evident a better performance of the VLES turbulence model. In a successive work, Tiftikçi & Kocar (2018) [14] present a simulation of a Light Water Reactor (LWR) unit cell subchannel, a typical rod bundle square array. This study compared three turbulence models, i.e., LES-WALE, VLES (k-ε), and VLES (k-ω). It was also made a comparison for the grid resolution influence on the three models. Find that VLES models present a better approximation of experimental results with a relatively coarse mesh.

A simulation of flux around and inside a semi-porous thermal-active square medium was presented by Vijaybabu et al. in 2017 [17]. The porous approach can simplify computational effort for thermal simulations of rod bundles arrays with control rods.

3.1.2 Corrosion and deposition

The corrosion, deposition of sediments, oxide layer formation and behaviour is an open problem that affect the integrity of the implant components, compromising the stability and the effective lifetime of the implant

[30]. The problem is present in almost all the types of reactors because metallic alloys are commonly employed in the pipes and other parts of the implant as the valves.

The IV generation nuclear reactors are very interesting because implement a close fuel cycle. Some of them are cooled by fluids susceptible to oxidation, or corrosive fluids. The active control of oxygen in the lead-bismuth eutectic coolant can be a strategy to create a thin protective oxide layer that reduces the corrosion process, which is a relevant topic related to the safety and lifespan of the nuclear plant. Chen et al., 2007 [20], have used the LBM to study corrosion mechanisms in structural materials of nuclear plants that use lead-bismuth eutectic as coolant. They find that the corrosive effect diminishes, and a thin protective oxide layer is formed; the natural convection can be implemented to obtain a better mix. Chen et al. in 2007 [21] expanded the previous research, including forced convection.

Li (2011) [24] studied the crud formation. This phenomenon affects the performance of PWR by deposition and possible corrosion of several compounds changing the reactor geometry and heat transfer characteristics (this problem is also known as Axial Offset Anomaly).

Park et al. in 2012 [27,28] presented results from a deposition process in a Reactor Building Floor Weir as an option for particle deposition after a Loss Of Coolant Accident: the deposition of several materials in this safety device was simulated for different geometries using 2D models. Particle sedimentation near the weirs (barriers) was studied analyzing the velocity fields of the fluid as an indicator of sedimentation probability.

Tamura et al. in 2017 [22] and 2018 [23] presented a simulation of a cold trap in a Fast Breading Reactor to control hydrogen and oxygen concentration when liquid sodium is used as a coolant. The cold trap is simulated in a three-dimensional model using a modified low Reynolds number LBM for the impurity deposition of particles (LR-LBM-IDM). This model replaces the fluid cells with solid cells after a deposition condition is reached.

3.1.3 Other applications

Fan, et al. in 2009 [25] simulate extreme conditions in a PWR vessel when a cold-water injection from a High-Pressure Injection (HPI) system flows from the cold leg tubes to the upper side of the reaction chamber after a Small Break Loss of Coolant Accident (SB-LOCA). The cold plums of water injected into the vessel by the HPI system represent a risk due to the high-temperature gradients. Details on LBM implementation on a graphic processing unit GPU are provided in [26].

Tamura et al. in 2012 [29] applied the finite differences FD-LBM to simulate the flow acoustic resonance present in the steam dyer pipes of a Boiling Water Reactor (BWR), that can generate fatigue and malfunction due to the sound generated vibrations during extended power uprate operation; the resonance mechanism starts with vortex generation in the safety relieve valve and generates an acoustical wave that travels in the main dryer steam lines.

Wahba in 2017 [19] developed a study using the LBM to simulate natural convection in simple geometries with a low Prandtl number liquid medium (e.g., mercury, sodium, potassium), commonly used in Liquid Metal Fast Nuclear Reactors as a coolant given its low viscosity and high heat capacity. Successfully simulate convective cells in simple closed geometries.

Gui et al. in 2019 [18] analyzed the characteristics of the flux in a pebble type High-Temperature Gas Reactor (HTGR). They observed the recirculation process, an intermittent periodic flow pattern of pebbles, which implies a corresponding intermittent pattern in the gas circulation. The LBM was integrated with the Boundary Immersed Method (BIM) and Discrete Element Method (DEM) to simulate the fluid-solid interaction between the gas and the pebbles. A brief description of the main literature items regarding the direct use of LBM as a CFD simulator applied to nuclear engineering problems is summarized in Table 3.1.

Table 3.1 LBM as a CFD tool for nuclear engineering problems.

Study, year	Reactor type	Nuclear engineering problem	Lattice	Operator	Turbulence model	Thermal model	CPU GPU	Validation	Highlights
Hazi & Mayer, 2005 [5]	PWR VVER-440	Flux around fuel rods triangular array Hexagonal primitive cell	*D3Q27*	BGK	LES (Smagorinsky) vs. None	-		Experimental	Strong dependence between the flow characteristics (secondary flow/pulsation) and the changes in the geometry. LBM as a turbulent CFD
Mayer & Házi, 2006 [6]	PWR VVER-440	Flux around fuel rods triangular array	*D3Q19 D3Q27*	BGK	LES (Smagorinsky)	-		Experimental Analytical	Only D3Q27 reproduces the flux in the turbulent regime
Mayer et al., 2007 [7]	PWR VVER-440	Flux around fuel rods triangular array	*D3Q19 D3Q27*	BGK	LES (Smagorinsky)	-		Experimental Analytical	Validated with experimental data, axial velocities, and Reynold stresses. Normal stress shows systematic error.
H. Chen et al., 2007 [20]	Liquid Metal	Corrosion process: natural convection	*D2Q9*	BGK (species transport)	-	*Secondary distribution*		Experimental Analytical	Natural convection can be a uniform mixing strategy to add a protective thin layer of oxide. Secondary distributions and modified BC can be used to simulate the corrosion process
Y. Chen et al., 2007 [21]	Liquid Metal	Corrosion process forced convection	*D2Q9*	BGK (species transport)	-	*Secondary distribution*		Analytical	Tested inlet/outlet strategies in forced convection to enhance the oxygen transfer
Fan et al., 2009 [25], Kaufman et al., 2009 [26]	PWR	Fast cooling of the reaction chamber after a LOCA	*D3Q13*	Hybrid - MRT	-	Hybrid MRT	GPU cluster	Numerical (benchmark)	Formation of cold plumes in the vessel.
Park, 2011[8]	VHTR	Flux in the lower plenum	*D3Q ?*	MRT	WALE vs. LES (Smagorinsky)	-	6 core/ 4 CPU	Numerical (FVM)	Qualitative agreement with flow characteristics of the benchmark for low and high Re

Li, 2011 [24]	PWR /BWR	Crud formation coolant-wall interaction	*D2Q9*	BGK (species transport)		*Secondary distribution*		Analytical (benchmark)	LBM for species transport and deposition phenomena
Park et al., 2012 [27] [28]	-	Particle sedimentation in a Reactor Building Floor Weir after a LOCA	*D2Q9*	BGK	-	-		Experimental Numerical (benchmark)	Velocity field to determine the probability of particle sedimentation. Potential of weirs as emergency control devices
Tamura et al., 2012 [29]	BWR	Acoustic resonance in steam dryer lines	*D3Q13*	FD-LBM modified	LES Smagorinsky	-	acceleration	Experimental	Flow-acoustic resonance mechanism. Computational optimization of FD-LBM
Tiftikçi et al., 2013 [9]	PWR	Flux around fuel rods 2x2 array with bundle grid spacer	*D3Q19*	BGK	-	-		Analytical	Simulations in the laminar regime. LBM to handle velocity flow and pressure drops around complex structures
Carrasco, 2013 [10]	PWR	Flux in the lower plenum	*D3Q19*	BGK	-	-		Analytical Numerical (benchmark)	Multiscale procedure to zoom-in instabilities at high Re
Park, 2015 [11]	VHTR	Flux in the lower plenum	*D2Q9*	MRT	LES Smagorinsky	-	6 cores	Experimental Numerical (FVM) (Benchmark)	Turbulent flow passing staggered tube bundles array. Near the wall, the discrepancy is high, need of grid refinement
Tiftikci and Kocar, 2015 [12]	LMFBR	Flux around fuel rods Hexagonal primitive cell Helical wire spacers	*D3Q27*	BGK	LES VLES(k-e)	-		Experimental	Velocity profiles, friction factor, and Reynolds stresses validation. Inclusion of VLES model
Tiftikci and Kocar, 2016 [15]	PWR VVER-440	Flux around fuel rods triangular array	*D3Q19*	BGK	LES	*Secondary distribution*		Experimental Numerical (FVM)	Space grid effect in heat transfer and flow characteristic. Mesh refinement to obtain better temperature domains
Tiftikçi and Kocar, 2016 [13]	-	Flux around fuel rods triangular array	*D3Q15 D3Q19 D3Q27*	Regularized LBM	LES (Smagorinsky-Lilly, Van-Driest) VLES	-		Experimental Numerical (FVM)	D3Q15 doesn't reproduce turbulence. D3Q19 and D3Q27coherent results with VLES. At walls LES falls, Finer mesh drives to better results

Tiftikçi and Kocar, 2016 [16]	LMFBR	Flux around fuel rods 7 pin bundle array Hexagonal primitive cell	*D3Q27*	BGK	VLES WALE	*Secondary distribution (D3Q9*)	Experimental	VLES gives better agreement with experimental correlations. LBM can be implemented for T-CFD simulations of sodium-cooled fast breeder reactors
Vijaybabu et al., 2017 [17]		Porous approach to control rods. Thermal flux	*D2Q9*	BGK	-	*Secondary distribution*	Numerical (FVM)	Porous approach to thermal active zone affects heat transfer and flow characteristics
Wahba et al., 2017 [19]	LMFBR.	Natural circulation Low Pr number	*D2Q9*	BGK	-	*Secondary distribution (D2Q5*)	Numerical (LBM)	Lower Prandtl number reduces the effect of convection, higher oscillation amplitude and a longer period
Tiftikçi & Kocar, 2018 [14]	LWR PWR	Flux around fuel bars Periodic square array	*D3Q27*	BGK	LES WALE VLES (k-ε) VLES (k-ω)	-	Experimental	For intermediate grid resolution VLES (k-ε) and VLES (k-ω) models match with experimental data
Tamura et al., 2017 [22] and 2018 [23]	FBR	Cold trap, impurity precipitation in a mesh wire matrix	*D3Q15*	LR-LKS deposition	-	-	Analytical (Benchmark) Experimental	Validates Low-Re LR-LKS Model with impurity precipitation for oxygen. LR-LKS improves stability, reduces time
Gui et al., 2019 [18]	HTGR	Flux around pebbles Pebbles recirculation	*D2Q9*	BGK IBM-DEM	-	-	Experimental	Simulation of helium flux and pebble movements in recirculation condition, intermittent flux pattern

3.2 Neutronics: Transport and Diffusion

The second group of applications of the LBM in nuclear engineering problems regards the Neutronics: neutrons transport (NT) and neutrons diffusion (ND).

The neutronics is the basis for understanding the energy generation in the core of a nuclear reactor. A common nuclear plant uses thermal neutrons and/or high-speed neutrons produced by the fission process to obtain new fissions in the fuel. Inside the reactor the neutrons (and gamma radiation) emitted in the fission process travel inside different material media from the fuel domain to the surroundings, composed of different materials such as light-water or solid walls that can act as shields or as reflectors. The radiation can interact with these media through different reactions, like scattering or absorption. The probabilities of having the different types of interactions are normally considered by the material properties, of which the most important one is the total macroscopic cross-section $\Sigma_t = 1/\lambda$, it is inversely proportional to the mean free path value λ, and includes the absorption cross-section and scattering cross-section.

After early works in the '90s, such as [31], the viability of using the Cellular Automata to simulate neutron transport was established. Cellular Automata model for neutron transport is applied to two benchmark problems in [32]:

I. a neutron pulse that propagates from the center of the computational domain (this particular problem is not easy to be solved by traditional harmonic expansion due to the difficulty in representing the single initial event).
II. the evolution of a distributed source in scattering medium. The LBM evolved, taking profit from Cellular Automata's advantages as an alternative to traditional stochastic models

The LBM treats the complicated Neutron Transport phenomena as simple linear calculations. In early works, the solutions were obtained for isotropic scattering medium and with domains dimensions significantly larger than the mean free path; the multi-group solution was obtained and tested with some 1D, 2D, or 3D simulations. It is possible to enhance the efficiency of the LBM model for complex geometries using the finite volume (FV)-LBM or Mesh Refinement schemes.

Some issues concerning the use of LBM in Neutronics:

- mainly two research groups are working on the topic, i.e., Wang, Ma et al. ([33-42]) and Brinda, Gairola, Agarwal et al. ([43-49]).
- Neutron flux calculations in complex geometric arrays with different scattering/absorbing and reflective media can be found in [36,38,40,42,43,50,51].
- The simulations are carried out searching not just for steady-state solutions but also for time-dependent trends in [33-35,39,47,48].

- Solution to criticality problems related with the time-stability of the neutron flux are presented in [36,37,39,40,44-47].
- Interaction between thermal field and neutronics was researched in [52].

The LBM is adapted to solve NT (or ND) equations with an angular discretization scheme *DxQM* that considers scattering effects. Hybrid schemes using the FV approach to handle different meshes and represent complex domains [35,39]. Mesh refinement strategies are adopted to optimize resolution, handle curved geometries, and reduce computational cost [36-38].

The linear Boltzmann Neutron Transport Equation (NTE), Eq. 3.1, substantially describes the transport process by a conservation law. The first two terms on the left side of the equation represent the effects of the advection on the neutron flux $\Phi(\boldsymbol{r}, E, \Omega, t)$, and the scattering and absorption are represented by $\Sigma_t(r, E)$, while the right side represents the neutron source $s(\mathbf{r}, \mathrm{E}, \Omega, \mathrm{t})$.

$$\frac{1}{v}\frac{\partial \Phi(\boldsymbol{r}, E, \Omega, t)}{\partial t} + \Omega \cdot \nabla \Phi(\boldsymbol{r}, E, \Omega, t) + \Sigma_t(\boldsymbol{r}, E)\Phi(\boldsymbol{r}, E, \Omega, t) = s(\boldsymbol{r}, E, \Omega, t) \qquad (3.1)$$

The NTE is a seven-dimensional equation (three dimensions for space **r**, one dimension for energy E, two dimensions for angular space Ω, and one for time t) for a group of neutrons with velocity v. A first way to solve this equation could be a stochastic approach such as a Monte Carlo (MC) technique. It can be applied using ad-hoc random functions; generally, single neutrons are simulated during all their time-life, and the process is repeated several times for each neutron to derive statistically the Neutron Flux $\Phi(\mathbf{r}, \mathrm{E}, \Omega, \mathrm{t})$. Alternative, *deterministic* methods or different *statistical* methods can be applied (by its statistical nature LBM cannot be consider as a deterministic method or an ad-hoc random method); in this case, due to the difficulty in obtaining analytical solutions for complex geometries, some approximations are commonly used to simplify the partial differential equations before solving them by a numerical method:

- The energy is discretized, normally using multi-group approximations
- The angular dimension is discretized, commonly using the Discrete Ordinate Method (DOM or Sn) or Spherical Harmonics Method (SHM or Pn).

The multi-group simplification discretizes the continuous energy space of the neutrons into a series of non-overlapping energy groups, assuming an average and constant energy for all the neutrons belonging to each group; a classical (but rather simplified) approach uses only two groups: fast and thermal neutrons.

The DOM method discretizes the continuous angular variable into a series of non-overlapping solid angles and replaces the continuous direction *S* variables with a discrete set of direction vectors *Sn*. This discretization implies the use of Gaussian quadrature, i.e., for 1D is common to found *Q2, Q4, Q8,* and higher discretization quadrature up to *Q20*. In this way, a multigroup-Sn-NTE is obtained,

and the related partial differential equations can be solved by numerical methods such as FEM or FVM, as well as the LBM which also emerges as an option to discretize and solve the NTE working like a DOM but with a simpler angular discretization implementation. This makes the LBM more adaptable to different meshes (structured or arbitrary grid frameworks) and can provide a possible unique framework to neutronics and CFD calculations.

Methods like DOM and SHM are similar for what regards their formulation, using linear variants of the Boltzmann equation to calculate the evolution of the density distribution of neutrons.

In the LBM based approach, collisions among neutrons are neglected and the neutrons scattering is only related to the interaction between the neutrons and the nuclei of the propagation media. The discretized transport equation for the monochromatic neutron group g expresses the balance between collision and streaming of the neutron density distribution functions $\Psi_{\alpha,g}(\boldsymbol{r},t)$ in each of the discretized angular directions α, and is the basis for the Neutron Transport Lattice Boltzmann Method (NT-LBM), in this equation (Eq.3.2), s represents the source terms (truncation to first order is common and truncation to second order is called High order LBM or H-LBM scheme):

$$\Psi_{\alpha,g}(\boldsymbol{r}+\boldsymbol{e}_{\alpha}\Delta t, t+\Delta t)-\Psi_{\alpha,g}(\boldsymbol{r},t) = -\frac{1}{\tau_N}\left(\Psi_{\alpha,g}(\boldsymbol{r},t)-{\Psi_{\alpha,g}}^{eq}(\boldsymbol{r},t)\right)+\Delta t\, s_{\alpha,g}+\Delta t^2\, s_{\alpha,g} \qquad (3.2)$$

To ensure neutron conservation, the neutron angular flux $\Phi_g(\boldsymbol{r},t)$ must be equal to the summation of the local distribution functions $\Psi_{\alpha,g}(\boldsymbol{r},t)$ over all the angular directions α, the same condition must be fulfilled by the equilibrium distribution function ${\Psi_{\alpha,g}}^{eq}(\boldsymbol{r},t)$. Some models consider redundant the first right term of the Eq. 3.2 (the BGK collision term) for not interacting particles, then no equilibrium function is calculated, and the source term includes all the relevant effects as the scattering and absorption. In this thesis, this approach is called *no BGK term* and is adopted for the simulations.

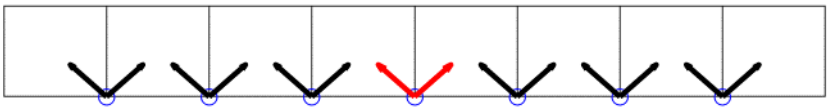

Figure 3.1 Lattice model D1Q2 for mono-dimensional problems, two possible angular directions.

In neutronic applications of the LBM, the common notation for the grid type *DxQM* differs from the *DxQy* notations used in the CFD-LBM because here *M* represents the number of possible angular directions in the scattering process, i.e., the lattice *D1Q20* is spatially similar to the CFD lattice *D1Q3*, but here *Q20* represents the discretization scheme adopted for the angular space for scattering. Figure 3.1 represents the simplest *D1Q2* lattice; the arrows represent two different neutron density distributions propagating to left and right neighbor cells in each time step.

If the zero-order *integral moment* of the probability function $\Psi_{\alpha,g}(\boldsymbol{r},t)$ is calculated, the scalar neutron flux $\Phi_g(\boldsymbol{r},t)$ in each grid, point can be obtained from a simple summation over the α index for all the *M* angular directions as:

$$\Phi_g(\boldsymbol{r},t) = \sum_{\alpha} w_\alpha \Psi_{\alpha,g}(\boldsymbol{r},t) \tag{3.3}$$

Applying a Chapman-Enskog expansion, it is possible to recovery the NTE (3.1) from the discrete Neutron Transport Lattice Boltzmann equation (3.2), relating the relaxation time τ_{N} for the neutron probability distribution with the transport process: the value of τ_{N} is physically related to the probability of a collision of the neutrons with the background nuclei of the media, consequently with the mean free path λ and with the macroscopic cross-section. In particular, the relationship for a group of neutrons with velocity v is given in Eq.3.4:

$$\lambda v = \left(\tau_N - \frac{1}{2}\right)\Delta t c_s^2 \tag{3.4}$$

The boundary conditions in NT problems include inlet flux conditions, reflective boundaries, vacuum boundaries, and bare boundaries, each one with an implementation on the LBM: specific descriptions of these BC can be found in the sub-chapter 3.3.

It is possible to consider the LBM in a first view as an Sn-like method where angular directions are tied to the spatial mesh. Comparative advantages for parallelization of the LBM over Sn could be lost under anisotropic flux due to the use of distributions with high angular quadrature that could induce coupling between not neighboring lattice points. However, the *finite*-LBM scheme or Sn-LBM introduced in [33] and [52] decouple the angular and spatial discretization (avoiding the coupling between not neighboring lattice points) and shows that LBM is a flexible solver for the Sn approximation that can hold the parallelization properties by applying the Spatial-Angular parallel model proposed in [38] that splits the angular discretization as an additional dimension on the computer memory array.

Erasmus in 2012 [50] confirmed the applicability of the LBM for neutron transport. He proposed a modified collision scheme named *"first collision source method"* to overcome blind spots in the domain, which are drawbacks in the numerical method linked to the fact that the propagation of neutral particles in LBM (neglecting the scattering) are constrained to move on the grid, and some zones of the domain cannot be reached by a neutron propagating in straight line. With the proposed scheme and the angular and spatial discretization refinement, it can overcome this drawback, and LBM becomes as accurate as other numerical methods. In the same way, Erasmus and Heerden in 2013 [51] present an angular refinement scheme to mitigate the ray effects (anomalous propagation in some diagonal grid directions).

Bindra and Patil in 2012 [43] used the NT-LBM (*no BGK term)* to simulate NT problems in one dimensional and two-dimensional arrays, searching a steady-state solution for the neutron flux solving the Linear Boltzmann Equation. The proposed scheme applies to anisotropic scattering terms, and the scattering integral is replaced by a summation on the angular Gaussian quadrature. They tested the NT-LBM with the Heaviside benchmark problems with and without scattering terms. The base for this work is the previous work of Ma et al. 2011 for one-dimensional radiation transfer [53]. In Bindra, 2013 [44], the previous work is extended using an NT-LBM (*no BGK term)* framework to solve NT problems. Here a one-dimensional problem including two media, source, and reflector, is simulated, and the criticality constant (eigenvalue problem) for a simple benchmark was found, validating the application of the NT-LBM in criticality problems.

McCulloch in 2013 [45] analyzed some possible solutions for heat radiation and neutrons transport problems implementing the weighted summations for the scattering term proposed in the previous models. For heat radiation, it was calculated the radiative heat transfer also including conduction and convection heat transfer mechanisms. The solutions for the radiation problem in 1D and the conductive-convective-radiative heat transfer in 2D were presented, showing the NT-LBM (*no BGK term)* capability to solve multi-physics problems in a single framework. For NT, the steady-state criticality problems in one-dimensional geometries were calculated with a multi-group approach (fast and thermal neutrons groups considered). Different slab geometries were tested, and a good agreement with the benchmark values for fuel domains bigger than 3 mean free paths (without reflectors) was found.

Agarwal et al. in 2015 [46] used the NT-LBM (*no BGK term)* for criticality problems in one-dimensional geometry (Isaa cell benchmark) and 2D arrays (BWR matrix benchmark with fuel and moderator) composed of two materials and using a multi-group approach (fast and thermal neutrons). They compared the performance of *D1Q2* vs. *D1Q4* and *D2Q4* vs. *D2Q8* angular quadrature and found that the LBM has a good degree of accuracy for solving eigenvalue problems in NT a high quadrature model improves the accuracy in the determination of the K_{eff} eigenvalue.

Gairola et al. in 2016 [47] implemented the NT-LBM (*no BGK term)* framework to solve time-dependent non-equilibrium neutron transport and criticality problems of a reactor through a model that assumes isotropic scattering. Two grids were proposed for the time-dependent problem *D2Q8* and *D2Q16* to solve the neutron flux in a heterogeneous medium composed of several materials. Two benchmarks were successfully solved: a 2D nuclear checkboard with an array of pure scattering and absorption regions around a source and a BWR primitive cell with two different regions. They found some numerical artifacts known as ray effects.

Using the NT-LBM (*no BGK term)* framework in time-dependent one-dimensional problem, and then in a 2D NT checkboard benchmark problem with monoenergetic neutron source at the center of the domain and pure scattering and pure absorptive array of blocks, Gairola & Bindra in 2017

[48] compared the results from the *D2Q8* LBM with the DOM *S6* solutions: a good agreement near the source was found, but numerical ray effects appear in both methods far from the source (near the boundaries of the domain).

In 2017 Wang et al. [34] solved the linear Boltzmann equation for NT in transient and steady-state problems. They used 20 angular directions in a one-dimensional problem for transient and steady-state solutions of a monoenergetic neutrons flux; different geometric configurations were tested (symmetric and asymmetric, regions bigger than 5 mean free paths). For thick regions of several mean free paths the method reproduces the expected results.

Wang et al. in 2017 [33] developed the *finite*-LBM scheme for transient problems of radiation transport (RT) and NT that handles multidimensional scattering terms in transient problems. While the previously discussed works presented a low angular resolution, the method proposed is a complete integration of the Sn technique into LBM. The angle discretization and the spatial discretization are explicitly unlinked in this model, and each angular direction is independent following a Lattice Boltzmann equation for each spatial direction i and each angle α the distribution functions must be written using an additional subindex $\Psi_{\alpha,i,g}(\boldsymbol{r},t)$ instead of $\Psi_{\alpha,g}(\boldsymbol{r},t)$ (used in the previous models), this is the clue to have local dynamic rules for a high angular resolution and be highly parallelizable.

A hybrid framework FV-LBM was proposed by Wang et al. in 2017 [35] to simulate NT and RT. This method showed flexibility in the geometric representation of the domains using unstructured meshes (tetrahedral or triangular) with good computational efficiency. The tested benchmarks were a one-dimensional array composed of two material domains, a two-dimensional square array with two materials, and a two-dimensional representation of a spherical source-shell array: these simulations showed the possibility to use the hybrid scheme in transient and steady-state neutron flux problems with complex curved geometries.

In the work of Ma et al. (2017) [36], the optimization of the NT-LBM is proposed, based on a refinement technique called SAMR (Structured Adaptive Mesh Refinement) the resolution in a specific region of the space can be improved, this technique allows to make a progressive mesh (grid) refinement subdividing the domain into blocks and applying a successive grid refinement in the different blocks until some convergence criterion is reached; the proposal overcomes the classic Adaptive Mesh Refinement drawbacks such as the data storage problems and subsequently reduces computational demand allowing accurate results in the simulations of NT problems. The SAMR model was tested with two-dimensional benchmarks at steady-state and time-dependent conditions using the multi-group approach.

Wang et al. in 2018 [37] improved the grid refinement using a technique called SSAMR (Streaming-based block Structured Adaptive Mesh Refinement) to overcome discontinuities in the

flux calculation, using the streaming process in the LBM to optimize the communication between the blocks. Besides, this study presented the theoretical deduction of the neutron's diffusion equation from the NT-LBM to show the physical meaning of the scheme: the dimensionless relaxation time describes the characteristic time that it takes to evolve from a non-equilibrium local distribution to a local equilibrium distribution and depends on the collisions between the neutrons and the background atoms in the media (mean free path). Specifically, through the Chapman-Enskog expansion, the neutron diffusion equation was derived as a first-order approximation of the NT-LBM, then it was theoretically showed that NT-LBM is more accurate than the ND equation to model neutronic problems. The model was tested with source-driven three-dimensional and two-dimensional benchmarks and in criticality problems.

Ma et al. in 2019 [38] developed a Multiblock Adaptive Mesh Refinement Scheme MB-AMR for NT in the LBM framework, using the *finite* Boltzmann equation and a multi-group Sn approach to the discretization problem. The Multi-Block approach divides the domain into fixed subdomains, and the AMR dynamically defines finer or coarser grids to solve neutron fluxes. The proposed method was tested with several benchmarks in one- and two-dimensions such as a Multilayer shield problem, Reed's cell short pulse transient, a square homogenous source-driven problem, and a MOX-type reactor, i.e., a complex geometric configuration with UO_2 and mixed-oxide (MOX) fuels surrounded by light water reflectors.

An hybrid model (neutron finite volume NT-FV-LBM) to solve the Neutron Discrete Velocity Boltzmann Equation was presented by Wang et al. in 2019 [39]. The effect of the discretization of the angular direction was studied, and it was found that it is possible to converge to a solution independent of the velocity discretization scheme; was highlighted the need to include the polar angle in the scattering, i.e., implementing a *D3QM* scheme even if the simulation represents a two-dimensional domain. The neutron diffusion solution converges to NT-FV-LBM solution in relatively low scattering media but is more accurate for higher scattering media.

In 2019 Wang et al. [40] have developed the high-order Lattice Boltzmann Method HLBM for multi-group neutron diffusion: the idea was to derive a method with a higher-order expansion from the Chapman-Enskog method which could lead to more accurate calculations of the source term. This ND-HLBM solves the multi-group neutron diffusion in the transient regime and criticality problems. The modified model drives to more accurate simulations.

It is interesting to see how new technologies allow simulating problems with complex geometries thanks to the increasing computational power and the more efficient schemes implemented for the numerical methods. The use of GPU hardware architectures allows the LBM to improve its capacities thanks to the intrinsic parallelism of the method. In Wang et al. (2019) [41], the implementation of the LBM (GPU-ND-LBM) to solve stationary and transient problems in neutron diffusion (using single and multiple GPUs) was presented. The code used a Predictor-Corrector

Quasi-Static Method to compute the accelerated neutron diffusion: this method factorizes the neutron flux in two parts: shape (quasi-stationary) and amplitude (time-dependent only). In this way, the computational time is reduced. The validation was done using benchmarks for steady-state, eigenvalue problems, and one space-time kinetic problem (a step perturbation transient system). The method can be implemented in a multi-group approximation using, e.g., two neutron groups: fast and thermal. It was highlighted that *"for the LBM approach, the non-linear term is local, and the non-local term is linear"* this implies an advantage for parallel computation. The diffusion equation is a low-order isotropic approximation of the neutron transport equation, and for this reason, Wang et al. in 2019 [42] improved the previous work with a GPU Neutron Transport LBM (GPU-NT-LBM). The method was tested with a mono-dimensional transient benchmark, a two-dimensional benchmark of a typical PWR, and a two-dimensional iron-water benchmark.

Agarwal et al. in 2020 [49] implemented a multi-group NT-LBM (*no BGK term)* for criticality problems in optically thin regions (mean free path close to system's dimension) and highly anisotropic scattering systems. In conclusion, this work improved the NT-LBM and validated the use of the method to solve criticality problems with multi-group and non-homogenous scattering, also for optically thin slabs.

Wang et al. in 2020 [52] presented an analysis of the use of LBM in multi-physics simulations of nuclear reactors, particularly coupling neutronics and heat transfer physics in a single model. The proposed Neutron Transport Heat Transfer Lattice Boltzmann Method NT-HT-LBM was validated in transient and steady-state simulations (compared with hybrid FVM-LBM results) and showed a simple unified framework that can be used in large-scale parallel computations of the nuclear reactor physics with the integration of classical neutronic approximations as LBM-Sn or LBM-Pn.

The main research papers regarding the use of the LBM in neutronic problems are summarized in Table 3.2.

Table 3.2 LBM applied to Neutronics.

Study /year	Neutronics	Benchmark/ problem	Criticality problem	Multi-group	Grid	Model	GPU/ CPU	Validation	Highlights
Erasmus, 2012 [50] [51]	Neutron transport	localized source in a scattering and absorbing material	-	-	*D3Q27*	NT-LBM First collision source method	GPU	Numerical MC DOM(Sn)	Overcome blind spots and ray effects. Angular refinement scheme to overcome problems in far nodes
Bindra and Patil, 2012 [43]	Neutron/ radiation transport	1D: Heaviside neutron flux (source moderator) 2D: (anisotropic scattering)	-	-	*D1Q2 D2Q4*	NT-LBM *No BGK term*	-	Numerical SHM(Pn) DOM(Sn)	Inclusion of scattering (isotropic and anisotropic) Steady-state problems
Brinda, 2013 [44]	Neutron transport	1D: source reflector	yes	-	*D1Q2*	NT-LBM *No BGK term*	-	Numerical SHM(Pn)	Solve the criticality problem in two regions slab geometry, *power iteration method*
McCulloch, 2013 [45]	Neutron/ radiation transport	1D: slab geometries	yes	yes	*1DQ2*	NT-LBM RT-LBM *No BGK term*	-	Numerical SHM(Pn)	Coupled model for heat transfer including radiation LBM in criticality problems with source regions > 3 mfp
Agarwal et al., 2015 [46]	Neutron transport	1D: Imaa two-region 2D: BWR	yes	yes	*D1Q2 D1Q4 D2Q4 D2Q8*	NT-LBM *No BGK term*	-	Numerical MC DOM(Sn)	High angular quadrature improves the eigenvalue calculation. Linear convergence (mesh resolution)
Gairola et al., 2016 [47]	Neutron transport, transient	2D: Checkboard array of scattering and absorptive blocks; BWR primitive cell	yes	-	*D2Q8 D2Q16*	NT-LBM *No BGK term*	-	Numerical DOM(Sn)	Drawback: ray effects
Gairola and Bindra, 2017 [48]	Neutron/ radiation transport	1D: time-dependent RT homogenous media 2D: NT Checkboard array	-	-	*D1Q2 D2Q8*	NT-LBM *No BGK term*	-	Semi-Analytic (Pn) Numerical DOM(Sn)	Drawback: ray effects. Near the boundaries and far from the source DOM S6 and LBM *D2Q8* don't match. Transient solutions
Wang et al., 2017 [34]	Neutron transport, transient	1D: asymmetric position	-	-	*D1Q20*	NT-LBM	-	Transport and diffusion approximation	NT-LBM validated for time-dependent and steady-state problems, symmetric and asymmetric source positions

Wang et al., 2017 [33]	Neutron/ radiation transport Steady-state, transient	2D: source and isotropic scattering /absorptive medium array	-	-	*D2Q9*	*finite* NT-LBM (Sn-LBM)	-	Numerical FVM, MC, Nodal synthetic kernel method (N-SK2) Analytic	Multidimensional extension of NT-LBM. Independent angular and spatial discretization.
Wang et al., 2017 [35]	Neutron transport Transient, steady-state	1D: 2regions 2D: Square; Spherical shell	-	-	*D1Q16* *D2Q48*	NT-FV-LBM	-	Numerical Nodal synthetic kernel method (N-SK2) Analytic	Complex geometry domain representation using triangular mesh
Ma et al., 2017 [36]	Neutron transport Mesh refinement	2D: Loosely coupled sources square TWILG reactor	yes	yes	*D1Q3* *D2Q9* *D3Q15*	NT-LBM-SAMR	-	Benchmark Numerical LBM vs LBM-SAMR	Block structure Adaptive mesh refinement: SAMR reduces computational cost (i.e. 60%). SAMR solve discontinuities in block interfaces
Wang et al., 2018 [37]	Neutron transport Mesh refinement.	2D: Loosely coupled sources square TWILG reactor 3D: source-driven	yes	yes	*D1Q2* *D2Q4* *D3Q6*	LBM-SSAMR	-	Benchmark	SSAMR overcomes discontinuity in neutron flux reduces computational cost (i.e. 80%). using the streaming process to communicate blocks. Diffusion equation recovery from NT-LBM:
Ma et al. 2019 [38]	Neutron/ radiation transport Mesh refinement	1D: Multilayer shield, Reed's cell, short pulse transient 2D: homogenous source-drive, MOX reactor	yes	yes	*D1Q3* *D2Q9*	MB-AMR *Finite* NT-LBM (Sn-LBM)	4-core	Analytical Numerical DOM(Sn)	Multi block AMR: Flexibility, accuracy, stability and computationally efficient method. Steady-state and time-dependent multi-group solutions
Wang et al., 2019[39]	Neutron Transport Steady-state transient	1D and 2D: Asymmetric source	-	-	*D2Q4* *D2Q8* *D2Q12* *D2Q25* *D3Q12* *D3Q24* *D3Q48*	NT-FV-LBM	-	Numerical Diffusion Transport Analytical	Lattice independent solution for sufficiently high quadrature. Triangular and quadrilateral mesh The polar angle needs to be considered even in 2D problems. Diffusion theory more accurate for high scattering medium
Wang et al., 2019 [40]	Neutron diffusion. transient	2D: source-driven, PWR (7domains) 3D:	yes	yes	*D1Q2* *D2Q4* *D3Q6*	HLBM (P1-LBM)	-	Numerical LBM vs HLBM vs FEM, FDM	HLBM (high order) is more accurate than LBM simulation with low truncation error.

Wang et al., 2019 [41]	Neutron diffusion	2D: Heterogenous PWR core, TWILG reactor	yes	yes	*D2Q4*	GPU-ND-LBM (P1-LBM	GPU	Benchmark Numerical	GPU parallelization of the ND-LBM. Steady-state, and transitory problems
Wang et al., 2019 [42]	Neutron Transport	2D: Heterogenous MOX reactor 1D: reed cell, iron water shield	-	yes	*D1Q20* *D2Q6*	finite GPU-NT-LBM (Sn-LBM)	GPU	Benchmark Numerical DOM (Sn)	Computational acceleration using Spatial-Angular parallelization mode
Agarwal et al., 2020 [49]	Neutron transport	1D: inhomogeneous thin media	yes	yes	*D1Q2,4,8, 16,32*	NT-LBM *No BGK term*	-	Numerical DOM(Sn)	Inhomogeneous scattering. Criticality value converges with a high angular discretization for thin media <5 mfp
Wang et al., 2020 [52]	Neutron transport coupled to heat transfer transient, steady-state:	1D: Pure absorptive material 2D: Fuel plate with temperature feedback, molten salt reactor	yes	yes	*D1Q3* *D2Q4* *D2Q9*	HT-LBM SN-LBM P1-LBM SP3-LBM	-	Numerical P1, FVM-LBM (COMSOL)	Unified framework for Sn-LBM, P1-LBM, SP3-LBM. Implemented for multi-physics models coupling heat transfer and neutron transport in a single framework

3.3 Numerical Simulations by LBM

This section presents some simulations in the nuclear reactor engineering field, implementing the LBM variants for thermal fluid flow and neutron transport; in this way some relevant results reported by the cited authors were replicated. The codes were developed using Palabos library in C++ [54-55] for CFD, and Matlab scripts for Neutronics.

3.3.1 CFD simulations

Figure 3.2 shows a two-dimensional simulation of flow on stage rod bundles in a turbulent regime. The primitive cell represents the PWR VVER-440 reactor geometry (with a triangular array of fuel rods, one central circle, and four quarter circles in the corners) for a high Reynolds number (*Re=20000*); the effect of the LES model to filter the turbulence and present smoother results is evident: the simulation shows how the main flux is positive in the *x*-direction but, the *y*-velocity field is linked to recirculation and vortex presence in each cell. Our results are similar to Park's [11] results.

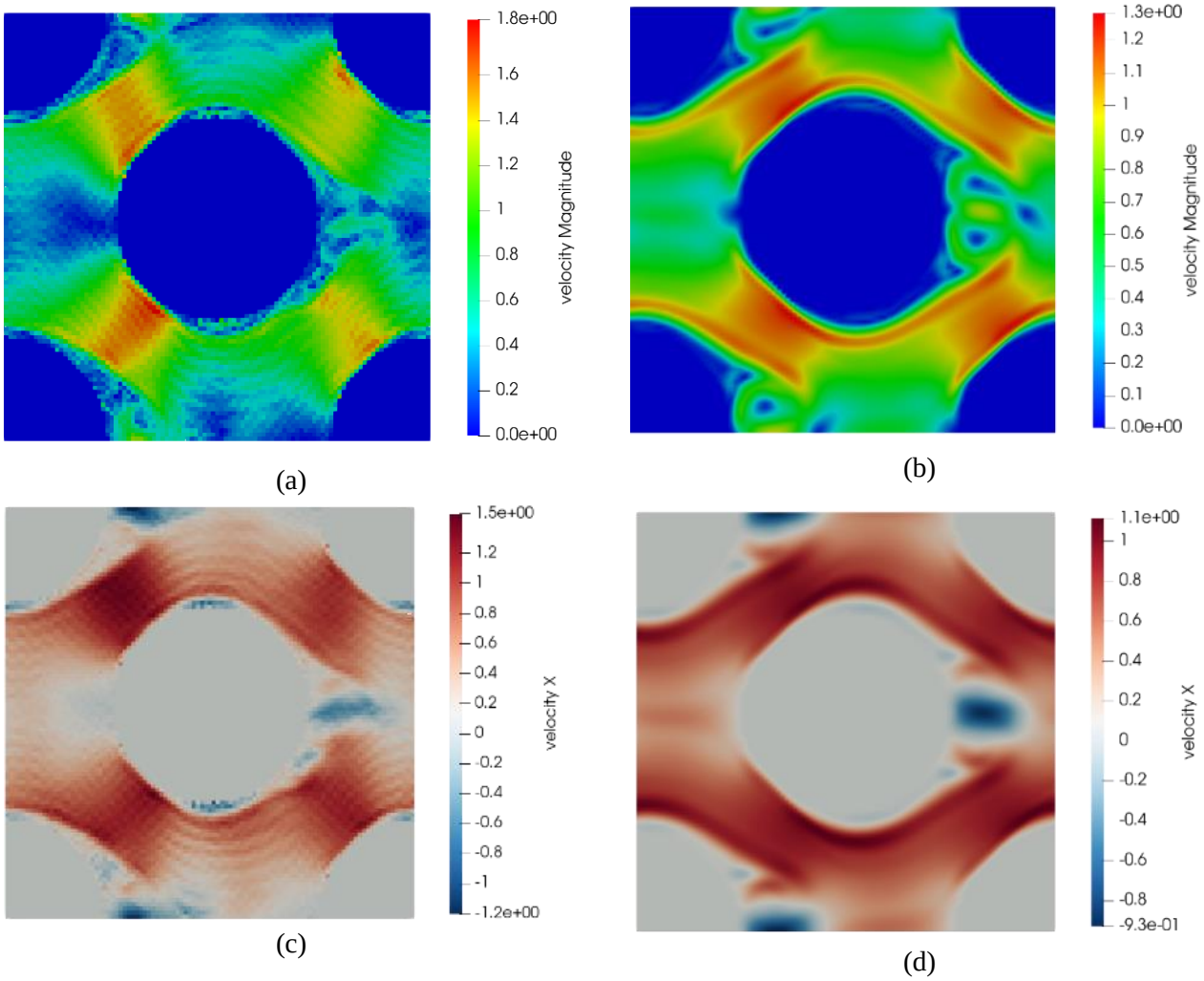

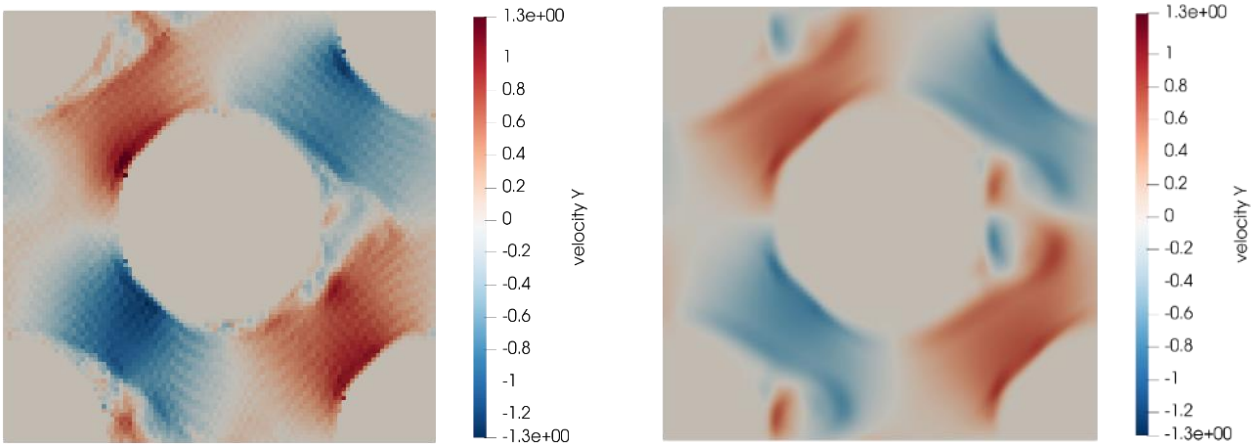

Figure 3.2 Stage rod bundles in turbulent regime (Re=20000) [11]: (a) Direct Numerical Simulation (DNS) of the velocity magnitude; (b) Smagorinsky Large Eddy Simulation (LES) of the velocity magnitude; (c) x velocity DNS; (d) x velocity LES; (e) y velocity DNS; (f)

Figure 3.3 shows the results from a thermal-fluid-dynamic simulation of a coolant (at 293 K) around a single hot rod (at 600 K) into a channel are represented, with a constant flow velocity at the inlet in the x-direction. The hot fluid is mixed following the characteristic vorticity of the turbulence. It is interesting to see how the flow characteristics are linked with the thermal field. The Palabos library was used in our simulations with a *D3Q19* lattice for CFD and a secondary thermal field approach with a *D3Q7* lattice and LES-Smagorinsky turbulence model.

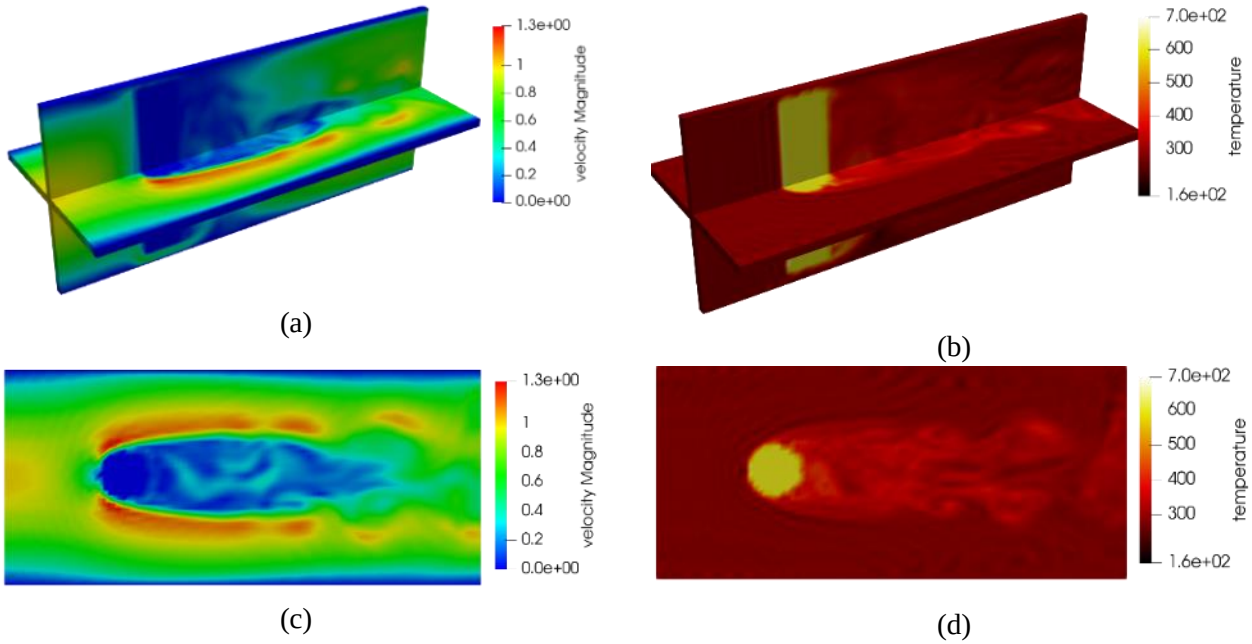

Figure 3.3 Thermal flow around a single hot-rod (Re=400) using LES turbulence model (a) Velocity magnitude three-dimensional representation; (b) Temperature field three-dimensional representation; (c) Velocity magnitude top side view; (d) Temperature field top-side

3.3.2 Neutronics simulations

There are a great number of benchmarks in one and two dimensions that are solved by validated numerical methods as DOM or MC-based methods and used by the researchers to test the LBM approach to Neutronics; many of them are related to the calculation of the scalar neutron flux in different configurations

with two or more regions including an active zone that emits the neutrons and represents the radioactive atoms in the nuclear reactor core. The results of this section can be generalized to radiation transfer, based on the Ma et al. work [53].

The specific algorithm considering source terms $s_{\alpha,g}$, absorption Σ_a, and scattering Σ_s is based on the following NT-LBE:

$$\Psi_{\alpha,g}(\boldsymbol{r}+\boldsymbol{e}_\alpha \Delta t, t+\Delta t) = \Psi_{\alpha,g}(\boldsymbol{r},t) + \Delta t(s_{\alpha,g} - \Sigma_a(r,E)\,\Psi_{\alpha,g}(\boldsymbol{r},t) + w_\alpha \Sigma_s(r,E)\Phi_g(\boldsymbol{r},t)) \qquad (3.5)$$

For criticality problems, the multiplication factor K_{eff} is considered in the source term $s_{\alpha,g}$, note the use of the zero-order moment $\Phi_g(\boldsymbol{r},t)$ to calculate the scattering term.

Considering a simple one-dimensional *D1Q2* model, the Left side boundary condition can be implemented as:

- Reflective BC, Eq.3.6:

$$\Psi_{1,g}(\mathbf{0}, t+\Delta t) = \Psi_{2,g}(\mathbf{0}, t) \qquad (3.6)$$

- Imposed flux F Dirichlet BC, Eq. 3.7:

$$\Psi_{1,g}(\mathbf{0}, t+\Delta t) = F \qquad (3.7)$$

- Special case of a Dirichlet BC, called vacuum BC, Eq:3.8:

$$\Psi_{1,g}(\mathbf{0}, t+\Delta t) = 0 \qquad (3.8)$$

- Imposed Neumann BC or zero gradient, Eq.3.9:

$$\Psi_{1,g}(\mathbf{0}, t) = \Psi_{1,g}(\mathbf{1}, t) \qquad (3.9)$$

Heaviside benchmark

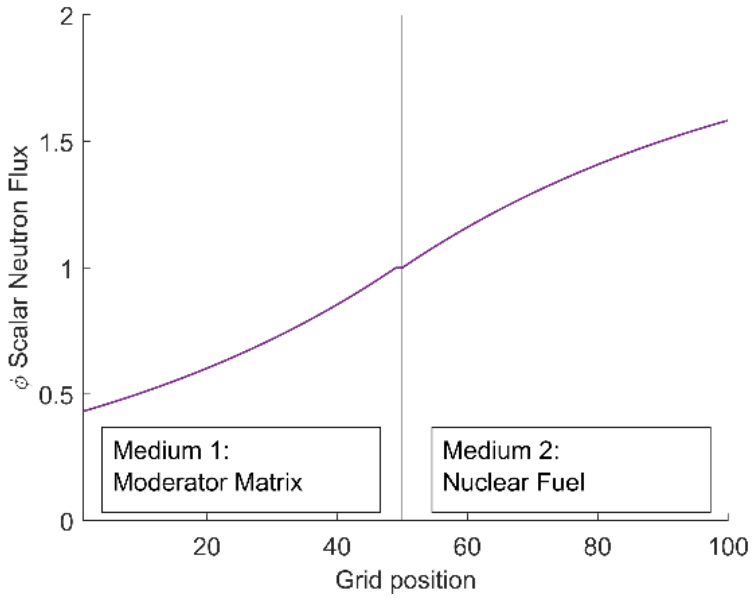

(a)

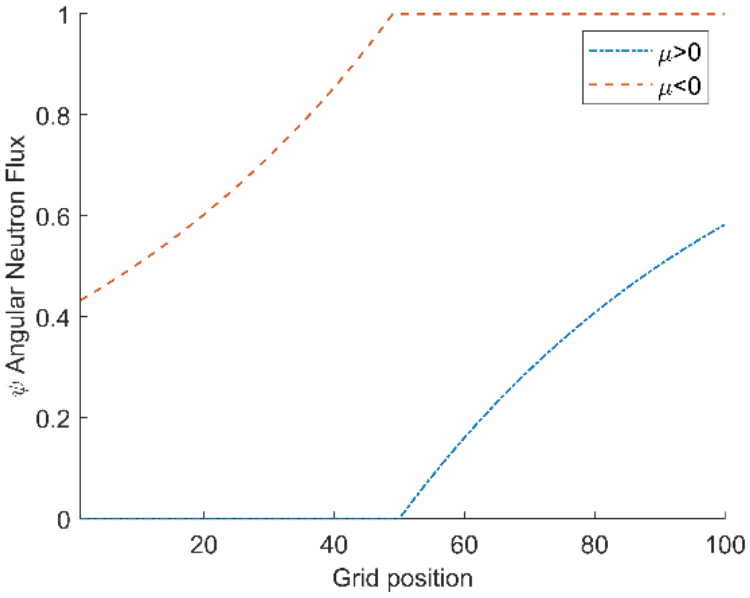

(b)

Figure 3.4 One-dimensional steady-state neutron problems Heaviside benchmark, region 1 is a pure absorptive medium, region 2 is the nuclear fuel (without scattering); (a) Scalar neutron flux vs. grid position for Heaviside benchmark. (b) Scalar neutron flux in each direction.

This benchmark has an analytic solution and was also presented for Radiative Transport (photons) [53]. The LBM solution reproduce the expected solutions as was showed in Fig 3.4 in concordance with the results showed in [43]. No scattering is considered in this simulation, note the absence of neutrons travelling to the right in the moderator matrix, (medium 1). The mismatch in the interface can be low if a finest grid is considered.

Bare benchmark

Figure 3.5 shows a bare nuclear source in all the geometric domain. This simulation considers isotropic scattering and zero flux BC. Results of our simulations replicate the results presented in [43] validated with SHM. The steady state distribution of the scalar neutron flux is symmetric and shows a peak in the center of the domain.

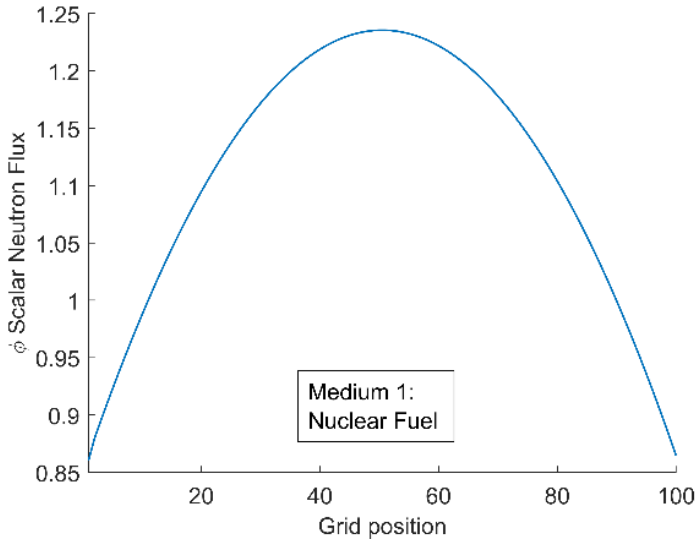

Figure 3.5 Scalar neutron flux for bare nuclear fuel benchmark with isotropic scattering term, [43].

Criticality problems

Of great importance is the calculation of the K_{eff} eigenvalue, known as the criticality problem. It consists in finding eigenvalue solutions to the NTE because, at least in principle, a reactor might work in critical conditions (i.e., with $K_{eff}=1$).

Figure 3.6 shows a one-dimensional benchmark problem used for criticality problems: here, the *power iteration method* was used to determine the value of the constant K_{eff}. This iterative method starts guessing the source term and the value of K_{eff} and then these two values are updated using the neutron flux calculated in each time step; the process is repeated until a convergence criterion is reached (some further details of the implementation can be found in [45]). The results coincide with the values presented by [44] K_{eff} =1.2752 (LBM), K_{eff} =1.2753(SHM), and the normalized curve for the scalar neutron flux as depicted in Fig. 3.6. This benchmark considers zero flux BC.

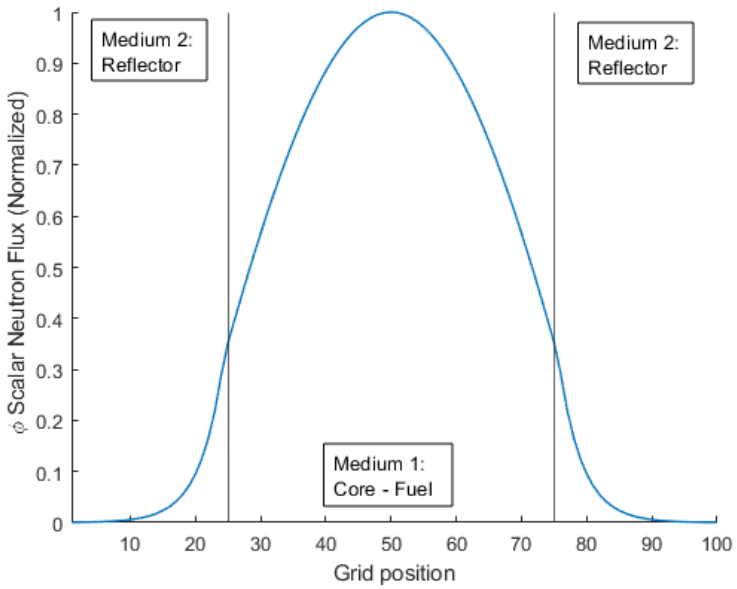

Figure 3.6 One-dimensional benchmark for criticality problems, normalized results. Central fuel region surrounded by reflector (without scattering) [44].

Isaa Benchmark

In this configuration two zones are considered the nuclear fuel medium 1 (absorption Σ_a=1, scattering Σ_s=0.5, source term S=1) and the moderator medium 2 (absorption Σ_a=0.8, scattering Σ_s= 0.4). The left side BC is considered reflective, and the right-side BC is vacuum. Results are presented in Fig. 3.7. The scalar neutron flux is appreciable in Fig.3.7(a). The angular flux presented in Fig 3.7(b) shows evidence of the scattering effect by the presence of neutrons travelling in the negative direction in the inactive zone. The convergence to the reference *solution presented in* [46] K_{eff} *=1.6479* is appreciable in Fig. 3.7(c).

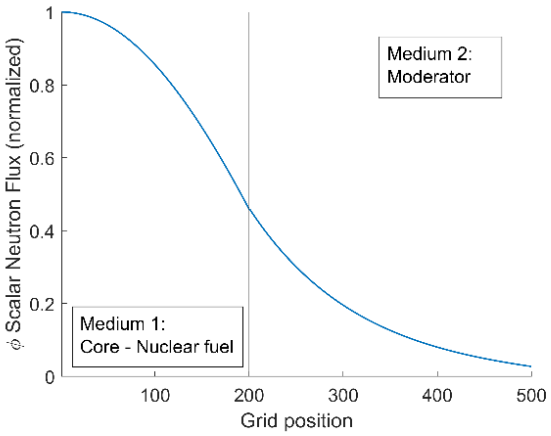

(a)

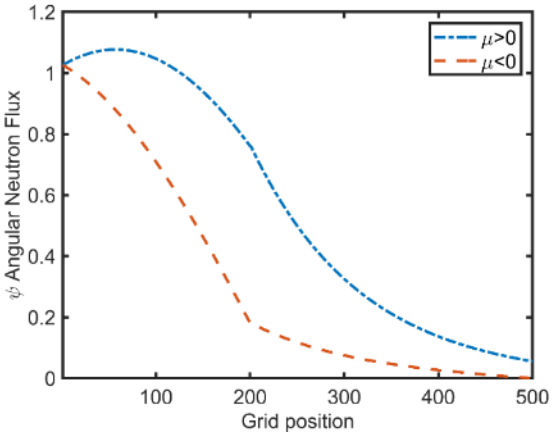

(b)

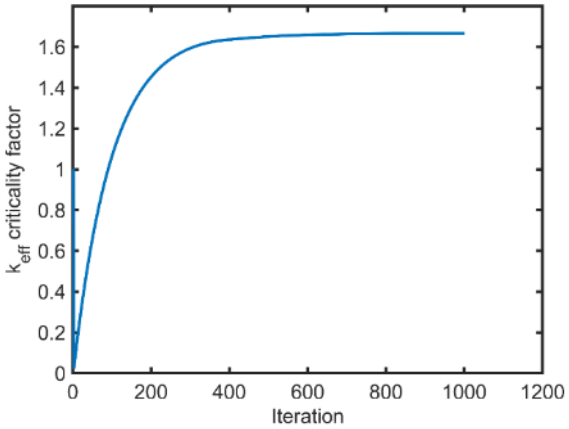

(c)

Figure 3.7One-dimensional benchmarks for criticality problems, normalized results for Isaa cell benchmark. (a) Scalar neutron flux (b) angular neutron flux, (c) criticality factor by the power iteration method. Reference solution K_{eff} =1.6479 presented in [46].

Checkboard benchmark

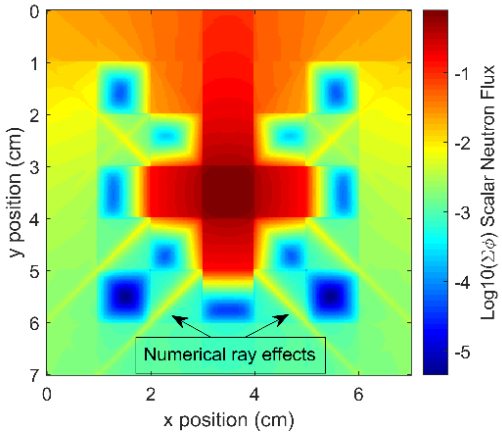

(a)

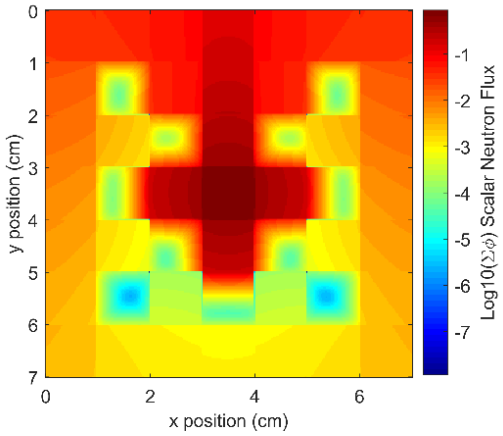

(b)

Figure 3.8 Two-dimensional checkboard benchmark presented in [47,48], scalar neutron flux in a logarithmic scale, the nuclear source is in the center surrounded by absorptive control bars and a diffusive medium. (a) D2Q8; (b) D2Q4.

Figure 3.8 represents the two-dimensional checkboard benchmark the nuclear source is in the center surrounded by absorptive control bars and a diffusive medium. A strong neutron flux is projected to the upside direction by the absence of a control bar. This benchmark was presented in [47,48] obtaining similar results. The scalar neutron flux is presented in a logarithmic scale. It is remarkable that the numerical artifacts, or ray effects, are appreciable using the *D2Q*8 lattice.

Application example: porous media for nuclear waste disposal

Some simulations concerning the use of porous materials to handle nuclear waste were performed, the two-dimensional algorithm *D2Q*8 was implemented. This illustrative example is included to show a common strategy to represent complex geometric domains using the LBM (Fig. 3.9).

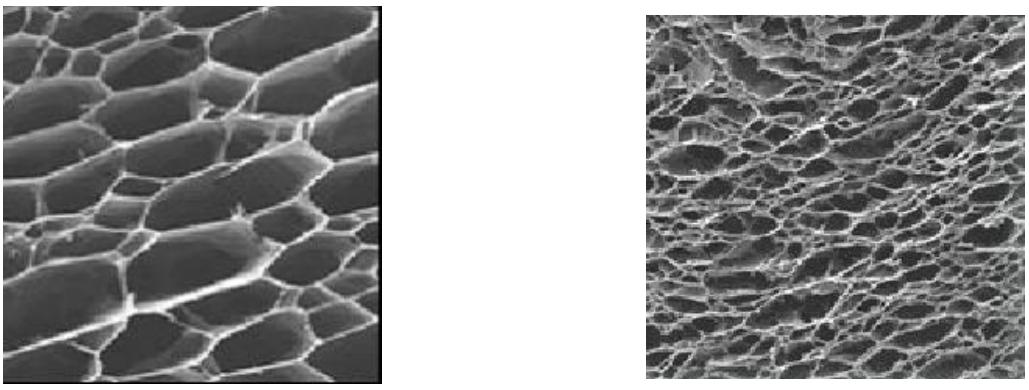

(a)

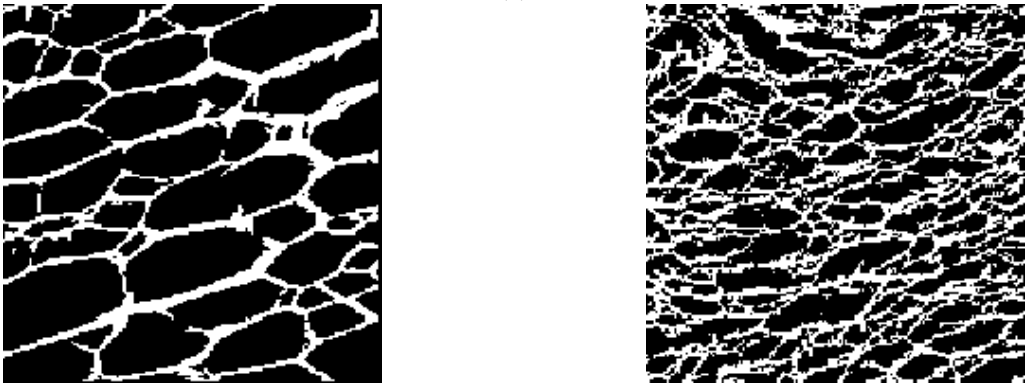

(b)

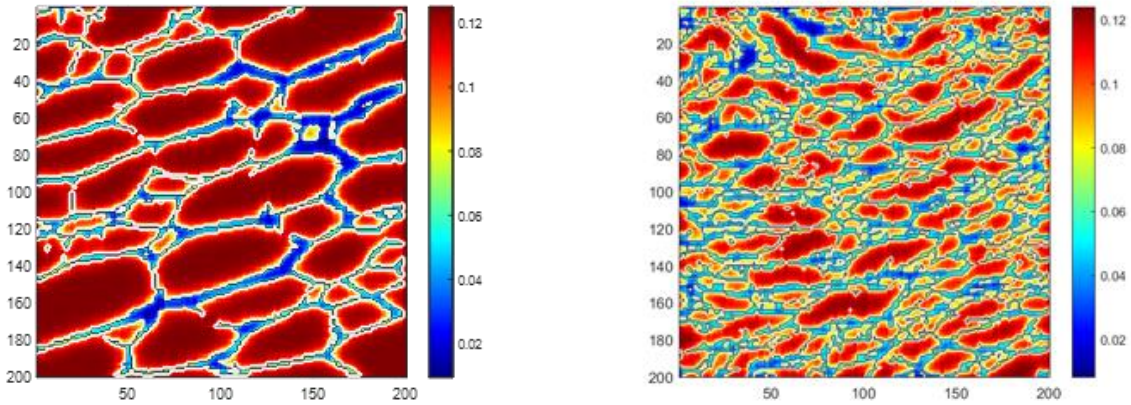

(c)

Figure 3.9 NT-LBM to calculate the radiation field considering complex geometries of porous media. (a) Microscopy image (adapted from [56]); (b) Boolean mask; (c) calculated radiative field (the units are arbitrary).

The main steps followed were:

1. a microscopic image of the porous material was obtained (adapted from [56]). Fig. 3.9(a).
2. the image was filtered using a threshold to obtain a Boolean mask (a matrix containing 1 and 0 to represent the presence or not of the foam material). Fig. 3.9(b).
3. the Boolean mask was used to assign the dynamics of each node in the lattice (the dynamic is linked to the physical properties, for example assign to each node the characteristics of a source, a reflector media, or absorptive media).
4. the LBM NT algorithm for *D2Q8* was used for the steady-state radiative field calculation. Fig. 3.9(c).

For this example, two different foam structures are compared, it is visible how the model captures the complex geometry of the foam. Also, it is visible, from the calculated radiative field, that the second foam, with small units could generate a better absorption. Use of porous materials to handle nuclear material (including nuclear waste) are of great interest, because can be used as containers, buffer separators or filters for decontamination, [57-59].

3.4 Conclusions

In this chapter, a Systematic Literature Review concerning the use of the Lattice Boltzmann Method in Nuclear Reactor Problems was presented, including data from 45 research items from 2005 to 2020. Moreover, benchmark simulations were performed implementing the main Lattice Boltzmann variants proposed in the literature. Additionally, an original application example to evaluate the use of porous materials in nuclear waste disposal was presented.

Two main categories of Nuclear Reactor problems treated with the Lattice Boltzmann Method were identified: Computational Fluid Dynamics and Neutronics problems.

- Computational Fluid Dynamics problems include the mixing process of the coolant, corrosion and deposition of impurities, flow acoustic resonances, hot and cold plumes temperature gradients, and coolant with low Prandtl number (liquid-metal).
- Neutronics problems include neutron flux and K_{eff} eigenvalue calculations, known as criticality problems.
- In Computational Fluid Dynamics problems, it is possible to adapt the Lattice Boltzmann Method with turbulence models, high discretization schemes in three-dimensional lattices, thermal models, and mesh refinement strategies.
- In Neutronic problems, the Lattice Boltzmann Method is adapted to solve the neutron transport and/or neutron diffusion equations with an angular discretization scheme that can account for scattering effects.
- The validation of the LBM results is commonly made by the comparison with experimental measurements of derived macroscopic variables (as friction factor, or velocity field for Computational Fluid Dynamics) or with a direct comparison of the solutions of well-established benchmarks with other numerical methods such as Finite Volume Method (for Computational Fluid Dynamics) or Direct Ordinate Method (for neutronics).
- The simulations include flow around fuel bundle arrays at high Reynolds number with turbulence model, flow around a hot cylinder, and neutron flux distributions with scattering.
- The neutron transport algorithm with scattering and participating media was validated. This variant of the Lattice Boltzmann Method represents an interesting approach to radiative heat transfer phenomena because it is not limited to neutrons and can be applied to the transport of "neutral particles" as photons.

The interest in applying the Lattice Boltzmann Method to Nuclear Reactors problems is increasing, and the related research items show this tendency. Furthermore, it is foreseeable in the literature the perspective to develop a multi-physics platform based on the Lattice Boltzmann Method that may include:

- 2D and 3D high discretization schemes;
- turbulence models;
- thermal field models;
- radiative heat transfer;
- neutron transport models;
- mesh refinement;
- species transport.

It is important to consider that the flexibility of the method opens the opportunity to develop hybrid models to study complex processes, including microphysics (deposition, oxidation, and chemical reactions).

LBM is arriving at a mature development, and the potential of this numerical method is a strong reason to conduct a better-directed effort to validate their use as a high-fidelity multi-physics simulation tool on the nuclear reactor field extendible to other fluid and energy systems.

Finally, to access all the potential of this numerical method, it is possible to exploit the intrinsic parallelization features of the LBM using, for example, computing platforms such as GPUs and CPU clusters. This will enhance the spatial and temporal resolution of the results and improve the computational effort.

REFERENCES

[1] J. Wang, Q. Wang, M. Ding, Review on neutronic/thermal-hydraulic coupling simulation methods for nuclear reactor analysis, Annals of Nuclear Energy. 137 (2020) 107165. https://doi.org/10.1016/j.anucene.2019.107165.

[2] J.A. Bocanegra Cifuentes, D. Borelli, A. Cammi, G. Lomonaco, M. Misale, Lattice Boltzmann Method Applied to Nuclear Reactors—A Systematic Literature Review, Sustainability. 12 (2020) 7835. https://doi.org/10.3390/su12187835.

[3] T. Ferreras-Fernández, H. Martín-Rodero, F.J. García-Peñalvo, J.A. Merlo-Vega, The systematic review of literature in LIS: an approach, in: Proceedings of the Fourth International Conference on Technological Ecosystems for Enhancing Multiculturality - TEEM '16, ACM Press, Salamanca, Spain, 2-4 November, 2016, 2016: pp. 291–296. https://doi.org/10.1145/3012430.3012531.

[4] P.V. Torres-Carrion, C.S. Gonzalez-Gonzalez, S. Aciar, G. Rodriguez-Morales, Methodology for systematic literature review applied to engineering and education, in: 2018 IEEE Global Engineering Education Conference (EDUCON), IEEE, Santa Cruz de Tenerife, Canary Islands, Spain, 17-20 April 2018, 2018: pp. 1364–1373. https://doi.org/10.1109/EDUCON.2018.8363388.

[5] Y. Hazi, G. Mayer, Flow in Rod Bundles, in: Proceedings of the International Conference "Nuclear Energy for New Europe 2005," Bled, Slovenia, 5-8 September 2005, 2005: p. 118.1-118.10.

[6] G. Mayer, G. Házi, Direct numerical and large eddy simulation of longitudinal flow along triangular array of rods using the lattice Boltzmann method, Mathematics and Computers in Simulation. 72 (2006) 173–178. https://doi.org/10.1016/j.matcom.2006.05.011.

[7] G. Mayer, J. Páles, G. Házi, Large eddy simulation of subchannels using the lattice Boltzmann method, Annals of Nuclear Energy. 34 (2007) 140–149. https://doi.org/10.1016/j.anucene.2006.10.002.

[8] J.W. Park, Application of mesh free lattice boltzmann method to the analysis of very high temperature reactor lower plenum, Atw. 56 (2011) 636–640.

[9] A. Tiftikçi, H. Ayhan, C. Kocar, C.N. Sökmen, Simulation of spacer grid with mixing vane on a typical pwr fuel rod bundle system using lattice boltzmann method, in: The 15th International Topical Meeting on Nuclear Reactor Thermal - Hydraulics, NURETH-15, Pisa, Italy, 12-17 May 2013, 2013: p. 324:1-324:12.

[10] A. Carrasco, Application of the Lattice Boltzmann Method to Issues of Coolant Flows in Nuclear Power Reactors, Master Thesis, Technische Universitat Munchen - Universitat Politecnica de Catalunya BarcelonaTech, 2013.

[11] J. Park, Numerical Simulation of Turbulent Flow Over Staggered Tubes Using Multi-Relaxation Time Lattice Boltzmann Method, Atw. 59 (2014) 96–105.

[12] A. Tiftikci, C. Kocar, Turbulent Flow Simulations Of Wire-wrapped Fuel Pin Bundle Of Sodium Cooled Fast Reactor In Lattice-Boltzmann Framework, in: International Conference Nuclear Energy for New Europe, Portorož, Slovenia, 14-17 September 2015, 2015: p. 208.1-208.8.

[13] A. Tiftikçi, C. Kocar, Lattice Boltzmann simulation of flow across a staggered tube bundle array, Nuclear Engineering and Design. 300 (2016) 135–148. https://doi.org/10.1016/j.nucengdes.2016.01.020.

[14] A. Tiftikçi, C. Kocar, Investigation of turbulence models for a fully-periodic LWR unit-cell in lattice-Boltzmann framework, Progress in Nuclear Energy. 104 (2018) 160–171. https://doi.org/10.1016/j.pnucene.2017.09.011.

[15] A. Tiftikci, C. Kocar, Investigation of heat transfer and turbulence characteristics of a triangular rod array in lattice-boltzmann framework, BgNS TRANSACTIONS. 21 (2016) 14–19.

[16] A. Tiftikci, C. Kocar, Investigation of Thermal Turbulent Flow Characteristics of Wire- wrapped Fuel Pin Bundle of Sodium Cooled Fast Reactor in Lattice- Boltzmann Framework, in: International Conference Nuclear Energy for New Europe, Portorož, Slovenia, 5-8 September 2016, 2016: p. 501.1-501.12.

[17] T.R. Vijaybabu, K. Anirudh, S. Dhinakaran, Mixed convective heat transfer from a permeable square cylinder: A lattice Boltzmann analysis, International Journal of Heat and Mass Transfer. 115 (2017) 854–870. https://doi.org/10.1016/j.ijheatmasstransfer.2017.08.033.

[18] N. Gui, Z. Li, Z. Zhang, X. Yang, J. Tu, S. Jiang, Numerical study of pebble recirculation in a two-dimensional pebble bed of stationary atmosphere using LB-IB-DEM coupled method, Annals of Nuclear Energy. 124 (2019) 58–68. https://doi.org/10.1016/j.anucene.2018.09.018.

[19] M.A. Wahba, A.A. Abdelrahman, N.M. El-Sahlamy, M.F.A. Rabbo, Double SRT Thermal Lattice Boltzmann Method for Simulating Natural Convection of Low Prandtl Number Fluids, IJES. 6 (2017) 21–35. https://doi.org/10.9790/1813-0612022135.
[20] H. Chen, Y. Chen, H.-T. Hsieh, J. Zhang, A lattice Boltzmann modeling of corrosion behavior and oxygen transport in the natural convection lead-alloy flow, Nuclear Engineering and Design. 237 (2007) 1987–1998. https://doi.org/10.1016/j.nucengdes.2007.01.016.
[21] Y. Chen, H. Chen, J. Zhang, Numerical investigation on enhancement of oxygen transfer by forced convection in liquid lead–bismuth eutectic system, International Journal of Heat and Mass Transfer. 50 (2007) 2139–2147. https://doi.org/10.1016/j.ijheatmasstransfer.2006.11.002.
[22] A. Tamura, S. Takahashi, H. Nakata, A. Takota, Development of Evaluation Method for Cold Trap in Fast Breeder Reactor: Part 1 — Numerical Analysis of Impurity Precipitation on Mesh Wire, in: 2017 25th International Conference on Nuclear Engineering, American Society of Mechanical Engineers, Shanghai, China, 2-6 July 2017, 2017: p. 67702:1-67702:7. https://doi.org/10.1115/ICONE25-67702.
[23] A. Tamura, S. Takahashi, H. Nakata, A. Takota, A numerical analysis method of impurity precipitation on mesh wire of cold trap in fast breeder reactor, Journal of Nuclear Engineering and Radiation Science. 4 (2018) 031015:1-031015:9. https://doi.org/10.1115/1.4039037.
[24] Z. Li, Simulation of the Crud Formation Process Using the Lattice Boltzmann Method, Master Thesis, University of Illinois at Urbana-Champaign, 2011.
[25] Z. Fan, Y. Kuo, Y. Zhao, F. Qiu, Visual simulation of thermal fluid dynamics in a pressurized water reactor, Vis Comput. 25 (2009) 985–996. https://doi.org/10.1007/s00371-008-0309-x.
[26] A. Kaufman, Z. Fan, K. Petkov, Implementing the lattice Boltzmann model on commodity graphics hardware, J. Stat. Mech. 2009 (2009) P06016:1-P06016:26. https://doi.org/10.1088/1742-5468/2009/06/P06016.
[27] J.W. Park, K.S. Lee, W.S. Kim, J. Kim, Computational Study on the Particle Sedimentation Performance of a Reactor Building Floor Weir by Means of Two-dimensional Lattice Boltzmann Method, in: Proceedings of the 2012 20th International Conference on Nuclear Engineering Collocated with the ASME 2012 Power Conference ICON E20-POWER2012, Anaheim, California, USA, 30 July - 3 August 2012, 2012: pp. 411–418. https://doi.org/10.1115/ICONE20-POWER2012-54182.
[28] J.W. Park, Development of two-dimensional lattice Boltzmann code DG2LBM for computational fluid dynamic problems in nuclear reactor safety component design, Atw. 57 (2012) 176–181.
[29] A. Tamura, K. Okuyama, S. Takahashi, M. Ohtsuka, Development of numerical analysis method of flow-acoustic resonance in stub pipes of safety relief valves, Journal of Nuclear Science and Technology. 49 (2012) 793–803. https://doi.org/10.1080/00223131.2012.703943.
[30] F. Cattant, D. Crusset, D. Féron, Corrosion issues in nuclear industry today, Materials Today. 11 (2008) 32–37. https://doi.org/10.1016/S1369-7021(08)70205-0.
[31] M.J. Gaeta, B. Nassersharif, A Stochastic Cellular Automata Model for Neutron Transport, Nuclear Science and Engineering. 113 (1993) 56–69. https://doi.org/10.13182/NSE93-A23993.
[32] B. Nassersharif, Cellular Automata Simulation of Neutron Transport, in: Education and Training Modeling and Simulation 2012, ETMS 2012, San Diego, CA, USA, 28-31 October 2012, 2012: pp. 43–47.
[33] Y. Wang, L. Yan, Y. Ma, Lattice Boltzmann solution of the transient Boltzmann transport equation in radiative and neutron transport, Phys. Rev. E. 95 (2017) 063313:1-063313:9. https://doi.org/10.1103/PhysRevE.95.063313.
[34] Y.-H. Wang, L.-M. Yan, B.-Y. Xia, Y. Ma, Lattice Boltzmann method for simulation of time-dependent neutral particle transport, Nuclear Science and Techniques. 28 (2017) 36:1-36:11. https://doi.org/10.1007/s41365-017-0185-z.
[35] Y. Wang, L. Yan, Y. Ma, W. Li, Finite volume lattice Boltzmann scheme for neutron/radiative transfer on unstructured mesh, Annals of Nuclear Energy. 109 (2017) 227–236. https://doi.org/10.1016/j.anucene.2017.05.022.
[36] Y. Ma, Y. Wang, K. Song, Q. Sun, Adaptive Mesh Refinement for Neutron Transfer With Lattice Boltzmann Scheme, in: 25th International Conference on Nuclear Engineering, American Society of Mechanical Engineers, Shanghai, China, 2-6 July 2017, 2017: pp. 1–9. https://doi.org/10.1115/ICONE25-66093.
[37] Y. Wang, M. Xie, Y. Ma, Neutron transport solution of lattice Boltzmann method and streaming-based block-structured adaptive mesh refinement, Annals of Nuclear Energy. 118 (2018) 249–259. https://doi.org/10.1016/j.anucene.2018.04.013.

[38] Y. Ma, Y. Wang, M. Xie, Multiblock Adaptive Mesh Refinement for the SN Transport Equation Based on Lattice Boltzmann Method, Nuclear Science and Engineering. 193 (2019) 1219–1237. https://doi.org/10.1080/00295639.2019.1620052.
[39] Y. Wang, M. Xie, Y. Ma, Neutron discrete velocity boltzmann equation and its finite volume lattice boltzmann scheme, CiCP. 25 (2019) 1446–1468. https://doi.org/10.4208/cicp.OA-2017-0203.
[40] Y. Wang, Y. Ma, M. Xie, High-order lattice Boltzmann method for multi-group neutron diffusion solution, Progress in Nuclear Energy. 110 (2019) 341–353. https://doi.org/10.1016/j.pnucene.2018.10.014.
[41] Y. Wang, Y. Ma, M. Xie, GPU accelerated lattice Boltzmann method in neutron kinetics problems, Annals of Nuclear Energy. 129 (2019) 350–365. https://doi.org/10.1016/j.anucene.2019.02.009.
[42] Y. Wang, Y. Ma, M. Xie, GPU accelerated lattice Boltzmann method in neutron kinetics problems II: Neutron transport calculation, Annals of Nuclear Energy. 134 (2019) 305–317. https://doi.org/10.1016/j.anucene.2019.06.020.
[43] H. Bindra, D.V. Patil, Radiative or neutron transport modeling using a lattice Boltzmann equation framework, Phys. Rev. E. 86 (2012) 016706:1-016706:7. https://doi.org/10.1103/PhysRevE.86.016706.
[44] H. Bindra, Lattice Boltzmann method for nuclear reactor physics, in: Transactions of the American Nuclear Society, Washington, D.C., USA, 10-14 November 2013, 2013: pp. 1399–1401.
[45] R. McCulloch, Advances in radiation transport modeling using lattice boltzmann methods, Master Thesis, Kansas State University, 2015.
[46] G. Agarwal, S. Singh, H. Bindra, S. Mishra, Solution of Neutron Transport Equation for Criticality Estimation Using Lattice Boltzmann Method, in: Transactions of the American Nuclear Society, Washington, D.C., USA, 8-12 November 2015, 2015: pp. 696–699.
[47] A. Gairola, H. Bindra, G. Agarwal, S. Singh, Lattice Boltzmann Method for Solving Time-Dependent Radiation Transport and Reactor Criticality Problems, in: 2016 24th International Conference on Nuclear Engineering ICONE24, American Society of Mechanical Engineers, Charlotte, North Carolina, USA, 26-30 June 2016, 2016: pp. 1–8. https://doi.org/10.1115/ICONE24-60058.
[48] A. Gairola, H. Bindra, Lattice Boltzmann method for solving non-equilibrium radiative transport problems, Annals of Nuclear Energy. 99 (2017) 151–156. https://doi.org/10.1016/j.anucene.2016.08.011.
[49] G. Agarwal, S. Singh, H. Bindra, Multi-group lattice Boltzmann method for criticality problems, Annals of Nuclear Energy. 140 (2020) 107260–107268. https://doi.org/10.1016/j.anucene.2019.107260.
[50] B. Erasmus, The Lattice Boltzmann Method applied to linear particle transport, Master Thesis, North-West University, 2012.
[51] Erasmus, B., Van Heerden, F. A, The Lattice Boltzmann Method applied to neutron transport, in: Proceedings of the 2013 International Conference on Mathematics and Computational Methods Applied to Nuclear Science and Engineering, United States: American Nuclear Society - ANS, Sun Valley, Idaho, USA, 5-9 May 2013, 2013: pp. 1335–1345.
[52] Y. Wang, M. Xie, Y. Ma, Analysis of the multi-physics approach using the unified lattice Boltzmann framework, Annals of Nuclear Energy. 143 (2020) 107500–107513. https://doi.org/10.1016/j.anucene.2020.107500.
[53] Y. Ma, S. Dong, H. Tan, Lattice Boltzmann method for one-dimensional radiation transfer, Phys. Rev. E. 84 (2011) 016704. https://doi.org/10.1103/PhysRevE.84.016704.
[54] Home - Palabos - UNIGE, Home - Palabos - UNIGE. (2020). https://palabos.unige.ch/ (accessed June 2, 2020).
[55] J. Latt, O. Malaspinas, D. Kontaxakis, A. Parmigiani, D. Lagrava, F. Brogi, M.B. Belgacem, Y. Thorimbert, S. Leclaire, S. Li, F. Marson, J. Lemus, C. Kotsalos, R. Conradin, C. Coreixas, R. Petkantchin, F. Raynaud, J. Beny, B. Chopard, Palabos: Parallel Lattice Boltzmann Solver, Computers & Mathematics with Applications. (2020) S0898122120301267. https://doi.org/10.1016/j.camwa.2020.03.022.
[56] B. Yao, J. Chen, Y. Li, Y. Wen, M. Wu, G. Shi, Oriented Graphene Foam with Tunable Wettability by Electrocapillary for Switchable and Ultra-Fast Imbibition, Adv. Mater. Interfaces. 3 (2016) 1600774. https://doi.org/10.1002/admi.201600774.
[57] S.-C. Jang, Y. Haldorai, G.-W. Lee, S.-K. Hwang, Y.-K. Han, C. Roh, Y.S. Huh, Porous three-dimensional graphene foam/Prussian blue composite for efficient removal of radioactive 137Cs, Scientific Reports. 5 (2015) 17510. https://doi.org/10.1038/srep17510.

[58] T. Woignier, J. Primera, J. Reynes, Nanoporous Glasses for Nuclear Waste Containment, Journal of Nanomaterials. 2016 (2016) 4043632. https://doi.org/10.1155/2016/4043632.
[59] S. Petlitckaia, A. Marchal, A. Poulesquen, Synthesis of Geopolymer Foam for the Decontamination of Liquid Nuclear Waste, in: Poromechanics VI, n.d.: pp. 929–936. https://doi.org/10.1061/9780784480779.115.

4. APPLICATION TO NATURAL CIRCULATION LOOPS

Natural circulation is a thermo-fluid-dynamic phenomenon in which a fluid circulates by the presence of a temperature gradient or a heat source. Buoyancy forces generate the natural convection due to density differences in a fluid that is differentially heated. The density differences have their origin in the thermal expansion of the fluid. This phenomenon is intrinsically complex and nonlinear, but its implementation in energy systems is of interest because the fluid circulates without additional mechanisms as pumps.

The aim of this chapter is to present a single-phase Natural Circulation Loop (NCL), simulated by the Lattice Boltzmann Method (LBM), and study the thermo-hydrodynamic characteristics under different operation conditions. The model is validated by comparison with the analytical model proposed by Cheng et al. [1] for the temperature distribution along the loop and the relationship between the Reynolds number at steady-state and the modified Grashof number. Additionally, the empirical correlation between the Nusselt and Reynolds numbers is used to validates the heat transfer performance. It was found the existence of at least two thermohydraulic regimes with the presence of eddies. The transition regime starts with Reynolds numbers higher than 320. Apparently, this value is low compared to the classic turbulent transition Reynolds number. However, some other authors have found vortices formation near this value for hydrodynamic problems as the cylindrical obstacle in a flow simulated by LBM (e.g., [2]). Moreover, as was pointed by Swapnalee and Vijayan [3], closed Natural Circulation Loops presents the transition regime at lower Reynolds numbers than the considered values for straight pipes. Additionally, simulations are presented for a case study considering different heater and heat sink configurations.

Far away from an extensive review of the thermal variants of the LBM, this chapter presents a novelty example that shows the applicability of thermal LBM on thermal fluid dynamics and energy systems. If even the LBM was successfully applied to natural circulation in cavities and channels, NCL has not been simulated yet, and this work can be considered the first approach to fill this gap.

This chapter shows results from experimental works developed with single and parallel-coupled NCLs [5], with different inner diameters [4], and Lattice Boltzmann Simulations [6,7].

4.1 Context

Some analytical relationships can predict the flow characteristics of the Natural Circulation Loops under selected operational parameters such as geometric dimension, fluid properties, source, and sink characteristics for laminar regime [3], and transition or turbulent regime [1]. Those relationships have been validated by comparison with experimental data from laboratories around the world. The stability of NCL is a primordial problem because, under some operational parameters and loop geometries, the flow direction can be inverted, and the system flow can become chaotic [8], an undesirable situation for critical engineering applications that require a predictable heat flux removal. In recent years experimental works found that localized pressure losses can stabilize the loops [9], also was found that an NCL with a small inner diameter is stable and can work connected in parallel [4,5] with small disturbances even if the power provided to one parallel loop changes.

Previous works evaluate the performance of rectangular-shaped single-phase NCL with heat end exchangers mainly by developing analytical models, simulations, or experiments. Early computational works use one-dimensional models, e.g., Rao 2002 [10]. This model considers the temperature profiles along the end heat exchangers, which work in counterflow (heater and heat sink). Later Finite Element Method simulations were developed by Rao et al. 2005 [11]. They developed a one-dimensional model (including equations for the heat end exchangers) to test the effect of different thermal excitation functions on the time to reach the steady-state. They found that maximum and minimum temperature values during the transient response are equal, but the delay in the circuit response changes for each excitation simulated (ramp, step, exponential). This one-dimensional approach allows the calculation of a longitudinal temperature profile along the NCL pipes. Additional studies focus on dynamic and total pressure variation, e.g., Rao et al. 2008 [12]. Single-phase CO_2 NCL with heat end exchangers has been investigated in steady-state using finite differences and the one-dimensional model by Kumar and Gopal 2009 [13], validating their approach by comparing the results with analytic expressions for the temperature and volume flow rate.

Yadav et al. 2012 [14] simulate a rectangular NCL with heat end exchangers using a CFD model. They proposed a nondimensional correlation for the Reynolds number and the modified Grashof number in the turbulent regime (7000<Re<360000). Later Yadav et al. in 2014 [15] performed a simulation with different tilt angles and found that the tilt angle increases the mass flow rate and decreases the heat exchange. Moreover, they also found that higher operating pressure reduces the time to reach the steady-state. They confirmed the Swapnalee and Vijayan empirical correlation for the turbulent regime [3] as well as the previously proposed computational correlation [16] (valid from 27000<Re<180000). Both correlations have small changes but take the same functional form. Cheng et al. 2018 [17], using a 3D CFD model, simulate the transient response of a single-phase NCL evaluating mass flow rate and energy generation. They use Vijayan's correlation [3,18] for the laminar regime (originally proposed for imposed heat flux at the heater) with a good fitting for the tested Reynolds numbers (lower than 100). The simulation showed the temperature gradient on the heat exchangers walls generating an asymmetric condition. Recently a study on the jump of heat transfer coefficient by tilting a square NCL (single and coupled) was developed using 2D and 3D numerical models, with a simplified geometrical model (Dass, and Gedupudi 2021 [19]).

4.2 Analytical model

One-dimensional analysis of a single NCL is presented in this section. The physics of the NCL can be derived from basic principles as the momentum conservation presented in Eq.4.1 and the energy equation in each section of the loop. The momentum equation expresses the balance between the buoyancy force (using Boussinesq hypothesis) and the friction on the loop:

$$\rho a \beta \oint T\, dx = \frac{\dot{m}^2}{2\rho} \sum_i \left(\frac{f f_i L_i}{D_i} + K_i \right) \frac{1}{A_i^2} \tag{4.1}$$

In this equation, x is the one-dimensional position variable along the entire loop, $\dot{m}$ represents the mass flow rate, and the subscript i refers to each sub-element in the geometry of the loop with a friction factor $f f_i$, length L_i and a diameter D_i and an area A_i; T is the temperature, β the fluids thermal expansion coefficient, ρ the fluid's density and a the gravity . The energy balance in the heater drives to the equation Eq.4.2, where c_p is the fluid's specific heat:

$$\frac{\dot{m}}{\rho A_H} \frac{\delta T}{\delta x} = \frac{q}{c_p\, \rho A_H L_H} \tag{4.2}$$

At the two vertical legs, the heat balance for an adiabatic condition drives to Eq.4.3:

$$\frac{\dot{m}}{\rho A_{leg}}\frac{\delta T}{\delta x} = 0 \tag{4.3}$$

At the cooler, the energy equation (Eq.4.4) must consider the sink temperature T_{sink} and the overall heat transfer U; of course, the mass flow rate also determines the temperature change.

$$\frac{\dot{m}}{\rho A_L}\frac{\delta T}{\delta x} = -\frac{UL_L(T - T_{sink})}{c_p \rho A_L} \tag{4.4}$$

Using this set of equations (Eq. 4.1-4.4), it is possible to obtain the temperature along each position of the loop. The integration of Eq.4.2 drives to Eq.4.5, which represents the relation between the mass flow rate $\dot{m}$ and the temperature difference between the hot and cold legs $T_h - T_c$:

$$T_h - T_c = \frac{q}{c_p \dot{m}} \tag{4.5}$$

For the mass flow rate: this equation can be rearranged in Eq.4.6:

$$\dot{m} = \frac{q}{c_p(T_h - T_c)} \tag{4.6}$$

Considering a fully developed flow correlation, the friction factor ff_i has a simple relation with the Reynolds number $Re_{ss,i}$ expressed in Eq.4.7:

$$ff_i = \frac{64}{Re_{ss,i}} \tag{4.7}$$

The pressure loss can be absorbed in the summation of the right side of the momentum equation (Eq.4.1) as an equivalent length using $K_i = \frac{ff_e L_e}{D_e}$, and using the Eq.4.7 the integration along the loop drives to Eq.4.8:

$$\oint T\,dx = \frac{\dot{m}^2}{2\rho^2 a\beta}\sum_i \frac{64}{Re_{ss,i}}\left(\frac{L_i}{D_i}\right)\frac{1}{A_i^2} \tag{4.8}$$

In a simplified case of uniform diameter along the loop, and using a single Reynolds number for all the regions $Re_{ss} = \dot{m}D/\nu\rho A$, the Eq.4.8 can be reduced to the proportion expressed in the Eq.4.9:

$$(T_h - T_c)H \propto \frac{\dot{m}^2}{2\rho^2 a\beta}\frac{64}{\frac{\dot{m}D}{\nu\rho A}}\left(\frac{L}{D}\right)\frac{1}{A_i^2} \tag{4.9}$$

Using the relation for the mass flow rate (Eq. 4.6) and simplifying common terms, a relationship between the temperature difference $T_h - T_c$ and the parameters of the fluid can be derived, Eq.4.10, (using Prandtl number as $Pr = \nu/\alpha$ and the area as $A = \pi/4D^2$):

$$T_h - T_c \propto \sqrt{\frac{128\ q\ L/D}{\pi\ D^3\ H\ a}} \cdot \sqrt{\frac{\alpha}{c_p\ \rho\ \beta} \cdot Pr} \tag{4.10}$$

It must be noted that if the experimental data are near to this relationship, this indicates that the NCL satisfies the conservation principles. A complete solution using nondimensional groups and the conservation equation for the NCL is known as Vijayan's theory [40]. This theory is also applicable for turbulent regimes if a

convenient form from the friction factor is used instead of Eq.4.7, which is valid only for the laminar regime. The complete solution presented by Vijayan [40] drives to the relation between the Reynolds number at steady-state, the modified Grashof number, and the geometric factor N_G (Eq 4.11).

Using Eq. 4.10 it is possible to obtain the original Vijayan's theory equation (Eq.4.11) valid for laminar flow. In fact, considering both the mass flow rate, Eq. 4.6, and the average temperature difference Eq. 4.10, the steady-state Reynolds number can be expressed by Eq.4.11, where N_G takes into account the friction along the NCL:

$$Re_{ss} = \sqrt{\frac{4}{128}}\sqrt{\frac{4\ a\ \beta\ D\ H\ \rho^2\ q}{\pi\ \mu^3\ c_p\ N_G}} = 0.178\sqrt{\frac{a\ \beta\ D^3\ H\ \rho^2\ q}{A\ \mu^3\ c_p\ N_G}} = 0.178\sqrt{\frac{Gr_m}{N_G}} \qquad (4.11)$$

If the heater consists of an end heat exchanger, the boundary condition at the heater changes to imposed temperature. Cheng et al. [1] deduce a similar one-dimensional model, defining a convenient geometrical factor N_G^*, as expressed in Eq.4.12.

$$N_G^* = \frac{1}{2}\sum_i (f\frac{L_i}{D} + K) \qquad (4.12)$$

And writing the modified Grashof number Gr_m^* in the form of Eq.4.13:

$$Gr_m^* = \frac{a\ \beta\ D\ H^2(T_H - T_C)}{\nu^2} \qquad (4.13)$$

The steady-state Reynolds number can be obtained by Eq.4.14:

$$Re_{ss} = \sqrt{\frac{Gr_m^*}{N_G^*}} \qquad (4.14)$$

Following the previous considerations, it can be shown that this last equation Eq. 4.14 (Cheng et al. model) is equivalent to Eq. 4.11 (Vijayan model) by using Eq. 4.7 into Eq. 4.12 to rewrite N_G^*. In fact, Eq. 4.8 and 4.9 are valid for the two systems.

4.3 Experimental data

4.3.1 Setup description

During the development of this thesis, active participation was done in the construction and testing of an original experimental setup. The original setup consists of four rectangular NCLs connected at the bottom. The obtained experimental results obtained with this setup were published in [4] comparing the single natural circulation loop and the parallel-connected loops; comparing two experimental setups characterized by different inner tube diameters in [5]. This section presents a brief description of the more relevant experimental results using the parallel-connected NCL setup.

Fig. 4.1 shows a sketch of the experimental setup. Each rectangular loop has an independent power supplier at the bottom side and a heat sink at a controlled temperature at the upper side. The setup is described in Table 4.1. All the geometric characteristics of the NCLs are reported in Table 4.2.

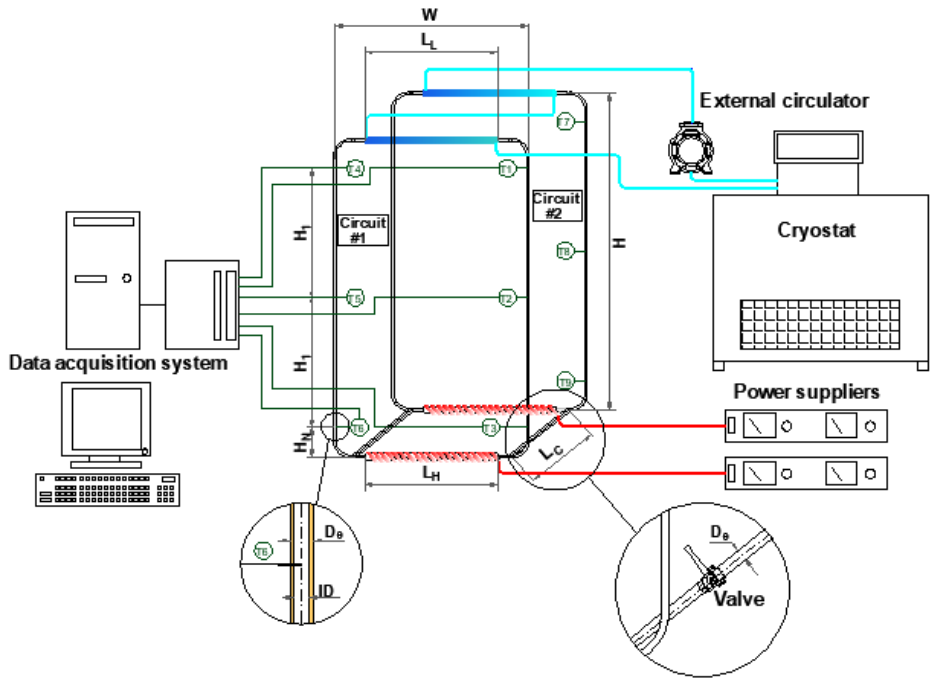

Figure 4.1 Experimental setup, only two parallel NCL are shown. Each loop has three thermocouples per vertical leg. (adapted from [4,5])

Table 4.1 Experimental setup description.

Horizontal and vertical pipes	Copper
Parallel connection	Regulable; silicone tubes
Work-fluid	Distilled water
Heater	Nichrome wire - Joule effect
Cooler	Coaxial heat exchanger controlled by a cryostat (LAUDA VC2000) maximum outlet-inlet temperature difference of 1 K
Thermal insulation	Neoprene + low emission film the maximum heat loss was calculated lower than 5%
Temperature measurement	T-type shielded calibrated thermocouples are used (outside diameter of 0.5 mm; precision ±0.1 K). Six thermocouples on each rectangular loop, three for each vertical tube whereas Two thermocouples measure the outlet-inlet temperature difference in the cooler
Data acquisition and storage	National Instruments data acquisition (Lab PC+, SCXI-1000, SCXI-1102, SCXI-1303) and an electronic ice point. The fluid temperature map was acquired every second (1.0 s), and each of these temperatures was obtained as an average of 100 readings

Table 4.2 Geometric parameters of the vertical Natural Circulation Loops experimental setups.

Parameter	**NCL-A**	**NCL-B**
Internal tube diameter *(ID), m*	0.007	0.004
Number of connected loops	4	2
Width *(W), m*	0.590	0.590
Height *(H), m*	0.975	0.975
Thermocouples distance gap *(H_1), m*	0.400	0.400
Height first thermocouple *(H_N), m*	0.0875	0.0875
Heated length *(L_H), m*	0.380	0.380
Cooled length *(L_L), m*	0.400	0.400
Total length *(L_t), m*	3.130	3.130
Connecting tube length *(L_c), m*	0.100	0.100
Connecting int. diam. tube *(D_c), m*	0.004	0.007
Aspect ratio *(L_t/W)*	5.30	5.30
Aspect ratio *(H/W)*	1.65	1.65
Aspect ratio *(L_c/D_c)*	14.28	25.00
Internal heat exchanger volume *(V_H), m^3*	$1.46 \cdot 10^{-5}$	$4.77 \cdot 10^{-6}$

Procedure A (No connected loops). The heat transfer rate at the heaters was increased from 20 W to 100 W with steps of 20 W (**NCL-A**; ID=7 mm) and from 20 W to 90 W with steps of 10 W (**NCL-B**; ID=4 mm), respectively. The same procedure was repeated at different heat sink temperatures T_{sink} of 10 °C, 20 °C, and 30 °C.

Procedure B (connected loops at different heat transfer rates); in this case, the performance with connected parallel loops (**NCL-A** and **NCL-B**) was measured with one loop subjected to variable heat transfer rate, while the neighbor loop remains with the same constant heat transfer rate of 40 W. This test was repeated with different heat sink temperatures T_{sink} of 10 °C, 20 °C, and 30 °C.

4.3.2 Experimental results

The transient response of the circuits, working in parallel, is depicted in Fig. 4.2. When the heater power is incremented in one loop, the average temperature difference between the legs oscillates until it reaches a steady-state. The influence on the parallel circuits is small.

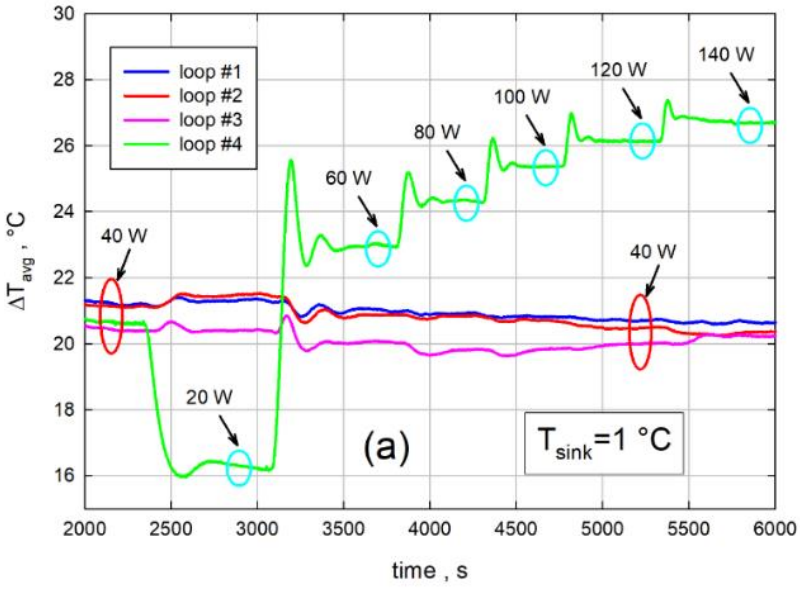

Figure 4.2 Time series for loops #1, #2, and #3 at constant power of 40 W, loop #4 varying power from 20 W to 140 W for two heat sink temperatures; (a) T_{sink}= 1 °C, (b) T_{sink}= 30 °C. NCL-A. (adapted from [4,5]).

The Vijayan correlation was verified under the different experimental procedures (disconnected or parallel connected loops), as shown in Fig. 4.3. Even changing the diameter of the pipes, the correlation is valid.

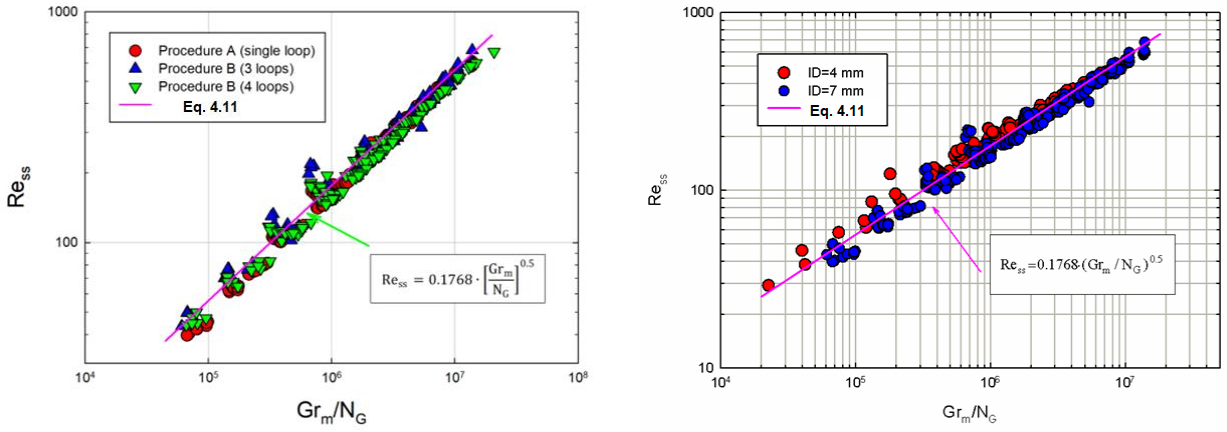

(a) (b)

Figure 4.3 Comparison between experimental data and Vijayan's correlation [40]. (a) NCL-A (b) NCL-A and NCL-B. (adapted from [4,5])

4.4 The Lattice Boltzmann Method formulation for natural thermal flow

The interest in simulating the natural circulation in rectangular closed loops was born from the experimental observations around the stable behavior of those small diameter circuits and the wide applicability of Vijayan's theory. The development of a simulation allows understanding the effects of different parameters. Moreover, it allows observing some physical details that cannot be measurable without affecting the thermo-fluid-dynamic of the system, as the evolution of the entire thermal field or the velocity profiles along all the loops. To develop a NCL numerical model based on LBM, it is necessary to introduce a thermal variant of the original method, which will be presented in this section.

The BGK LBM described in the introduction is isothermal. The higher moments of the populations linked to the internal energy cannot be calculated accurately using the typical velocity discretization (*D2Q9*, *D3Q19*, *D3Q27*). Only zero-order (density), first-order (momentum), and second-order moments (stress tensor)'are calculated accurately using those “first neighbor” lattices. To include thermal effects in the LBM, there are three common strategies

1. Multispeed: more vectors are included in the velocity base.
2. Double Distribution Function (DDF): a second LBE is solved for the thermal field.
3. Hybrid: LBM is used to calculate the evolution of the local density and velocity, and a secondary numerical model (as FD) is coupled to calculate the thermal field.

A review resuming those different approaches to a thermal-LBM can be found in [20]. The multispeed approach includes additional velocities linking a node with first, second, and third neighbors in the lattice (e.g., *D2Q17*). The equilibrium distributions usually include higher-order velocity terms. The multispeed modification allows the calculation of the internal energy using the third-order moment of the density distribution function. However, it implies a serious drawback: the algorithm loses the local characteristic, and the parallelization capabilities of the LBM are degraded because the memory allocation and communication between nodes is more complex than the simple first neighbor lattices, where the collision and stream algorithm is local, and the calculus can be distributed in different computational cores. Two additional limitations in the multispeed models severely restrict their applications, i.e., the severe numerical instability and the narrow range of temperature variation. However, this approach can be suitable for Rayleigh Bernard’s natural convection simulations, including *“viscous heating, heat conduction, and linear and non-linear acoustic effects”* [21]. Some other approximations that use regularized (expanded equilibrium distribution to third-order Taylor expansion) and non-Boussinesq approximations are recently developed [22] and tested with large temperature differences and Rayleigh numbers. On the other hand, the DDF strategy uses the classical velocity discretization and equilibrium term, but two concurrent lattices are calculated and coupled in each timestep; this expansion can produce stable and accurate results even with a large temperature difference. Finally, the hybrid approach can be very useful and shows the versatility of the LBM; the key point to adopt this approach is to properly couple the LBM with the thermal numerical model (FD, FVM, FEM); this can be done similarly that in the DDF coupling but careful considerations must be considered regarding the physical and lattice units used in each numerical method.

In this thesis, we adopt the DDF approach, a concise presentation of this Lattice Boltzmann Method for two dimensional models is included here, and it is easily extensible to three-dimensional models following a similar formulation. Fig. 4.4 represents the two lattices, a *D2Q9* lattice for density and momentum field and a *D2Q5* lattice for the temperature field. The *D2Q5* quadrature is enough to obtain accurate results for the thermal field; results from *D2Q4*, *D2Q5*, and *D2Q9* are similar, but *D2Q4* is less stable than *D2Q5* [23], and for this reason is convenient to adopt *D2Q5* to optimize memory consumption and ensure stability.

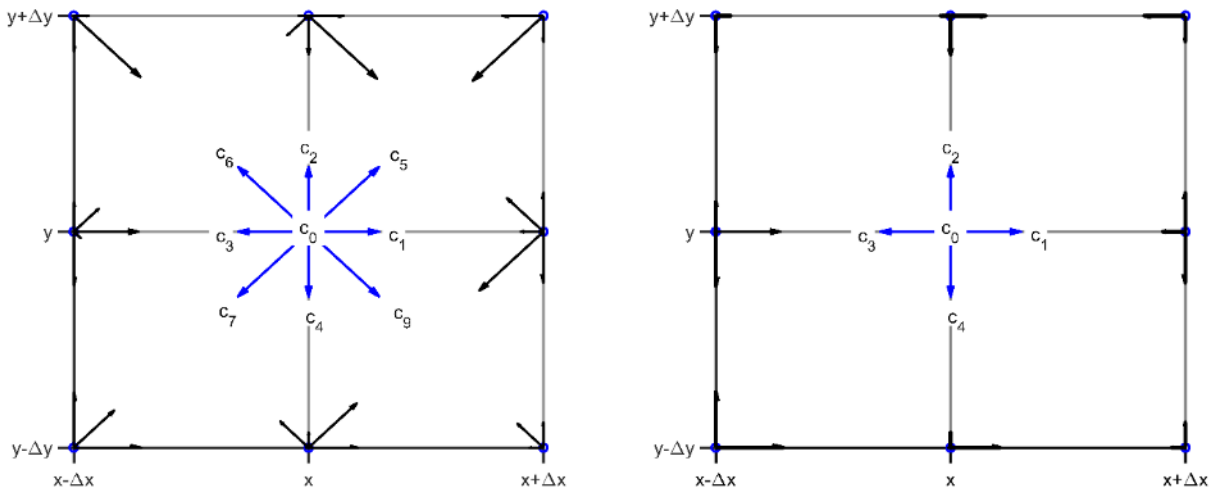

(a) (b)

Figure 4.4 Representation of the two lattices composed of interconnected nodes, every single node has some vectors representing the populations of the two density functions. (a) D2Q9 hydrodynamic lattice for f_i populations, (b) D2Q5 thermal lattice for g_i populations. The blue vectors represent the discrete velocity base $\boldsymbol{c_i}$.

The general physical equations for a thermo-fluid dynamic problem are the Navier-Stokes equation (Eq.4.15), the continuity equation (Eq. 4.16), and the energy equation (Eq.4.17). Here, $\boldsymbol{u}$ represents the macroscopical fluid velocity, F the body-force term, υ the kinematic viscosity, k the thermal conductivity, ρ fluid density, T the temperature, and t the time.

$$\frac{\partial u}{\partial t} + \boldsymbol{u} \cdot \nabla \boldsymbol{u} = \upsilon \nabla^2 \boldsymbol{u} + \frac{\nabla p}{\rho} + F \tag{4.15}$$

$$\frac{\partial \rho}{\partial t} + \nabla \cdot \rho \boldsymbol{u} = 0 \tag{4.16}$$

$$\frac{\partial T}{\partial t} + \boldsymbol{u} \cdot \nabla T = \nabla \cdot (k \nabla T) \tag{4.17}$$

Instead of directly discretizing and simulating those equations, two discretized Lattice Boltzmann Equations (LBE) are solved. The first LBE is presented in Eq. 4.18 for the density-momentum or *hydrodynamic field* (f_i) and the second LBE in Eq. 4.19 for the *thermal field* g_i.

$$f_i(\boldsymbol{r} + \boldsymbol{c_i}\Delta t, t + \Delta t) - f_i(\boldsymbol{r}, t) = -\frac{1}{\tau}\Big(f_i(\boldsymbol{r}, t) - f_i^{eq}(\boldsymbol{r}, t)\Big) + \Delta t\, F_i \tag{4.18}$$

$$g_i(\boldsymbol{r} + \boldsymbol{c_i}\Delta t, t + \Delta t) - g_i(\boldsymbol{r}, t) = -\frac{1}{\tau_g}\Big(g_i(\boldsymbol{r}, t) - g_i^{eq}(\boldsymbol{r}, t)\Big) \tag{4.19}$$

The left side of Eq. 4.18 and 4.19 represents the transport of the populations between the nodes of the lattice at position $\boldsymbol{r}$ and $\boldsymbol{r} + c_i \Delta t$ after each timestep Δt. The right side of these equations represents the collision process, in this case using the BGK approximation that relaxes the populations f_i, g_i to the equilibrium populations f_i^{eq}, g_i^{eq}, this process is characterized by a relaxation time for each lattice, τ proportional to the viscosity ν Eq. 4.20 and τ_g proportional to the thermal diffusivity α Eq.4.21.

$$v = \frac{1}{3}(\tau - 0.5) \tag{4.20}$$

$$\alpha = \frac{1}{3}(\tau_g - 0.5) \tag{4.21}$$

The equilibrium function for the hydrodynamic field f_i^{eq} and the thermal field g_i^{eq} are presented in Eq. 4.22 and Eq. 4.23, respectively. It is possible to consider a lower order approximation for the equilibrium distribution of the thermal field (Eq.4.23), but to avoid the possible stability and accuracy degradation, the equilibrium term is considered in a similar Taylor expansion as in Eq.4.22.

$$f_i^{eq}(\boldsymbol{r}, t) = w_i \rho \left(1 + \frac{\boldsymbol{c_i} \cdot \boldsymbol{u}}{{c_s}^2} + \frac{(\boldsymbol{c_i} \cdot \boldsymbol{u})^2}{2{c_s}^4} - \frac{\boldsymbol{u} \cdot \boldsymbol{u}}{{c_s}^2}\right) \tag{4.22}$$

$$g_i^{eq}(\boldsymbol{r}, t) = w_i T \left(1 + \frac{\boldsymbol{c_i} \cdot \boldsymbol{u}}{{c_s}^2} + \frac{(\boldsymbol{c_i} \cdot \boldsymbol{u})^2}{2{c_s}^4} - \frac{\boldsymbol{u} \cdot \boldsymbol{u}}{{c_s}^2}\right) \tag{4.23}$$

Additionally, the external force is included in the term F_i. In natural convection, F_i represents a buoyancy force by thermal expansion of the fluid. The Boussinesq hypothesis can be used to model the force term Eq. 4.24, a small change in the density has only an effect in the buoyancy force term, then it is possible to use a force term proportional to the temperature and control the strength of this effect by a proportional constant [24].

$$F_i = -\beta\, \rho_0\, (T - T_0) g \tag{4.24}$$

The thermal field is coupled with the hydrodynamic field through the velocity $\boldsymbol{u}$ in the equilibrium function Eq. 9. For a complete two-way coupling, the thermal field affects the hydrodynamic field via the force term F_i given in Eq. 10. Table 1 presents the velocity base $\boldsymbol{c_i}$ ·and the corresponding weights w_i for the two lattices. The propagation constant for each lattice is ${c_s}^2 = 1/3$ for *D2Q9* and ${c_s}^2 = 1/2$ for *D2Q5*.

Table 4.3 Velocity discretization sets for D2Q9 Hydrodynamics, and D2Q5 Thermal lattices, w_i weights, and components of the i velocity vector $\boldsymbol{c_i} = (c_{ix}, c_{iy})$.

	$\boldsymbol{i}$	0	1	2	3	4	5	6	7	8
D2Q9	w_i	4/9	1/9	1/9	1/9	1/9	1/36	1/36	1/36	1/36
	c_{ix}	0	1	0	-1	0	1	-1	-1	1
	c_{iy}	0	0	1	0	-1	1	1	-1	-1
D2Q5	w_i	1/3	1/6	1/6	1/6	1/6	-	-	-	-
	c_{ix}	0	1	0	-1	0	-	-	-	-
	c_{iy}	0	0	1	0	-1	-	-	-	-

The macroscopic quantities are calculated for integral moments of the density functions f_i, g_i as described below:

- For the calculus of the density, the zero-order moment (Eq. 4.25) is used:

$$\rho(\boldsymbol{r}, t) = \int f(\boldsymbol{r}, \boldsymbol{c}, t) d^3c = \sum_{i=1}^{y} f_i(\boldsymbol{r}, t) \tag{4.25}$$

- For the calculus of the momentum, the first-order moments (Eq. 4.26) are used:

$$\boldsymbol{u}(\boldsymbol{r},t)=\frac{1}{\rho}\int|\boldsymbol{c}|f(\boldsymbol{r},\boldsymbol{c},t)d^3c=\frac{1}{\rho}\sum_{i=1}^{y}\boldsymbol{c_i}f_i(\boldsymbol{r},t) \tag{4.26}$$

- The temperature corresponds to the zero-order moment of g_i (Eq.4.27):

$$T(\boldsymbol{r},t)=\int g(\boldsymbol{r},\boldsymbol{c},t)d^3c=\sum_{i=1}^{y}g_i(\boldsymbol{r},t) \tag{4.27}$$

The velocity field $\boldsymbol{u}$ calculated from f_i (Eq. 4.26) enter in Eq. 4.22, affecting the equilibrium temperature distribution. On the other hand, the temperature affects the flux, as presented in Eq. 4.24 using the zero-order moment of g_i (Eq. 4.27) to calculate the thermal field T, by this, the model can be considered coupled in two-ways. For example, a single-way coupling is possible for simulation of chemical species transport, i.e., the passive field (chemical species concentration) does not affect the flux.

This model is suitable for low Reynolds number thermal flows. Under some conditions, as reducing the Prandtl number, the Reynolds number can be over 1000, generating convergence issues. However, considering the validation data and relationships reported by [3], the range of interest for this work remains in the low Reynolds number zone, and viscosity filters or other turbulence models are not necessary.

One of the first works using LBM to simulate Rayleigh-Bernard convection was presented by Shan in 1997, [24] which assumed a DDF approach using a passive advection-diffusion equation for the thermal field (this component does not contribute to the momentum equation and affects only by a body force modeled as a Boussinesq type force). This kind of approach does not account for viscous heat or compression work; the author validated the model with theoretical and experimental results. Guo et al. 2002 [25] presented a DDF model based on a simplified Shan and Shen approach applied to simulate Boussinesq equations, particularly the natural convection in a cavity. D'Orazio and Succi, 2004 [26] simulated natural convection in a 2D channel by a DDF approach for the thermal energy density. They added a term directly to the Boltzmann equation to account for viscous heating. Furthermore, they introduce new thermal boundary conditions. The model is applicable for large temperature differences. Mohamad and Kuzmin, 2010 [27] presented an analysis regarding three different strategies to add the force term to the LBM-BGK and tested it in natural convection into a cavity, finding that all the schemes produced similar results even if each author claims that their schemes are more accurate than the others. Huang et al. 2011 [23] demonstrated that different lattices for the thermal field (called *D2Q4*, *D2Q5*, and *D2Q9*) can give similar results in the simulation of natural convection. In the same way, under complex boundary situations, Li et al. 2017 [28] showed a convenient behavior of the *D2Q5* lattice, with even better performance than the *D2Q9* scheme, for example, with curved geometries.

Sousa et al. 2010 [29] used the DDF and a temperature jump boundary condition to simulate heat transfer in a microchannel. More complex heat transfer situations have effectively simulated with LBM as multiphase (nanofluids) thermal flows introducing hybrid approaches to couple grids and reducing the two fluid components to a single equivalent component [30]. The LBM approach can simulate variable transport coefficients (variable viscosity and thermal diffusivity) in natural convection [31]. Considering a regularized scheme for the advection-diffusion of the thermal field, i.e., filtering the non-equilibrium higher moments and leaving only the first order non-equilibrium moment to contribute to the diffusion, it is possible to suppress numerical noise and increase the robustness of the DDF-LBM [32]. Choi and Kim presented a comparative study of different methods to study natural convection in a cavity [33]. DDF has been effectively applied to the natural circulation of nanofluids into a curved boundaries cavity [34], natural convection of ferrofluids linear heated cavity [35], natural circulation heated by active blocks [36,37], turbulent Rayleigh-Bernard convection in a channel [38], natural circulation in a cavity with low Prandtl number fluid [39]. As was proposed by Hosseini et al. 2019 [40] and Alipour Lalamia and Kalteh 2019 [41], the method is suitable for the simulation of nanofluids in a channel or nanofluids in an enclosure in the

presence of a magnetic field [42]. Conjugated heat transfer can also be simulated, but inconsistencies in heat fluxes must be corrected at interfaces when heterogeneous media are considered. Almost all the cited works were developed considering a two-dimensional LBM, but it is possible to implement three-dimensional models based on DDF-MRT for natural convection, as was presented by Li et al. [43]. Some other applications to natural circulation have been performed as the air circulation in a single-chapel greenhouse [44].

By a *hybrid* approach, some examples can be found concerning the natural circulation of a nanofluid in a square cavity [45] or a solar power plant [46]. A comparison between hybrid and DDF was presented by Feng et al., 2018 [22]. A complete review of the thermal LBM can be found in [20,47,48].

4.5 Natural circulation loops: LBM results

The experimental results show two interesting behaviours of the NCL that motivates the simulations:

I. The transient behaviour with the presence of oscillations in the temperature until reach a steady-state, those oscillation depends on the consider thermal conditions.
II. The steady-state behaviour that relates the flow velocity (expressed by the Reynolds number) with the temperature difference between the adiabatic vertical legs (expressed by the modified Grashof number).

4.5.1 Model description

Figure 4.5 and Table 4.4 resumes a schematic representation of the simulated loop and the main geometrical parameters considered. The developed numerical model considers a simplified geometry: a square mini-loop with a small diameter with fixed temperatures at the heater and cooler. The heater and the heat sink are located in a horizontal configuration. This type of loop is known as HHHC (horizontal heater horizontal cooler). In a second step, the effect of considering different heater-cooler configurations is studied.

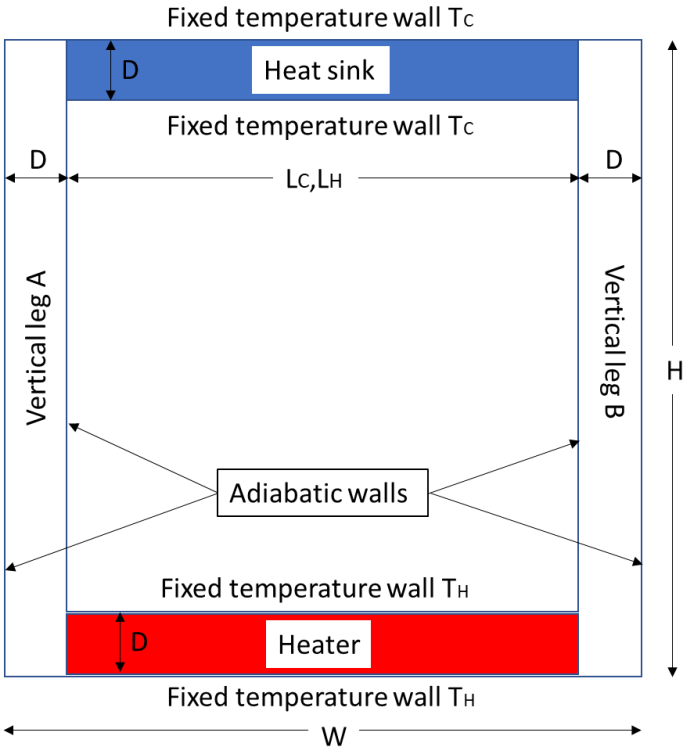

Figure 4.5 Simulated setup sketch.

Table 4.4 Geometric parameters of the vertical experimental setup. All the lengths are in m

Parameter		**Parameter**	
Width ***(W)***	0.250	Total length (L_t)	1.0
Height ***(H)***	0.250	Aspect ratio (L_t/W)	4.0
Internal tube diameter ***(D)***	0.010	Aspect ratio (H/W)	1.0
Heated length $(\boldsymbol{L_H})$	0.230	Aspect ratio (D_c/L_c)	1/23
Cooled length $(\boldsymbol{L_C})$	0.230		

The Rayleigh number (Ra) varied from 10^3 to 10^7 to observe the thermohydraulic behavior of the loop considering the velocity of the fluid into the channel (Reynolds number), the heat transfer characteristics (Nusselt number), and the thermal field characterized by the temperature difference between the two vertical legs (modified Grashof number). Even if the bulk results consider a computational fluid with a Prandtl number equal to one, some runs were made to observe the effect of changing this parameter.

The geometry described in Fig. 4.5 and Table 4.4 is modeled using a uniform square lattice. Multiblock allocation strategy is used to optimize memory usage, dividing the loop into four domains: heater, cooler, and the two adiabatic vertical legs A and B, i.e., the central nodes are excluded. The diameter is considered uniform along the two vertical legs, cooler and heater sections. A two-dimensional model of the HHHC single-phase NCL is implemented using the DDF approach proposed by He and Luo [49].

Boundary conditions:

A non-slip boundary condition called bounce back was implemented along all the loop for the hydrodynamic distribution. This boundary condition simulates a wall halfway between the wet and solid nodes. The implementation is simple, and the algorithm reflects the upcoming populations to the wall [50]. The behavior of this kind of BC induces a parabolic Poiseuille velocity profile (at low Reynolds number - laminar regime), Fig. 4.6.

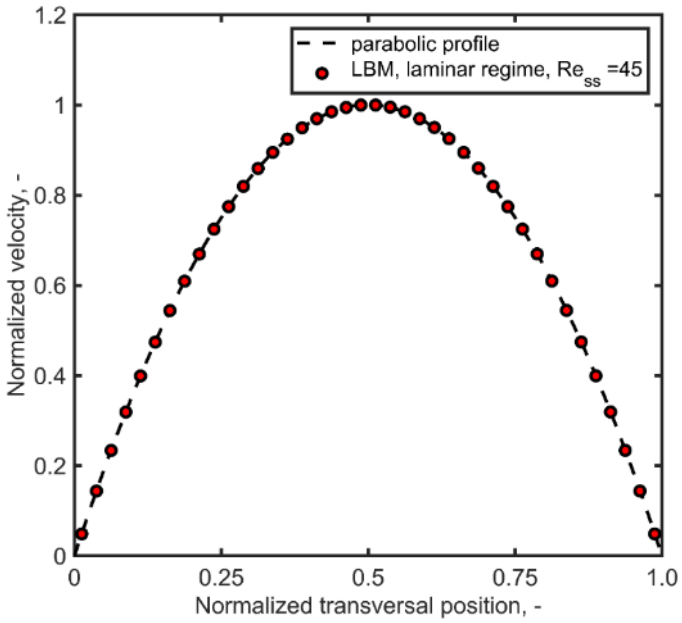

Figure 4.6 Poiseuille parabolic profile in the NCL for low Reynolds number.

The boundary conditions for the temperature field are composed of adiabatic vertical legs and fixed temperature at the heater and heat sink walls. The adiabatic condition is obtained by extrapolating the

temperature in the neighbor nodes to vanish the temperature gradient at the wall. The constant temperature boundary condition at the cooler and heater is a Dirichlet type boundary condition for the secondary (or thermal) distribution.

Initial condition:

Uniform Density was established for all the computational domains. The LBM assumes low-density changes near the incompressible regime.

The initial velocity field can be established as zero, and after some time, the symmetry breaks, and the fluid starts to flow in one direction (clockwise or counterclockwise); alternatively, an initial low-velocity field can be set to impose a flow direction and accelerate the convergence to the steady-state.

The initial temperature field can be established in several ways:

i. Set the cooler temperature for all the domains.
ii. Set a temperature average for all the domains.
iii. Set the heater temperature for the heater pipe, the cooler temperature for the cooler pipe, and a gradient field in the vertical legs.

The first two options are useful to test the thermal boundary conditions at the cooler and heater; meanwhile, the third one reduces the convergence time to the steady-state. The second condition was selected to perform the simulations. The thermohydraulic behavior at the steady-state under the three listed initial conditions is similar.

To control the flow direction, it is possible to implement three different strategies:

i. break the symmetry of the loop positioning the heater (or cooler) with a little offset
ii. establish an initial temperature difference between the vertical legs
iii. set a small initial velocity in one direction.

Condition iii) was adopted to perform the numerical "experiments". All three strategies were tested and effectively established a flow direction. However, it is more interesting to note that the third strategy does not alter the loop symmetry. In fact, both flow directions are possible. For high Rayleigh numbers, we obtain circulation in clockwise and counterclockwise directions because the initial circulation of the fluid is complex, and the small initial velocity does not fix the flux direction.

Lattice units and physical units

The relationship between the computational units (or *Lattice Units*) and the physical units is not straightforward in LBM because the computational length scale and time scale are linked through the relaxation parameter, including an additional free parameter into the unit conversion, by this conversion factors between the lattice units and the physical units must be carefully adopted. A different approach based on normalized quantities and dimensionless groups was adopted; in this way, the LBM results and the physical units are directly comparable [51]. The following quantities were considered in the physical analysis:

- The temperature normalization is implemented using $T_H = 1$, for the heater and $T_C = 0$ for the heat sink [52].
- The fluid in the loop is characterized by a given Prandtl number Eq.4.28:

$$Pr = \frac{\nu}{\alpha} = \frac{\tau}{\tau_g} \tag{4.28}$$

- Reynolds number at steady state Re_{ss} Eq. 4.29 is referenced to pipe diameter D:

$$Re_{ss} = \frac{u_{rms}\, D}{\nu} \tag{4.29}$$

- Global Rayleigh (Ra) number, Eq. 4.30, is referred to the temperature difference between the heat source and the heat sink $T_H - T_C$. The vertical height of the loop H, the gravity a and the thermophysical properties of the fluid (β coefficient of expansion, γ thermal diffusivity, and ν fluid viscosity). Ra is an input parameter that is fixed before the simulation starts.

$$Ra = Gr\, Pr = \frac{a\, \beta\, (T_H - T_C) H^3}{\alpha\, \nu} \tag{4.30}$$

- Modified Grashof number Gr_m is defined in Eq. 4.31. Note that this number differs from the Grashof number Gr defined in Eq.16 because it considers the average temperature difference between the hot and cold legs (ΔT_{avg}) as the thermal gradient that determines the thermohydraulic behavior and considers the pipe diameter D as a relevant characteristic dimension. However, this number cannot be determined *a priori* but can be determined after the steady-state is reached, performing an average on the thermal field of each vertical leg.

$$Gr_m = \frac{a\beta\Delta T_{avg} D^2 H}{\nu^2} \tag{4.31}$$

- Local Nusselt number Nu , Eq. 4.32, and average Nusselt number $\overline{Nu}$ at the heater, Eq. 33, can be evaluated utilizing the gradient of the thermal field.

$$Nu = \frac{\partial T}{\partial y} \tag{4.32}$$

$$\overline{Nu} = 1/M \sum_{k=1}^{M} \frac{\partial T}{\partial y} \tag{4.33}$$

- Considering M the number of lattice nodes in the heater direction, the wall temperature T_W, the neighbor nodes temperature T_{W+1} and T_{W+2}, N the number of cells in the perpendicular direction y. $\overline{Nu}$ is calculated by a first-order finite difference scheme FD1 Eq. 4.34 or a more accurate second-order scheme FD2 approximations Eq. 4.35.

$$\overline{Nu} \approx 1/M \sum_{k=1}^{M} \frac{T_W - T_{W+1}}{\Delta y}\, N \tag{4.34}$$

$$\overline{Nu} \approx 1/M \sum_{k=1}^{M} \frac{3\, T_W - 4\, T_{W+1} + T_{W+2}}{2\, \Delta y}\, N \tag{4.35}$$

Stability and convergence

The convergence of the system to the steady-state is determined by calculating when the relative standard deviation of the Nusselt number is below a given threshold (up to 10^{-16}). When this condition is reached, the simulation finish. Additionally, the convergence of the temperature difference between the hot and cold legs (ΔT_{avg}) and Reynolds number was studied. In the laminar regime, those quantities converge. The simulations do not present computational instabilities or divergencies in the tested Rayleigh number range.

Resolution effects on flow conditions are investigated, calculating Re_{ss} under the same operation conditions. The following spatial resolution values were tested: 500(diverge) 1000 2000, 4000, 8000, and 10000 grid points per meter. It was noted that the Re converges for a resolution up to 4000; thus, 40 mesh points per pipe diameter was used in the simulations, i.e., 1000x1000 lattice.

Computational considerations

The NCL model was implemented in C++ language using the parallel Lattice Boltzmann library PALABOS [53]. The routine was tested in an Intel® Xeon® Platinum 8260 CPU, 2.40 GHz, workstation, using MPI (message passing interface) protocol for the parallel running on 48 cores. The maximum calculus velocity has an approximate value of 250 MSUPS (Mega Site Updates Per Second) for resolution 10000 grid points/m and 200 MSUPS for the simulations with 4000 grid points/m.

4.5.2 Thermo-hydraulic behaviour

The convergence to the steady-state of the circuit is depicted in Fig. 4.7(a). In particular, the normalized temperature difference between the adiabatic vertical legs is presented at different time steps iterations in this figure. For higher Ra (and Re_{ss}) values, the time from the rest-state to the start of the natural convection is shorter, and the normalized temperature between the legs decreases. The transient has fewer oscillations for low Ra (and Re_{ss}) because the fluid is moving slowly, and during the circulation of the fluid, the heater and cooler had enough time to change the temperature of the fluid effectively. A similar result was noted by Cheng et al. [1]. In this work, they do not present the dimensionless form of the temperature and only note an "absolute" increment of ΔT_{avg}, but it is obvious that corresponding to the imposed heat and heat sink temperatures (T_H-T_C) in their experiments their results are congruent with the simulations presented here. Moreover, the transient behaviour can be comparable with previous results from Garibaldi and Misale [54] for small inner diameter mini loops, the oscillations increment when the heating power increases. As was noted by [5], the efficiency decreased, incrementing the Rayleigh number. Fig. 4.7(b) presents a phase diagram comparing the simultaneous convergence of the temperature difference and the velocity. An increment in the phase between the velocity and the temperature oscillations is noticeable for higher Reynolds numbers.

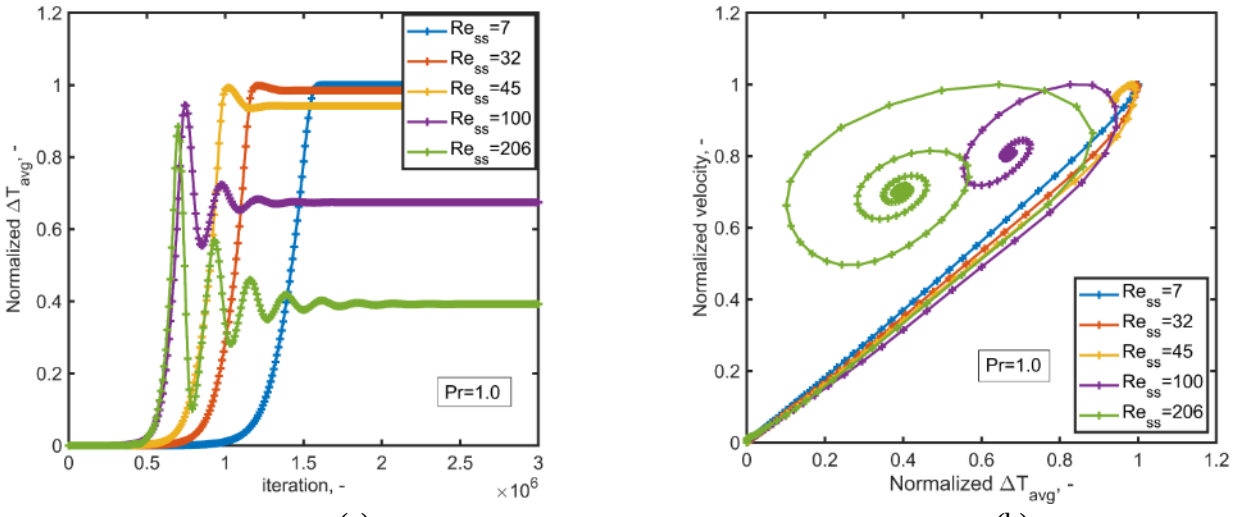

Figure 4.7 Transient response of the NCL simulated by LBM for different Reynolds numbers, Prandtl number 1.0. (a) ΔT_{avg} vs. time, (b) phase diagram normalized velocity vs. normalized ΔT_r.

Figure 4.8 presents the typical response of the NCL for a low Reynolds number ($Re_{ss} = 100$). The velocity field is characterized by a parabolic velocity profile parallel to the pipe, without vorticity, Fig. 4.8a. The

temperature field presented in Fig. 4.8b shows a low variation of the temperature in the vertical legs, and it was expected that the fluid temperature increases in the heater and the temperature decrease in the heat sink.

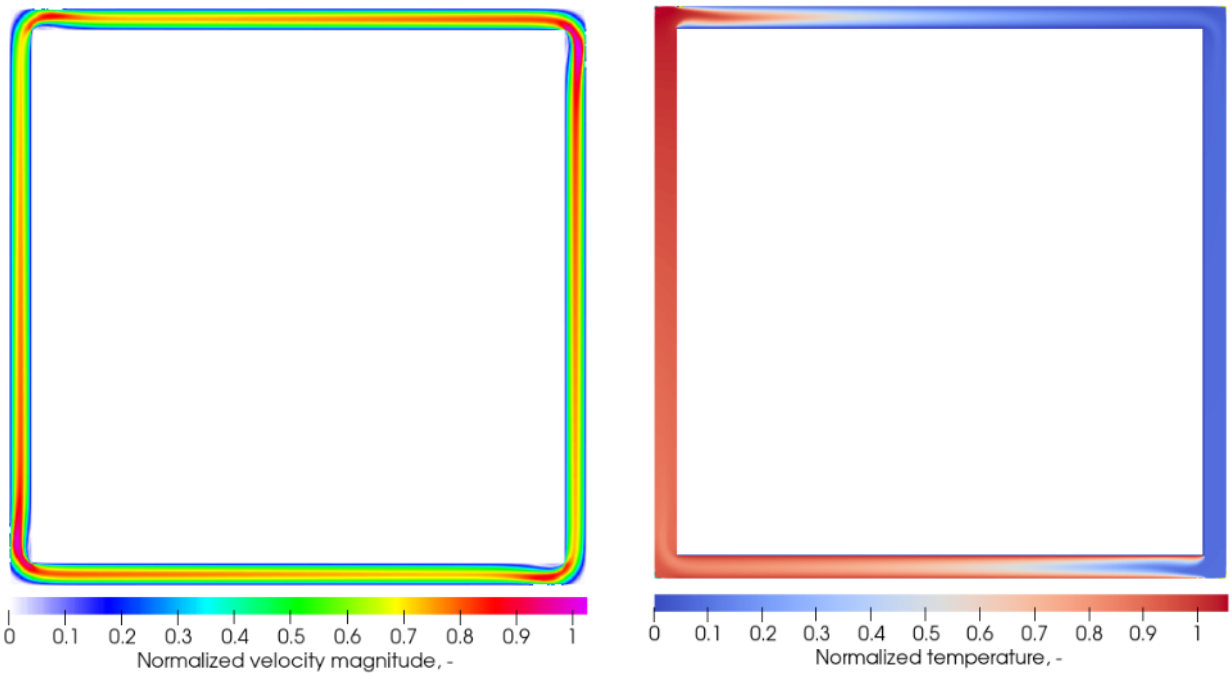

(a) (b)

Figure 4.8 Thermohydraulic response of the loop at low Reynolds number at steady-state ($Re_{ss} = 67, Pr = 1.0$) (a) Normalized velocity magnitude (b) Normalized thermal field.

The Cheng et al. [1] model for a single-phase NCL with fixed temperatures at the sink and the source is used to validate the current LBM approach. The considered Cheng et al. model was confirmed experimentally for $Re_{ss} < 100$ [1]. This theoretical model is based on a one-dimensional analysis of the loop in the laminar regime uses the Boussinesq approximation for accounting for the buoyancy effect by the fluid's thermal expansion and not considers axial heat conduction, viscous dissipation, or changes in the fluid physical properties by effects of the temperature. Heat source and heat sink temperatures are constants. Under those considerations, they obtained the relationship presented in Eq. 4.36 for the Reynolds number at steady-state Re_{ss} and the modified Grashof number Gr_m (Eq. 4.31) and the N_G dimensionless geometrical factor that accounts for frictional effects, Eq. 4.37. It is possible to show that this model is equivalent to the model proposed in [3,18] for the turbulent region in a NCL with a heat flux boundary condition at the heater.

$$Re_{ss} = \sqrt{\frac{Gr_m}{N_G}} \tag{4.36}$$

The geometrical parameter N_G accounts for local and concentrated losses considering the frictional coefficient (calculated using $ff = 64/Re$) and the local resistance coefficient K.

$$N_G = \frac{1}{2}\sum_i \left(ff\,\frac{L_i}{D} + K\right) \tag{4.37}$$

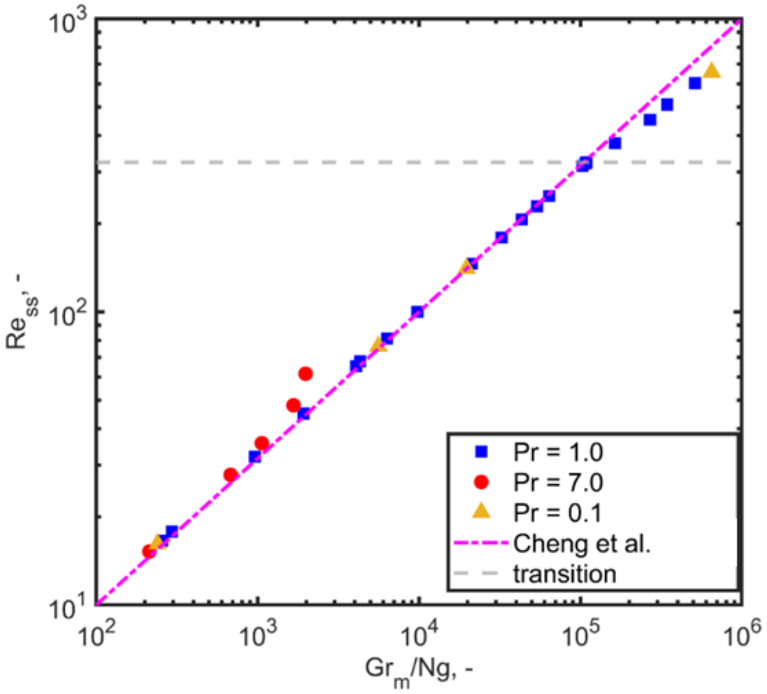

Figure 4.9 Description of the thermohydraulic behavior of the NCL by the relationship between Re_{ss} and Gr_m/N_G (Eq. 4.36).

Figure 4.9 presents a comparison between the theoretical model and numerical results obtained by the LBM approach considering two different Prandtl numbers. The LBM results reproduce the theoretical model for low Reynolds numbers. The LBM results for Prandtl number 7 show a small deviation for the points corresponding to high *Ra* numbers even when the flow regime remains laminar. A change in the slope in this graphic is noticed over $Re_{ss} = 320$. The velocity field over this transition limit shows vortex formation near the heater and heat sink walls, which is different to the laminar flow field presented in Fig. 4.8.

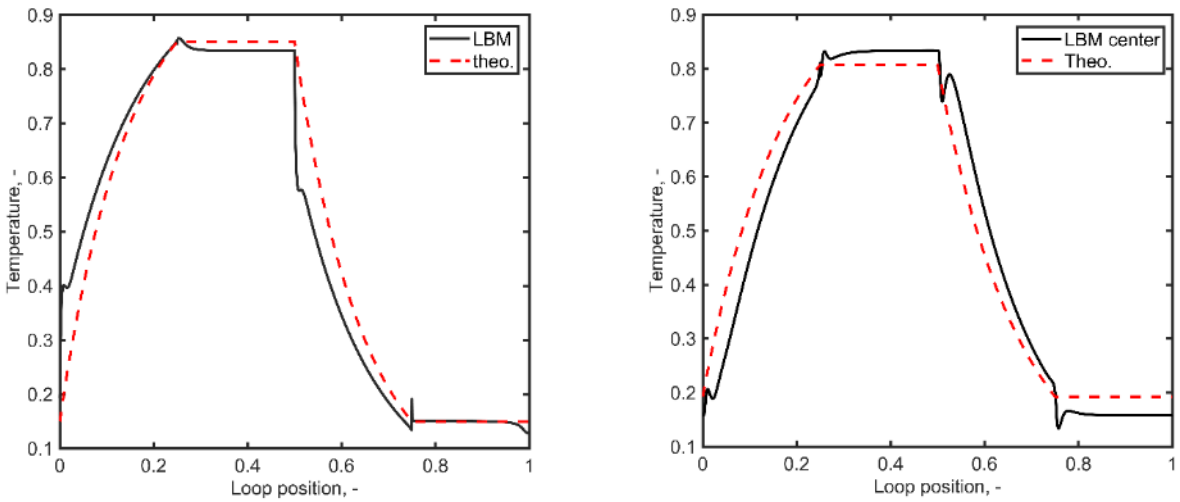

(a) (b)

Figure 4.10 Dimensionless temperature distribution along the NCL, $Re_{ss} = 100$. (a) Temperature average over the cross-sections, (b) Temperature at the tube center.

The analytical model allows the calculation of the temperature along each section of the circuit. A comparison between the one-dimensional theoretical model and the LBM results, taking the average

temperature on each section, is presented in Fig. 4.10(a), and taking the temperature at the center of the tube is presented in Fig. 4.10(b). The one-dimensional and LBM results present the same shape, but some differences are visible considering the average temperature of each cross-section. This difference with the one-dimensional theoretical model is lower considering the temperature at the center of the tube. The difference indicates the significance of the axial temperature distribution mainly in the first part of each pipe. The diffusion of the temperature field homogenizes the temperature profile, and the effect on the longitudinal temperature profile is less notorious.

Nusselt (Nu) number accounts for the convective heat transfer characteristics. The average Nusselt number along the heater simulated by the LBM is calculated by Eq. 4.34 (FD) and Eq. 4.35 (FD2). Fig. 4.11 compares the computational average Nusselt number along the heater and the empirical relationship proposed by Cheng et al. in Eq. 4.38 [1]. The simple expression $Nu = 3.66$ (laminar regime) commonly accepted for the heat transfer of a developed (laminar) flow in a pipe does not reflect the heat transfer characteristics along the loop. The empirical expression and the simulations show that the heat transfer is characterized by lower Nu numbers (below 3.66) in the laminar regime and increases with the Reynolds number with a non-linear dependency.

$$Nu = 0.2072\ Re_{ss}^{\ 0.4713} \qquad (4.38)$$

The LBM results match the Eq. 4.38 for low Reynolds number below 200, from this value to the critical Reynolds number that determines the transition to non-laminar flow (Re_{ss} around 320), the exponent of the Eq. 4.38 decreases, and after that, a different relationship with a higher increment is noticed.

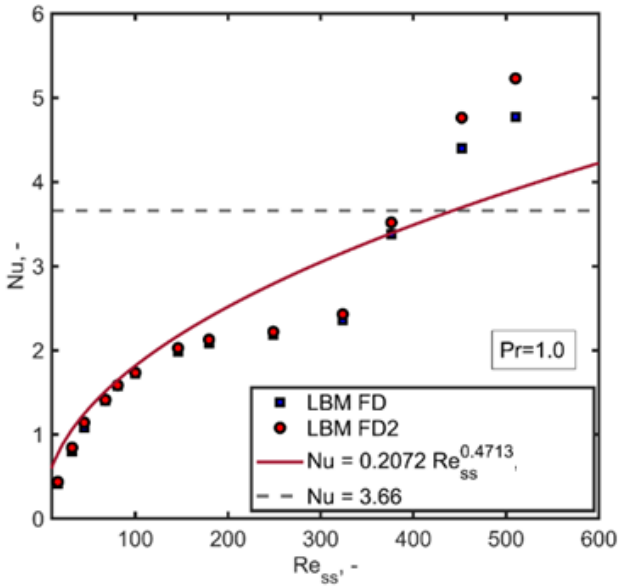

Figure 4.11 LBM Nusselt number for the heater vs. Reynolds number at steady state, calculated by finite differences, FD Eq. 4.20 and FD2 Eq. 4.21, compared with the empirical correlation Eq. 4.38.

Transition to a non-laminar regime

The validity of the theoretical model is limited to the laminar regime. In the present study, we found a non-laminar flow pattern for values of Gr_m around 10^5, equivalent to a steady-state Re_{ss} around 320. This limit was obtained considering $Pr = 1.0$. In the logarithmic diagram presented in Fig. 4.9, a change in the slope is visible near this quantity. Under the study range considered here for the Rayleigh number, the simulations for $Pr = 7.0$ do not show this regime transition.

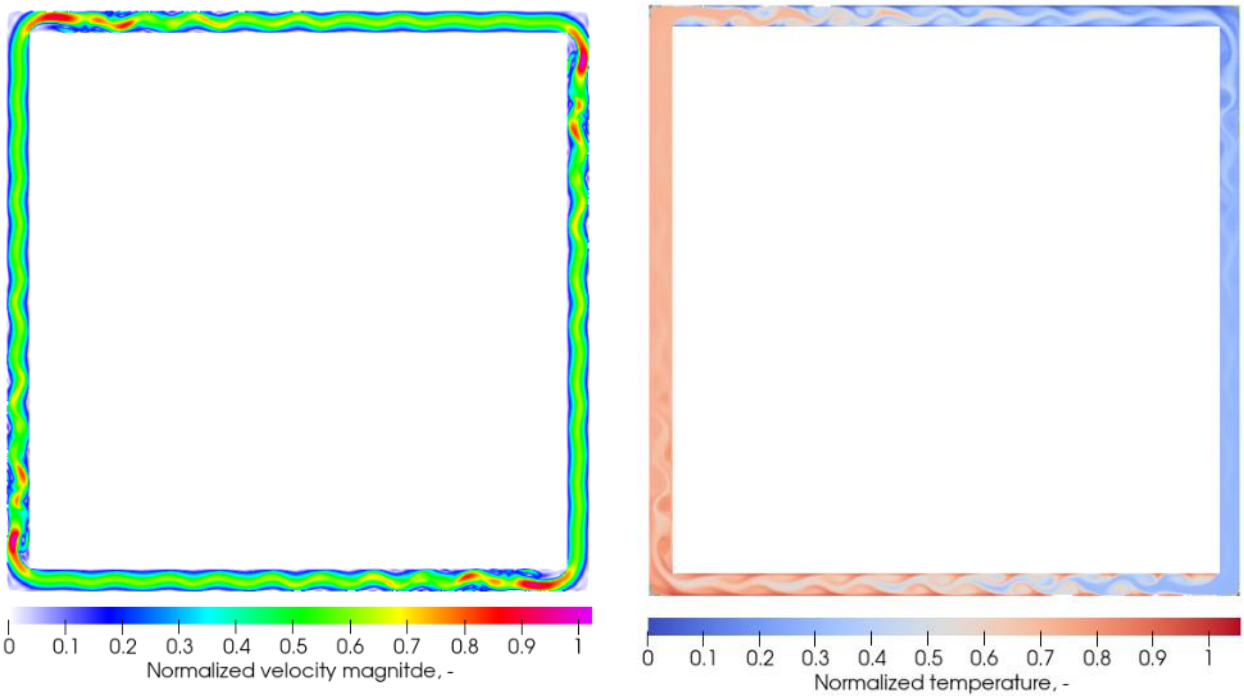

(a) (b)

Figure 4.12 Thermohydraulic response of the loop at high Reynolds number at "steady-state" ($Re_{ss} = 510, Pr = 1.0$) (a) Normalized velocity magnitude (b) Normalized thermal field.

The change in the flow regime is visible in the flow and thermal field presented in Fig. 4.12, characterized by vorticities formation near the wall that enhances the convective heat transfer by recirculation of the fluid across the heater and heat sink pipes. Those vorticities travel in the same direction as the mean flux and remain attached to the walls. Moreover, a sensible change is visible in the transient response of the circuit. Fig. 4.13(a) depicts an example of the transient response of the temperature near the limit of the transition regime ($Re_{ss} = 324$) and in the non-laminar regime ($Re_{ss} = 510$). Some eddies were visible during the temperature oscillations near the limit of the transition regime, but the system reached a steady-state with a laminar flow after some time. On the other hand, the system does not reach a steady-state for a higher Reynolds number, and the temperature oscillations continue around a central value, Fig. 4.13(a). A detail of this pseudo-steady-state is depicted in Fig. 4.13(b). Finally, the phase diagrams presented in Fig. 4.14(c) give detail about these two examples. For Re_{ss}*=324*, the system's dynamic changes abruptly after some oscillations and converge to a steady-state, Fig 11(a). In the other case, the small oscillations around the pseudo-steady-state temperature presented in Fig. 11(b) induce oscillations in the flow's velocity.

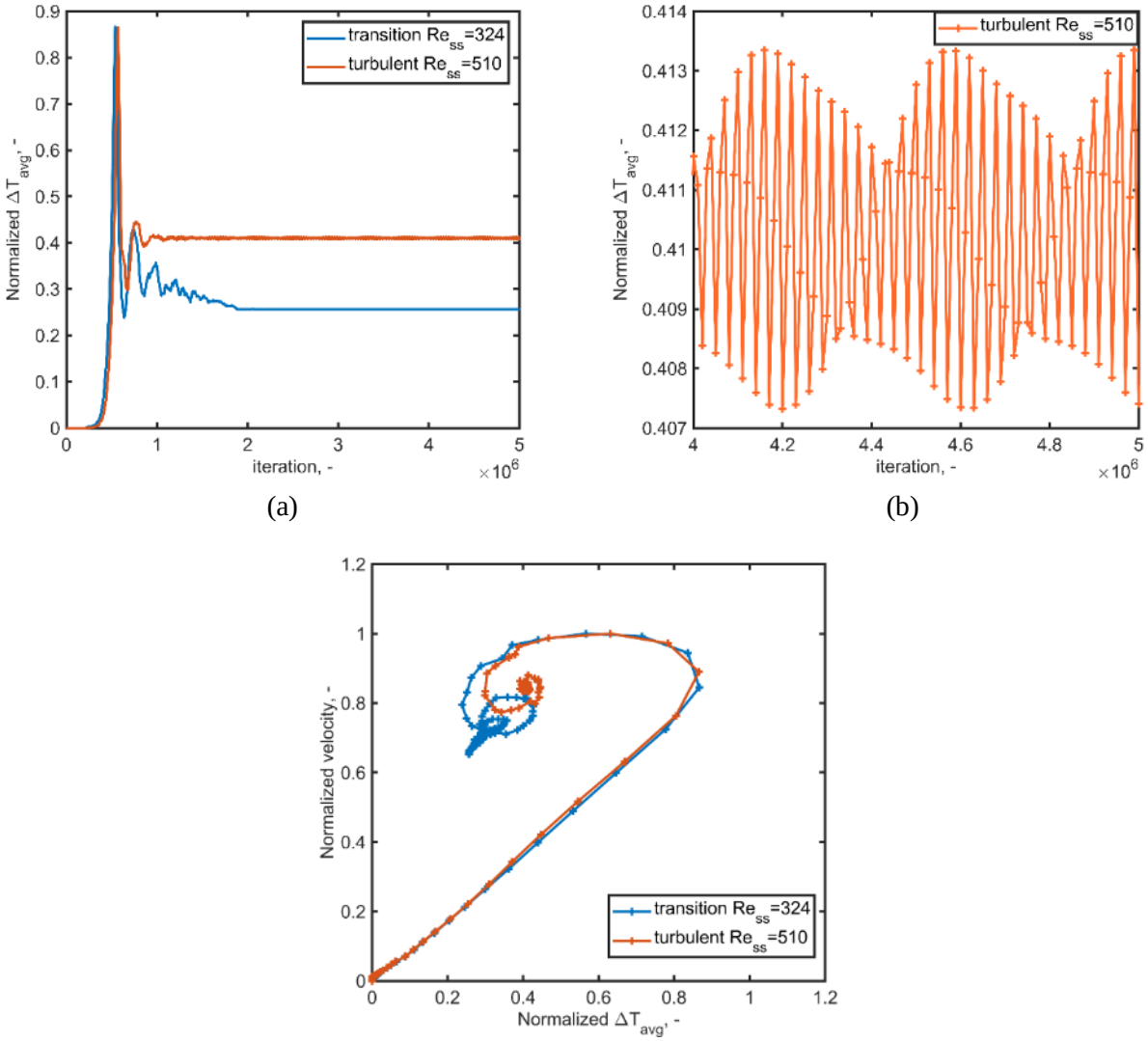

Figure 4.13 Response of the NCL at the transition regime ($Re_{ss} = 324$) and ($Re_{ss} = 510$). (a) temperature evolution, (b) detail of the temperature pseudo-convergence for $Re_{ss} = 510$, (C) Phase diagrams for temperature and velocity oscillations. $Pr = 1.0$.

The vorticity highly influences the temperature distribution along the circuit for the non-laminar regime near the heater and heat sink walls and in the first section of the vertical legs Fig. 4.14 (a). The temperature profile at the center of the tube presents higher oscillations, Fig. 4.14(b). The oscillations in the average temperature profile decrease with a lower Prandtl number, as shown in Fig. 4.14(c) considering the case $Re_{ss} = 660$, $Pr = 0.1$. Interestingly, the shape of the temperature profile predicted by the one-dimensional model only has a rough similarity to the LBM results, maybe because the vorticity is a three-dimensional effect that cannot be accurately represented assuming a one-dimensional model.

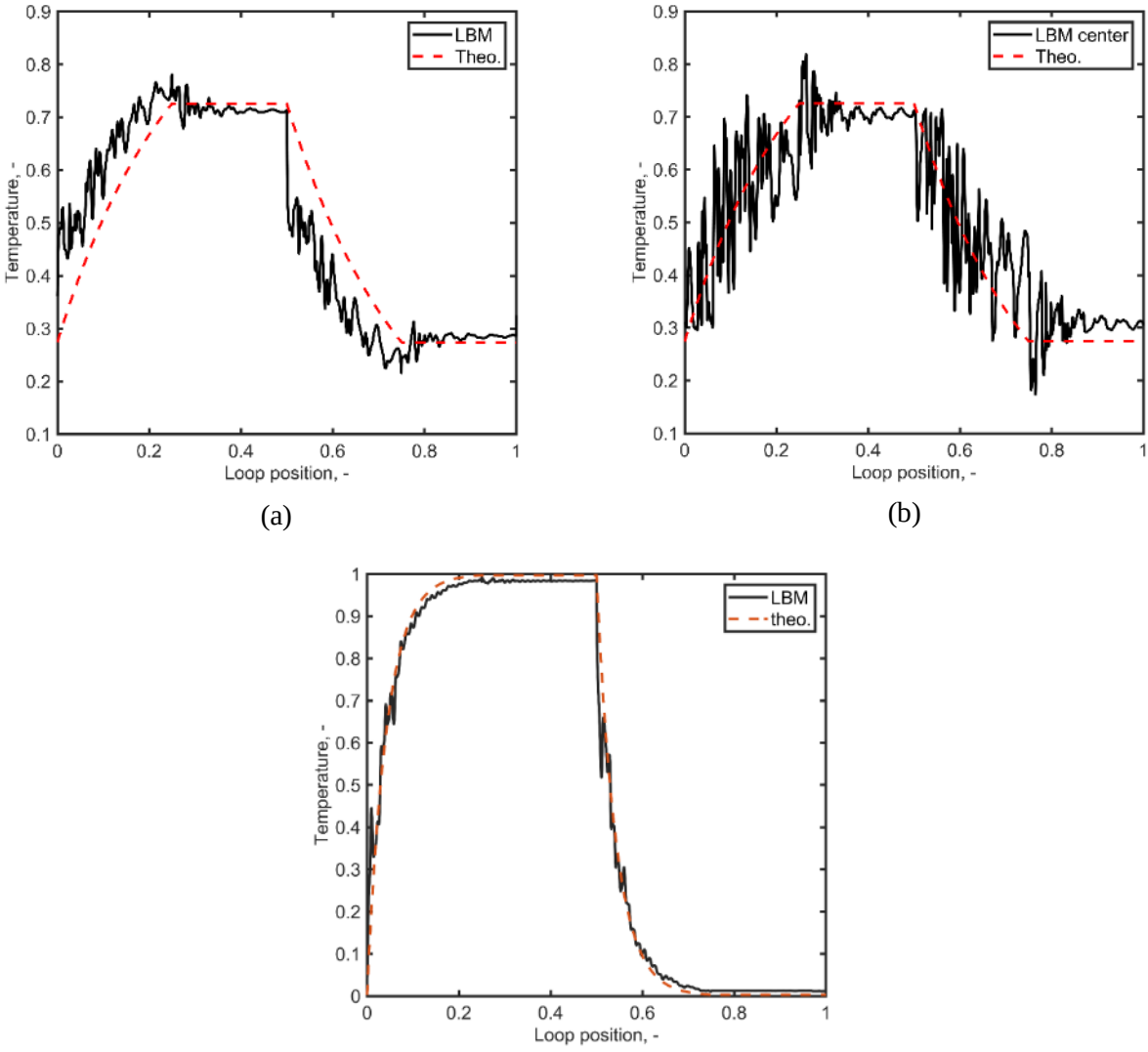

Figure 4.14 Dimensionless temperature distribution along the NCL (a) average temperature over the cross-sections $Re_{ss} = 510, Pr = 1.0$. *(b) Temperature at the tube center*$Re_{ss} = 510, Pr = 1.0$. *(c) average temperature over the cross-sections* $Re_{ss} = 660, Pr = 0.1$.

The origin of this non-laminar regime at a low Reynolds number, lower than the accepted critical values, 2000 for transition and 2300 for the turbulent regime, is unknown and more research is necessary to determine if it is a physical phenomenon or only a pure numerical artifact. However, some hypotheses that can explain this behavior are:

1. The bends in the corners are acute, and the corner itself can act as an obstacle for the flow,

2. By the simplified geometrical model, the fluid experiments at the corners an expansion and a contraction by the local pipe diameter change.

3. Additionally, the fluid experiments an acceleration caused by the Boussinesq force, mainly at the heater and heat sink.

4. Moreover, vorticity is a three-dimensional effect that is simulated approximatively using two-dimensional models.

The necessity to refine the LBM numerical approach emerges from this hypothesis, considering accurate three-dimensional models with a high mesh resolution to resolve small turbulences. Of course, the computational load increments considerably with those upgrades. It is necessary to consider that the eddies' presence does not necessarily imply a "*fully turbulent regime* with the subsequent energy cascade from the large eddies to the small ones". In fact, our results do not cancel the validity range of the relationships proposed by Eq. 4.36. However, they indicate the necessity to conduct experiments at higher Reynolds values (overcoming the implicit difficulty to remain in single-phase at high Rayleigh numbers, maybe by selecting an adequate working fluid characterized by a low Prandtl number).

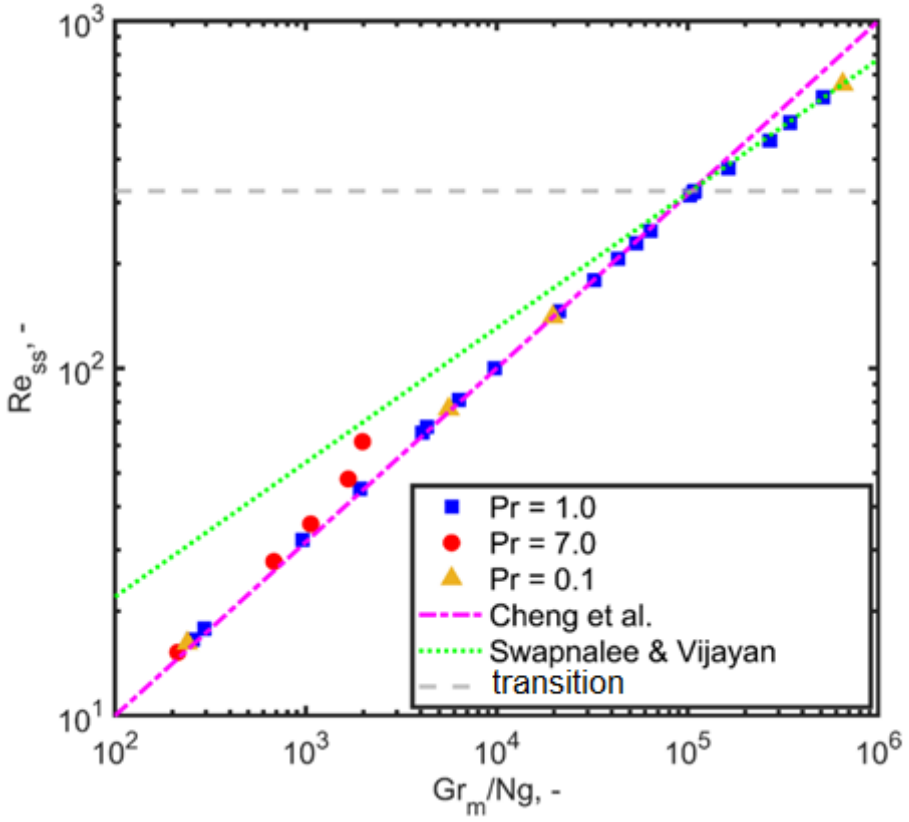

Figure 4.15 Description of the thermohydraulic behavior of the NCL by the relationship between Re_{ss} and.Gr_m/Ng, including the Eq. 4.39 for the transition regime proposed by Swapnalee and Vijayan [3].

The transitions region in closed loops in HHHC configuration is expected to occur at lower values of Reynolds number than the accepted value for straight pipes, as was reported by several authors as Creveling et al. [55] ($Re = 1500$), Hallinan and Viskanta [56] ($Re = 340$), or Swapnalee and Vijayan [3] ($Re = 898$). Those last researchers propose to use a different friction factor for the turbulent regime, $ff = 0.316/\ Re^{0.25}$, and $ff = 1.2063\ /Re^{0.416}$ for the transition zone to calculate the relationship of the figure. If this friction law is considered the exponent in Eq. 4.36 changes as is showed in Eq. 4.39. The idea behind the use of this friction law for the transition zone is presented in Fig. 4.15.

$$Re_{ss} = \left(\frac{Gr_m}{N_G{}'}\right)^{0.364} \qquad (4.39)$$

Effects of Prandtl number

The main set of curves were obtained simulating a Prandtl number equal to 1. In LBM, that means that both lattices have the same relaxation time (physically have the same diffusivity ratio, i.e., viscosity and thermal

conductivity). When the value of the Prandtl number was changed to a higher value ($Pr = 7.0$), lower values of $\mathrm{Gr_m}$ are reached with the same initial setup (global Rayleigh number), and lower Reynolds number values at steady state were obtained. However, all the points fall in the same trend as shown in Fig.4.15.

A few tests were conducted for a lower Prandtl number $Pr = 0.1$ and were in concordance with this observation. On the other hand, it is interesting that the transient behavior is different considering two Prandtl numbers at similar Reynolds numbers, as depicted in Fig. 4.16. The evolution of the average temperature difference between the vertical legs depicted in Fig.4.16(a) shows in the case of $Pr = 7.0$ a higher number of oscillations and subsequently takes more time to arrive at steady-state than the $Pr = 1.0$ case. This fact is also visible in the phase diagrams presented in Fig. 4.16(b).

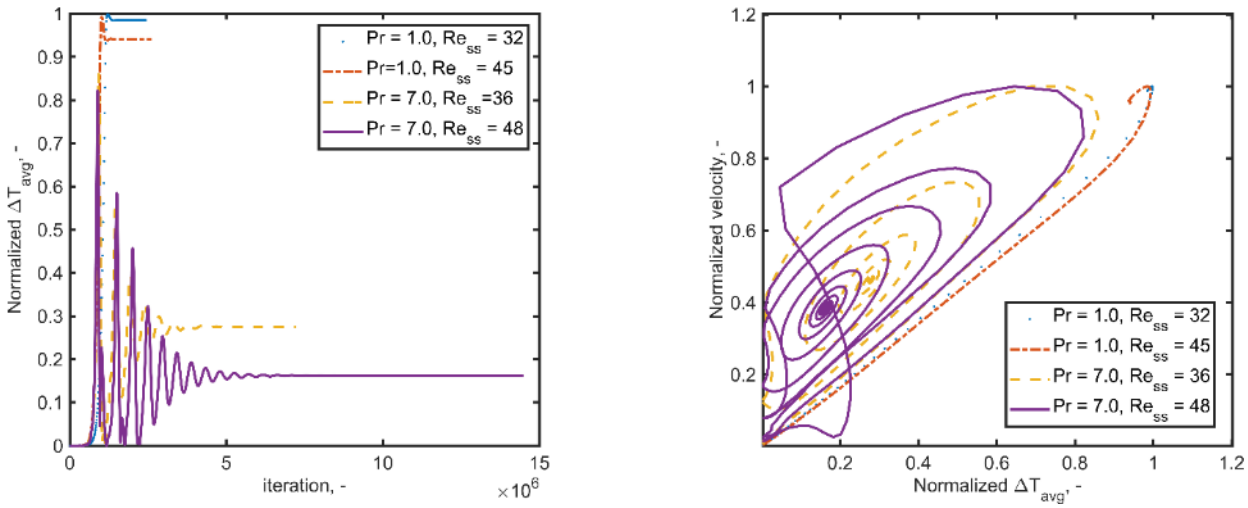

(a) *(b)*

Figure 4.16 Transient response of the NCL simulated by LBM for different Reynolds numbers and Prandtl numbers. (a) ΔT_{avg} vs. time, (b) phase diagram: normalized velocity vs. normalized ΔT_r.

The increment of the Prandtl number implies a dominance of the momentum transport over the thermal conduction, which means that the fluid transports the heat mainly by convection. The fluid increase or decreases (locally) its temperature with more difficulty, and of course, this makes the convection difficult because the body force term is considered linear dependent on this temperature change. On the contrary, a fluid with a low Prandtl number is easily heated and therefore the density changes are quickly induced with a subsequent higher flow rate.

Effects of the heater and cooler configuration

This section presents results considering a case study of a (mini) Natural Circulation Loop suitable for electronic cooling or solar PV panel cooling. The position of the heater and the cooler gives origin to several loop configurations named as Horizontal Heater Horizontal Cooler (HHHC), Horizontal Heater Vertical Cooler (HHVC), Vertical Heater Horizontal Cooler (VHHH), and Vertical Heater Vertical Cooler (VHVC) [57]. This study shows the effects of changing the loop configuration (HHHC, HHVC, VHHC, VHVC) on the flow characteristics and the thermal effectiveness.

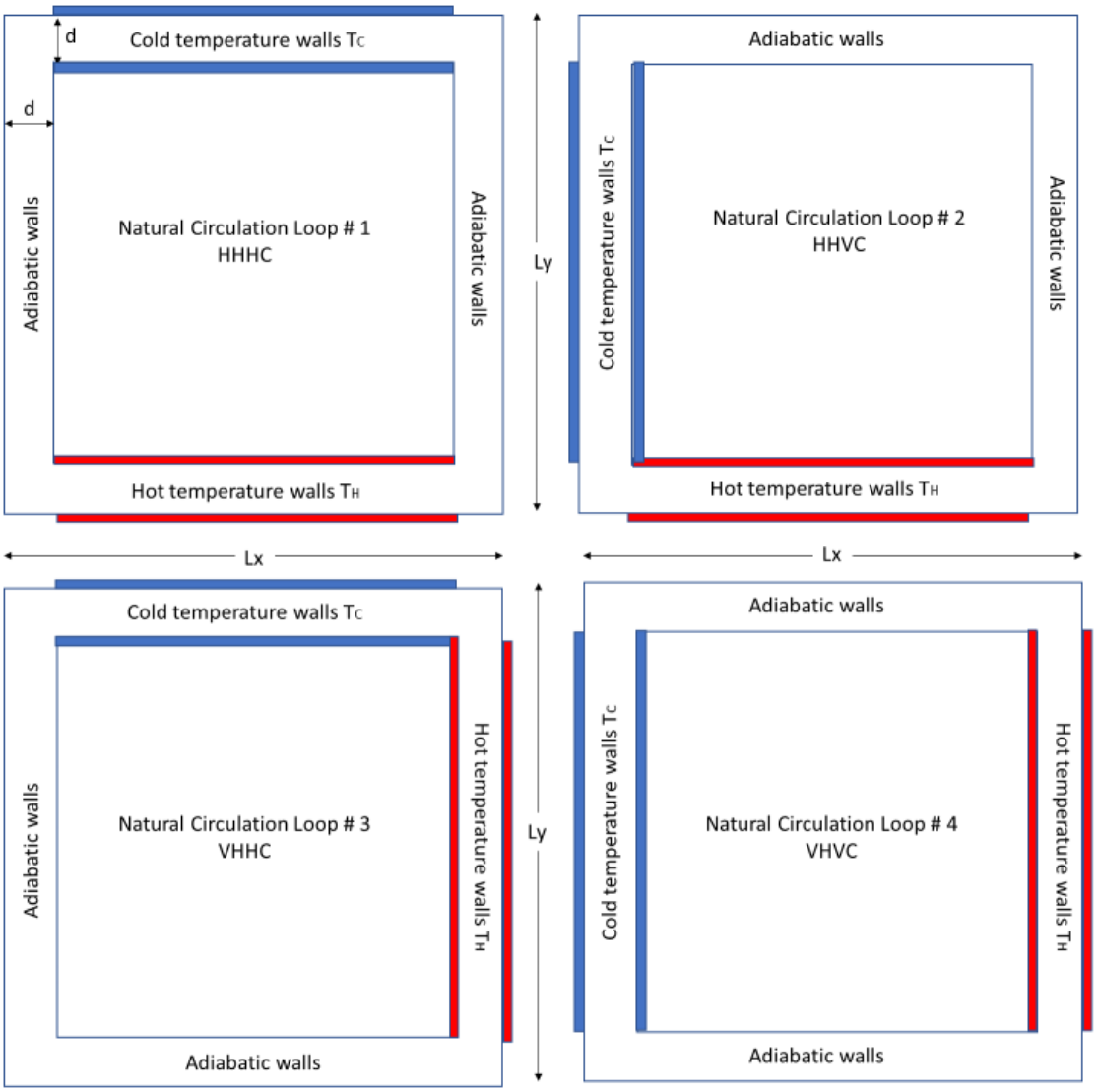

Figure 4.17 Loop configurations: Horizontal Heater Horizontal Cooler (HHHC), Horizontal Heater Vertical Cooler (HHVC), Vertical Heater Horizontal Cooler (VHHH), and Vertical Heater Vertical Cooler (VHVC).

The comparison among the four configurations was made at the same operating conditions in the laminar regime. Those operating conditions can be resumed in the Rayleigh number, in this case, the value 10^6 was selected. A schematic representation of the loop and the tested configurations is presented in Fig. 4.17. The loop considered here works with the fixed temperature at the heater (T_H) and cooler (T_C), also known as *NCL with heat end exchangers* [17].

As was expected, the HHHC loop is the only symmetrical configuration considered, and the flow in both senses (clockwise and counterclockwise) is possible. We observe this fact under several runs of the code. On the other hand, the vertical position of the cooler or the heater forces the flow in the loop in the considered geometry in a counterclockwise sense. Fig.4.18 shows the flow under the four configurations analyzed here.

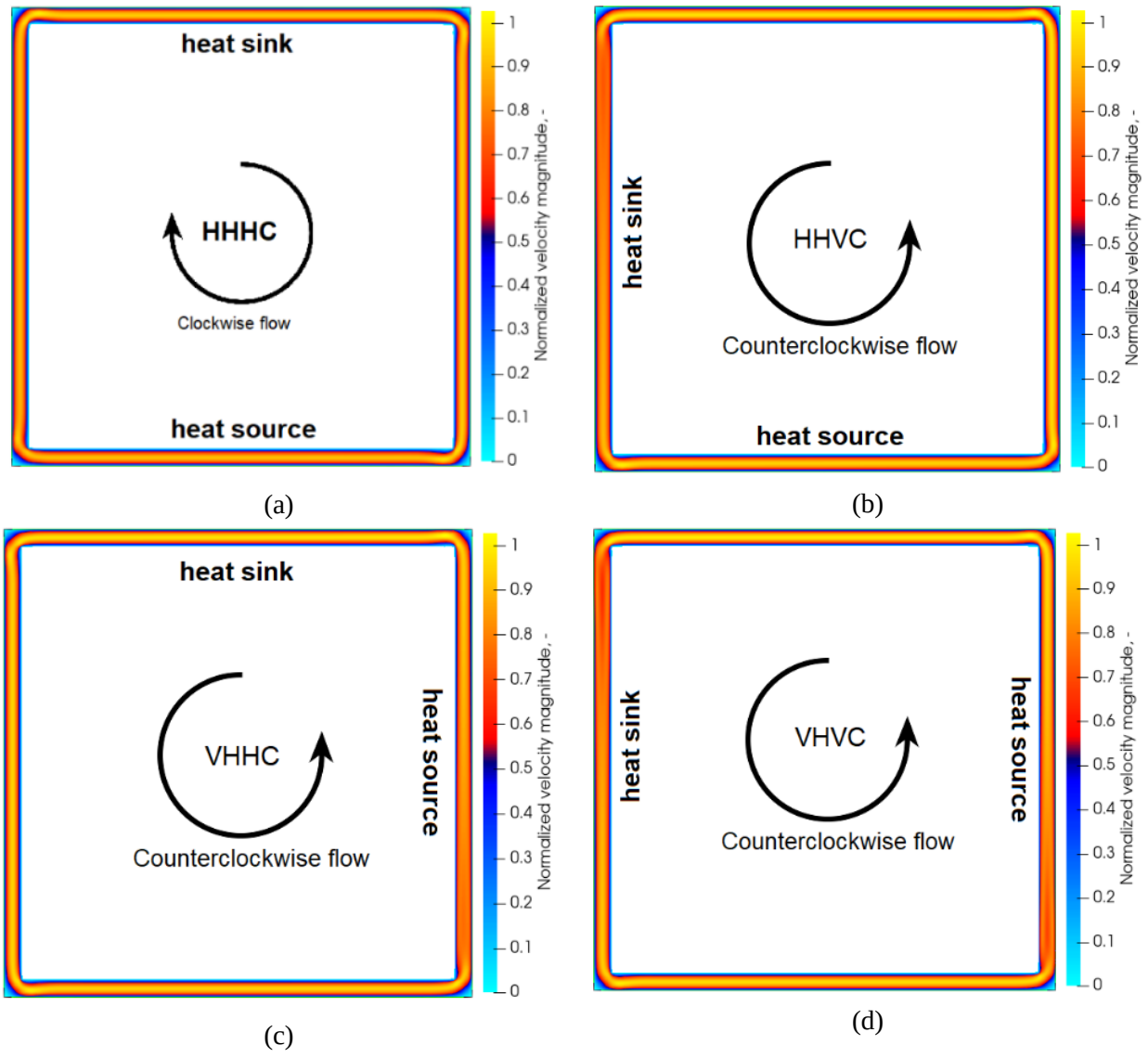

Figure 4.18 Normalized velocity magnitude and flow direction along the loops at steady-state (a) HHHC; (b) HHVC; (c) VHHC; (d) VHVC.

In Fig. 4.18, the flow pattern is laminar in all the cases. The velocity decreases to zero near the walls and presents the maximum in the center of the tube. However, some small perturbances are noted at the corners, probably by the 90° elbows. Moreover, a big deviation for the expected parabolic profile was noted at the inlet of the vertical heaters or coolers. This effect can be explained by the buoyancy force acting against the fluid flow in those vertical pipes. This interesting fact is depicted in Fig. 4.19(a), the cross-section velocity profile at different locations along the vertical heater shows a sensible decrease of the velocity at the center near the inlet (three diameters), and then the effect vanishes, and the parabolic profile is developed. Fig. 4.19(b) depicts the longitudinal velocity profile for the VHVC loop to illustrate this phenomenon at the center of the pipe. However, the effect on the cross-section averaged velocity is almost imperceptible.

Fig. 4.20 shows the transient behavior of the four circuits. The oscillation during the transient is more evident for the HHHC configuration, similar for HHVC and VHHC, and very reduced for VHVC. Also, it is visible in the figure that the time to reach the steady-state changes for each configuration. Similar behaviors were experimentally observed by Vijayan et al. [58] and Chen et al. [59]. They found experimentally that for HHHC and HHVC the time to start the circulation is higher than the time to start the flow with vertical heaters, in which cases the flows start when the heating power is provided.

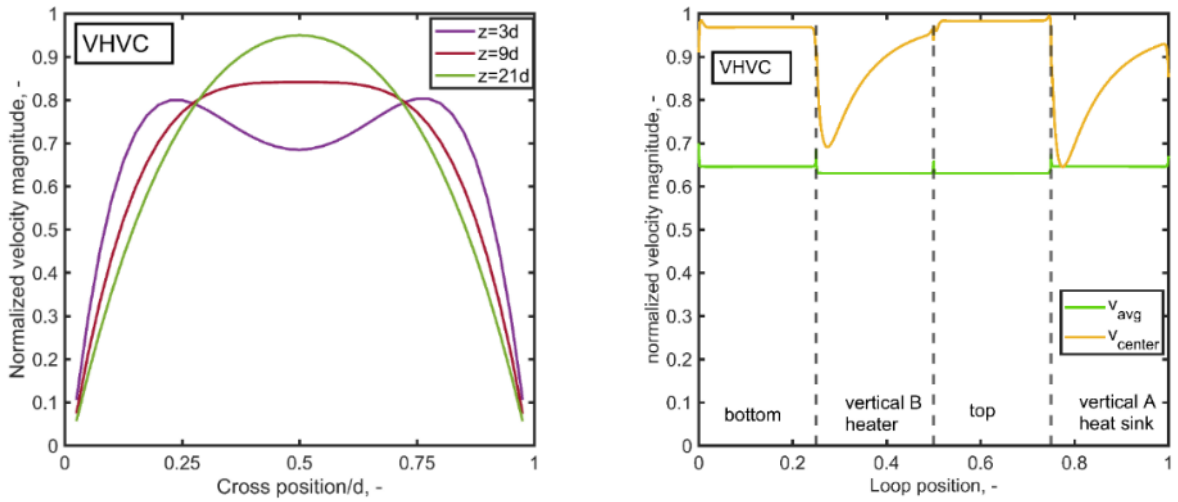

Figure 4.19 VHVC velocity profile (a) Cross-section (b) Longitudinal section at the center of the pipe v_{center}, and cross-section average velocity $v_{avg.}$

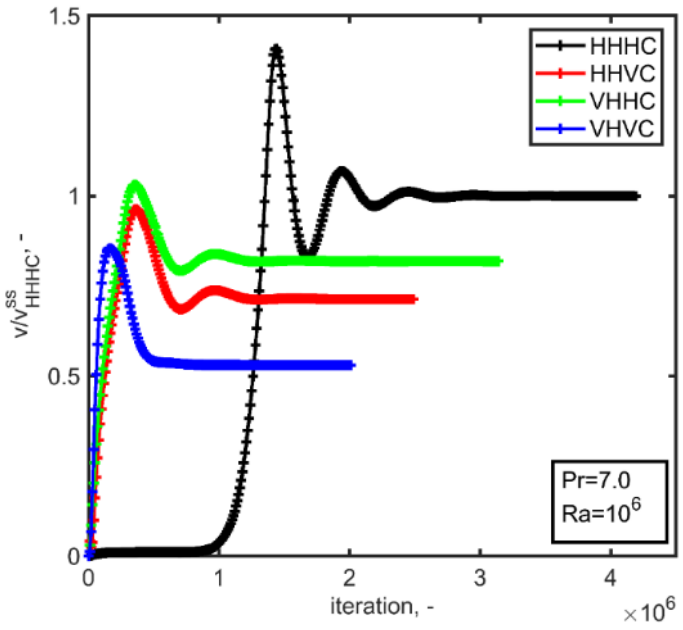

Figure 4.20 Transient of the velocity, normalized to the HHHC velocity at steady-state.

Fig. 4.21 shows the thermal field at the steady-state. It can be noticed that the main temperature gradient is obtained at the heaters and heat sinks. Moreover, the other pipes present a minimum temperature variation. In fact, this figure provides a visual probe of the adiabatic condition of those unheated pipes. Also, it is interesting to note that in the HHHC one adiabatic pipe is hot, and the other is cold, as in the VHVC configuration. On the other hand, the HHVC and VHHC configurations have only one adiabatic section, hot and cold, respectively. Fig.4.22 presents the normalized temperature profile along the longitudinal axis.

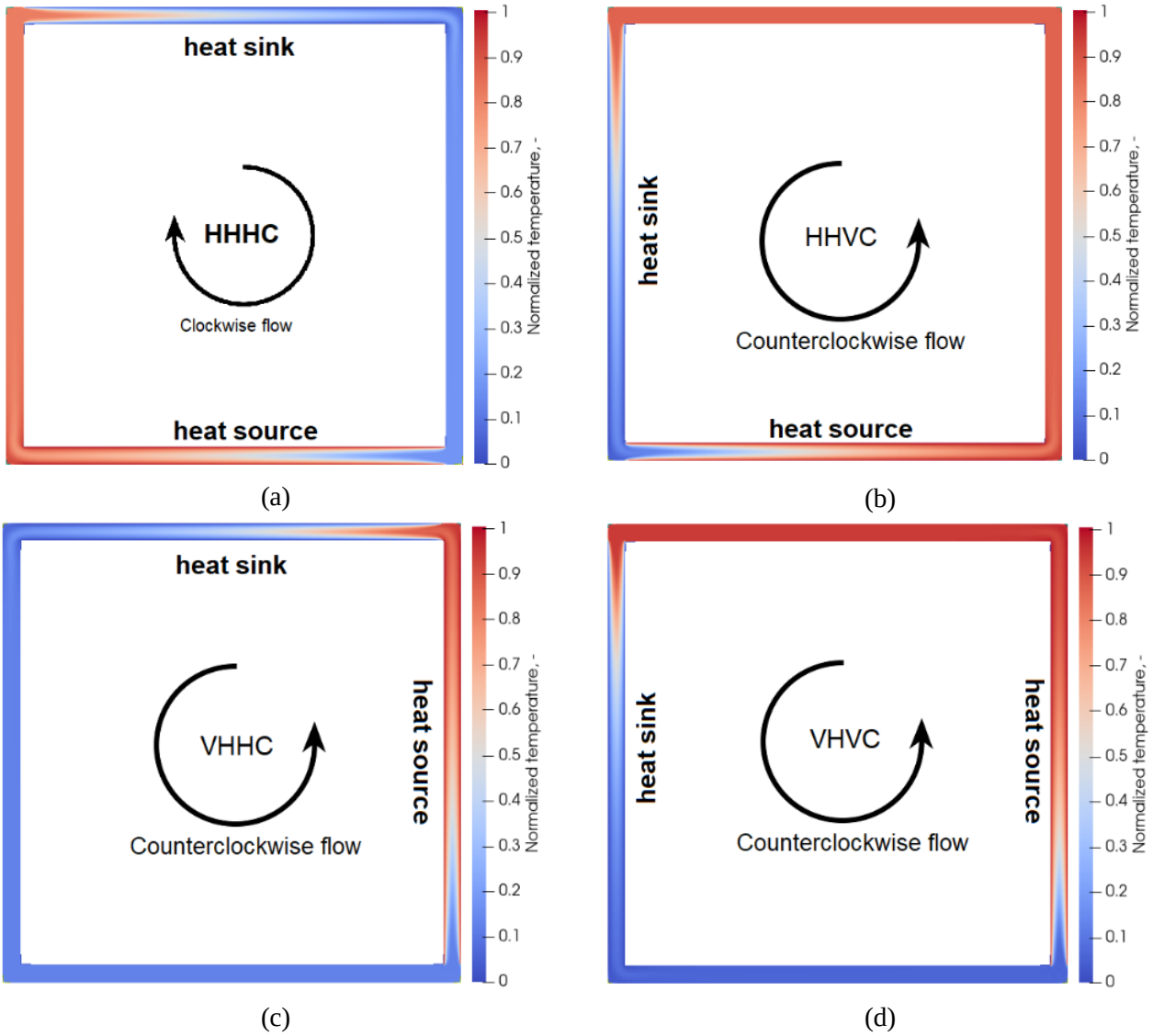

Figure 4.21 Thermal field and flow direction along the loops at steady-state. (a) HHHC; (b) HHVC; (c) VHHC; (d) VHVC.

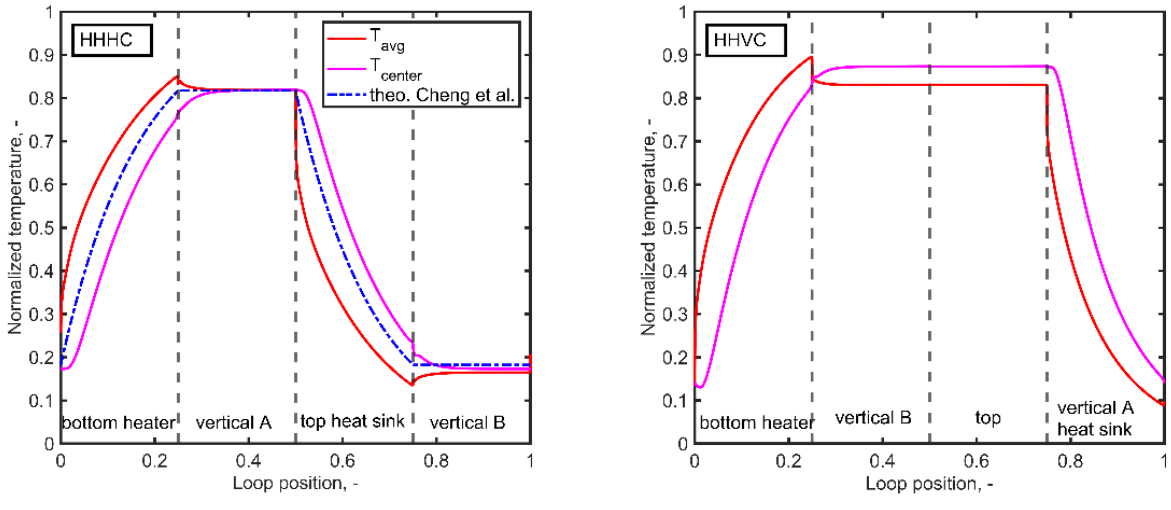

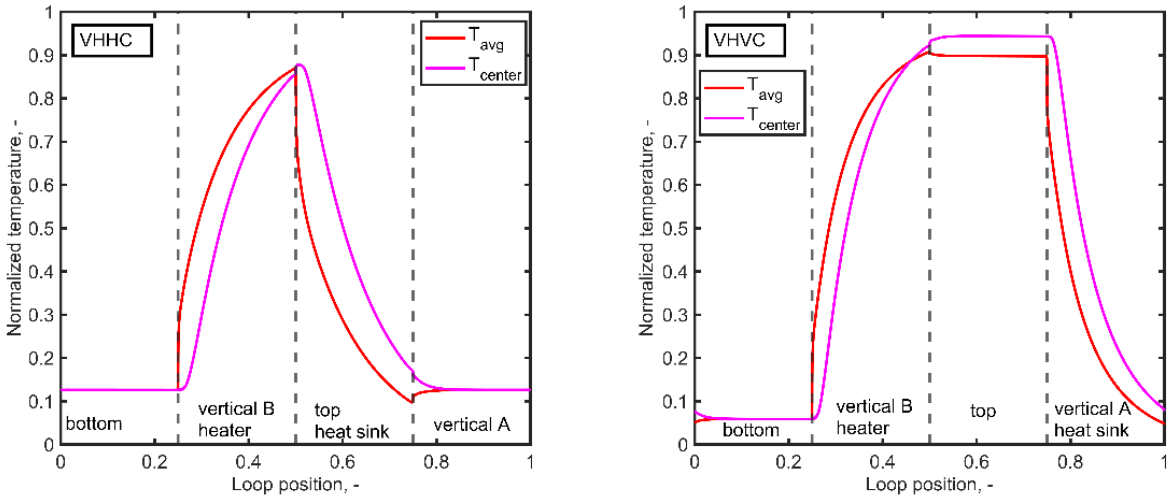

(c) (d)

Figure 4.22 Temperature profile at steady-state along the loop (following the flow direction). (a) HHHC; (b) HHVC; (c) VHHC; (d) VHVC.

To compare the performance of the four circuits, some parameters and nondimensional groups were calculated (Table 4.5). The percentual differences referenced to the HHHC values are included for the HHVC, VHHC and VHVC loops.

Table 4.5 Thermohydraulic parameters were evaluated at steady-state, considering the four heater-cooler configurations. The comparison took the Horizontal Heater Horizontal Cooler values as a reference.

Nondimensional parameter	**Loop configuration**			
	HHHC	HHVC	VHHC	VHVC
Transient time, timesteps	4195300	2494300	3143900	2013000
		-41%	-25%	-52%
Reynolds number: Re_{ss}	15.2	10.9	12.5	8.1
		-28%	-18%	-47%
Heater average Nusselt number: $\overline{\mathrm{Nu}}$	1.78	0.43	0.43	0.37
		-76%	-76%	-79%
Heat sink temperature difference: $T_{sink}^{in} - T_{sink}^{out}$ -	0.58	0.74	0.70	0.85
		+28%	+21%	+47%
Heat sink effectiveness: ε_{sink}	0.71	0.89	0.80	0.94
		+25%	+13%	+32%

Table 4.5 shows the simulation steps needed to reach the steady-state. The Reynolds number referenced to the pipe diameter is used to evaluate the flow regime. It is noted that the highest value is obtained in the HHHC configuration. The Nusselt number expresses the proportion between the convective and conductive heat transfer. The average Nusselt number $\overline{\mathrm{Nu}}$ was numerically calculated for the heater in all the configurations using the temperature gradient near the wall. The theoretical Nusselt number for the HHHC configuration was calculated by fitting the thermal profile to the Cheng et al. model (Nu=1.60) and using the empirical correlation proposed by them (Nu=1.43). This value is lower than the common value for straight pipes Nu=3.66. The highest value was observed for the HHHC configuration. The temperature difference at the heat sink inlet and outlet is included $T_{sink}^{in} - T_{sink}^{out}$, the highest value was obtained for the VHVC configuration. Using the temperature values at the inlet T_{sink}^{in} and outlet T_{sink}^{out} of the heat sink, it is possible to obtain the effectiveness, Eq. 4.40, by comparing the steady-state temperature difference $T_{sink}^{in} - T_{sink}^{out}$,

with the maximum possible difference $T_{sink}^{in} - T_C$. The highest heat sink effectiveness was found in the VHVC configuration.

$$\varepsilon_{sink} = \frac{T_{sink}^{in} - T_{sink}^{out}}{T_{sink}^{in} - T_C} \tag{4.40}$$

4.6 Conclusions

In this chapter, a two-dimensional Lattice Boltzmann Model based on double distribution functions was developed to simulate a square single-phase Natural Circulation Loop with fixed temperatures at the heater and heat sink in the Horizontal Heater Horizontal Cooler configuration.

This numerical approximation is of great interest because the one-dimensional models and experimental techniques (based on some thermocouples along the loop and differential pressure meters) commonly applied to those thermohydraulic circuits give only rough details around the velocity profiles and the temperature field.

A theoretical model and an empirical relationship for the heat transfer proposed by Cheng et al. [1] for a similar circuit were used to validate this numerical approach. The thermohydraulic behavior predicted by the model is in concordance with the theoretical model and the empirical data.

This Lattice Boltzmann Model shows that the modified Grashof number is a parameter that controls the thermohydraulic regime at steady-state. However, this number is not selected *a priori* because it depends on the temperature difference between the vertical legs after the steady-state is reached. In typical LBM Rayleigh-Bernard natural circulation simulations, the global Rayleigh number controls the natural circulation and is fixed from the beginning of the simulation.

Some key points that summarize the simulated behavior are:

- A higher global Rayleigh number implies a higher modified Grashof number in the laminar regime.
- A higher modified Grashof number implies a higher flow rate (Re_{ss}). An extensive simulation campaign confirmed the non-linear relationship between these quantities predicted by the theory, and a validity limit for the laminar relationships was found for $Re_{ss} < 300$.
- For a lower Prandtl number, higher values of Reynolds number can be reached.
- The non-laminar regime can be simulated directly without turbulence models (as LES) for Reynolds numbers below 1000.
- More oscillations in the temperature field and higher convergence time were observed for a higher Prandtl number.
- The one-dimensional analytic model roughly describes the temperature distribution along the loop. On the other hand, the one-dimensional model oversimplifies the system and does not consider flux or conduction in transversal direction or corner effects. Slight deviations were found in the one-dimensional model, mainly at the beginning of each pipe section.
- Heat transfer characteristics can be obtained by calculating local Nusselt numbers using the temperature field at the heater (or cooler). The average Nusselt numbers are similar and comparable with the empirical relationship between Nu and Re_{ss} for Reynolds numbers below 200.

Moreover, a non-laminar flow regime was found with different heat transfer characteristics than those predicted by the theoretical model and the empirical data. The transition to this regime was observed for $Pr = 1.0$ and $Pr = 0.1$ over a Reynolds number of 300. Traveling vorticities near the walls of the heater and heat sink were observed in the simulations. Considering that the data presented in the literature [1] used for validation were limited for steady-state Reynold numbers below 100, this regime was not observed or

expected. However, numerical results that deviate from the laminar behavior proposed by Cheng et al. [1] can be described applying the modified friction factor proposed for the transient regime by Swapnalee and Vijayan [3].

The effect of considering different configurations for the loop was presented for the transient and the steady-state. Moreover, the observations agree with previous observations presented by Vijayan et al. [58]. Summarizing the interesting results of this case study:

- The Horizontal Heater Horizontal Cooler configuration gives the highest flow rate.
- Disturbances in the parabolic velocity profile were observed at the inlet of the vertical section that contains the heater or cooler.
- The natural circulation takes more time to take place in the Horizontal Heater Horizontal Cooler configuration, and this time is similar for the other three configurations.
- The time to reach the steady-state going from low to high is VHVC, HHVC, VHHC, and HHHC, respectively.
- The VHVC configuration reached higher heat sink effectiveness.
- The highest Nusselt number was obtained in the Horizontal Heater Horizontal Cooler configuration.

Finally, the simulation shows that this kind of square loop is suitable for cooling systems of small components (as electronics or solar PV panels) in all the studied configurations. Under the tested operational parameters, all the loops remain in the laminar regime; the dynamic was stable (no flux inversion), and all reached a steady state. However, the thermohydraulic performance depends strongly on the selected configuration.

REFERENCES

[1] H. Cheng, H. Lei, L. Zeng, C. Dai, Theoretical and experimental studies of heat transfer characteristics of a single-phase natural circulation mini-loop with end heat exchangers, International Journal of Heat and Mass Transfer. 128 (2019) 208–216. https://doi.org/10.1016/j.ijheatmasstransfer.2018.08.136.

[2] M. Carrillo, U. Que, J.A. González, Estimation of Reynolds number for flows around cylinders with lattice Boltzmann methods and artificial neural networks, Phys. Rev. E. 94 (2016) 063304. https://doi.org/10.1103/PhysRevE.94.063304.

[3] B.T. Swapnalee, P.K. Vijayan, A generalized flow equation for single phase natural circulation loops obeying multiple friction laws, International Journal of Heat and Mass Transfer. 54 (2011) 2618–2629. https://doi.org/10.1016/j.ijheatmasstransfer.2011.01.023.

[4] M. Misale, J.A. Bocanegra, D. Borelli, A. Marchitto, Experimental analysis of four parallel single-phase natural circulation loops with small inner diameter, Applied Thermal Engineering. 180 (2020) 115739. https://doi.org/10.1016/j.applthermaleng.2020.115739.

[5] M. Misale, J.A. Bocanegra, A. Marchitto, Thermo-hydraulic performance of connected single-phase natural circulation loops characterized by two different inner diameters, International Communications in Heat and Mass Transfer. 125 (2021) 105309. https://doi.org/10.1016/j.icheatmasstransfer.2021.105309.

[6] J.A. Bocanegra, A. Marchitto, M. Misale, Thermal performance investigation of a mini natural circulation loop for solar PV panel or electronic cooling simulated by Lattice Boltzmann method., International Journal of Energy Production and Management. (Accepted).

[7] J.A. Bocanegra, A. Marchitto, M. Misale, Study of a square single-phase Natural Circulation Loop using the Lattice Boltzmann Method, International Journal of Thermal Sciences. ((Under review)).

[8] D.S. Pilkhwal, W. Ambrosini, N. Forgione, P.K. Vijayan, D. Saha, J.C. Ferreri, Analysis of the unstable behaviour of a single-phase natural circulation loop with one-dimensional and computational fluid-dynamic models, Annals of Nuclear Energy. 34 (2007) 339–355. https://doi.org/10.1016/j.anucene.2007.01.012.

[9] M. Misale, M. Frogheri, Influence of pressure drops on the behavior of a single-phase natural circulation loop: Preliminary results, International Communications in Heat and Mass Transfer. 26 (1999) 597–606. https://doi.org/10.1016/S0735-1933(99)00046-9.

[10] N.M. Rao, M. Mishra, B. Maiti, P.K. Das, Effect of end heat exchanger parameters on the performance of a Natural Circulation Loop, International Communications in Heat and Mass Transfer. 29 (2002) 509–518.

[11] N.M. Rao, B. Maiti, P.K. Das, Dynamic performance of a natural circulation loop with end heat exchangers under different excitations, International Journal of Heat and Mass Transfer. 48 (2005) 3185–3196. https://doi.org/10.1016/j.ijheatmasstransfer.2005.02.022.

[12] N.M. Rao, B. Maiti, P.K. Das, Pressure variation in a natural circulation loop with end heat exchangers, International Journal of Heat and Mass Transfer. 48 (2005) 1403–1412. https://doi.org/10.1016/j.ijheatmasstransfer.2004.10.010.

[13] K. Kiran Kumar, M. Ram Gopal, Steady-state analysis of CO2 based natural circulation loops with end heat exchangers, Applied Thermal Engineering. 29 (2009) 1893–1903. https://doi.org/10.1016/j.applthermaleng.2008.08.002.

[14] A.K. Yadav, M. Ram Gopal, S. Bhattacharyya, CFD analysis of a CO2 based natural circulation loop with end heat exchangers, Applied Thermal Engineering. 36 (2012) 288–295. https://doi.org/10.1016/j.applthermaleng.2011.10.031.

[15] A.K. Yadav, M. Ram Gopal, S. Bhattacharyya, Transient analysis of subcritical/supercritical carbon dioxide based natural circulation loops with end heat exchangers: Numerical studies, International Journal of Heat and Mass Transfer. 79 (2014) 24–33. https://doi.org/10.1016/j.ijheatmasstransfer.2014.07.068.

[16] A.K. Yadav, M. Ram Gopal, S. Bhattacharyya, CO2 based natural circulation loops: New correlations for friction and heat transfer, International Journal of Heat and Mass Transfer. 55 (2012) 4621–4630. https://doi.org/10.1016/j.ijheatmasstransfer.2012.04.019.

[17] H. Cheng, H. Lei, C. Dai, Thermo-hydraulic characteristics and second-law analysis of a single-phase natural circulation loop with end heat exchangers, International Journal of Thermal Sciences. 129 (2018) 375–384. https://doi.org/10.1016/j.ijthermalsci.2018.03.026.

[18] P.K. Vijayan, Experimental observations on the general trends of the steady state and stability behaviour of single-phase natural circulation loops, Nuclear Engineering and Design. 215 (2002) 139–152. https://doi.org/10.1016/S0029-5493(02)00047-X.
[19] A. Dass, S. Gedupudi, Numerical investigation on the heat transfer coefficient jump in tilted single-phase natural circulation loop and coupled natural circulation loop, International Communications in Heat and Mass Transfer. 120 (2021) 104920. https://doi.org/10.1016/j.icheatmasstransfer.2020.104920.
[20] K.V. Sharma, R. Straka, F.W. Tavares, Current status of Lattice Boltzmann Methods applied to aerodynamic, aeroacoustic, and thermal flows, Progress in Aerospace Sciences. 115 (2020) 100616. https://doi.org/10.1016/j.paerosci.2020.100616.
[21] N. Frapolli, S.S. Chikatamarla, I.V. Karlin, Multispeed entropic lattice Boltzmann model for thermal flows, Phys. Rev. E. 90 (2014) 043306. https://doi.org/10.1103/PhysRevE.90.043306.
[22] Y.-L. Feng, S.-L. Guo, W.-Q. Tao, P. Sagaut, Regularized thermal lattice Boltzmann method for natural convection with large temperature differences, International Journal of Heat and Mass Transfer. 125 (2018) 1379–1391. https://doi.org/10.1016/j.ijheatmasstransfer.2018.05.051.
[23] H.-B. Huang, X.-Y. Lu, M.C. Sukop, Numerical study of lattice Boltzmann methods for a convection–diffusion equation coupled with Navier–Stokes equations, J. Phys. A: Math. Theor. 44 (2011) 055001. https://doi.org/10.1088/1751-8113/44/5/055001.
[24] X. Shan, Simulation of Rayleigh-Bénard convection using a lattice Boltzmann method, Phys. Rev. E. 55 (1997) 2780–2788. https://doi.org/10.1103/PhysRevE.55.2780.
[25] Z. Guo, B. Shi, C. Zheng, A coupled lattice BGK model for the Boussinesq equations, Int. J. Numer. Meth. Fluids. 39 (2002) 325–342. https://doi.org/10.1002/fld.337.
[26] A. D'Orazio, S. Succi, Simulating two-dimensional thermal channel flows by means of a lattice Boltzmann method with new boundary conditions, Future Generation Computer Systems. 20 (2004) 935–944. https://doi.org/10.1016/j.future.2003.12.005.
[27] A.A. Mohamad, A. Kuzmin, A critical evaluation of force term in lattice Boltzmann method, natural convection problem, International Journal of Heat and Mass Transfer. 53 (2010) 990–996. https://doi.org/10.1016/j.ijheatmasstransfer.2009.11.014.
[28] L. Li, R. Mei, J.F. Klausner, Lattice Boltzmann models for the convection-diffusion equation: *D2Q5* vs *D2Q9*, International Journal of Heat and Mass Transfer. 108 (2017) 41–62. https://doi.org/10.1016/j.ijheatmasstransfer.2016.11.092.
[29] A.C.M. Sousa, M. Hadavand, A. Nabovati, Three-dimensional simulation of slip-flow and heat transfer in a microchannel using the lattice Boltzmann method, in: Tallinn, Estonia, 2010: pp. 75–85. https://doi.org/10.2495/HT100071.
[30] Y. Zhou, Y.-H. Dong, An investigation of the lattice Boltzmann equation-based hybrid approach for simulation of sound generated by isotropic turbulence, Computers & Fluids. 100 (2014) 267–277. https://doi.org/10.1016/j.compfluid.2014.05.015.
[31] X.R. Zhang, Y. Cao, A lattice Boltzmann model for natural convection with a large temperature difference, PCFD. 11 (2011) 269. https://doi.org/10.1504/PCFD.2011.042179.
[32] R. Zhang, H. Fan, H. Chen, A lattice Boltzmann approach for solving scalar transport equations, Phil. Trans. R. Soc. A. 369 (2011) 2264–2273. https://doi.org/10.1098/rsta.2011.0019.
[33] S.-K. Choi, S.-O. Kim, Comparative Analysis of Thermal Models in the Lattice Boltzmann Method for the Simulation of Natural Convection in a Square Cavity, Numerical Heat Transfer, Part B: Fundamentals. 60 (2011) 135–145. https://doi.org/10.1080/10407790.2011.594403.
[34] M. Sheikholeslami, M. Gorji-Bandpy, S.M. Seyyedi, D.D. Ganji, H.B. Rokni, S. Soleimani, Application of LBM in simulation of natural convection in a nanofluid filled square cavity with curve boundaries, Powder Technology. 247 (2013) 87–94. https://doi.org/10.1016/j.powtec.2013.06.008.
[35] G.H.R. Kefayati, Natural convection of ferrofluid in a linearly heated cavity utilizing LBM, Journal of Molecular Liquids. 191 (2014) 1–9. https://doi.org/10.1016/j.molliq.2013.11.021.
[36] T. Naffouti, University of Tunis, J. Zinoubi, El Manar, C.S. Nor Azwadi, Malysia, R. Ben Maad, El Manar, Applied Thermal Lattice Boltzmann Model for Fluid Flow of Free Convection in 2-D Enclosure with Localized Two Active Blocks: Heat Transfer Optimization, JAFM. 9 (2016) 419–430. https://doi.org/10.18869/acadpub.jafm.68.224.24198.
[37] A. Doostali, M. Rezazadeh, Numerical study of natural convection in a cavity with discrete heat sources, Eur. Phys. J. Plus. 133 (2018) 511. https://doi.org/10.1140/epjp/i2018-12323-4.
[38] Y. Wei, H. Dou, Turbulent Rayleigh–Bénard convection scaling in a vertical channel using the lattice Boltzmann method, in: Ancona, Italy, 2016: pp. 45–52. https://doi.org/10.2495/HT160051.

[39] M.A. Wahba, A.A. Abdelrahman, N.M. El-Sahlamy, M.F.A. Rabbo, Double SRT Thermal Lattice Boltzmann Method for Simulating Natural Convection of Low Prandtl Number Fluids, IJES. 6 (2017) 21–35. https://doi.org/10.9790/1813-0612022135.
[40] S.A. Hosseini, N. Darabiha, D. Thévenin, Lattice Boltzmann advection-diffusion model for conjugate heat transfer in heterogeneous media, International Journal of Heat and Mass Transfer. 132 (2019) 906–919. https://doi.org/10.1016/j.ijheatmasstransfer.2018.12.034.
[41] A. Alipour Lalami, M. Kalteh, Lattice Boltzmann simulation of nanofluid conjugate heat transfer in a wide microchannel: effect of temperature jump, axial conduction and viscous dissipation, Meccanica. 54 (2019) 135–153. https://doi.org/10.1007/s11012-018-00937-6.
[42] A.K. Hussein, H.R. Ashorynejad, M. Shikholeslami, S. Sivasankaran, Lattice Boltzmann simulation of natural convection heat transfer in an open enclosure filled with Cu–water nanofluid in a presence of magnetic field, Nuclear Engineering and Design. 268 (2014) 10–17. https://doi.org/10.1016/j.nucengdes.2013.11.072.
[43] Z. Li, M. Yang, Y. Zhang, Lattice Boltzmann method simulation of 3-D natural convection with double MRT model, International Journal of Heat and Mass Transfer. 94 (2016) 222–238. https://doi.org/10.1016/j.ijheatmasstransfer.2015.11.042.
[44] F. Benabderrahmane, B. Draoui, M. Douha, N. Kaid, A. Merabti, A. Sahli, H. Moungar, The Lattice Boltzmann Method Use to Simulate Natural Convection in a Single-Chapel Greenhouse, IJDNE. 15 (2020) 499–505. https://doi.org/10.18280/ijdne.150406.
[45] S.-K. Choi, S.-O. Kim, Computation of turbulent natural convection in a rectangular cavity with the finite-volume based lattice boltzmann method, Journal of Computational Fluids Engineering. 16 (2011) 39–46. https://doi.org/10.6112/kscfe.2011.16.4.039.
[46] Y. Ma, M.M. Rashidi, R. Mohebbi, Z. Yang, Nanofluid natural convection in a corrugated solar power plant using the hybrid LBM-TVD method, Energy. 199 (2020) 117402. https://doi.org/10.1016/j.energy.2020.117402.
[47] L. Li, Y. Wan, J. Lu, H. Fang, Z. Yin, T. Wang, R. Wang, X. Fan, L. Zhao, D. Tan, Lattice Boltzmann Method for Fluid-Thermal Systems: Status, Hotspots, Trends and Outlook, IEEE Access. 8 (2020) 27649–27675. https://doi.org/10.1109/ACCESS.2020.2971546.
[48] N.A. Che Sidik, S. Aisyah Razali, Lattice Boltzmann method for convective heat transfer of nanofluids – A review, Renewable and Sustainable Energy Reviews. 38 (2014) 864–875. https://doi.org/10.1016/j.rser.2014.07.001.
[49] X. He, L.-S. Luo, Lattice Boltzmann Model for the Incompressible Navier–Stokes Equation, Journal of Statistical Physics. 88 (1997) 927–944. https://doi.org/10.1023/B:JOSS.0000015179.12689.e4.
[50] T. Kruger, H. Kusumaatmaja, A. Kuzmin, O. Shardt, G. Silva, E.M. Viggen, The Lattice Boltzmann Method, Principles and practice, Springer, Switzerland, 2017. DOI:10.1007/978-3-319-44649-3.
[51] S.S. Baakeem, S.A. Bawazeer, Abdulmajeed.A. Mohamad, A Novel Approach of Unit Conversion in the Lattice Boltzmann Method, Applied Sciences. 11 (2021) 6386. https://doi.org/10.3390/app11146386.
[52] L. Jahanshaloo, N.A.C. Sidik, A. Fazeli, M.P. H.A., An overview of boundary implementation in lattice Boltzmann method for computational heat and mass transfer, International Communications in Heat and Mass Transfer. 78 (2016) 1–12. https://doi.org/10.1016/j.icheatmasstransfer.2016.08.014.
[53] J. Latt, O. Malaspinas, D. Kontaxakis, A. Parmigiani, D. Lagrava, F. Brogi, M.B. Belgacem, Y. Thorimbert, S. Leclaire, S. Li, F. Marson, J. Lemus, C. Kotsalos, R. Conradin, C. Coreixas, R. Petkantchin, F. Raynaud, J. Beny, B. Chopard, Palabos: Parallel Lattice Boltzmann Solver, Computers & Mathematics with Applications. (2020) S0898122120301267. https://doi.org/10.1016/j.camwa.2020.03.022.
[54] P. Garibaldi, M. Misale, Experiments in Single-Phase Natural Circulation Miniloops With Different Working Fluids and Geometries, J. Heat Transfer. 130 (2008) 104506. https://doi.org/10.1115/1.2948393.
[55] H.F. Creveling, J.F. De Paz, J.Y. Baladi, R.J. Schoenhals, Stability characteristics of a single-phase free convection loop, J. Fluid Mech. 67 (1975) 65–84. https://doi.org/10.1017/S0022112075000171.
[56] K.P. Hallinan, R. Viskanta, Heat transfer from a vertical tube bundle under natural circulation conditions, International Journal of Heat and Fluid Flow. 6 (1985) 256–264. https://doi.org/10.1016/0142-727X(85)90059-1.
[57] M. Misale, Overview on single-phase natural circulation loops, in: International Conference on Advances in Mechanical & Automation Engineering, Rome (Italy), 2014: p. 13.

[58] P.K. Vijayan, M. Sharma, D. Saha, Steady state and stability characteristics of single-phase natural circulation in a rectangular loop with different heater and cooler orientations, Experimental Thermal and Fluid Science. 31 (2007) 925–945. https://doi.org/10.1016/j.expthermflusci.2006.10.003.

[59] L. Chen, X.-R. Zhang, B. Jiang, Effects of Heater Orientations on the Natural Circulation and Heat Transfer in a Supercritical CO2 Rectangular Loop, Journal of Heat Transfer. 136 (2014) 052501. https://doi.org/10.1115/1.4025543.

5. APPLICATION TO NANOFLUIDS GRAVITATIONAL SEDIMENTATION

The term ‘nanofluid’ was introduced by Choi [1] and refers to a colloidal suspension of nanoparticles in a base fluid. The physical properties of the nanofluids make very interesting their use in engineering applications. For example, in the heat transfer process, the nanofluid thermal conductibility is increased [2-4]. However, a significant challenge for applying nanofluids in engineering applications is their stability. The nanoparticles tend to aggregate and sediment by the gravity force, degrading the physical properties of interest.

Among the possible approximations to this physical problem, the analytical models of first-order and second-order are of great interest by the relatively simple description of the time-dependent sedimentation process [5]. The differential equations that express the time evolution of the nanoparticle concentration are commonly solved by numerical methods as the Finite Differences (FD) [6-9]. On the other hand, the CFD-based approaches consider two-phase models (fluid phase for the base-fluid and solid phase for the nanoparticles) and are solved using macroscopic numerical methods (Navier-Stokes based) or microscopic models (molecular dynamics) for each phase [10-17]. If only a single phase is considered to describe the nanofluid, the sedimentation cannot be modeled.

The Lattice Boltzmann Method (LBM) can be an alternative to simulate the nanofluid behavior from a mesoscopic point of view, taking advantage of the inherent microscopical behavior of the nanoparticles and the statistical macroscopic behavior of the fluid at the same time, described in LBM by the evolution of the probability density function. A milestone work was presented by Xuan and Yao, who simulate the nanofluids sedimentation and heat transfer using LBM [18,19]. Some other examples of simulating convective heat transfer were presented in [20,21], showing the versatility and applicability of the LBM to nanofluids. In contrast with those previous works, here the focus is only on simulating the gravitational sedimentation considering different sub-models for the sedimentation velocity and the diffusive behavior of the nanoparticles.

This chapter aims to present a numerical model for long-term nanofluid gravitational sedimentation based on the Lattice Boltzmann Method. The LBM is applied to solve the Mason-Weaver equation [5], including different sedimentation velocity and diffusion coefficient assumptions. Sedimentation curves, for different positions on the cavity containing the nanofluid, are calculated. The numerical results obtained from the LBM model are compared with experimental measurements of long-term sedimentation of water-alumina Al_2O_3 and finite differences FD numerical results to validate the presented algorithm. This chapter is based on an overview of the role of nanofluids gravitational sedimentation in solar collectors [22], experimental study of long-term gravitational sedimentation of Al_2O_3 nanofluids [23], and LBM applied to gravitational sedimentation of Al_2O_3 nanofluids [24].

5.1 Overview on nanofluid’s gravitational sedimentation

The nanofluid stability can be considered as the property to assume a uniform nanoparticle distribution in the base fluid for an extended period. Unfortunately, the presence of the gravitational field (a) and the possibility

of cluster formation cause the sedimentation of the nanoparticles that derives in a gradient with higher nanoparticle concentrations at the bottom of the container.

The nanoparticles have a higher density than the base fluid, e.g., in the case of water-Al_2O_3 nanofluid, the density ratio between the nanoparticles and the base-fluid (ρ_p/ρ_f) is close to four. The solid particles tend to *fall* in the base fluid. When a particle with radius $d/2$ falls in a fluid characterized by a dynamic viscosity μ can reach a terminal velocity S described by Eq. 5.1; this relationship is also known as the Stokes law:

$$S = \frac{2 \cdot (d/2)^2}{9} \cdot \frac{a \cdot (\rho_p - \rho_f)}{\mu} \tag{5.1}$$

Higher terminal velocity S means shorter stability periods. The sedimentation time can be approximated as the relation between the height of the container L and the terminal velocity $t_{sed} = L/S$. The Eq. 5.1 presents a simplification of the phenomena, and it does not take into account interparticle interactions or Brownian diffusive effect. However, it gives the idea that the formation of clusters must be avoided because the characteristic size ($d/2$) of the particles is directly linked to their terminal velocity.

5.1.1 Stabilization techniques

The stability of the nanoparticles in the base fluid can be incremented by different *stabilization techniques* such as adding a surfactant, varying the pH of the solution (*chemical stabilization techniques*), or using sonication, magnetic stirring, mechanic stirring, ball milling, or high-pressure homogenizer (*physical stabilization techniques*) [25-30].

The nanofluid stability is affected by the surface charge (zeta potential) of the particles. This electric potential is related to repulsive forces that oppose attractive van der Waals attractive forces. The suspensions with zeta potential in the range ±30 mV have limited stability, whereas they are stable above ±30 mV. When the zeta potential is below 5 mV, a significant aggregation process occurs. For example, by adjusting the pH, it is possible to alter the zeta potential and consequently the aggregation process reducing the fluid viscosity without altering thermal conductivity characteristics [31]. The zeta potential can be affected by sonication, e.g., on Al_2O_3-water nanofluid can be increased from initial values near 20 mV up to 30 mV by applying sonication. For a sonication period between 0 to 180 min, it was experimentally proven by [32] that a more stable and less viscous nanofluid (volumetric concentration $v_p = 0.5$ %, Al_2O_3-water) can be obtained. Besides, it is pointed out that sonication is one of the more commonly used stabilization techniques, but for some conditions it can lead to nanofluids instability (e.g., the dispersion of the nanofluid containing Al_2O_3 and a particular surfactant (CTAB) can be deteriorated by sonication [33]). If the sonication is longer than 5 hours, a decrease in this stability can be noticed [34]. Also was observed that discontinuous ultrasonic pulses cannot break the aggregates (Al_2O_3-water) [35].

5.1.2 Preparation methods

The procedure utilized to prepare the nanofluids can affect their stability. The preparation methods are subdivided in the *one-step method*, i.e., directly obtaining the nanoparticles and synthetizing the nanofluid, for example, by physical vapor deposition techniques, or the *two-step method*, i.e., first obtaining the nanoparticles generally as a dry powder and after that mixing and dispersing those nanoparticles on the base fluid [36]. The one-step method has some advantages as cluster size control and drawbacks as not scalable production for industrial applications by higher cost. The two-step method can be scalable for applications requiring more considerable nanofluid volume, but stabilization techniques are needed to ensure a homogenous suspension [37]. A valuable and common stabilization technique used during the nanofluid preparation is sonication. Incrementing the time and power of the sonication increases the nanoparticle dispersion and improves the stability in most nanofluids, with some exceptions [38].

5.1.3 Operation conditions

The effects of the operating conditions on the stability were investigated in [26,39-45]. The temperature cycling can increment the diffusion, and the aggregation probability of the nanoparticles, whereas the confinement in microchannels, can impact the sedimentation by a higher surface interaction area. Salinity can reduce the electrostatic repulsive force, as well as a strong external magnetic field can increment the agglomeration but, in some cases, can increase the thermal performance. Finally, the addition of a surfactant can decrease the heat transfer performance and increase the viscosity. When the system is not operating (during the storage time or rest time), the probability of the gravitational sedimentation increases. The high temperatures and possible phase change can diminish the dispersion of the nanoparticles by the possible evaporation-condensation cycle of the fluid phase.

5.1.4 Approaches to the study of nanoparticle sedimentation

Fig. 5.1 shows a diagram resuming the different approaches followed to study the nanofluids sedimentation subdivided on experimental, analytical, or CFD-based approximation.

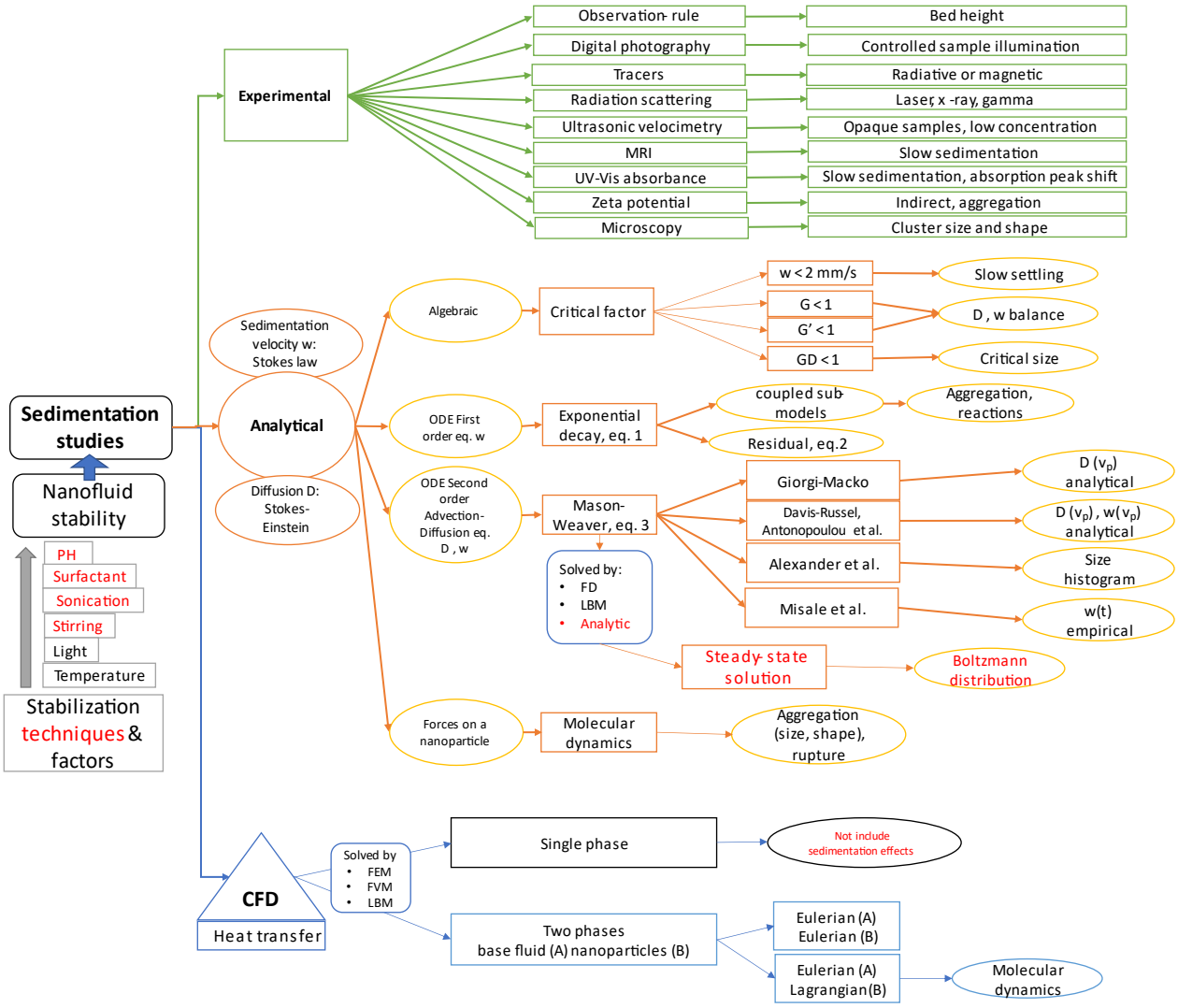

Figure 5.1 Scheme representing different approaches to the sedimentation studies in nanofluids.

The *experimental approach* can be assessed by several techniques that can be suitable for a *direct* study of sedimentation as bed height observation, digital photography, tracers, radiation scattering, or radiation

absorbance. On the other hand, zeta potential measurement or microscopy techniques can give *indirect* information concerning the nanofluid stability. The *analytical approach* is based on models that consider the gravitational effects on the nanoparticles. The relationship between gravitational sedimentation and diffusion is considered in second-order models through an advection-diffusion equation known as the Mason-Weaver model [5]. This model has been adapted for nanofluids taking different expressions for the diffusion and sedimentation parameters. The *CFD-based approach* is suitable for heat-transfer studies of nanofluids considering different flow conditions. This approach has been aborded in previous reviews [10,11].

Experimental approach

The experimental approach is followed by applying one or more laboratory techniques (classified here as *direct* or *indirect techniques*) to study different nanofluid samples and the effect of the following parameters on their stability. The effects of the initial volumetric concentration, the surfactant type, the light exposition, or the pH value are investigated. A summary of works that apply direct experimental techniques on nanofluid sedimentation is reported in this section, and some experimental details are presented in Table 5.1.

The direct techniques are implemented to measure settling rates and nanoparticles concentration and in particular:

- Deposition bed height determination (by photography or rule measure);
- Radiation scattering: Laser, X-ray, and gamma-ray (suitable for slow settling by the required acquisition time);
- Radioactive or magnetic tracers;
- Ultrasonic velocimetry (suitable for opaque samples at low concentration);
- Magnetic Resonance Imaging (MRI) (suitable for opaque samples and slow settling rate);
- Ultraviolet–visible (UV-Vis) spectral absorbance analysis.

Indirect techniques are used to determine the shape and measure the size of the clusters (microscopy techniques, Direct Light Scattering DLS) or determine the aggregation-repulsion electrical potential of the particles (zeta potential measurement). All these techniques were summarized in [30,46,47]. Additionally, in [48], it was investigated how the thermal conductivity measurement carried out by 3ω method (hot wire) can indirectly affect the sedimentation. This technique is a variation of the commonly used transient hot-wire for measuring fluids thermal conductivity, the temperature increments due to a hot wire immersed on the fluid is determined and the thermal conductivity is derived from this value. In the 3ω method, an oscillatory electrical stimulus is applied, and the transient effect is measured in the frequency-space instead of the time-space [49]. The sediment deposit affects the thermal conductivity of the immersed wire and can then be detected by this method.

In addition to the experimental techniques used in each study, it can be noted from the works presented in Table 5.1 that most of the studies concern the use of low nanoparticle concentrations (v_p < 1.0%) [27,47,50-56], only a few studies relate to the use of bigger concentrations [57-59]. It is also interesting to notice that the measurement periods go from a few hours to several days [53,57,58]. In these studies, the Authors used metallic nanoparticles and sonication as a stabilization technique. The use of surfactant as a stabilization technique is common [7,8,27,50-52,54-56,58] as the use of sonication with periods that goes from some minutes to several hours [27,47,50,51,53,55-59]. Not all the studies report explicitly the temperature at which the experiments were carried on, but it is reasonable to think that the room temperature condition was implemented in all the studies.

It is noticed that UV-Vis absorbance and digital photography are common *direct techniques*. The UV-Vis spectral absorbance analysis is based on the linear relationship between the absorbency intensity and the concentration of nanoparticles in fluid (Beer-Lambert law) [50]. The applicability limits of this law are discussed in [46]; some factors that affect the linearity of this law are the scattering, the deviations in

absorptivity coefficients, and the refractive index change at high nanoparticle concentrations, or the possible fluorescence of the sample. As the multiple light scattering (MLS), the UV-Vis absorbance is a non-destructive technique, but the MLS can be applied to opaque samples. Both techniques can give information about sedimentation phases and agglomeration processes. Furthermore, the UV-Vis spectral absorbance analysis can be used to determine size histograms of the nanoparticles measuring the absorption curve with a spectrophotometer and relating the peak frequency to the relative concentration of the nanoparticles [7,8]. Digital photography as an alternative technique is versatile [47,51,54,57], giving qualitative and quantitative data. It is common to use *indirect techniques*, mainly microscopy and zeta potential measurement, in addition to *direct techniques*, to obtain information about the size and shape of the nanoparticles.

Table 5.1 Overview of research items that follows an experimental approach to the study of nanoparticle sedimentation.

Study, year	Nanoparticle (size)	Base fluid	Concentration	Additives, surfactant	Sonication time	Temperature	Experimental technique	Indirect experimental technique	Measurement period	Theoretical Model	Main results
Hwang et al., 2006 [50]	MWCNT (10-30 nm) x (10 - 50 μm) fullerene (10 nm), CuO(33 nm), SiO_2 (12 nm), Ag	DI Water, Oil ethylene glycol, oil, silicon oil, and poly-a-olefin oil	1 vol%	Yes, SDS	2 h	293 K	UV–vis absorbance	Microscopy	800 h -/8 samples	-	Sedimentation curves, MWCNT have low stability, fullerene is stable for at least 800h.
Li et al., 2007 [51]	Cu (25 nm)	Water	0.1 vol%	Yes, CATB, SDBS, TX-10	1 h	298 K	Absorbency and photography qualitative	TEM, zeta potential	7 days	Aggregation DLVO	Zeta potential is linked with absorbance. Critical effect of pH
Tiraferri et al., 2008 [52]	nanoscale zero-valent iron (NZVI) (200 to 500 nm)	Water	1.5 g/L	Yes, green polymers Guar Gum, potato Starch, alginates	- Only shaken	298 K	UV–vis absorbance λ= 508 nm	TEM, DLS, Zeta potential	4000 s	First-order: Exponential decay rates	Aggregation of iron nanoparticles occurs in three phases.
Liu et al. 2011[53]	TiO2 (5 to 50 nm)	Water	20 mg/L	- NaCl and CaCl2 solutions (pH)	0.5,1 h	-	UV–vis absorbance λ= 312 nm, 286 nm	TEM, SEM, DLS, Zeta potential	30 days	Molecular dynamics, aggregation DLVO	Crystallinity and morphology does not affect the stability strongly
Rehman et al., 2012 [57]	Al_2O_3 (<50nm)	Water	1 wtl%, 3 %, 5 %	-	1, 2, 3 h	293 K	Bed height by digital photography	Particle sizing system	30 days	-	Sonication can overcome aggregation in the absence of surfactant, best stability 3%wt

											and 5%wt.
Witharana et al. 2012 [47]	Al_2O_3 10-(100nm)	Water	0.5 vol%	-	4 h	293 K	Digital photography, X-ray scattering)	Optical microscopy	30 min	-	Sedimentation phases are related to the cluster aggregation process
Witharana et al., 2013[58]	ZnO, Al_2O_3, and TiO_2	PG, EG in water (WPG, WEG)	1vol% 9vol%	Yes, Aerosol and others	0.5, 4 24, 38 h	293 K	Direct measure using a meter ruler	Zeta potential (particle size)	30- 60 days	Stokes law	Sedimentation velocity limit for stability, effects of light on particle size
Ghadimi and Metselaar, 2013 [27]	TiO_2 (25 nm)	Water	0.1 wt%	Yes, SDS	0 ,0.25, 3 h	298 K	UV–vis absorbance λ= 542 nm, photo	zeta potential, (TEM)	7 days	-	3 h sonication and surfactant (0.1 wt%) gives optimum stability
Mondragon et al. 2013 [60]	SiO2, Al2O3, NT	Water	0.5, 1, 5 V%	Yes, pH and SDS(NT)	2-3min	40,60,80 C	Backscattering	Zeta potential, TEM	48 H	-	Si, Al and NT remains stable for at least 48H, the influence of T is negligible
Alexander et al., 2013 [7]	Gold (12 to 92 nm)	Water	-	Yes, Ascorbate	-	298 K	UV–vis absorbance λ= 200-900 nm, TEM	TEM, DLS	210 h	Second order: Mason–Weaver	Diameter controls sedimentation rate
Alexanderet al. 2014 [8]	Gold (83 nm)	Water	-	Yes, Ascorbate	-	298 K	UV–vis absorbance λ= 300-900 nm	TEM	180 h	Second order: Mason–Weaver	Size histograms can be obtained from sedimentation experiments
Kamalgharibi et al. 2016	CuO	Water, Glycol	0.1 - 0.4 wt%	Yes, SDS, PVP and Triton X-	60-270 min	293 K	Direct measure sedimentation	X-ray diffraction, SEM, zeta	75 days	Stokes law	Optimum sonication time, lower

[55]				100			bed, photo	potential (DLS)			sedimentation velocity on glycol base fluids
Midelet et al. (2017)[54]	Gold (20 to 60 nm) / DNA assemblies	Water	0.42 vol%	Yes, carboxylate ligands	-	277 K	Digital photography	TEM	39 days	Second order: Mason-Weaver	Quantitative results from digital photography by analyzing color channels
Akhatov et al. 2018 [59]	SiO_2, (12 nm, 16 nm Al_2O_3 (50nm)	Water	1.5, 1,2 vol%	no	7-12 min	-	Bed height-photo	Laser diffraction, zeta potential (size)	80 min/72 h	-	Al <2% led to weak sedimentation. Si sediment less than Al
Gallego et al. [56]	Al_2O_3 (10 to 50 nm)	water	0.1, 0.5, 1.0 wt%	Yes, SDBS	20 min	293 K	UV-absorbance, digital photography	TEM, zeta potential	7 weeks	-	Thermophysical properties depends on surfactant content

Analytical approach

The simplest analytical model that predicts the nanoparticle concentration on time is based on the assumption that the concentration change rate depends directly on the concentration itself (Eq. 5.2). This equation is a first-order ordinary differential equation (ODE), or *first-order model*. The solution of this model conducts to an exponential decay of the nanoparticle concentration in time [61]. This model can describe the experimental data's tendency but does not give deep physical insight into the settling process because this approach does not account for the spatial dimension (it does not consider the height position to describe the sedimentation). The study [62] compares more complex mechanical models to explore the first-order simplification limits. They found that hetero aggregation with natural colloids (in natural waters) can play an important role. This model can be coupled with sub-models for the different processes as resuspension, mineralization, homo aggregation, hetero aggregation [61-63].

$$\frac{d\overline{v_p(t)}}{dt} = -\frac{S}{L}\,\overline{v_p(t)} \tag{5.2}$$

In this first-order ODE, $\overline{v_p(t)}$ represents the average nanoparticle concentration at a given time t for a nanofluid with a sedimentation velocity w calculated from the Stokes law in a height L. The typical solution to this equation takes an exponential form. Based on empirical results presented in [61] and [62] it is proposed that the solution to the first-order model can be better described considering not only the initial concentration $\overline{v_{p,ini}}$ but also the residual concentration $\overline{v_{p,res}}$, and a dissolution rate constant Kr as the following Eq. 5.3:

$$\overline{v_p(t)} = \left(\overline{v_{p,ini}} - \overline{v_{p,res}}\right)e^{-\left(\frac{S}{L}+Kr\right)t} + \overline{v_{p,res}} \tag{5.3}$$

An alternative approach to obtain more information about the relevant physics and a detailed calculus of the concentration of nanoparticles in time for different positions ($v_p(z,t)$) is possible through the second-order Mason-Weaver model [5]. Eq. 5.4 is an advection-diffusion equation for the concentration of nanoparticles. The model considers only one spatial dimension (z, oriented with the gravity) to describe the concentration profiles. This one-dimensional assumption is reasonable due to the length ratio between the container width (typically around some mm) and the nanoparticles size (below hundred nm). In works previously cited this model was used and adapted to nanoparticles sedimentation, in particular is remarkable the possible use of the Mason-Weaver model to obtain size distribution histograms [7,8].

$$\frac{\delta v_p(z,t)}{\delta t} = D \cdot \frac{\delta^2 v_p(z,t)}{\delta z^2} + S \cdot \frac{\delta v_p(z,t)}{\delta z} \tag{5.4}$$

The advection-diffusion equation (Eq.5.4) considers two different effects, i.e., the advection that changes the nanoparticle concentration by the action of bulk particle movement characterized by a sedimentation coefficient S and diffusion coefficient D that accounts for the Brownian effects. Different considerations can be made for the calculus of D and S. They can be considered constant coefficients, taking S from the calculus of the sedimentation velocity using the Stokes law (Eq. 5.1). The diffusion coefficient D can be determined from the Stokes-Einstein equation Eq. 5.5. Where k_B.is the Boltzmann constant and T the temperature.

$$D = \frac{k_B.T}{6 \cdot \pi \cdot \mu \cdot d/2} \tag{5.5}$$

It is possible to find an analytic solution to the Mason-Weaver equation under some conditions, e. g., when the convergence to the steady-state is reached (the nanoparticle distribution does not change “macroscopically” in time). The sedimentation process ideally starts from the initial state with a uniform

concentration of the nanoparticles and finishes at the steady state described by an exponential concentration gradient (Eq. 5.6).

$$v_p(t > t_{eq}, z) = v_{p,ini} \cdot B \cdot e^{(-z/z_0)} \quad (5.6)$$

The diffusion and sedimentation coefficients are the main parameters that control the dynamics of this process; these two parameters can be calculated from the diameter of the nanoparticles (Eq. 5.1 and Eq. 5.5). The effect of the diameter is to increase the sedimentation rate and diminish the bed height. The sedimentation bed height z_0 can be obtained by the simple relation $z_0 = D/S$, and the equilibrium time as $t_{eq} = 1.4 \cdot t_{sed} = 1.4 \cdot L/S$. B is a parameter that depends on z_0.

More complexity can be added to the Mason-Weaver model with modifications as the dependence of D and S to the local nanoparticle concentration or with modified expressions that account for aggregation effects [9,64-67]. It is possible to think that interparticle interaction forms clusters by aggregation and subsequently induces increments on D and S. This process could be more probable if the nanoparticle concentration is high. For example, a modified Mason-Weaver that accounts to this process setting a variable diffusion coefficient (lower than the one predicted by Stokes-Einstein for low concentrations but increasing to this value with higher nanoparticle concentrations) was presented in the recent work [65,66].

The aggregation process affects the sedimentation rate by the increment of the size of the clusters as described above, but those effects are not directly included in the second-order models [5,64-67]. A simple consideration to include the aggregation in those models is to set a modified effective viscosity that takes into account for the cluster effects [9]. The classical colloids theory of Derjaguin-Landau-Verwey-Overbeek (DLVO) accounts for interparticle interactions and aggregation effects but does not directly model the sedimentation. This theory considers the total interaction potential of the nanoparticles by two effects, i.e., the repulsive interaction (overlap between the double layers described by the zeta potential) and the attractive potential (van der Waals). This framework allows to model aggregation and the effect of a surfactant accounting for the change in the surface potential or zeta potential. For further references and limitations regarding the application of DLVO on nanofluids, see [68,69].

Models based on Molecular Dynamics models include the agglomeration–deagglomeration process and the effect of particle volume fraction, particle size, and aggregate structure on the sedimentation velocity of the suspended nanoparticles [14-17]. The advantage of this model is to give some insight around the microscopical processes, but with the limitation of a low unrealistic range for the considered number of particles. The sedimentation rate could be nonlinear dependent on the nanoparticle concentration, and the effect can drive to higher rates than free sedimentation rates calculated by Stokes law. However, for high concentrations, a hydrodynamic effect involving backflow causes a reduction in the sedimentation velocity. This nonlinear effect is stronger if bigger cluster sizes are considered [16]. The augmentation of the sedimentation velocities is confirmed by the model proposed in [15]. The Molecular Dynamics models could also be considered on the *CFD-based approach* that will be presented briefly in the next subsection.

The stability of the nanofluid can be predicted by the ratio between D and S by two dimensionless groups known as G Eq. 5.7 and G' Eq. 5.8. Moreover, it is possible to obtain a critical size of nanoparticle for a stable nanofluid, using the modified dimensionless group GD, including the relaxation time (from mean free path considerations) instead of $\cdot t_{sed}$ into Eq. 5.8 (e.g., critical size 1.4 μm for five days of stability of Al_2O_3-water) [70].

$$G = \frac{4 \cdot \pi \cdot (d/2)^4 \cdot a \cdot (\rho_p - \rho_f)}{3k_B.T} \quad (5.7)$$

$$G' = \frac{1}{3}\pi \cdot a \cdot (\rho_p - \rho_f)\sqrt{\frac{4 \cdot (d/2)^5 \cdot t_{sed}}{3 \cdot \mu \cdot k_B \cdot T}} \qquad (5.8)$$

A resume of the studies mentioned above is presented in Table 5.2. It is interesting to observe that the Stokes law is used to calculate the sedimentation coefficient in almost all the studies, assuming a spherical shape with a radius related to the nanoparticle size. From Tables 5.1 and 5.2, it is visible that some works compare the experimental and analytical approaches contrasting the predictions from the implemented model with experimental results using different nanofluids as gold-based [7,8,54,65], silica-based [9], mixtures [70], and some other metallic oxides as Al_2O_3 [14,16,62,63].

Table 5.2 Overview of the analytical approach to nanoparticles sedimentation.

Model, year	**Output variable**	**Spatial Dimension**	**Equation**	**Sedimentation**	**Diffusion**	**Aggregation/ rupture**	**Main input parameters**	**Nanofluid tested**	**Remark**
Mason-weaver 1924[5]	$v_p(z,t)$	1	ODE 2nd order	Yes, Stokes sedimentation law	Yes, Stokes-Einstein diffusion	No	*D*, diffusion *S*, sedimentation	Gold and assemblies [54]	Early theoretical work on colloidal stability
Jiang et al. 2010[14]	$v_p(z,t)$	2	Molecular dynamics	Yes	Yes	Yes Aggregation (position, size) Rupture maximum diameter	Maximum diameter Fractal dimension	Fullerence + H2O, Fullerence + Oil and CuO + Oil nanofluids	Account for the spatial structure of the clusters.
Ganguly 2011 [16]	$\overline{v_p(t)}$	-	Molecular dynamics.	Yes, Stokes sedimentation law	Yes, Brownian motion, stochastic Langevin term + diffusion term	Yes, attractive-repulsive potentials, aggregation rupture	Cluster size	CuO–water Al2O3–water	Sedimentation rate has a nonlinear dependence with nanoparticles concentration
Ni et al. 2011[15]	$v_p(z,t)$	3	Molecular dynamics.	Yes, Stokes sedimentation law	Yes Brownian motion, stochastic Langevin term + diffusion term	Yes, coagulation disaggregation	Hamaker constant	(only numerical): 10,25,50 nm	Above the proposed limit for the concentration, aggregation occurs
Jung et al. 2013[70]	Dimensionless groups G, G',GD < 1,	-	Algebraic (Previous G and G')	Yes	Yes	Yes (mean free path)	Relaxation time	LiBr-H2O Al_2O_3-H2O	Critical radius for stability based on relaxation time

Quik 2012,2014 [61][62]	$\overline{v_p(t)}$	-	set of ODE first order	Yes, Stokes sedimentation law	Yes, Brownian aggregation rate constant	Yes, homoaggregation, heteroaggregation	Attachment efficiency homoaggregation heteroaggregation Fractal dimension	CeO2 + organic material	Heteroaggregation accelerate the sedimentation rates (Natural waters)
Ezhenkova and S A Chivilikhin 2015 [64]	$v_p(z,t)$	1	ODE 2nd order Mason-Weaver basedSolved by FD,	Yes, Stokes sedimentation law	Yes Stokes-Einstein	No	*D*, diffusion *S*, sedimentation	-	Refractive index variation and trajectory of a laser through the sample
Markus 2015[63]	$\overline{v_p(t)}$	-	set of ODE first order	Yes, Stokes sedimentation law	_	Yes, homoaggregation, heteroaggregation mineralization resuspension	Fractal dimension Attachment efficiency	CeO2, TiO2+ organic material	Can include aggregation and other physic-chemical phenomena
Antonopoulou et al. 2018 [9] Davis and Russel 1989[67]	$v_p(z,t)$	1	ODE 2nd order Mason-Weaver based Solved by FD	Yes Stokes sedimentation law local concentration	Yes, local concentration	Yes Interparticle interactions effective viscosity	*D* (C_p), diffusion *S*(C_p), sedimentation Effective maximum concentration	colloidal silica 480 nm	Gravitational and centrifugal sedimentation
Giorgi-Macko 2020[65], [66]	$v_p(z,t)$	1	ODE 2nd order Mason-Weaver based Solved by FD	Yes Stokes sedimentation law	Yes, local concentration	No	*D*(C_p), diffusion *S*, sedimentation Diffusion curve parameters	Gold	Considers a lower diffusion coefficient

Alternative approach: CFD

The third possible approach to the study of nanofluid sedimentation is based on CFD methods. This approach is most suitable for heat transfer simulations with a mean flow of the base fluid instead of pure sedimentation studies (with a stationary fluid). The recent developments in modeling and simulating nanofluids by the CFD approach were reviewed in [10,11] (theory), and [12] (applications). CFD-based models can be categorized into two families: *single phase models* and *two-phase models*. The single-phase models consider the evolution of a single fluid and solve the macroscopic equations (normally the Navier-Stokes equations) by a numerical method. The equivalent fluid considered has properties representing the whole system: in this approach, relations to determine viscosity, thermal capacity, and other physical properties of the nanofluid are needed.

On the other hand, the two-phase models consider the continuum equations for the fluid phase (Eulerian model) and the second set of equations for the solid phase, i.e., the nanoparticles. For the second phase, it is possible to implement a Eulerian (equivalent fluid approach macroscopic equations [13,71]) or Lagrangian (Molecular Dynamics approach) to model the solid phase. The *single-phase models* cannot give information about the nanoparticle concentration gradient, then is necessary to implement a *two-phase model* to consider sedimentation effects by the CFD-based approach.

An alternative way to simulate a nanofluid can be attempted using Lattice Boltzmann Models (LBM). This CFD technique does not solve the macroscopic Navier-Stokes or energy equations, but it solves mesoscale equations for the evolution of the probability density function representing the fluid. A secondary LBM for the nanoparticle phase can be implemented. Moreover, it is possible to implement a hybrid LBM scheme coupling the liquid phase simulated by LBM with the solid phase simulated by another numerical method as a molecular dynamics approach. The innovative work of Xuan and Yao simulates sedimentation behavior [18] and convective heat transfer [19]. This numerical method can be applied to simulate heat transfer enhancement by nanofluids in forced and natural convection [20,21]. Ma et al. in 2020 [72] applied the method to triangular solar collectors.

5.2 Experimental data

Experimental data were obtained with a laser light absorbance setup developed to measure sedimentation at different heights on a cavity (total height 14 cm) filled by Al_2O_3-water nanofluid at 1% initial volumetric concentration [23]. Fig 5.2 shows the scheme of the setup and the measurement points along the cavity.

The two-step method was implemented to obtain the nanofluid in the initial concentration v_p=1% (*AL-6051 – Alfa Aeser Aluminum oxide Nanotek*® colloidal dispersion at 23% by weight in H_2O). Ultrasonic bath was used as a stabilization technique for three hours.

The results used to validate the proposed LBM numerical model are depicted in Fig. 5.3 Including the sedimentation curves at different cavity heights (distance gap 1 cm), from these curves, the average concentration (out of the sedimentation bed) is calculated.

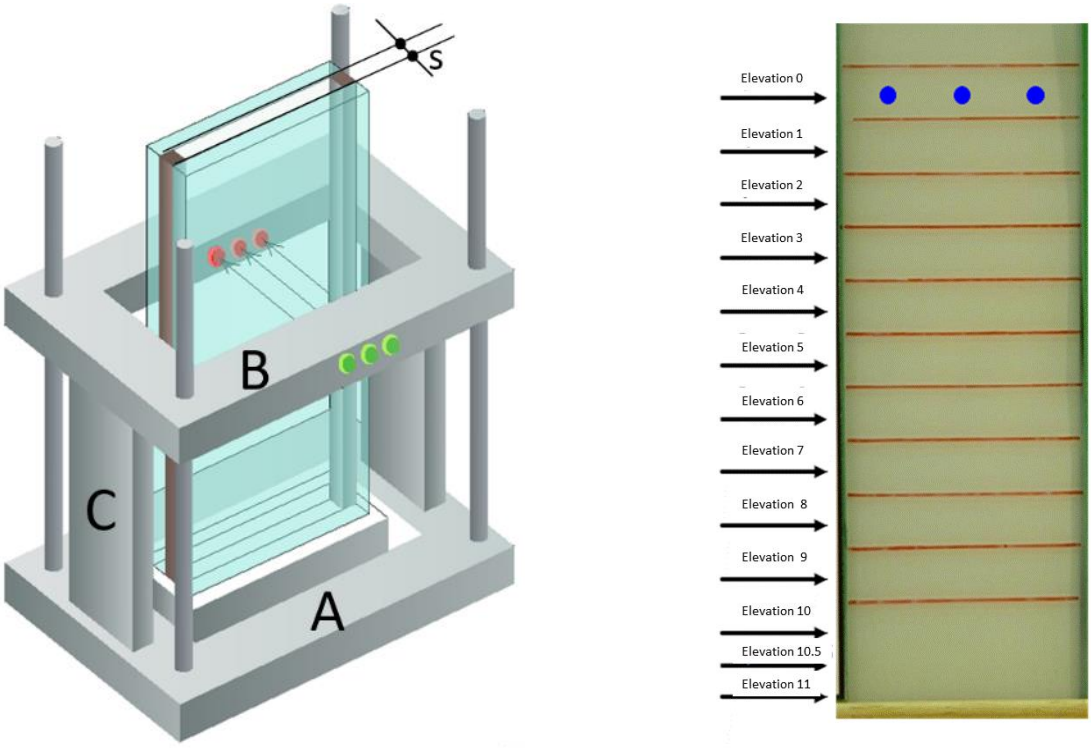

(a) *(b)*

Figure 5.2 Overview of (a) the experimental setup and (b) the thirteen measurement locations.

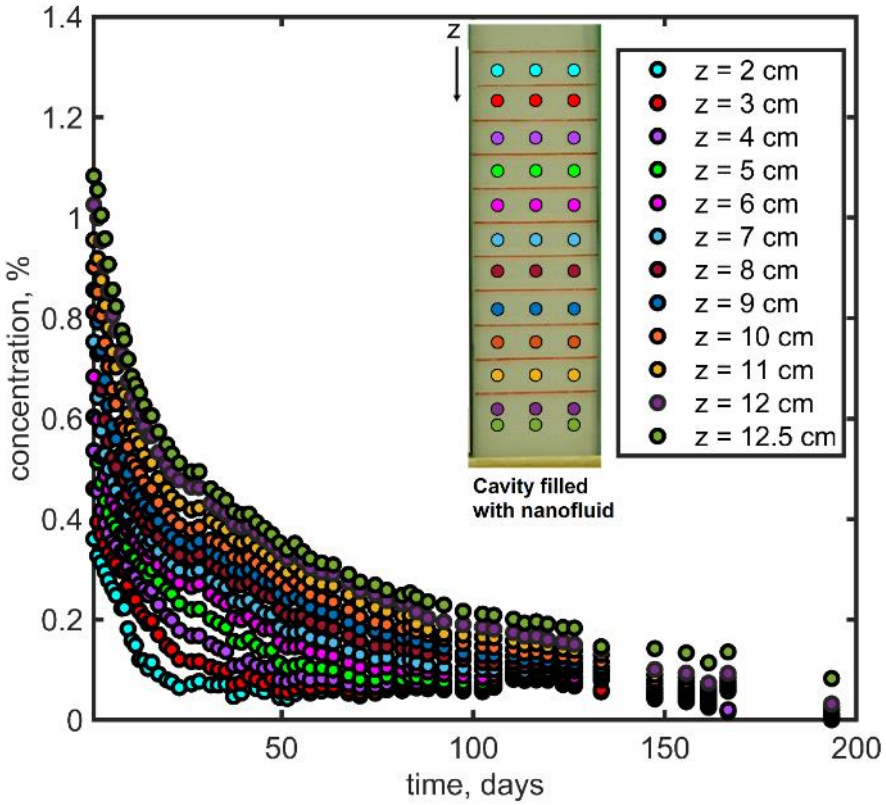

Figure 5.3 Experimental data concentration profiles for different heights (z).

5.3 Analytical sedimentation model

The second-order Mason-Weaver model [5], eq. 1, is a one-dimensional advection-diffusion equation for modeling the evolution of the local concentration of nanoparticles $v_p(z,t)$ under gravitational sedimentation. This equation can be deduced by analyzing the diffusive fluxes by the first Fick's law [6-8]. This model can be used to determine the sedimentation curves in time (t) at different heights (z) of a cavity containing the nanofluid. In contrast, first-order models can determine only the average concentration evolution, and the sedimentation curves predicted by these simpler models take an exponential decay form [61-63], in this work the second order model is selected because it gives more details concerning the sedimentation than the first order model.

$$\frac{\delta v_p(z,t)}{\delta t} = \frac{\delta}{\delta z}(D(v_p,t)\frac{\delta v_p(z,t)}{\delta z}) + \frac{\delta}{\delta z}\,(S(v_p,t)v_p(z,t)) \qquad (5.9)$$

The parameters *S* (sedimentation coefficient) and *D* (diffusion coefficient) are the parameters that control the sedimentation behavior in the above equation. This second-order differential equation can be reduced to a simple form (Eq.5.4) considering *S* and *D* constant quantities.

$$\frac{\delta v_p(z,t)}{\delta t} = D \cdot \frac{\delta^2 v_p(z,t)}{\delta z^2} + S \cdot \frac{\delta v_p(z,t)}{\delta z} \qquad (5.10)$$

Theoretical considerations to model these two parameters account for the equilibrium between drag and buoyancy forces to obtain the sedimentation coefficient (S_{theo} from Eq. 5.1), from the Stokes law for the sedimentation velocity, and the Brownian forces for the diffusion coefficient (D_{theo} from Eq. 5.5), from the Stokes-Einstein law.

This simplified approach considers spherical particles, and basically, the diameter of the nanoparticles determines the *S* and *D* coefficients. However, it is necessary to consider possible changes in those coefficients to account for agglomeration processes that change the nanoparticle's shape and limit the validity of those equations.

In this work, three sub-models for the nanoparticle's sedimentation velocity are implemented:

- *sub-model A*: Eq. 5.11, constant S_A (empirically determined approximately one order higher than S_{theo}):

$$\frac{\partial S_A}{\partial t} = 0;\ S_A = S_{exp} \approx 10\ S_{theo} \qquad (5.11)$$

- *sub-model B*: Eq. 5.12, $S_B(v_p)$ dependent on local concentration:

$$S_B(v_p) = S_{exp} + C^k \frac{(S_{theo} - S_{exp})}{C^k + C50^k} \qquad (5.12)$$

- *sub-model C*: Eq. 5.13, $S_C(t)$ time-dependent coefficient:

$$S_C(t) = S_A e^{-r\,t} \qquad (5.13)$$

The use of sub-models B and C implies the solution of the general Eq.5.9 instead of the reduced version Eq.5.4.

Additionally, the diffusion effect was studied by applying two conditions: constant D, and dependent the local nanoparticle concentration $D(v_p)$, Eq. 5.14. [65, 66].

$$D(v_p) = D_{exp} + C^{k\prime}\frac{(D_{theo} - D_{exp})}{C^{k\prime} + C50'^{k\prime}} \qquad (5.14)$$

The parameters that affect the functional forms of the sub-models (eq. 6-8) ($k, k', C50, C50'$) were adjusted considering possible critical volume fractions ($C50, C50'$ from 1% to 2%).

The sub-models considered that relate the sedimentation and diffusion coefficients to the local concentration were proposed in previous works concerning nanofluids [9,67], in particular the functional form of Eq. 5.12 and 5.14 was presented in [65,66].

The Eq. 5.13 implemented in the sub-model C was deduced empirically from the experimental data used for validation. Fig. 5.4 shows the time evolution of the sedimentation coefficient considering Eq. 5.12 and Eq. 5.13.

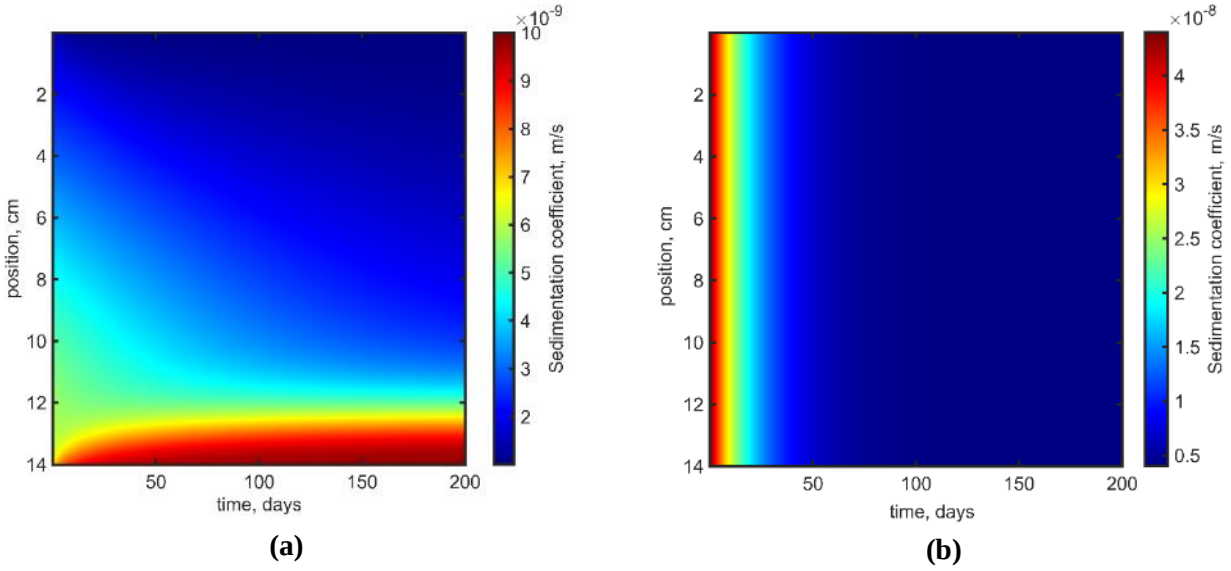

Figure 5.4 Sedimentation coefficient models (a) sub-model B: $S_B(v_p)$, (b) sub-model C: $S_C(t)$.

Interparticle interaction tends to form clusters by aggregation. Consequently, the nanoparticles effective hydrodynamic diameter increases and induces an increment of *S* and *D*. This process could be more probable if the nanoparticles concentration is high. Then the origin of the time-dependent or concentration-dependent sedimentation velocity and diffusion coefficient can be the simultaneous existence of aggregates of several sizes. Previous works suggest the existence of at least two different settling rates, characterized by faster sedimentation of big clusters at the beginning of the process (the initial high concentration facilitates the formation of the clusters). After the local concentration decreases, a slower settling rate of smaller clusters dominates the sedimentation [7,8,15,28,47,52].

In Fig. 5.5, different analytical models were compared with experimental data for the average nanoparticle concentration above the sedimentation bed (initial volumetric concentration 1%). All the models reproduce the general trend of the average concentration (nonlinear decrease in time). The *first-order model* overestimates the average volumetric concentration, and the *second-order model* underestimates the concentration in time after approx. 30 days, even if the diffusion coefficient is modeled as $D(v_p)$ the effect is imperceptible. The *second-order model* can give a better description of the evolution of the average nanoparticle concentration if the sedimentation velocity is adjusted with sub-models B or C. All the analytical models were adjusted, taking the initial concentration profile from the experimental measurements after one day, and the sedimentation velocity was set one order higher than the nominal value w, calculated by Stokes law for Al_2O_3 nanoparticles ($d = 40\ nm$) in water (Eq. 5.1).

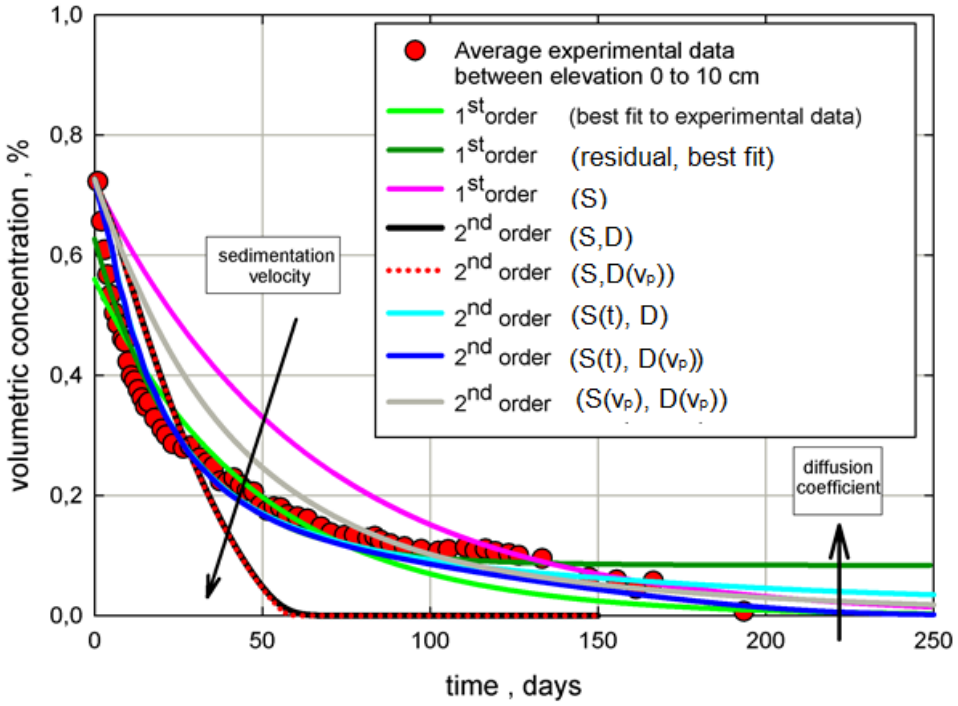

Figure 5.5 Comparison between analytical models and experimental data for the average nanoparticle concentration, Al2O3-water nanofluid, nominal initial concentration (●) average experimental data above the sedimentation bed; (——) first order model fitted to experimental data; (——) first order model with residual fitted to experimental data; (——) first order model; (——) second order model; (·····) second order model D(v_p).; (——) second order model with S(t), (——) second order model with S(t) and D(v_p); (——) second order model with S(v_p) and D(v_p).

5.3 The Lattice Boltzmann Method formulation for gravitational sedimentation

The LBM scheme commonly used for fluid dynamics presented in the introduction of this thesis has been modified here to simulate nanoparticles concentration, (C is used instead of v_p for a shorter notation). The LBM can be implemented to solve the Navier-Stokes equations and other partial differential equations (as the diffusion or advection-diffusion) [73,74].

For the simulations, the one-dimensional lattice (*D1*) containing two populations (*Q2*) in each node was adopted (*D1Q2* lattice). The characteristic velocity for this lattice is $c_0^2 = 1/2$, and the weights $w_i = 1/2$.

A one-dimensional approach was considered during the simulations, but the method described here can be easily implemented in 2D or 3D.

The BGK collision model [75] is one of the simplest and more used approximations to the collision operator: as was pointed out in previous chapters, it consists of relaxation from the incoming populations f to an equilibrium density function f^{eq} in a characteristic relaxation time τ. To solve the advection-diffusion, diffusion, or NS equations, the BGK operator is used but a lower order equilibrium distribution f^{eq} is considered. In particular, to solve the Mason-Weaver equation the equilibrium described in the Eq. 5.15 is adopted, [73,74]. The velocity u represents the sedimentation coefficient *S*, and the diffusion coefficient *D* is proportional to the characteristic relaxation time τ.

$$f_i^{eq}(\boldsymbol{z},t) = w_i C(\boldsymbol{z},t)\left(1 + \frac{\boldsymbol{c_i}\cdot\boldsymbol{u}}{c_0^2}\right) \qquad (5.15)$$

$C(\boldsymbol{z}, t)$ is the local concentration that can be obtained in each lattice node as a simple integral (summation) over the populations f_i, Eq. 5.16:

$$C(\boldsymbol{z}, t) = \sum_{i=1}^{2} f_i(\boldsymbol{z}, t) \tag{5.16}$$

The upper $z = L$ and lower $z = 0$ boundary conditions (BC) are implemented by two different schemes, the bounce back BB-BC and a finite difference scheme FD-BC based on Eq. 5.17.

$$\frac{\delta C}{\delta z} + C = 0 \quad for \quad z = 0;\ z = L \tag{5.17}$$

Denoting with C_i^n the concentration in the i position at timestep n, the terms of the Eq.5.17 can be expressed as described in Eq. 5.18 for the first term:

$$\frac{\delta C}{\delta z} = \frac{1}{4\Delta z}(C_1^n - C_0^n + C_1^{n+1} - C_0^{n+1}) \tag{5.18}$$

Eq. 5.19 for the second term:

$$C = \frac{1}{4}(C_1^n + C_0^n + C_1^{n+1} + C_0^{n+1}) \tag{5.19}$$

This FD BC was proposed by [6] to solve mass conservation problems in the numerical solution of the Mason-Weaver proposed by [7] and [8] using the FD method. We explore the applicability of this numerical scheme in the LBM algorithm. On the other hand, the bounce back BC is a standard BC for LBM, and the scheme is entirely local and only needs the inversion of the populations arriving at the boundary to fill the unknown values in the next timestep, for example, for the lower boundary this BC reduces to Eq.5.20:

$$f_2(0, t + \Delta t) = f_1(0, t) \tag{5.20}$$

5.5 Lattice Boltzmann Method results

The LBM simulates the primary behavior of the nanoparticle's sedimentation: the physical sedimentation parameter *S* (proportional to the $\boldsymbol{u}$ LBM computational parameter) controls the time that takes the sedimentation, while the diffusive parameter (proportional to τ LBM computational parameter) controls the height of the sedimentation bed, i.e., the deposit of the nanoparticles at the bottom of the cavity filled with the nanofluid. Above the sedimentation bed the local concentration of the nanoparticles decreases from the initial values. Fig. 5.6 shows this behavior considering the simpler sub-model A with *S* and *D* constant, the formation of the deposit in the sedimentation bed is evident by the increment in the local concentration.

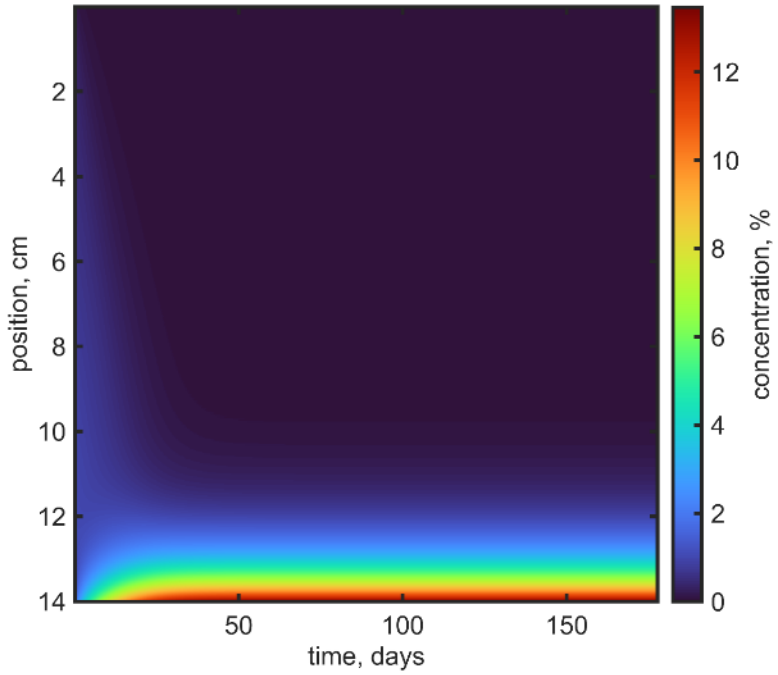

Figure 5.6 Evolution of the local nanoparticle concentration using LBM. Deposition bed at the bottom of the cavity using sub-model A.

5.3.1 Initial condition

The effect of the initial condition (IC), initial concentration gradient, on the evolution of the sedimentation curves is presented in Fig. 5.7, in which a *uniform concentration profile* of C_0=1% or **regular IC** (Fig. 5.7(a)) has been compared with an *adjusted initial concentration profile* or **adjusted IC** (from experimental data after one day Fig. 5.7(b). It is visible that the model predictions are sensitive to this consideration, and the time-dependent behavior at different heights presented in Fig. 5.3 is better obtained if the *adjusted initial profile* is selected. In this way, the settling predicted for the model starts immediately in all the heights.

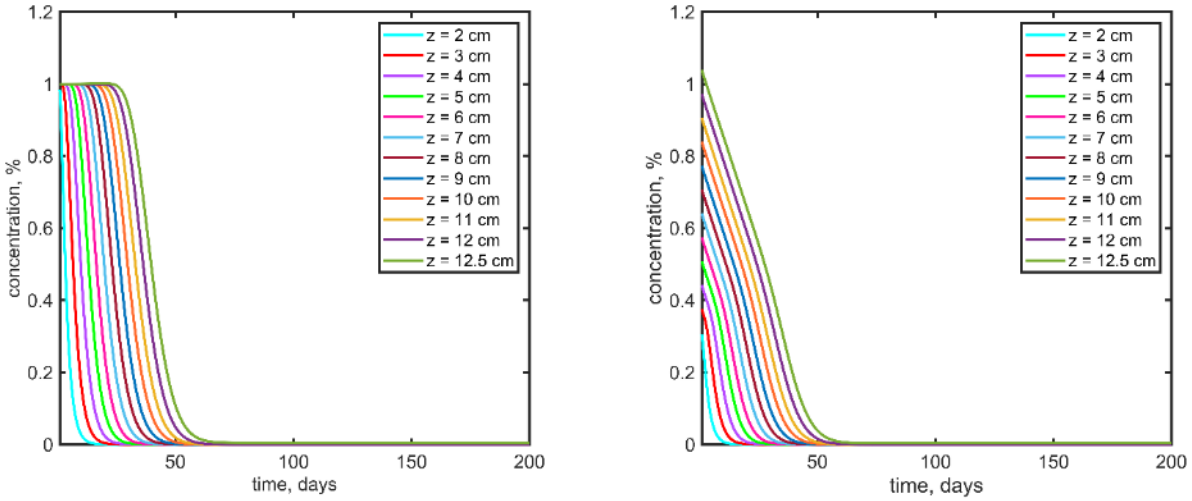

(a) (b)

Figure 5.7 Effect of the initial condition on the concentration sedimentation curves at different heights (z). (a) regular IC: uniform initial profile 1% (b) adjusted IC: initial profile adjusted to the experimental data after one day.

Figure 5.8 shows the time evolution of the average concentration profile considering the three different sub-models for the sedimentation coefficient. It is noticeable the convenience of considering the adjusted initial condition. For models A and B, after approximately 50 days, the numerical prediction for both IC converges. For model C, the convergence takes more time. In the results presented in the rest of the paper, only the adjusted IC is considered.

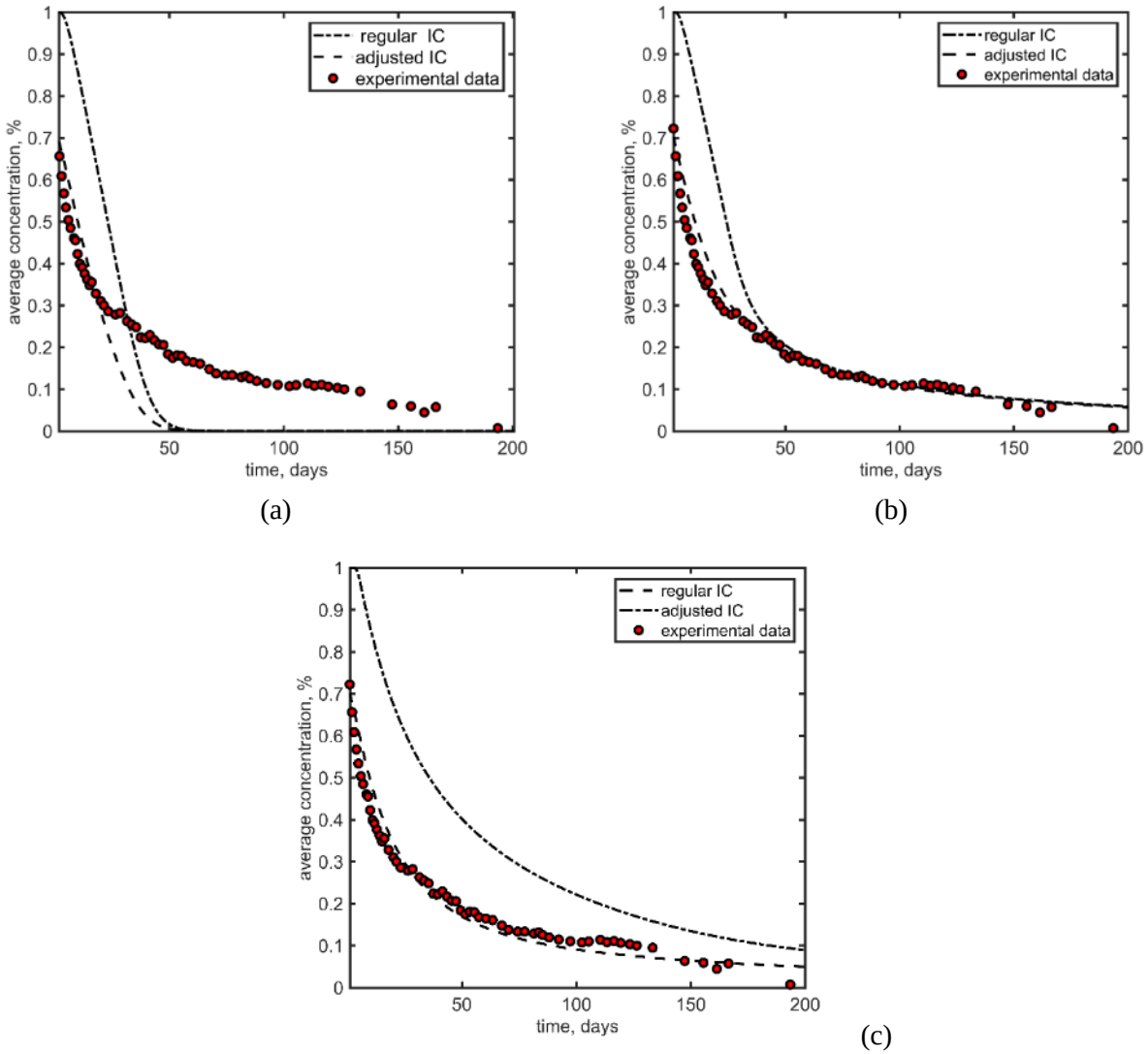

Figure 5.8 Effect of the initial condition (IC) on the average sedimentation curve. Regular IC refers to a uniform 1% initial volumetric concentration. Adjusted IC refers to an initial profile adjusted to the experimental data after one day. (a) model A: S constant S_A, (b) model B, S dependent on concentration $S_B(C)$, (c) model C: S dependent on time $S_C(t)$.

5.3.2 Sedimentation velocity effects

The effects of considering different sedimentation coefficient values and different sub-models were explored by contrasting the experimental results for the average concentration and the numerical predictions. The five average sedimentation curves in Fig. 5.9 represent the effect of changing the sedimentation coefficient *S* from $1x10^{-8}$ to $5x10^{-8}$ m/s. Higher is *S* faster is the concentration decay.

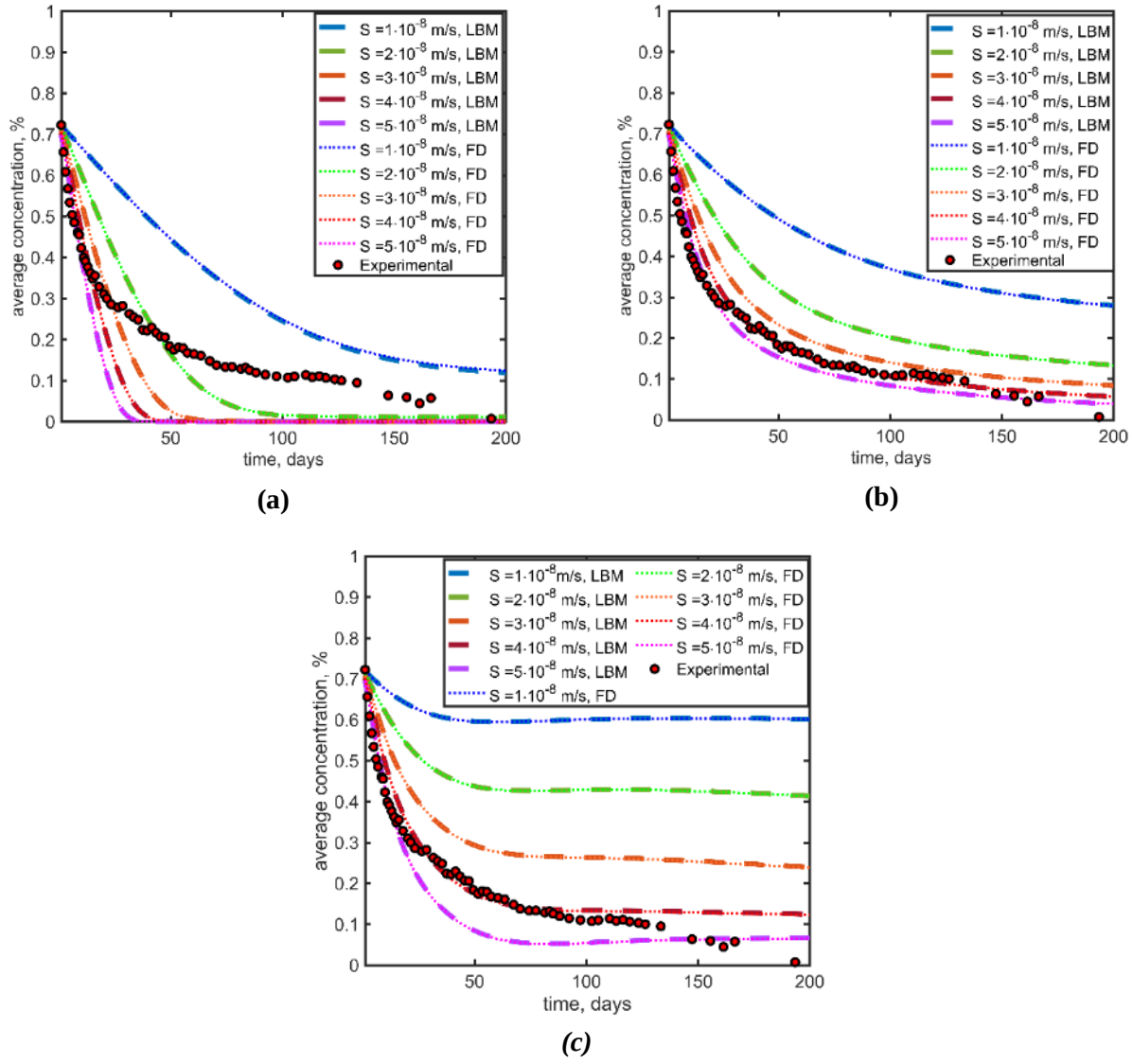

Figure 5.9 Effects of the sedimentation velocity S on the average concentration, experimental data at C_0=1.0%. (a) Sub-model A ($D=7.3 \cdot 10^{-11} m^2/s$), (b) Sub-model B ($D=7.3 \cdot 10^{-11} m^2/s$, $K=2$, $S_{50}=0.5$), (c) Sub-model C ($D= 3 \cdot 10^{-11} m^2/s$, $r=0.05$).

Additionally, results from the (explicit) finite difference (FD) method were included in Fig. 5.9 to validate the LBM solutions. The FD solutions are like the LBM solutions for the three sub-models A, B, and C, and the sedimentation curves overlap. The timestep for the FD is half the LBM timestep to ensure convergence of the solution. LBM curves were obtained after 180000 timesteps and FD curves after 360000 timesteps and using 1400 points for the spatial discretization in both FD and LBM. In the simulations, it is necessary to assume *S* values approximately one order higher than the value given by Stokes law (Eq.5.1). The diffusion coefficient was considered constant in all the simulations presented in this section.

The effect of considering the different sub-models for *S* was explored. The behavior of sub-model A, with *S* constant in time and space, is characterized by a faster decay rate of the average concentration in contrast to sub-models B and C (considering *S(C)* and *S(t)*, respectively). The fit to experimental data is better for sub-models B and C. By direct comparison of the sedimentation curves at different heights, presented in Fig. 5.10, it is evident that the predictions by model B were the most similar to the experimental curves; in particular, the concentration decay rate does not present a considerable variation for the different heights, and all the curves decrease in time. In models A (Fig.5.10(a)), and C (Fig.5.10(c)), some curves show an

increment of concentration in time, that can indicate the presence of the sedimentation bed at the first measurement point.

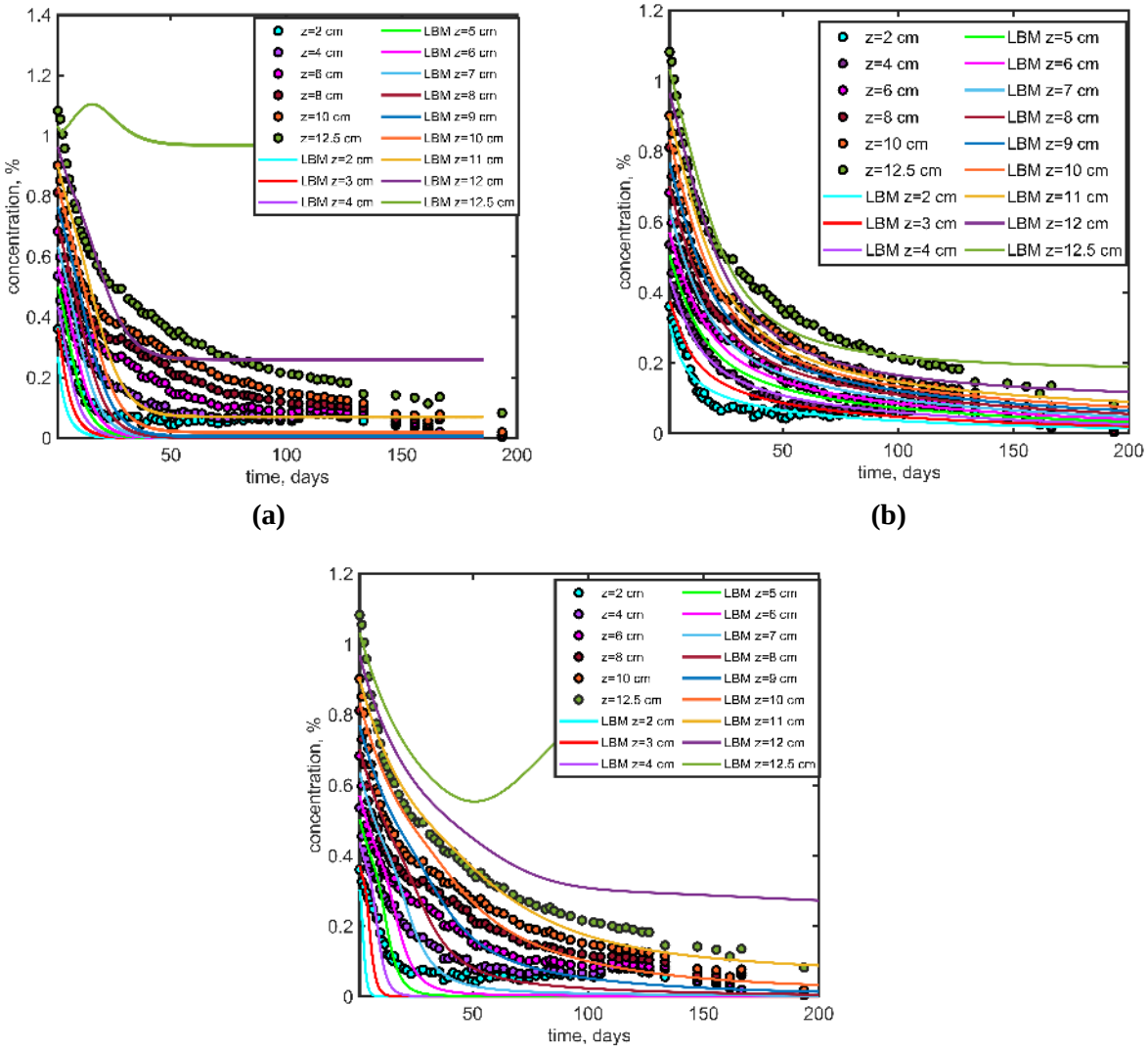

(a) **(b)**

(c)

Figure 5.10 Sedimentation curves at different heights considering the different sub-models for S, (a) model A: S constant, (b) model B, S dependent on concentration, (c) model C: S dependent on time.

5.3.3 Diffusion effects

Constant diffusive parameter D

Fig. 5.11 shows the effect of changing the value of the diffusion parameter. In this figure, each line represents the solution by changing the *D* value, with the same *S*. Higher is the value of *D* higher is the final concentration (*residual concentration).* This effect was expected because the diffusion coefficient is proportional to the Brownian effects that are contrary to sedimentation. The observed effect is similar using the three *S* sub-models.

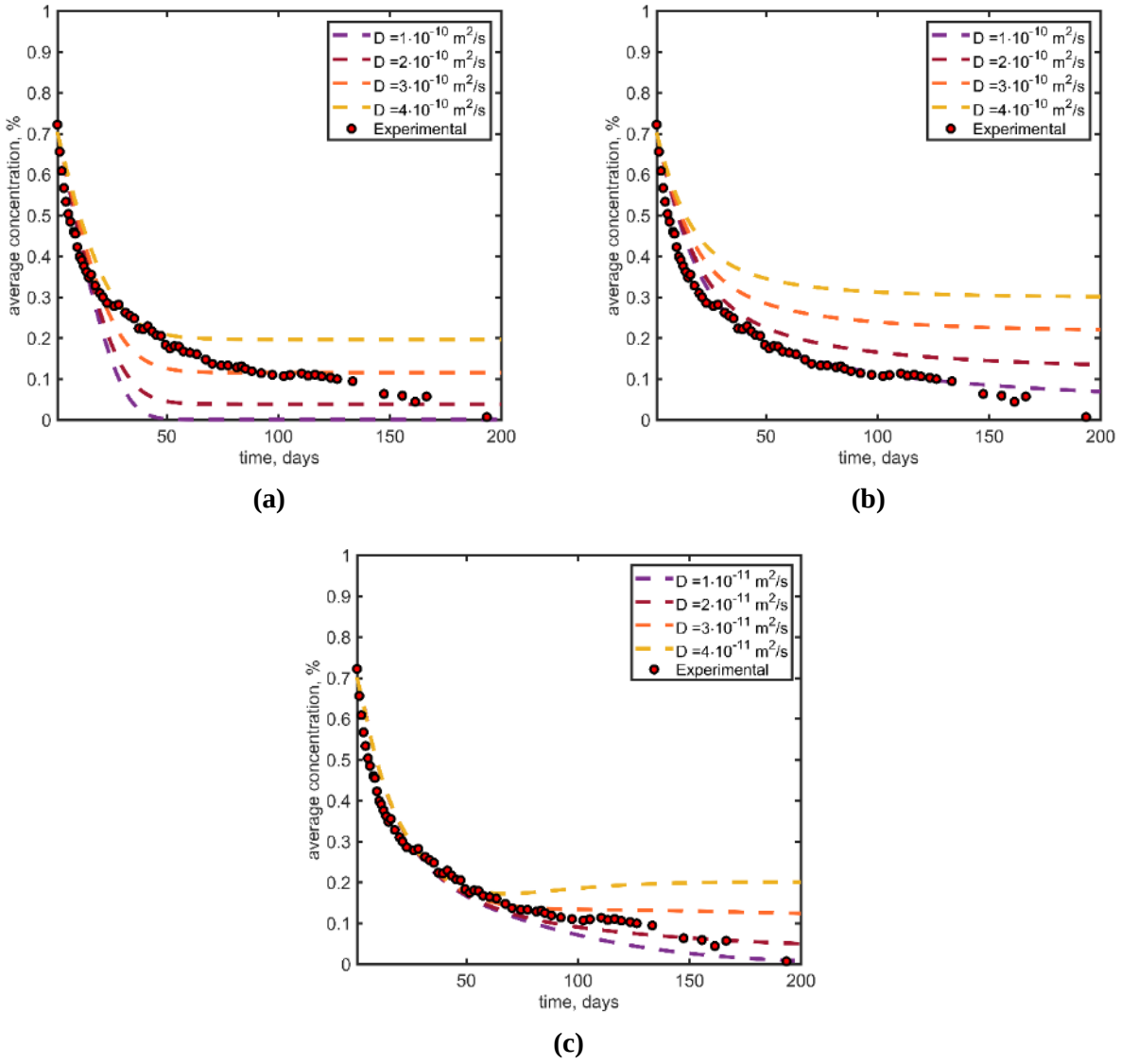

Figure 5.11 Sedimentation curves for different diffusion coefficients D, (a) sub-model A: S constant, (b) sub-model B, S dependent on concentration, (c) sub-model C: S dependent on time. (S=4·10^{-8}m/s).

Diffusive parameter dependent on local concentration

It is possible to consider more complex models for the diffusion coefficient as was proposed in [9,65-67]. In this section, some results obtained considering *D* dependent on local concentration, as described by Eq. 5.14, are presented [66,67]. In Fig. 5.12 are depicted the results considering *D* constant vs. *D(c)*, using the sub-model C for the sedimentation coefficient. The different lines in the figure represent different initial sedimentation coefficient values (S_A). The effect is similar for sub-models A and B. If the diffusion coefficient *D* depends on the local concentration, after sedimentation occurs, the local concentration trends to decrease (outside the sedimentation bed), implying a lower residual concentration. This diffusion sub-model captures the concentration decrement in the last 50 days, but some drawbacks related to stability degradation occur and must be considered.

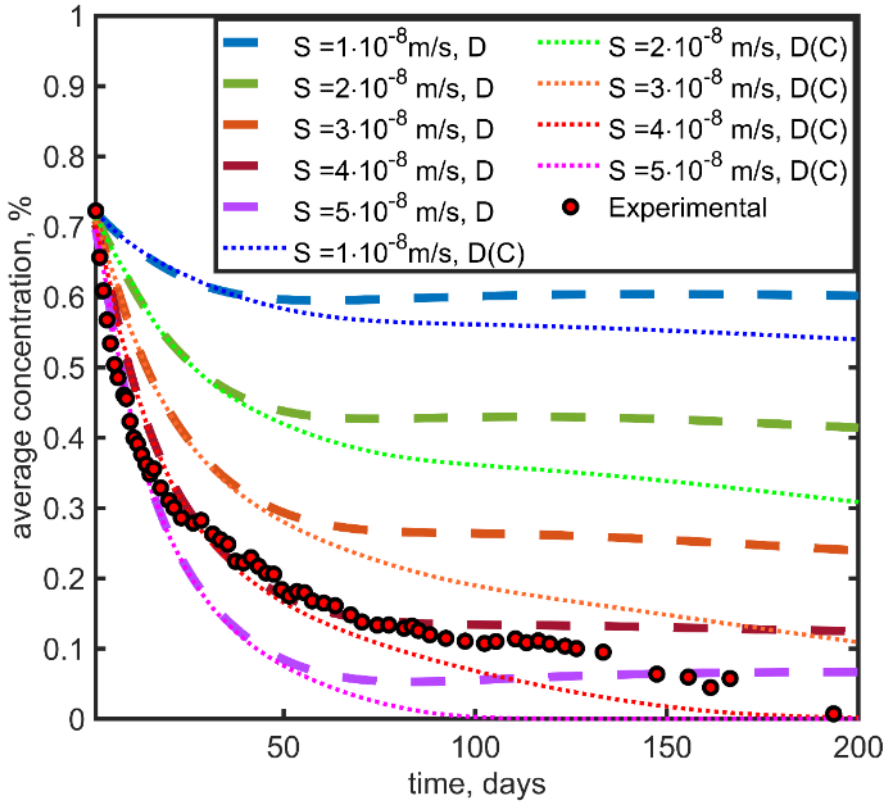

Figure 5.12 Effects of considering the diffusion coefficient dependent on local concentration for different sedimentation velocities. (sub-model C, r =0.05).

5.3.4 Stability and convergence

The implemented LBM algorithm is more stable than the FD scheme, i.e., the maximum timestep in LBM ensuring convergence is almost twice the maximum timestep for FD, which implies fewer computational steps to obtain a solution. For example, in Fig. 5.9 the LBM solutions were obtained using 180000 iterations; meanwhile, the FD solutions have required 360000 iterations. The mesh size is determinant to obtain the desired values for *S* and *D*. If a small value is selected for the mesh size, the *D* coefficient (proportional to Δx^2) trends to increase more than the *S* coefficient (proportional to Δx), and to set the correct physical value of *D*, it is necessary to set a small relaxation parameter value, compromising the convergence of the method, as can be noted in the stability maps commented below.

Varying the LBM parameters (the sedimentation velocity $u_{\max}$ and the relaxation time τ proportional to the diffusion coefficient), the stability behavior of the LBM algorithm was studied. The stable/unstable regions of the LBM depend strongly on the relation between the relaxation time and the maximum velocity. The stability condition is expected to deteriorate (maximum stable velocity) when decreasing the diffusion coefficient (proportional to τ). A typical stability condition for LBM is to take $\tau > 0.5$ (i.e., *sufficient* condition), but it is considered optimal using $\tau \geq 1$. Also is common to consider, for *D1Q3*, the limit $u_{\max} < \sqrt{2/3}$ and for *D2Q9* the limit $u_{\max} < \sqrt{1/3}$ as *necessary* stability conditions. In the performed validations, it is possible to remain in this stable zone to simulate the nanofluids sedimentation because the value for $u_{\max}$ is small compared with those limits.

Stability maps were drawn by evaluating the results of multiple simulations, considering different values for the relaxation time and the maximum sedimentation velocity (normalized by the lattice characteristic velocity). The stability map depends on how the boundary conditions are established. In Fig. 5.13 and 5.14

are represented the FD BC and the BB BC, respectively. Mass conservation was studied in each solution. BB conserves the system's total mass in a wide range of the parametric space. In contrast, FD BC mass is conserved only for low velocities, as shown in Fig. 5.13 (zones I and II). By means of this unstable and unprecise behavior of the FD BC the BB BC was preferred in this work to study the sub-models in the previous sections.

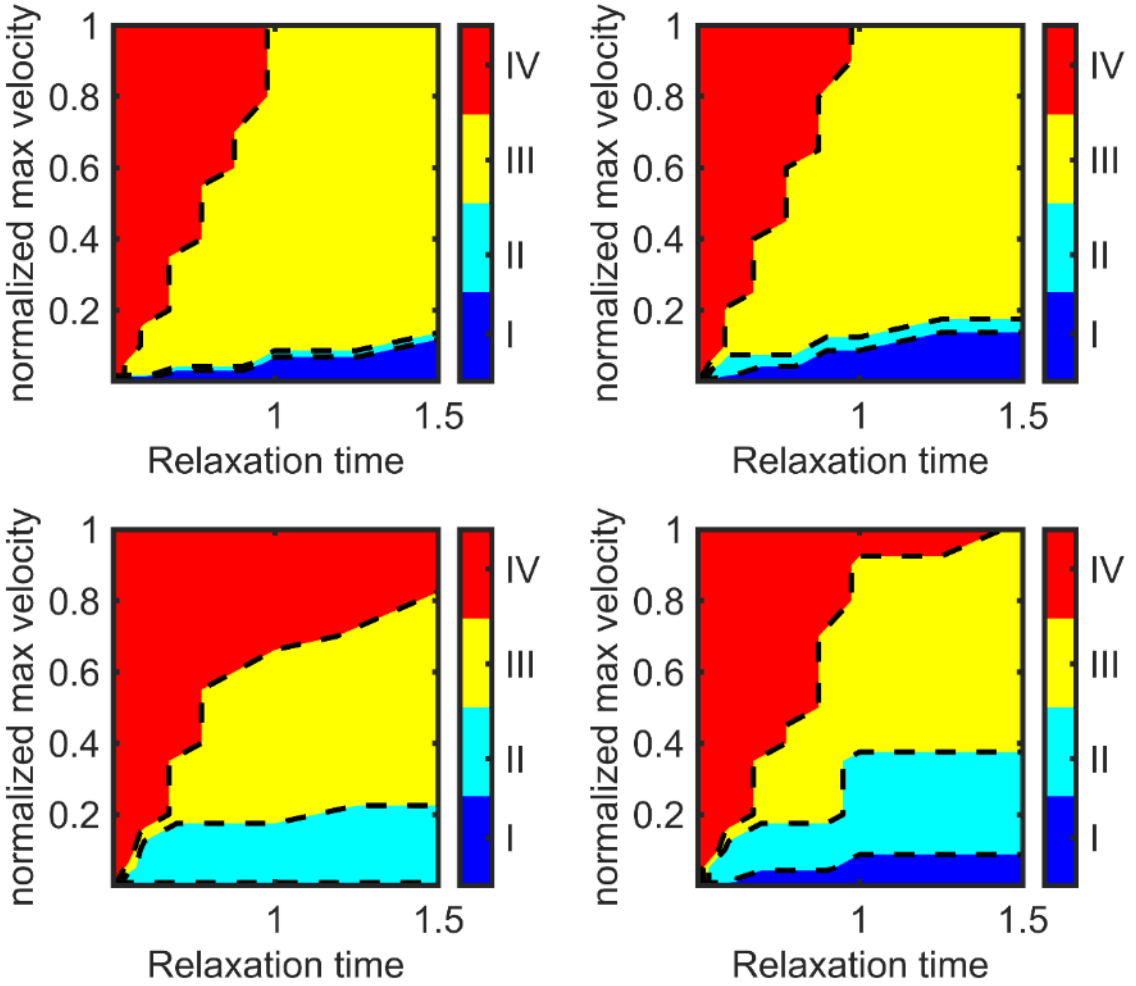

Figure 5.13 Stability maps considering FD BC and the different sub-models for S a) sub-model A: S constant, (b) sub-model B, S dependent on concentration, (c) sub-model B, S and D(C) dependent on concentration (d) sub-model C: S dependent on time. I Mass balance preserved, stable solution; II No mass-balance but stable solution, low precision degradation; III No mass-balance, high precision degradation; IV Divergence.

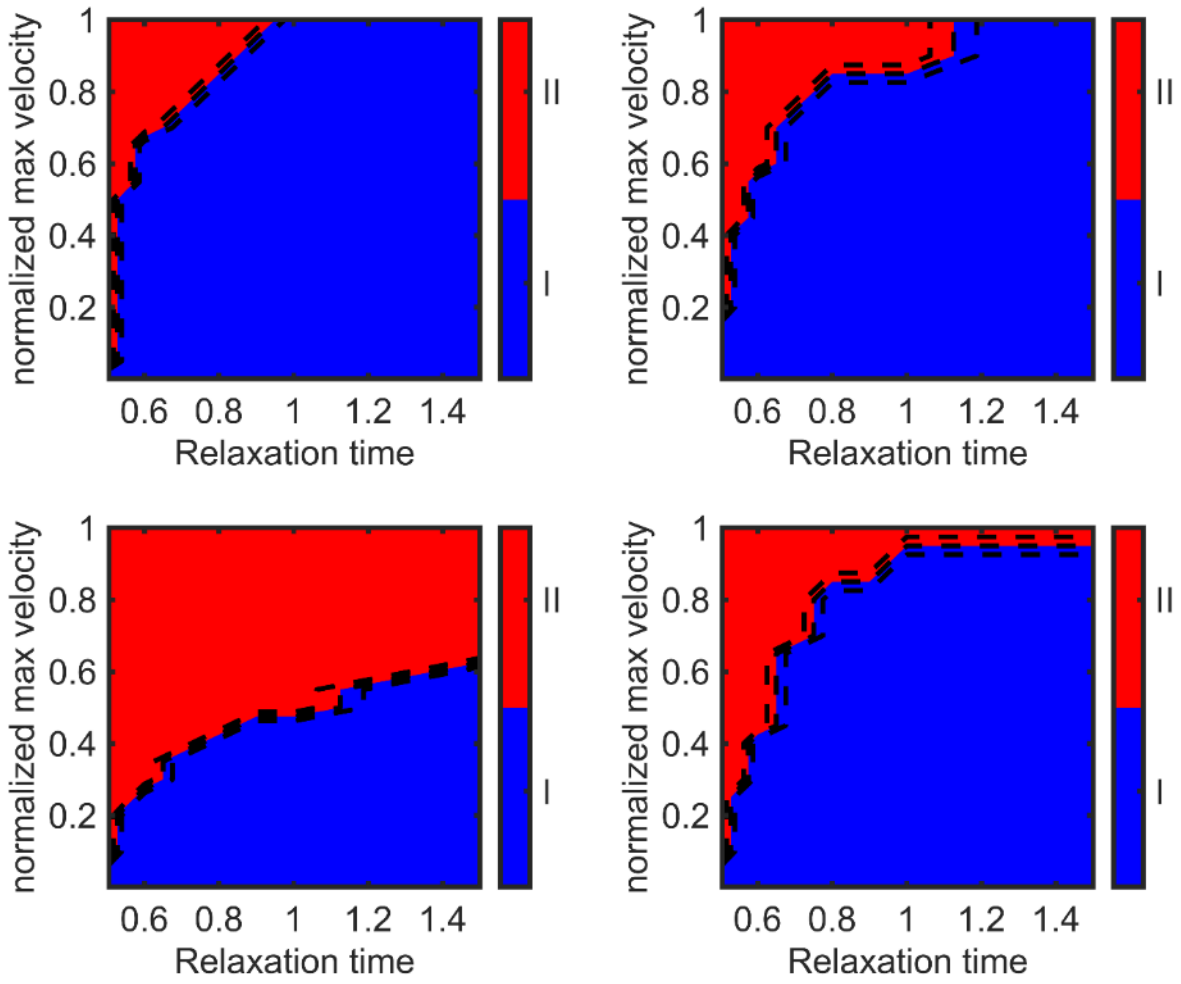

Figure 5.14 Stability maps considering BB BC and the different sub-models for S a) sub-model A: S constant, (b) sub-model B, S dependent on concentration, (c) sub-model B, S and D dependent on concentration (d) sub-model C: S dependent on time. I Stable solution; II Divergence.

5.6 Conclusions

This chapter presents a model based on the Lattice Boltzmann Method to simulate the gravitational sedimentation of nanofluids.

The proposed algorithm was validated by 1. comparing experimental results for water-Al_2O_3 nanofluid; 2. using numerical results using the finite difference method.

Moreover, the proposed algorithm also agrees with the first-order models for the average concentration [61-63].

Three different sub-models for the sedimentation coefficient have been implemented (constant, concentration-dependent, and time-dependent), as well as two diffusion coefficient sub-models (constant and concentration-dependent).

The sedimentation coefficient sub-models, concentration-dependent, and time-dependent represent better the sedimentation curves than the constant sedimentation coefficient model, which can be related to changes in the sedimentation velocity by different agglomeration phases. The probability of aggregation is proportional to the local concentration, and this probability decreases in time. Considering the diffusion coefficient

dependent on local concentration degrades the algorithm's stability (compared to constant diffusion coefficient simulations). However, for this specific application, the value of both coefficients is smaller enough to ensure a stable solution, and the diffusion sub-model can be applied with the three different S sub-models. The effect of considering this diffusive behavior causes a decrease in the residual concentration after the sedimentation occurs.

If a uniform initial density is set in the model as the initial condition, the sedimentation curves present stair-like variation, i.e., the recipient's middle seems to have no change in concentration. Meanwhile, the upper and lower section is becoming empty and filled with nanoparticles, respectively. On the other hand, if an initial concentration profile (adapted from the experimental measure after one day) is set as the initial condition, the concentration variation changes for all the height positions from the beginning, reproducing better the local sedimentation curves observed in the experiments.

The bounce back boundary condition performs better than the finite differences boundary condition. The mass balance is ensured in an extensive parameter’s region using the bounce back boundary condition. On the other hand, the finite differences boundary condition gives lower precision solutions. This boundary condition could be enough to obtain a solution because the velocity values are small. However, it is not a local algorithm affecting the parallelization opportunities.

Some advantages of using the Lattice Boltzmann Method to simulate gravitational sedimentation are:

1. direct one-way to couple with a fluid solver to calculate a more complex velocity field;
2. microscopic effects like corrosion, deposition, or chemical reactions, can be included by defining local rules:
3. the algorithm is easy to implement;
4. it can be easily parallelizable because the collision and streaming steps are local rules;
5. it is a stable method compared to the Finite Differences method;
6. it can handle variable diffusion and sedimentation coefficients directly, without requiring explicit modifications to include mixed derivatives.

REFERENCES

[1] S.U.S. Choi, J.A. Eastman, Enhancing thermal conductivity of fluids with nanoparticles, in: ASME International Mechanical Engineering Congress & Exposition, ASME, San Francisco, California, US., 1995: p. 9.

[2] S.K. Das, N. Putra, P. Thiesen, W. Roetzel, Temperature Dependence of Thermal Conductivity Enhancement for Nanofluids, Journal of Heat Transfer. 125 (2003) 567–574. https://doi.org/10.1115/1.1571080.

[3] H.U. Kang, S.H. Kim, J.M. Oh, Estimation of Thermal Conductivity of Nanofluid Using Experimental Effective Particle Volume, Experimental Heat Transfer. 19 (2006) 181–191. https://doi.org/10.1080/08916150600619281.

[4] H. Masuda, A. Ebata, K. Teramae, N. Hishinuma, Alteration of Thermal Conductivity and Viscosity of Liquid by Dispersing Ultra-Fine Particles, Netsu Bussei. 7 (1993) 227–233. https://doi.org/10.2963/jjtp.7.227.

[5] M. Mason, W. Weaver, The Settling of Small Particles in a Fluid, Phys. Rev. 23 (1924) 412–426. https://doi.org/10.1103/PhysRev.23.412.

[6] J. Midelet, A.H. El-Sagheer, T. Brown, A.G. Kanaras, M.H.V. Werts, The Sedimentation of Colloidal Nanoparticles in Solution and Its Study Using Quantitative Digital Photography, Part. Part. Syst. Charact. 34 (2017) 1700095. https://doi.org/10.1002/ppsc.201700095.

[7] C.M. Alexander, J.C. Dabrowiak, J. Goodisman, Gravitational sedimentation of gold nanoparticles, Journal of Colloid and Interface Science. 396 (2013) 53–62. https://doi.org/10.1016/j.jcis.2013.01.005.

[8] C.M. Alexander, J. Goodisman, Size histograms of gold nanoparticles measured by gravitational sedimentation, Journal of Colloid and Interface Science. 418 (2014) 103–112. https://doi.org/10.1016/j.jcis.2013.11.074.

[9] E. Antonopoulou, C.F. Rohmann-Shaw, T.C. Sykes, O.J. Cayre, T.N. Hunter, P.K. Jimack, Numerical and experimental analysis of the sedimentation of spherical colloidal suspensions under centrifugal force, Physics of Fluids. 30 (2018) 030702. https://doi.org/10.1063/1.5010735.

[10] M.R. Safaei, A. Jahanbin, A. Kianifar, S. Gharehkhani, A.S. Kherbeet, M. Goodarzi, M. Dahari, Mathematical Modeling for Nanofluids Simulation: A Review of the Latest Works, in: N.S. Akbar, O.A. Beg (Eds.), Modeling and Simulation in Engineering Sciences, InTech, 2016. https://doi.org/10.5772/64154.

[11] O. Mahian, L. Kolsi, M. Amani, P. Estellé, G. Ahmadi, C. Kleinstreuer, J.S. Marshall, M. Siavashi, R.A. Taylor, H. Niazmand, S. Wongwises, T. Hayat, A. Kolanjiyil, A. Kasaeian, I. Pop, Recent advances in modeling and simulation of nanofluid flows-Part I: Fundamentals and theory, Physics Reports. 790 (2019) 1–48. https://doi.org/10.1016/j.physrep.2018.11.004.

[12] O. Mahian, L. Kolsi, M. Amani, P. Estellé, G. Ahmadi, C. Kleinstreuer, J.S. Marshall, R.A. Taylor, E. Abu-Nada, S. Rashidi, H. Niazmand, S. Wongwises, T. Hayat, A. Kasaeian, I. Pop, Recent advances in modeling and simulation of nanofluid flows—Part II: Applications, Physics Reports. 791 (2019) 1–59. https://doi.org/10.1016/j.physrep.2018.11.003.

[13] X. Meng, X. Zhang, Q. Li, Numerical investigation of nanofluid natural convection coupling with nanoparticles sedimentation, Applied Thermal Engineering. 95 (2016) 411–420. https://doi.org/10.1016/j.applthermaleng.2015.10.086.

[14] W. Jiang, G. Ding, H. Peng, H. Hu, Modeling of nanoparticles' aggregation and sedimentation in nanofluid, Current Applied Physics. 10 (2010) 934–941. https://doi.org/10.1016/j.cap.2009.11.076.

[15] Y. Ni, J. Fan, Y. Hu, Numerical study of instability of nanofluids: the coagulation effect and sedimentation effect, Nanoscale Res Lett. 6 (2011) 183. https://doi.org/10.1186/1556-276X-6-183.

[16] S. Ganguly, S. Chakraborty, Sedimentation of nanoparticles in nanoscale colloidal suspensions, Physics Letters A. 375 (2011) 2394–2399. https://doi.org/10.1016/j.physleta.2011.04.018.

[17] W. Jiang, G. Ding, H. Peng, H. Hu, Modeling of nanoparticles' aggregation and sedimentation in nanofluid, Current Applied Physics. 10 (2010) 934–941. https://doi.org/10.1016/j.cap.2009.11.076.

[18] Y. Xuan, Z. Yao, Lattice Boltzmann model for nanofluids, Heat Mass Transfer. (2004). https://doi.org/10.1007/s00231-004-0539-z.

[19] Y. Xuan, K. Yu, Q. Li, Investigation on flow and heat transfer of nanofluids by the thermal Lattice Boltzmann model, PCFD. 5 (2005) 13. https://doi.org/10.1504/PCFD.2005.005813.

[20] N.A. Che Sidik, S. Aisyah Razali, Lattice Boltzmann method for convective heat transfer of nanofluids – A review, Renewable and Sustainable Energy Reviews. 38 (2014) 864–875. https://doi.org/10.1016/j.rser.2014.07.001.
[21] N.A.C. Sidik, R. Mamat, Recent progress on lattice Boltzmann simulation of nanofluids: A review, International Communications in Heat and Mass Transfer. 66 (2015) 11–22. https://doi.org/10.1016/j.icheatmasstransfer.2015.05.010.
[22] M. Misale, J.A. Bocanegra, A. Marchitto, Overview on gravitational sedimentation of nanofluids and its role in solar collectors, Renewable Energy. (under review).
[23] M. Misale, J.A. Bocanegra, A. Marchitto, Long term experimental study on gravitational sedimentation of water - Al2O3 nanofluid at different volumetric concentrations, Colloids and Surfaces A: Physicochemical and Engineering Aspects. (under review).
[24] J.A. Bocanegra, A. Marchitto, M. Misale, Lattice Boltzmann Method applied to gravitational sedimentation of Al2O3 nanofluid, Powder Technology. (under review).
[25] K.H. Solangi, S.N. Kazi, M.R. Luhur, A. Badarudin, A. Amiri, R. Sadri, M.N.M. Zubir, S. Gharehkhani, K.H. Teng, A comprehensive review of thermo-physical properties and convective heat transfer to nanofluids, Energy. 89 (2015) 1065–1086. https://doi.org/10.1016/j.energy.2015.06.105.
[26] S. Chakraborty, P.K. Panigrahi, Stability of nanofluid: A review, Applied Thermal Engineering. 174 (2020) 115259. https://doi.org/10.1016/j.applthermaleng.2020.115259.
[27] A. Ghadimi, I.H. Metselaar, The influence of surfactant and ultrasonic processing on improvement of stability, thermal conductivity and viscosity of titania nanofluid, Experimental Thermal and Fluid Science. 51 (2013) 1–9. https://doi.org/10.1016/j.expthermflusci.2013.06.001.
[28] D. Wu, H. Zhu, L. Wang, L. Liu, Critical Issues in Nanofluids Preparation, Characterization and Thermal Conductivity, CNANO. 5 (2009) 103–112. https://doi.org/10.2174/157341309787314548.
[29] A. Ghadimi, R. Saidur, H.S.C. Metselaar, A review of nanofluid stability properties and characterization in stationary conditions, International Journal of Heat and Mass Transfer. 54 (2011) 4051–4068. https://doi.org/10.1016/j.ijheatmasstransfer.2011.04.014.
[30] W. Yu, H. Xie, A Review on Nanofluids: Preparation, Stability Mechanisms, and Applications, Journal of Nanomaterials. 2012 (2012) 1–17. https://doi.org/10.1155/2012/435873.
[31] E.V. Timofeeva, J.L. Routbort, D. Singh, Particle shape effects on thermophysical properties of alumina nanofluids, Journal of Applied Physics. 106 (2009) 014304. https://doi.org/10.1063/1.3155999.
[32] I.M. Mahbubul, T.H. Chong, S.S. Khaleduzzaman, I.M. Shahrul, R. Saidur, B.D. Long, M.A. Amalina, Effect of Ultrasonication Duration on Colloidal Structure and Viscosity of Alumina–Water Nanofluid, Ind. Eng. Chem. Res. 53 (2014) 6677–6684. https://doi.org/10.1021/ie500705j.
[33] L. Yang, K. Du, X.S. Zhang, B. Cheng, Preparation and stability of Al2O3 nano-particle suspension of ammonia–water solution, Applied Thermal Engineering. 31 (2011) 3643–3647. https://doi.org/10.1016/j.applthermaleng.2010.11.031.
[34] Z. Haddad, C. Abid, H.F. Oztop, A. Mataoui, A review on how the researchers prepare their nanofluids, International Journal of Thermal Sciences. 76 (2014) 168–189. https://doi.org/10.1016/j.ijthermalsci.2013.08.010.
[35] B. Tajik, A. Abbassi, M. Saffar-Avval, M.A. Najafabadi, Ultrasonic properties of suspensions of TiO2 and Al2O3 nanoparticles in water, Powder Technology. 217 (2012) 171–176. https://doi.org/10.1016/j.powtec.2011.10.024.
[36] V. Sridhara, L.N. Satapathy, Al2O3-based nanofluids: a review, Nanoscale Res Lett. 6 (2011) 456. https://doi.org/10.1186/1556-276X-6-456.
[37] Babita, S.K. Sharma, S.M. Gupta, Preparation and evaluation of stable nanofluids for heat transfer application: A review, Experimental Thermal and Fluid Science. 79 (2016) 202–212. https://doi.org/10.1016/j.expthermflusci.2016.06.029.
[38] A. Asadi, F. Pourfattah, I. Miklós Szilágyi, M. Afrand, G. Żyła, H. Seon Ahn, S. Wongwises, H. Minh Nguyen, A. Arabkoohsar, O. Mahian, Effect of sonication characteristics on stability, thermophysical properties, and heat transfer of nanofluids: A comprehensive review, Ultrasonics Sonochemistry. 58 (2019) 104701. https://doi.org/10.1016/j.ultsonch.2019.104701.
[39] T.B. Gorji, A review on optical properties and application of nanofluids in direct absorption solar collectors (DASCs), Renewable and Sustainable Energy Reviews. (2017) 23.

[40] A.K. Hussein, D. Li, L. Kolsi, S. Kata, B. Sahoo, A Review of Nano Fluid Role to Improve the Performance of the Heat Pipe Solar Collectors, Energy Procedia. 109 (2017) 417–424. https://doi.org/10.1016/j.egypro.2017.03.044.
[41] S.K. Verma, A.K. Tiwari, Progress of nanofluid application in solar collectors: A review, Energy Conversion and Management. 100 (2015) 324–346. https://doi.org/10.1016/j.enconman.2015.04.071.
[42] K Sopain, A.N. Al-Shamani, Sohif Mat, M H Ruslan, Azher M Abed, Effect of Using Nanofluids in Solar Collector: A Review, (2015). https://doi.org/10.13140/RG.2.1.3660.3603.
[43] P.K. Nagarajan, J. Subramani, S. Suyambazhahan, R. Sathyamurthy, Nanofluids for Solar Collector Applications: A Review, Energy Procedia. 61 (2014) 2416–2434. https://doi.org/10.1016/j.egypro.2014.12.017.
[44] F.S. Javadi, R. Saidur, M. Kamalisarvestani, Investigating performance improvement of solar collectors by using nanofluids, Renewable and Sustainable Energy Reviews. 28 (2013) 232–245. https://doi.org/10.1016/j.rser.2013.06.053.
[45] O.Z. Sharaf, R.A. Taylor, E. Abu-Nada, On the colloidal and chemical stability of solar nanofluids: From nanoscale interactions to recent advances, Physics Reports. 867 (2020) 1–84. https://doi.org/10.1016/j.physrep.2020.04.005.
[46] D. Dhinesh Kumar, A. Valan Arasu, A comprehensive review of preparation, characterization, properties and stability of hybrid nanofluids, Renewable and Sustainable Energy Reviews. 81 (2018) 1669–1689. https://doi.org/10.1016/j.rser.2017.05.257.
[47] S. Witharana, C. Hodges, D. Xu, X. Lai, Y. Ding, Aggregation and settling in aqueous polydisperse alumina nanoparticle suspensions, Journal of Nanoparticle Research. 14 (2012) 851. https://doi.org/10.1007/s11051-012-0851-3.
[48] M.M. Tawfik, Experimental studies of nanofluid thermal conductivity enhancement and applications: A review, Renewable and Sustainable Energy Reviews. 75 (2017) 1239–1253. https://doi.org/10.1016/j.rser.2016.11.111.
[49] D.-W. Oh, A. Jain, J.K. Eaton, K.E. Goodson, J.S. Lee, Thermal conductivity measurement and sedimentation detection of aluminum oxide nanofluids by using the 3ω method, International Journal of Heat and Fluid Flow. 29 (2008) 1456–1461. https://doi.org/10.1016/j.ijheatfluidflow.2008.04.007.
[50] Y. Hwang, H.S. Park, J.K. Lee, W.H. Jung, Thermal conductivity and lubrication characteristics of nanofluids, Current Applied Physics. 6 (2006) e67–e71. https://doi.org/10.1016/j.cap.2006.01.014.
[51] X. Li, D. Zhu, X. Wang, Evaluation on dispersion behavior of the aqueous copper nano-suspensions, Journal of Colloid and Interface Science. 310 (2007) 456–463. https://doi.org/10.1016/j.jcis.2007.02.067.
[52] A. Tiraferri, K.L. Chen, R. Sethi, M. Elimelech, Reduced aggregation and sedimentation of zero-valent iron nanoparticles in the presence of guar gum, Journal of Colloid and Interface Science. 324 (2008) 71–79. https://doi.org/10.1016/j.jcis.2008.04.064.
[53] X. Liu, G. Chen, C. Su, Effects of material properties on sedimentation and aggregation of titanium dioxide nanoparticles of anatase and rutile in the aqueous phase, Journal of Colloid and Interface Science. 363 (2011) 84–91. https://doi.org/10.1016/j.jcis.2011.06.085.
[54] J. Midelet, A.H. El-Sagheer, T. Brown, A.G. Kanaras, M.H.V. Werts, The Sedimentation of Colloidal Nanoparticles in Solution and Its Study Using Quantitative Digital Photography, Part. Part. Syst. Charact. 34 (2017) 1700095. https://doi.org/10.1002/ppsc.201700095.
[55] M. Kamalgharibi, F. Hormozi, S.A.H. Zamzamian, M.M. Sarafraz, Experimental studies on the stability of CuO nanoparticles dispersed in different base fluids: influence of stirring, sonication and surface active agents, Heat Mass Transfer. 52 (2016) 55–62. https://doi.org/10.1007/s00231-015-1618-z.
[56] A. Gallego, K. Cacua, B. Herrera, D. Cabaleiro, M.M. Piñeiro, L. Lugo, Experimental evaluation of the effect in the stability and thermophysical properties of water-Al2O3 based nanofluids using SDBS as dispersant agent, Advanced Powder Technology. 31 (2020) 560–570. https://doi.org/10.1016/j.apt.2019.11.012.
[57] H. Rehman, M. Batmunkh, H. Jeong, H. Chung, Sedimentation Study and Dispersion Behavior of Al_2O_3–H_2O Nanofluids with Dependence of Time, Adv Sci Lett. 6 (2012) 96–100. https://doi.org/10.1166/asl.2012.2135.
[58] S. Witharana, I. Palabiyik, Z. Musina, Y. Ding, Stability of glycol nanofluids — The theory and experiment, Powder Technology. 239 (2013) 72–77. https://doi.org/10.1016/j.powtec.2013.01.039.

[59] J.S. Akhatov, E.T. Juraev, T.I. Juraev, V.N. Avdievich, Study of Sedimentation Process in Nanofluids with Various Concentrations of SiO2 and Al2O3 Nanoparticles, Appl. Sol. Energy. 54 (2018) 428–432. https://doi.org/10.3103/S0003701X18060026.
[60] R. Mondragón, C. Segarra, R. Martínez-Cuenca, J.E. Juliá, J.C. Jarque, Experimental characterization and modeling of thermophysical properties of nanofluids at high temperature conditions for heat transfer applications, Powder Technology. 249 (2013) 516–529. https://doi.org/10.1016/j.powtec.2013.08.035.
[61] J.T.K. Quik, M.C. Stuart, M. Wouterse, W. Peijnenburg, A.J. Hendriks, D. van de Meent, Natural colloids are the dominant factor in the sedimentation of nanoparticles, Environmental Toxicology and Chemistry. 31 (2012) 1019–1022. https://doi.org/10.1002/etc.1783.
[62] J.T.K. Quik, D. van De Meent, A.A. Koelmans, Simplifying modeling of nanoparticle aggregation–sedimentation behavior in environmental systems: A theoretical analysis, Water Research. 62 (2014) 193–201. https://doi.org/10.1016/j.watres.2014.05.048.
[63] A.A. Markus, J.R. Parsons, E.W.M. Roex, P. de Voogt, R.W.P.M. Laane, Modeling aggregation and sedimentation of nanoparticles in the aquatic environment, Science of The Total Environment. 506–507 (2015) 323–329. https://doi.org/10.1016/j.scitotenv.2014.11.056.
[64] S.I. Ezhenkova, S.A. Chivilikhin, Mathematical modeling of sedimentation process of nanoparticles in gradient medium, J. Phys.: Conf. Ser. 643 (2015) 012111. https://doi.org/10.1088/1742-6596/643/1/012111.
[65] F. Giorgi, P. Macko, J.M. Curran, M. Whelan, A. Worth, E.A. Patterson, Sedimentation-Diffusion Behaviour of Nanoparticles, 2020. https://doi.org/10.21203/rs.3.rs-25349/v1.
[66] D. Coglitore, S.P. Edwardson, P. Macko, E.A. Patterson, M. Whelan, Transition from fractional to classical Stokes–Einstein behaviour in simple fluids, R. Soc. Open Sci. 4 (2017) 170507. https://doi.org/10.1098/rsos.170507.
[67] K.E. Davis, W.B. Russel, An asymptotic description of transient settling and ultrafiltration of colloidal dispersions, Physics of Fluids A: Fluid Dynamics. 1 (1989) 82–100. https://doi.org/10.1063/1.857526.
[68] V. Dahirel, M. Jardat, Effective interactions between charged nanoparticles in water: What is left from the DLVO theory?, Current Opinion in Colloid & Interface Science. 15 (2010) 2–7. https://doi.org/10.1016/j.cocis.2009.05.006.
[69] J. Zhang, H. Zeng, Intermolecular and Surface Interactions in Engineering Processes, Engineering. 7 (2021) 63–83. https://doi.org/10.1016/j.eng.2020.08.017.
[70] J.-Y. Jung, J. Koo, Y.T. Kang, Model for predicting the critical size of aggregates in nanofluids, J Mech Sci Technol. 27 (2013) 1165–1169. https://doi.org/10.1007/s12206-013-0224-6.
[71] R. Sadeghy, M. Haghshenasfard, S.Gh. Etemad, E. Keshavarzi, Investigation of alumina nanofluid stability using experimental and modified population balance methods, Advanced Powder Technology. 27 (2016) 2186–2195. https://doi.org/10.1016/j.apt.2016.08.003.
[72] Y. Ma, M.M. Rashidi, R. Mohebbi, Z. Yang, Nanofluid natural convection in a corrugated solar power plant using the hybrid LBM-TVD method, Energy. 199 (2020) 117402. https://doi.org/10.1016/j.energy.2020.117402.
[73] A.A. Mohamad, Lattice Boltzmann Method, first, Springer, London, U.K., 2011. DOI: 10.1007/978-0-85729-455-5.
[74] T. Kruger, H. Kusumaatmaja, A. Kuzmin, O. Shardt, G. Silva, E.M. Viggen, The Lattice Boltzmann Method, Principles and practice, Springer, Switzerland, 2017. DOI:10.1007/978-3-319-44649-3.
[75] P.L. Bhatnagar, E.P. Gross, M. Krook, A Model for Collision Processes in Gases. I. Small Amplitude Processes in Charged and Neutral One-Component Systems, Phys. Rev. 94 (1954) 511–525. https://doi.org/10.1103/PhysRev.94.511.

6. APPLICATION TO ACOUSTICAL PROBLEMS

This chapter presents an extensive literature review concerning applications of the Lattice Boltzmann Method to acoustics[1]. Additionally, simulation examples are included to illustrate some key points. All the included simulations were developed using C++ and the Palabos Library [1] and LBsim opensource code.

As was pointed out in previous sections, the Lattice Boltzmann Method is developed as an improvement of the Lattice Gas Automata (LGA). Wave propagation has been simulated using the LGA. The acoustical problems tackled by simulations with LGA go from simple wave propagation to thermoacoustic effects. Some LGA issues such as anisotropy or statistical noise become a minor obstacle when the method evolves to LBM. A summary of the literature items is included in Annex A.

Great potential for the LBM in acoustics can be noticed by the increasing number of publications concerning acoustical topics over the years. Although there is a previous review focused on aeroacoustics applications [2], the content presented in this chapter is not limited to aeroacoustics and is the first extensive literature review including a wide spectrum of acoustical applications of the method. The results presented in this chapter are considered to be very useful to identify research gaps.

To summarize, the LBM simulates the acoustical field and simultaneously can simulate the main flow field directly in the time domain. The possibility of including appropriate boundary conditions, handling turbulences, and implementing stable LBM variants for low viscosity simulations makes this numerical method very attractive. However, the method's main drawback is the need to use a lattice fine enough to solve high frequencies.

6.1 Lattice Boltzmann Method formulation for acoustics

6.1.1 BGK single relaxation time

The simplest LBM considering a single relaxation time (SRT) can be applied to simulate the propagation of waves. The early work of Chopard and Luthi [3] presents some LBM applications, in particular (radio) wave propagation in an urban area, extendable to sound-wave propagation. The SRT LBM is resumed in Eq. 6.1. For each cell located at **r**, in a given time t, $f_i(\boldsymbol{r},t)$ represents the lattice population in the i direction (characterized by a specific velocity and a weight parameter w_i); the relaxation time τ is a lattice parameter linked to the viscosity, f_i^{eq} the equilibrium (a polynomial approximation of a Maxwell-Boltzmann distribution):

$$f_i(\boldsymbol{r}+\boldsymbol{c_i}\Delta t, t+\Delta t) - f_i(\boldsymbol{r},t) = -\frac{1}{\tau}\left(f_i(\boldsymbol{r},t) - f_i^{eq}(\boldsymbol{r},t)\right) \tag{6.1}$$

The acoustic capabilities of the LBM were tested by Fraser and Hall [4] starting from a comparison of the average sound speed of a wave propagating in a *D2Q9* grid with the theoretical value of $c_0 = 1/\sqrt{3}$, finding dependence on the relaxation parameter (variation up to 5%) and only a slight dependence on the amplitude

[1] *Part of this work was presented at the 30th International Conference on the Discrete Simulation of Fluid Dynamics (DSFD 2021) in Viterbo, Italy, on September 13-17, 2021*

of the pulse. Parallel reflection, diagonal reflection, and diffraction phenomena were also tested with numerical experiments. For parallel reflection, the standing wave patterns were obtained without complete cancellations on the nodal position, perhaps by a mismatch in the quantization cells and the wavelength. Simulations of wave reflection and diffraction on different blocks in a 2D domain were performed by Saidi et al. [5]; as a curiosity, they use high amplitude waves with a density ratio of 10%.

Haydock and Yeomans [6] present the simulation of acoustic streaming around a cylinder and between two plates. This model uses a hexagonal grid *D2Q7*. The method has an intrinsically overestimated attenuation but makes it possible to reproduce the analytical solution. The great capacity of the model to predict streaming around obstacles that can affect the diffusion of a secondary chemical species was pointed out, also proposing an extension of the study to scattering around bubbles. In this work, the standing wave was spatially initialized, setting an initial density distribution in space and a null velocity field $\boldsymbol{u} = 0$, obtaining a one-dimensional planar wave. The wavenumber k and the relatively small density variation for the acoustic wave $\Delta\rho/\rho_0 < 0.01$ can be implemented using the simple relation Eq. 6.2 for the spatial density distribution:

$$\rho(t) = \rho_0 + \Delta\rho \, cos(k\, x) \qquad (6.2)$$

Buick et al. [7] developed a simulation of standing waves between perfect reflectors in a *D2Q7* grid using a BGK model. The density and velocity fields were initialized according to linear wave theory (small amplitudes). The damping effect of two cases of a confined wave in a pipe with no-slip BC and a non-confined wave (using periodic BC) was simulated with good agreement with the analytical predictions. They found the presence of acoustic streaming cells near the walls. In a successive work, Buick et al. [8] simulated acoustic waves in linear conditions, ($\Delta p \ll p_0$) and non-linear conditions (high amplitude soundwaves) they found a change in the waveform after some acoustic cycles. Simulation of the propagation of a shockwave developed from a high-amplitude sinuous wave (1% pressure ratio) by Buick et al. [9] using BGK model *D2Q7* reproduces Burger's equation with accuracy, showing the capabilities of LBM in non-linear acoustics. The waveform distortion from a sinuous to an N-type shape was simulated and agreed with the theory. The study was done in unbounded media, using periodic conditions and an equivalent 154 dB sound. Buick et al. [10] presented some examples of the application of LBM in acoustics and again demonstrated its capacity to be applied in non-linear acoustics, also showing musical acoustics simulations of flow through brass player lips and airflow in an organ groove.

In the article by Brès et al. [11], the acoustic properties of the LBM were researched using:

i. planar wave propagation,
ii. temporal decay of a standing planar wave in a periodic domain,
iii. spatial decay of Gaussian pulse propagation.

In this work, the method was studied for near field, less than 1 m; the method showed low dispersion and low dissipation with good fitting to theoretical solutions. Good fitting of the amplitude change was found in time but with an additional change in the wave's frequency. The relative numerical error was inverse to the number of points per wavelength $Nppw$: with $Nppw = 12$ there was an error low enough. For simulations with lower resolution $Nppw = 4$, the frequency change was significant. A relatively low dispersion was found in the Gaussian pulse for resolutions up to $Nppw = 8$ for 10 kHz. The computational absorptive loss (dB/wavelength) scales as 1/*Nppw*. In conclusion, the engineering use of the method is possible with a sufficient grid resolution.

6.1.2 Sound Sources

To simulate harmonic sound sources, Viggen [12] introduces the **point source method**, Eq. 6.3, that imposes an oscillatory density value in a source cell (lattice node) with a given frequency $1/T$. It was found that

fixing a low viscosity (relaxation time τ near to 0.5, i.e., relaxation frequency $\omega = 1/\tau$ near to 2.0) noise is induced in the solution of the SRT LBM and deviations from the imposed wavelength. In Fig.6.1, the pressure profile in a given time for a monopolar source at the center of a domain is presented. The low viscosity effect is noticed comparing the SRT and the MRT (multiple relaxation times). The MRT shows a more stable behavior for low viscosity. Also is noted that near to the point source, the behavior is anomalous in both models presenting high amplitudes.

$$\rho(t) = \rho_0 + \rho_s \, sin(\frac{2\pi}{\mathrm{T}} \, t) \tag{6.3}$$

The propagation of circular wavefronts from a monopole source was presented, with a decrease in amplitude following the square inverse law. It has also shown the possibility of simulating a plane wavefront with a line of source points near a wall. The Doppler effect is simulated with a point source in a constant velocity field. Some other simulations were presented in Viggen's work as the single and double-slit diffraction experiment, as shown in Fig. 6.2. Lastly, a standing wave simulation is performed in 1D. It was found that viscosity cannot be neglected in LBM, and it is almost impossible to simulate ultrasounds for the excessive grid resolution requirements. Viggen [13] presented a resume of this work centered on the point source method.

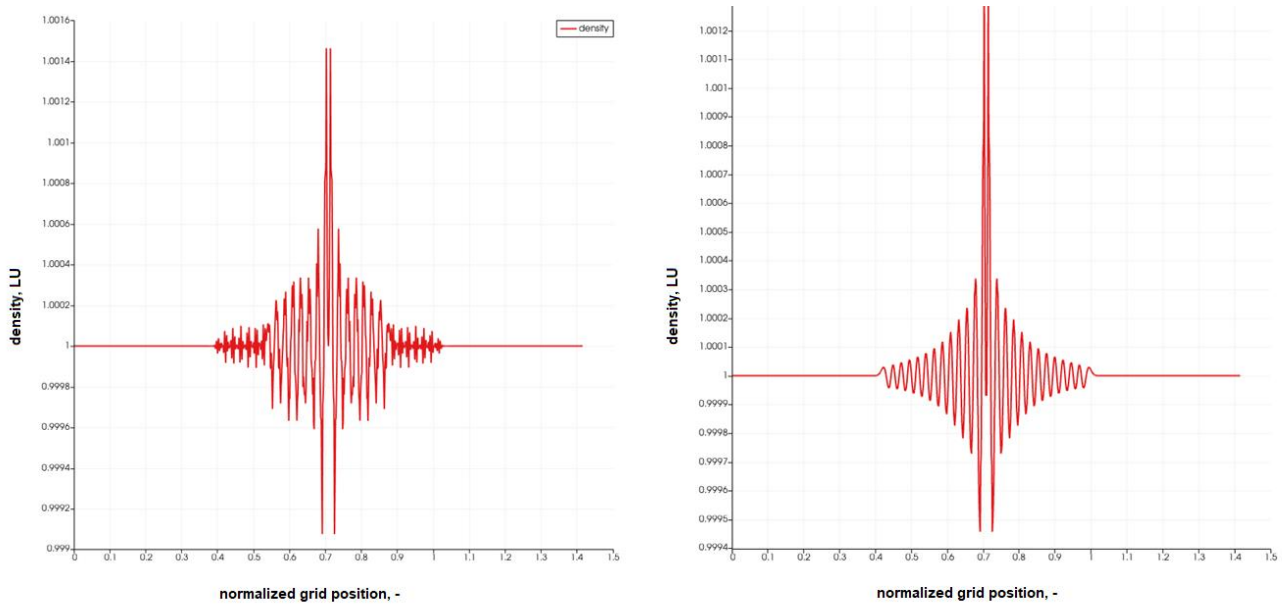

(a) (b)

Figure 6.1 Point source method [12,13] in a square domain, density field over the diagonal (ω =1.999) (a) SRT (b) MRT.

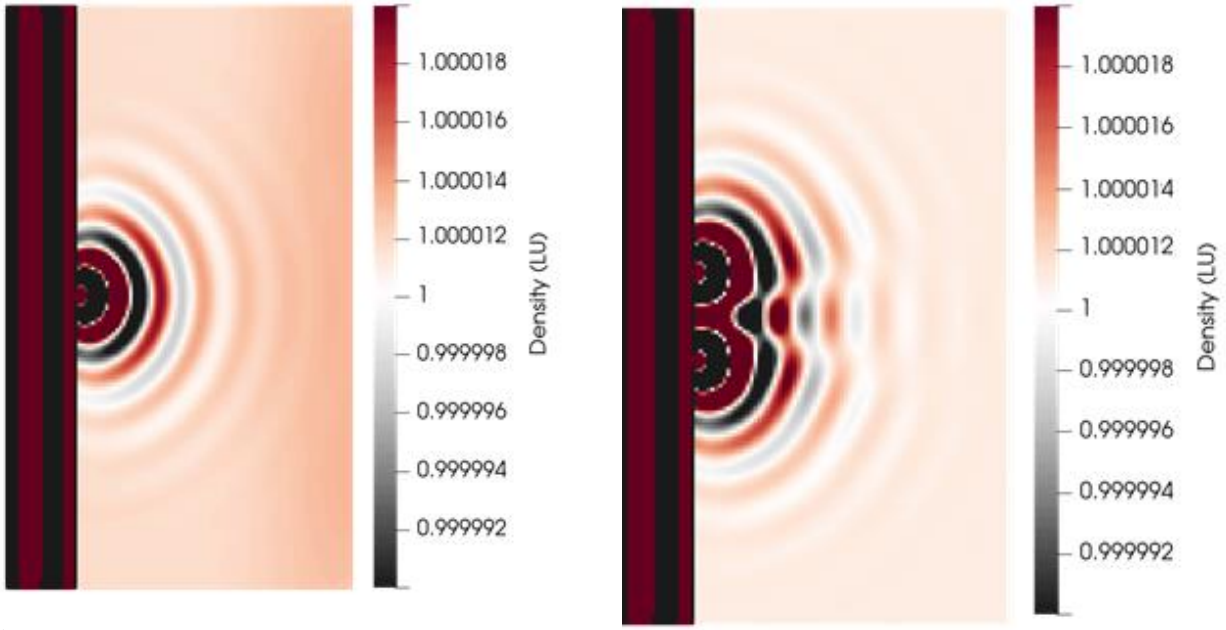

(a) (b)

Figure 6.2 Diffraction of a planar wave through orifices using two-dimensional D2Q9 SRT LBM, (a) density field for one orifice diffraction (b) density field for two orifices diffraction [12].

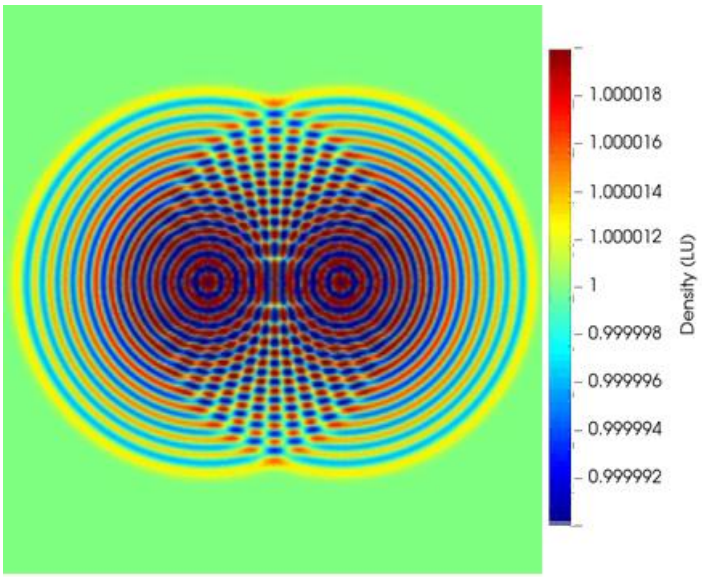

Figure 6.3 Interference of two synchronous harmonic monopoles, using two-dimensional D2Q9 LBM (MRT).

Viggen [14,15] presented his subsequent developments concerning sound sources in the LBM method with multipole models. Previous models for the sound source (*point source method*) simply replaced the lattice's density-inducing unphysical states. The multipole approach adds a source term directly in the LBE acting as a particle source *r*. In these papers, the MRT regularized BGK operator is implemented to allow convergence at a low viscosity. The interference between two harmonic sources is presented in Fig. 6.3. The constructive and destructive pattern is well known in this simulation. Observing the circular wavefronts in the zone without interference isotropic, propagation can be noticed. A low viscosity (ω =1.9999) was implemented in this *D2Q9* MRT-LBM.

6.1.3 Improving SRT stability

Several proposals exist to enhance the stability of SRT LBM. Some of them are implemented using a projection of the collision operator in the moment space, including multiple relaxation times MRT (one for each moment considered). Alternatively, it is possible to increment the number of velocities in the quadrature (multi-speed approach), expanding the equilibrium function to high order (high order or H-LBM), using equilibrium function with temperature terms, using energy-dependent velocities, using an additional distribution for the thermal field (DDF), or implementing hybrid models to solve the energy equation with other numerical methods as finite differences. A brief description of some of these models and examples of their application in acoustics are presented below.

BGK SRT stability is improved by using MRT or regularized R-LBM schemes; the R-LBM scheme is based on determining the pre-collision distribution function through recomputing the equilibrium and non-equilibrium parts before the collision step. Acoustic Multipole Sources (AMS) for regularized LBM R-LBM and MRT were revised by Zhuo and Sagaut_[16]. The Forced Density Function or point source method for monopoles cannot be expanded to multipolar sources (unphysical distortion of the flow), but by introducing a source term in LBE, the AMS can be generated. The analysis was made comparing RLBM with different MRT schemes for punctual sources (monopole, dipole, and quadrupole).

The LBM can be written in a generalized form (Eq. 6.4) where Λ_{ij} is a matrix with the relaxation times for the different moments. This is the Multiple Relaxation Time scheme; note that the collision term is a BGK operator.

$$f_i(r + \boldsymbol{c_i}\Delta t, t + \Delta t) - f_i(r,t) = \Lambda_{ij}\left(f_i(r,t) - f_i^{eq}(r,t)\right) \tag{6.4}$$

In the paper of Marié et al. [17], the dispersion and dissipation for LBM were studied from a theoretical point of view using von Neumann stability analysis and the dispersion of a Gaussian pulse in *D3Q19*, comparing SRT and MRT approaches. The stability analysis also found that the different propagation modes (shear and acoustics) could interfere with each other, involving unstable situations. In both cases, the dispersion shows the dependence on wavenumber. The MRT model shows more stability than SRT.

Different collision models are compared in Fig. 6.4. To decrease the attenuation is necessary to set a low viscosity and then choose a value for the relaxation parameter near 0.5 (or a relaxation frequency near 2.0). The MRT and the regularized models remain stable, reducing the viscosity value. For this simulation, the entropic model shows instabilities for ω =1.9999.

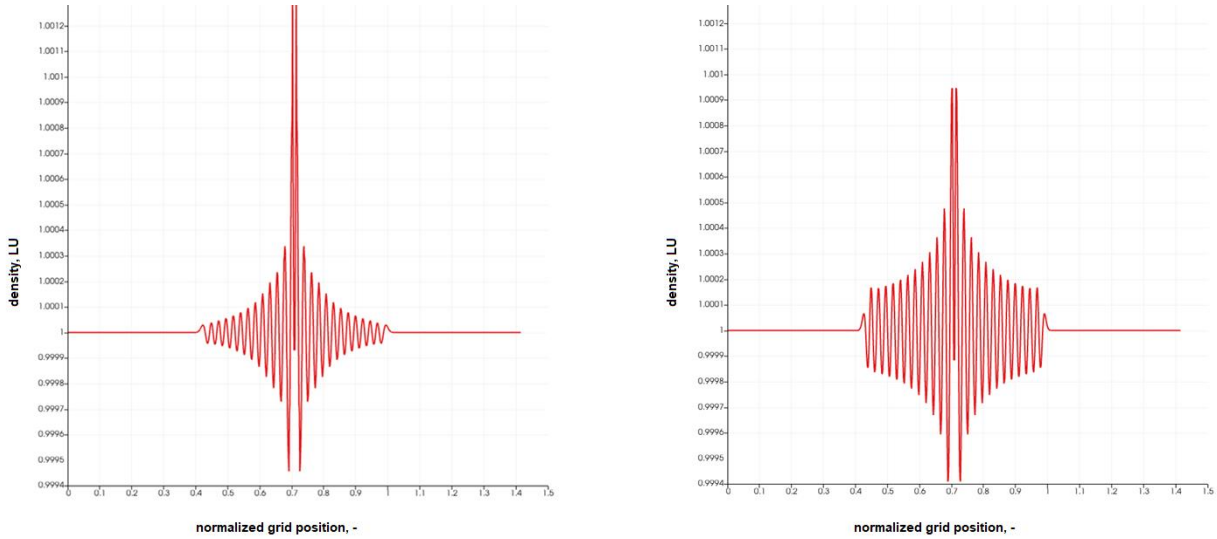

(a) (b)

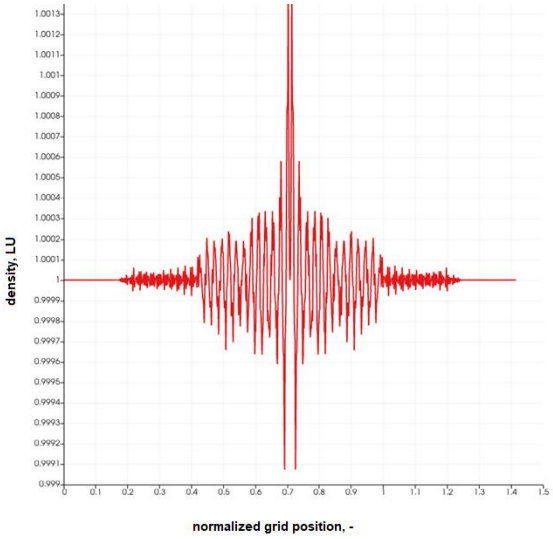

(c)

*Figure 6.4 Point source method [12,13] in a square domain, pressure field over the diagonal (**ω** =1.9999) (a) MRT (b) Regularized (c) Entropic.*

6.1.4 Thermal approach - adjustable sound speed

Historically the LBM was restricted to simulating isothermal waves, but the model can be applied to adiabatic waves. The isothermal BGK method can reproduce the weakly compressible NS equations recovering sound wave propagation. However, for adiabatic acoustics, the application of SRT LBM is inaccurate and can diverge.

An attempt to include thermal and acoustic effects in the LBM was presented by Zhang and Feng [18], showing the results of simulating thermo-acoustic oscillations in a resonant tube. Some non-linear effects such as shock waves and larger amplitude acoustic oscillations, along with acoustic streaming, were observed. The results are compared with the previous LBM and LGK (Gas Kinetic Algorithm). Another work in thermoacoustic was presented by Rafat et al. [19] using the LBM to simulate acoustic streaming in a standing wave tube in a thermoacoustic refrigerator that is streaming through a stack with high-temperature and low-temperature reservoirs. Normally Rayleigh streaming is simulated by DNS and involves low amplitude simulation; in this work, the high-amplitude recirculating flow structures are simulated, and their predominant role in thermoacoustic heat exchange is found. An empty resonator is implemented, and then a flat plate is introduced in the resonator to take account of the stack material. Mesh refinement is implemented to resolve the boundary layer effects (no-slip BC for flat plate and pipe walls), the system is stimulated by harmonic resonance frequency. When a plate was introduced, two types of streaming were found: Rayleigh streaming cell and a second type called edge streaming. The key to distinguish between them is the maximum velocity magnitude that is two orders high in the second case and presents two streaming cells at the edges.

The sound speed c_0 emerges from the equation of state for an ideal gas in the isothermal lattice Boltzmann models, $c_s = (p/\rho)^{1/2}$, instead of when an adjustable sound speed is required, the relation must include the ratio between specific heats ($\gamma = c_P/c_V$) Eq. 6.5. This approach allows one to perform simulations with large pressure variations; however, the first isothermal approach is enough to simulate shock wavefronts, as noted before.

$$c_s = (\gamma \frac{p}{\rho})^{1/2} \tag{6.5}$$

The propagation of sound waves was studied under a variable sound speed BGK-*D2Q9* model in Buick and Cosgrove [20]; the propagation of a plane wave and the non-linear acoustic response was simulated. Different media compressibility can be represented by changing the sound speed; if the proportion of populations at rest are altered, the sound speed can be adjusted, but the viscosity changes. In this paper, an alternative solution was implemented: directly in the Lattice Boltzmann Equation (LBE), an additional body force term $\alpha\nabla\rho$ was added, representing an additional force proportional to the density gradient $\nabla\rho$ as shown in Eq. 6.6.

$$f_i(\boldsymbol{r}+\boldsymbol{c_i}\Delta t, t+\Delta t) - f_i(\boldsymbol{r},t) = -\frac{1}{\tau}\left(f_i(\boldsymbol{r},t) - f_i^{eq}(\boldsymbol{r},t)\right) + 3w_i\alpha\nabla\rho\cdot\boldsymbol{c_i} \tag{6.6}$$

The parameter α can change the sound speed of the model to an effective sound speed c_{eff} as shown in Eq. 6.7:

$$c_{eff} = \sqrt{{c_s}^2 - \alpha} \tag{6.7}$$

With this model, the fluid viscosity does not change, varying the sound speed. The model was implemented to test the propagation of a planar wave in one dimension without bounding; the simulation was performed to measure the sound speed and compare this value with the effective sound speed predicted by the model with good agreement. It was found that non-linearity in wave propagation, the development of a saw-toothed profile for a starting sinuous wave, does not depend only on the amplitude but also on the speed of sound, agreeing with the theory. This model has a large range of variance for c_{eff}, and it can be used to model two-phase wave propagation, temperature gradients, or acoustical lenses. In the paper by Buick et al. [21], the propagation of acoustic waves in an immiscible binary fluid was attempted using different acoustic impedance for each fluid. They applied a DDF model for the fluid and the previous relation for the variable sound speed in each chemical species (different impedance for each medium). Pulses and plane waves were simulated, the reflections and transmission at the interface were correctly simulated, and therefore, the model was applied to the propagation of a plane wave through a bubble finding a standing wave in the bubble.

Multi-speed

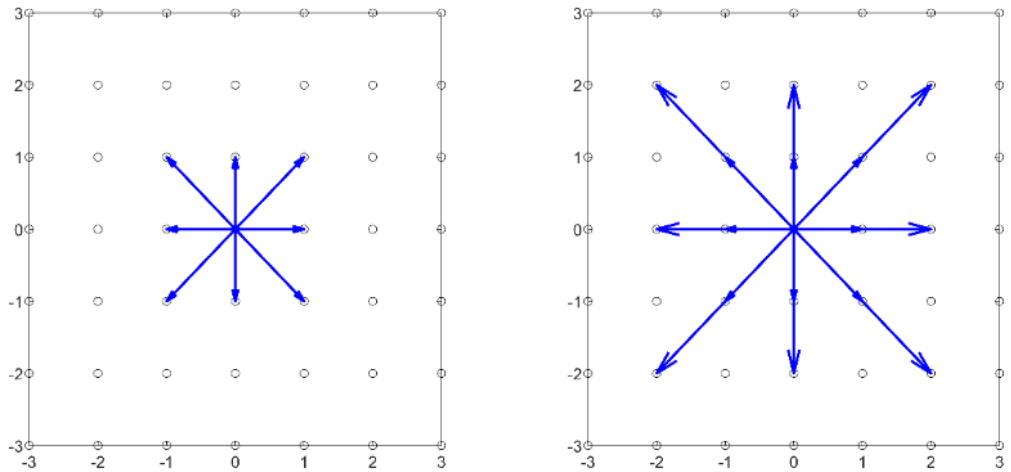

(a) (b)

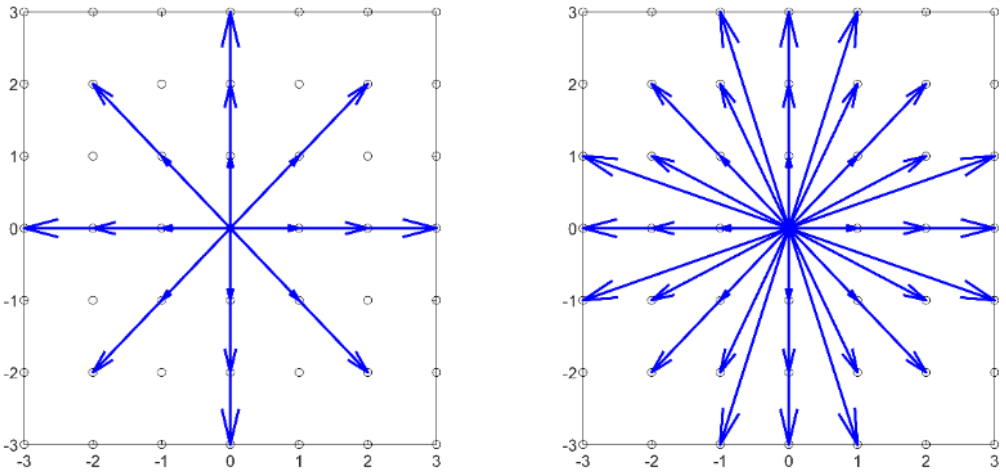

(c) (d)

Figure 6.5 To expand stability and apply LBM to adiabatic acoustic multi-speed approach has been suggested [22]. LBM models include more velocities in the quadrature. a. D2Q9, b. D2Q17, c. D2Q21, d. D2Q37.

The inclusion of more velocities in the velocity base can improve the stability of the LBM and guarantee the inclusion of thermal effects using a single density distribution function. Li and Shan [22] developed an LBM for adiabatic acoustics using a high-order velocity quadrature *D2Q17*. The model was validated with the propagation of a Gaussian pulse. Under this approach, the collision operator can be the simplest BGK SRT. Some multi-speed lattices are represented in Fig. 6.5 as a reference.

FD-LBM

The acoustical and thermal properties of the LBM were reviewed in Lallemand and Luo [23], in particular for energy-conserving (thermal) models. The coupling between the shear and acoustic model is inconvenient and emerges in SRT-LBM and generates an anisotropic propagation. This problem emerges from three characteristics:

1. The simple discretization model (time and space),

2. The linearity of the collision model,

3. The energy conservation constraint.

In Lallemand and Luo [23] paper, the Hybrid Thermal Lattice Boltzmann equation HT-LBM was proposed; the mass and momentum equations are solved with an MRT and the energy equation by an advection-diffusion equation. This model includes the effect of the specific heat ratio γ in the state equation, Eq. (2), and therefore in the sound speed and attenuation improving stability to the standard thermal SRT LBM. This work is the basis for a new numerical method derived from BE known as FD LBM (Finite-Difference Lattice Boltzmann Method).

Kam et al. [24] also worked with 2D thermoacoustic waves under different BC (sudden or gradual increases and decreases of wall temperature) and compared the results with analytical and numerical Direct Aeroacoustics Simulations (DAS) of NS. In general, they found good agreement between the results. The SRT-LBM was modified to compute the expansion coefficients of the equilibrium function only in terms of the velocity base and imposing the complete recovery of the NS equations. They found some parameters coupled with the thermal properties using only one distribution function; this method is called FD-LBM [23]. The feasibility of simulating non-linear coupling in thermoacoustic problems with solid boundaries was

demonstrated. Pressure waves and temperature waves can be simulated with almost identical results as DAS and half the computational time. The discretized BGK LBE in the non-dimensional form is presented in Eq. 6.8:

$$\frac{\delta f_i}{\delta t} + \frac{\boldsymbol{c_i}}{c} \cdot \frac{\delta f_i}{\delta r} = -\frac{1}{K_n \tau}\left(f_i - f_i^{eq}\right) \tag{6.8}$$

The previous LBE can be solved using an expansion of f_i in terms of Knudsen number K_n, Eq. 6.9, and the use of the equilibrium population as $f_i^{(0)} = f_i^{eq}$. Additionally, for the equilibrium distribution, a polynomial expansion of f_i^{eq} only in c_i terms (instead of $c_i \cdot \boldsymbol{u}$) was adopted:

$$f_i = f_i^{(0)} + K_n f_i^{(1)} + {K_n}^2 f_i^{(2)} + O({K_n}^3) \tag{6.9}$$

This leads to the proposed scheme mostly solved by different numerical methods for stream and collide steps; in this way, the LBE is solved for velocity and temperature fields with nonlinear effects. This method is not strictly an LBM, and for this reason, it is called a hybrid FD-LBM.

Resuming LBM reproduce wave phenomena (reflection, diffraction, streaming, interference). Acoustic sources can be simulated by the point source method for monopoles or by adding a source term in the LBE for dipoles and quadrupoles. The basic model presents an increased attenuation and is not stable for low viscosity. MRT, multispeed, regularized LBM, and FD-LBM increase the LBM's stability in the low viscosity limit. The isothermal model considers a fixed sound speed, but this value could be adjustable considering thermal LBM variants.

6.1.5 Aeroacoustics

Aeroacoustics problems are characterized by the interaction between the mean fluid flow and acoustic waves. Two strategies can be adopted to solve numerically the aeroacoustics problem the hybrid methods and the one-step simulations. In the hybrid methods, the fluid flow (or aerodynamic problem) is solved by a numerical method (DNS with LES or RANS), and the acoustic field is computed by Lighthill's inhomogeneous wave equation, Ffowcs Williams and Hawkings (FWH) equations, or by linearized Euler equation. LBM can be applied in both ways. Of course, it is very interesting to observe the one-step capabilities of the LBM that solve the aerodynamic and the acoustic problem simultaneously.

The Helmholtz resonator is considered a benchmark in aeroacoustics, and the results of the simulations can be compared with analytical expressions and experimental data. Mallick et al. [25] presented a simulation of the Helmholtz resonator excited by a grazing flow, using RNG turbulence models. Mesh refinement techniques were adopted to increase the edge-lip resolution to account for vortex shedding. Previous simulations in 2D were able to find the resonance frequency but failed in amplitude calculation. The isotropy of wave propagation in the LBM compared to FD was researched by Wilde [26] and [27], where the low attenuation and symmetry show a good possibility of using the LBM in acoustics. The Helmholtz resonator benchmark case was simulated, finding relatively good matching with experimental results and a high-noise signal, perhaps due to turbulences. A second benchmark case of turbulent noise from an edge was implemented. In the reference [28], a simulation of a flow-acoustic problem was simulated under turbulent flux. The code was validated using the Helmholtz resonator benchmark. The phase difference and attenuation of low amplitude waves were measured and found a limit of 12 Nppw for a phase velocity error of 1%. The model shows isotropic characteristics and similar attenuation as theory predictions.

Crouse et al. [29] showed the capabilities of the LBM using canonical acoustic problems (with traveling and standing waves) for:

1. one-dimensional traveling plane wave (single frequency and white noise),

2. Two-dimensional cylindrical wave,
3. standing wave Kundt tube excited by a simple harmonic frequency wave,
4. The Helmholtz resonator.

The first two problems can be used to determine the numerical dispersion (doubling the grid resolution reduces the RMS errors around three times, possible error saturation, second-order accuracy of the method, minimum 5 to 6 PPWL). Problems 3 and 4 are related to resonance in confined spaces.

Li et al. [30] tested the capability to simulate aeroacoustics problems (solving the acoustic field and the unsteady flow in the one-step calculation) with three problems:

1. one-dimensional acoustic pulses,
2. two-dimensional acoustic pulses,
3. propagation of acoustic vortices in uniform streaming.

The traditional monoatomic treatment of the LBM was expanded to include a diatomic gas more convenient to aeroacoustics, considering more degrees of freedom for the molecules and using a thermal LBM-MRT. It included temperature dependence on the sound speed. Li et al. [31] worked on the propagation of a 2D Gaussian pulse with the same extended model with uniform flow $0.01 < Ma < 0.9$ and found agreement with theoretical results.

Tsutahara et al. [32] presented an alternative model for the hybrid FD-LBM, including high order quadrature *D2Q21* and *D3Q39*, f_i^{eq} expanded to 3rd order, (see Eq 6.10), and a negative viscosity term to reduce viscosity. For diatomic gases, a model with an additional distribution function and degree of freedom (DOF) for internal energy (rotation) was proposed and tested with:

1. a compression-rarefaction wave formed by a step pressure gradient to check the sound speed of the model (2D and 3D),
2. aeolian tone generated by a cylinder (see Fig. 6.6),
3. 3. edge tone generation (3D).

$$f_i^{eq}(\boldsymbol{r},t) = w_i\rho\left[1 - 2B(\boldsymbol{c_i}\cdot\boldsymbol{u}) + 2B^2(\boldsymbol{c_i}\cdot\boldsymbol{u})^2 + B(\boldsymbol{u}\cdot\boldsymbol{u}) - \frac{4}{3}B^3(\boldsymbol{c_i}\cdot\boldsymbol{u})^3 - 2B^2(\boldsymbol{c_i}\cdot\boldsymbol{u})(\boldsymbol{u}\cdot\boldsymbol{u})\right] \quad (6.10)$$

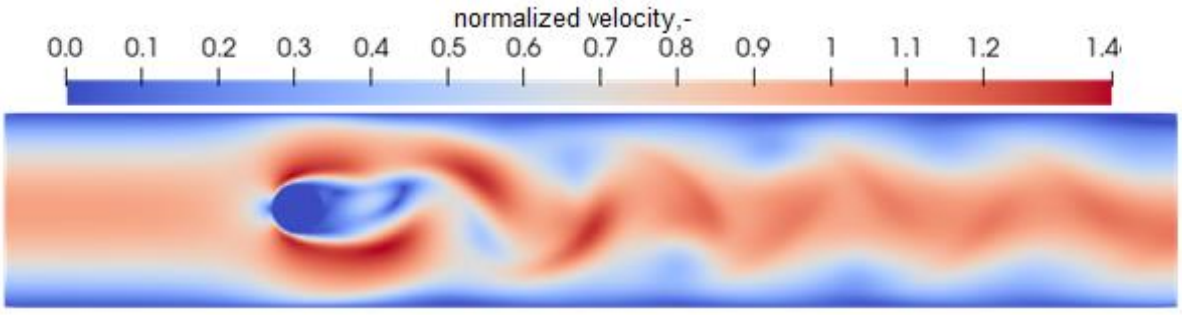

(a)

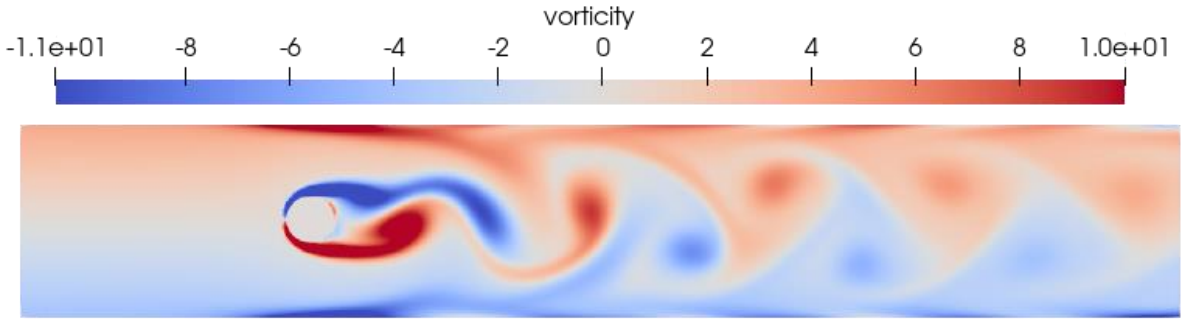

(b)

Figure 6.6 Simple aeroacoustics problem: the aeolian tone generated by a cylinder in a mean flow [32,33].(a) velocity field (b) vorticity field.

Fu et al. [34] developed an improved model for aeroacoustics simulation. The application of LBM-BGK in aeroacoustics is limited by the low Mach number limit and the monoatomic gas approach (related to instability at low viscosities and unrealistic specific heat ratio γ). A good short review of previous attempts to improve the LBM was presented in this paper; the problem was not from the LBE, but instead, it was the simplification applied through the BGK collision operator that did not account for non-linear terms related to interparticle collisions (it only considered inelastic translational collisions). Previous attempts were based on using a high order LBM, multispeed LBM, including an additional DOF, or a secondary energy distribution and FD-LBM to handle the specific heat ratio. Instead of expanding the continuous equilibrium distribution, including rotational DOF, the proposed approach was to modify the equilibrium distribution by imposing the recovery of the state equation for a diatomic gas and the Euler equations (without a small Mach number assumption). The proposed distribution function was the classical Maxwellian distribution plus three terms that account for particle-particle collisions. The validation was done by simulations of benchmark aeroacoustics problems in contrast with DNS (FD): 1. plane Gaussian pulse propagation and 2. three-pulse propagation (pressure, vorticity, and entropy) in a stream. *D2Q9* and the new equilibrium function were sufficient to obtain results such as previous works using *D2Q13*.

The Taylor expansion of the equilibrium function using $\boldsymbol{c_i \cdot u}$ has an inner $Ma << 1$ assumption; it is possible to avoid this assumption by a polynomial expansion, as shown in Eq. 6.11 using c_i with coefficients $(A_i, Ax_i, Ay_i, Bxx_i, Byy_i, Bxy_i)$ to be determined by the constraints:

$$f_i^{eq}(r,t) = A_i + (Ax_i)(c_{ix}) + (Ay_i)(c_{iy}) + (Bxx_i)(c_{ix})^2 + (Byy_i)(c_{iy})^2 + (Bxy_i)(c_{ix}c_{iy}) + \cdots \qquad (6.11)$$

Marié et al. [35] compared LBM and NS high order schemes for aeroacoustics problems, for plane-wave propagation, following a theoretical analysis to obtain three propagation modes with a respective dispersion and dissipation relation for each propagation mode, with and without flow. They found that the error in the LBM is only due to space and time discretization with the same dispersion as the NS and a lower dissipation.

A comparison between the Lattice Boltzmann Equation (LBE) and the pseudo-spectral methods for direct numerical simulations was made by Peng et al. [36]. They studied the decaying of homogeneous isotropic turbulence and radiated noise characteristics. The results from the LBE contain high-frequency oscillations due to acoustic waves in the system (absent in the pseudo-spectral method). The resolution required for the LBE method is approximate twice the pseudo-spectral method requirement. The LBE method could be considered an applicable numerical method for decaying turbulence thanks to the relatively low numerical dissipation and relatively small numerical dispersion with isotropic behavior, ensuring the conservation of angular momentum (or vorticity).

The acoustic waves generated by a rapidly rotating elliptic cylinder were simulated by Tsutahara et al. [37], who found how the wave is produced by the interaction of the shed vortex and the edge of the cylinder, the aspect ratio increases the sound level to a saturation level. In this formulation, the convection term considers the relative velocity between the convection velocity and the grid velocity, it uses a *D2Q21* model, and the equilibrium function is expanded to the third order. The aspect ratio and rotation velocity parameters determine the acoustic irradiation pattern. The pressure shows a linear relation with the Mach rotation speed and a non-linear behavior with aspect ratio; the pressure spectrum for the near and far-field are also calculated and show how the cylinder interacts with the shedding vortices.

Aeroacoustics noise generated by a flow passing through a porous material was simulated by Hasert et al. [38]. The validation for sound generation and propagation was attempted in this paper by two test cases: one-dimensional standing wave (propagation) and sound emission by a rotating Vortex pair. NRBC CBC was adopted. Preliminary results for the flow through the porous media showed the vorticity induced in the fluid.

The work of Xu and Sagaut [39] points to the development of a modified MRT scheme with optimal dissipation dispersion properties for acoustic propagation; a Dispersion Relation Preserving scheme was obtained by a minimization technique applied to the free parameters of the MRT. In this way, the dissipation was also optimized, and stability with low viscosity was guaranteed; the results were compared with classical MRT solutions. The optimization method was tested with acoustical problems: 1. monochromatic harmonic point source; and 2. Gaussian pulse propagation. It was shown how the optimal MRT is better than MRT and traditional SRT-BGK; stability was enhanced for low viscosity, and spurious waves could be annihilated.

Machrouki et al. [40] simulated the scattering of sound with a base flow; a jet was used and a cube obstacle behind a fence. The results were compared with experimental data and agreed on the dipole nature of the source and its location; the flow structure was also correctly simulated. The method reproduced the experimental results relatively well, but the angle of the jet separation was underestimated; in an acoustical way, the noise production was similar but differed for high frequencies, perhaps needing more refinement of the grid near the obstacle. The turbulence was under- or overestimated in certain geometrical zones.

The work of Tsutahara [33] presented a specific review of works related to a modified hybrid scheme FD-LBM; in the paper, differences were shown between the isothermal and the thermal model. The aeroacoustic problems presented here include

1. aeolian tone produced by a circular obstacle in a flow;
2. vortex-vortex interaction;
3. effects of nose shape of a train in the sound produced in a tunnel;
4. sound produced by a drop falling and colliding with a water surface;
5. the scattering of sound from a drop.

The evolution of a disturbance in a base flow was addressed by Vergnault et al. [41]; the base flow LBM scheme (BFLBM) was developed to obtain a solution of the effect of the base flow on the disturbance. Meanwhile, the BF has little effect from the disturbance. This method splits the flow into two components: disturbed and undisturbed (base flow). This method is not faster or cheaper but allows one to compute the base flow with another numerical scheme and compute the perturbation propagation with the LBM. The traditional boundary condition can be used but by reconstructing the population function with the base flow information. The authors performed simulations to study the LBMBF in contrast with the LBM:

1. For the propagation of a Gaussian pulse in a constant flow (periodic BC Mach 0.25), the LBMBF shows an exponential increasing error, but until 10^6 iterations, the results were almost the same.
2. For the propagation of a Gaussian pulse in a subsonic flow (closed BC). Similar results were obtained.

3. For the Poseiulle flow simulation, the comparison is a little more complex because the analytical BF differs from the LBM calculated BF (semi steady), but the LBMBF is still validated.
4. Additionally, the authors validate the application of the LBMBF as vortex in a base flow Coutte profile. And the propagation of a sinuous source in a Mach 0 and Mach 0.74 flow.

This scheme was validated and can be used for source detection coupling with LBM backward as the inverse time method to detect noise sources implemented by Vergnault et al. [42]. The basis of the method is to split the LBE into a mean and a perturbation component; the solution is implemented in 2D, and it was shown how it could work. Using a backward propagation scheme can induce some instabilities, but it is possible to detect the sound sources using a sensitivity analysis and storing data of the boundaries. This LBMBF method was previously reported in two papers, one to describe the time-reversal model to detect a source [43], and in a successive work [44] to develop the *ad-joint* problem in the LBM to obtain sensibility (derivatives of CFD variables) applied to an optimization problem, in particular to noise reduction.

Zhou and Dong [45] shows a hybrid approach to aeroacoustics problems; the flow field is decoupled from the acoustical field, and they are solved with LBE as DNS (NS solution for aerodynamic fluctuations near field) plus Lighthill's Acoustic Analogy for the far-field acoustic field. The model is applied to the simulation of noise generated by turbulence (forced and isotropic), the coupling is one way (there is no feedback from the acoustic field to the mean flow); the paper includes the analysis of two forcing schemes to generate the isotropic permanent turbulence (stochastic or deterministic approach) both can capture the fluctuating acoustic pressure. The LBM is suitable to be incorporated in a hybrid approach to aeroacoustics noise.

This work researched the possibility of obtaining the noise spectrum (including broadband noise) from turbulent flow in different systems. Three aeroacoustics cases were modeled by Brionnaud et al. [46]: 1. duct flow passing through an orifice, 2. subsonic jet through a pipe and, 3. flow-through wheel gear. An MRT-*D3Q27* with a local wall LES turbulence model was implemented because the vortex is the cause of the noise. The method was validated by comparison with experimental data.

Sound generation by vortex pair (co-rotating and counter-rotating) in a two-dimensional space was simulated by Guo and Chen [47]; the influence of viscosity was researched by adding a wall in the domain. For a co-rotating vortex pair, the far-field sound synchronizes with the vortex pair motion and is altered by the viscous effect of the wall (rebounding of the vortex pair). For counter-rotation near a flat wall, the sound emission relates closely to the trajectory of the vortex pair. The method agrees with the analytic predictions and shows that it is suitable for direct acoustic calculation from unsteady flows.

Recently Gorakifard et al. 2021 [48], and Feuchert 2021 [49] presents a work regarding the acoustics properties of the cumulant LBM, analyze dispersive and dissipative properties of the algorithm and show the improvement with respect to the BGK-SRT, even with low grid definition below 6 Nppw dissipation error was below 1% and dispersive error below 3%. This LBM consists in the calculation of the collision operator between cumulants of the central moments instead of a direct collision of the probability distribution, is considered an MRT collision operator, the cumulants are similar to the central moments except for a logarithmic function and are interesting because give a measure for the deviation from the thermodynamic equilibrium given by the maxwell-Boltzmann distribution, Geier et al. 2015 [50]. In Gorakifard et al. 2021 [48] work, the cumulant LBM is applied to study the aeolian tone of one and two cylinders with additional splitter plates behind the cylinder (an additional model for the fluid-structure is implemented, and the oscillation of the splitters is also simulated). In Feutcher 2021 [49], the cumulant LBM is implemented for turbulent flow in a channel with obstructions and an orifice leading the flow into the environment.

6.1.6 Non-reflective Boundary Conditions

To avoid unphysical wave reflections at the boundaries of a simulation in a finite domain, the development of Non-Reflective Boundary Conditions (NRBC) is a necessity.

There are several types of NRBC:

1. Zero Gradient (ZG): set the normal gradient of the populations (with respect to the boundary) equal to zero. This works for mean flow but reflects acoustic waves.
2. Absorbing Boundary Condition (ABC): a sponge zone (buffer) with an added dissipation term.
3. Perfectly Matched Layer (PML) method: Like ABC, the buffer impedance has a perfect match with the interior boundary to avoid reflections.
4. Characteristic Boundary Conditions (CBC) is a characteristics-based method: the wave amplitude variations are computed, and the conservation equations are solved at the boundary using the previously calculated wave amplitude.
5. Continuous method (C1): across the boundary, the first derivatives of populations have to remain continuous. Additionally, the first derivatives of inward populations are set to zero.
6. Extrapolation Method (EM): unknown populations are obtained by extrapolating the populations of the neighboring nodes.

A simple approach to obtain an NRBC consists of including sponge zones (ABC) in the boundaries with artificial dissipation or higher viscosity. However, these zones must be tuned (too much viscosity can reflect the outgoing waves, low viscosity increment has no practical effect), and the simulation of an additional buffer zone impacts the computational costs. On the other hand, CBC, C1, and EM represent a different approach based on analytical expressions without extending the computational domain. A brief presentation of works that adapts those NRBC schemes to LBM, suitable for acoustic simulations (ZG is excluded), is presented below.

In Fig. 6.7, a point source is simulated using a MRT, and the 500 x 500 cell domain contains an ABC in the upper zone (sponge width = 100 cells). The sponge strength profile $\sigma(x)$ is based on an *arctan* function to avoid impedance mismatch and reflections at the interface, the increased absorption is effective, and the wave practically disappears in this buffer zone (except for the first - shock - wavefront that is attenuated but given its higher pressure is not completely absorbed).

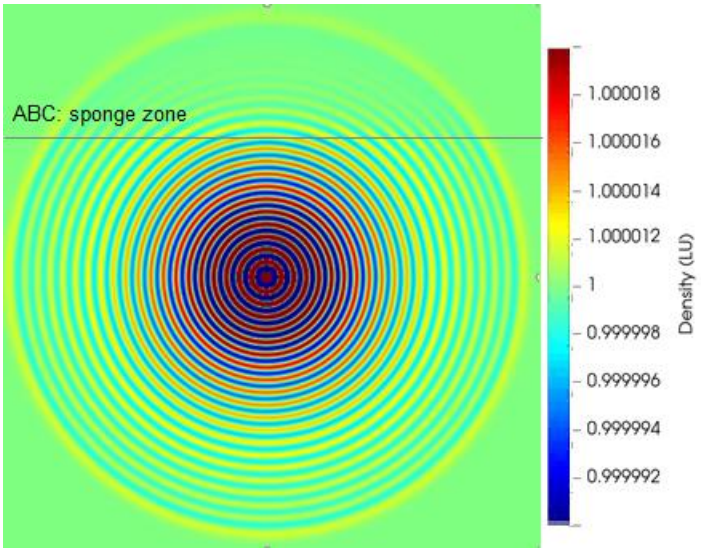

Figure 6.7 Point source simulated by MRT LBM (500 x 500 cells) with an ABC in the upper zone (sponge width = 100 cells).

Xu and Sagaut [51] compared some ABC boundary conditions; all the formulations were implemented as an additional damping term F_{damp} in the LBE. This theoretical work classifies and compares diverse types of absorption terms in the LBE (MRT). The additional damping term F_{damp} is defined for an objective physical quantity q in terms of a precomputed physical quantity q_{ref} and a sponge strength profile $\phi(x)$ in *x* direction as shown in Eq. 6.12:

$$F_{damp} = \phi(x)(q - q_{ref}) \tag{6.12}$$

The MRT-LBE can be written in a generalized form (Eq. 6.13) Λ_{ij} is a matrix with the relaxation times for the different moments and Γ_{ij} is a matrix with the absorption coefficients $\sigma(x)$ for each moment. In the equation, different options to choose the reference state $f_i^{ref}(r,t)$ and the possible representations of the mesoscopic distribution $f_i^*(r,t)$ are tested, the simplest case being $f_i^{ref}(r,t) = f_i^{eq}(r,t)$ and $f_i^*(r,t) = f_i(r,t)$.

$$f_i(r + \boldsymbol{c_i}\Delta t, t + \Delta t) - f_i(r,t) = \Lambda_{ij}\left(f_i(r,t) - f_i^{eq}(r,t)\right) + \Delta t\Gamma_{ij}(f_i^{ref}(r,t) - f_i^*(r,t)) \tag{6.13}$$

A BC based on PML is not straightforward in LBM because it must be formulated in population terms instead of macroscopic variables such as pressure or velocity. A starting point for a PML NRBC is the addition of a sponge buffer ABC with a dissipative term in the LBE; this approach has a drawback because the mismatch in impedance at the interface can reflect the wave, which tends to increment the sponge zone buffer size to obtain a minimum impedance mismatch and effective absorption. For this reason, the PML represents an upgrade of the ABC, ensuring a perfect impedance match at the boundary. Najafi-Yazdi and Mongeau [52] propose a PML for LBM. This PML was tested for Gaussian pulse propagation (2D and 3D) and vortex dissipation. It remains necessary to implement an optimum value of dissipation coefficient for a given PML thickness. This PML is stable for any direction of wave propagation and tends to make an exponential attenuation of incoming waves. Similarly, Tekitek et al. [53] implement the Perfectly Matched Layer (PML) BC for an MRT model. A first-order damping term is included in LBE for the sponge zone and imposing continuity at the interface with the original domain.

The works of Kam et al. [54] and 2007 [55] compare the performance of several NRBC for LBM. The NRBCs tested in this work are of three types: filtering type (FM) mixed with EM, C1 continuous type, and absorbing boundary condition (ABC) type. Six different schemes are tested: EM0, EM0/FM, EM1, EM1/FM, C1, and ABC. Of these six, only EM0/FM, EM1/FM, and ABC (best performing) can yield results comparable to DNS simulation with no reflections (using a much larger computational domain).

Izquierdo and Fueyo [56] proposed CBC-NRBC implementation for the LBM; the idea is to set non-reflective Dirichlet boundary conditions for both velocity and pressure. The Local One-Dimensional Inviscid (LODI) equations are solved at the boundary to obtain the wave variations (only for the normal component) and then are used to solve the conservation equations. The proposed CBC-NRBC was developed for an isothermal MRT model and tested not only for Gaussian acoustic pulses but also for mean flow output conditions and vortex shedding dissipation. This kind of NRBC does not need an extended domain. In the same way, three Characteristic Boundary Conditions (CBC) were adapted for LBM by Wissocq et al. [57], all based in local one-dimensional inviscid (LODI) approximation:

1. Baseline LODI;
2. 2D extension of the LODI-2D including transverse waves
3. local-streamline LODI.

These methods were adapted following different schemes "classical Zou/He BC", *"regularized Bounce Back"* or *"regularized FD"* schemes to calculate unknown population at the boundary that avoids

unphysical reflections. The *"regularized Bounce Back" and "regularized FD"* schemes are more stable and in particular, for high Reynolds numbers, the *"regularized FD"* works better, the Baseline LODI is improved for pure acoustical waves, including transverse waves, but for vortex, the best results were obtained with local streamline-LODI.

6.2 Applications

6.2.1 Porous media and sound absorption

In this section, applications of LBM to study the sound absorption mechanism in porous media and some other systems such as perforated plates are presented.

Early work such as the paper by Inamuro [58] use *D3Q15* to simulate the flux in porous media at different Reynolds numbers. The empirical results were confirmed; for high Reynolds numbers travelling vortex appears . They found that the method is useful to study the microscopic properties of a fluid in porous media. The geometry used is composed of spheres in a fluid; the work is not directly linked to acoustics but shows that the scale of the phenomena is in the order of LBM capabilities.

In the review by Ayub et al. [59], continuum approaches and discrete molecular-based methods were compared regarding acoustical absorption in nanoscopic fibers. LBM and the Discrete Monte Carlo Method extended to Molecular Dynamics were compared in their successive review [60]. This work lists the advantages, disadvantages, and limitations of the molecular approach to wave propagation in nanochannels and briefly summarizes LBM research in acoustics. The comparison points to a better capability of Monte Carlo over LBM. The main limitation is its inability to simulate heat transfer effects and high compressibility (as in a complex molecular gas), but as was shown in previous sections, these issues can be overcome with more sophisticated LBM schemes.

Porous materials and dissipation of acoustic energy with and without mean flow were simulated by Chevillotte et al. [61]. The LBM was implemented in three different ways:

- the first is a *direct microscopic model* of the channel, a perforated plate system to find the flow distortion through the hole. The viscous dissipation is related to the hole viscous boundary layer and the outside additional viscous effect (at both sides of the perforated plate) normally taken into account by an end correction.
- The second, a *surface approach* was used to replace the porous media with an equivalent time-domain impedance condition; the time domain surface impedance condition was implemented combining three filters: Low Pass, Medium Pass, and High Pass with seven coefficients using and storing the last five time steps and using a mean flow estimation.
- Thirdly, a *bulk approach* was followed using an equivalent fluid with three parameters to characterize the porous media (tortuosity, open porosity, and flow resistivity), replacing the fluid cells with another density and leaving the same sound speed, but making a match between the normal stresses in the interface.

We use these three categories to group some works concerning sound absorption and porous materials.

Direct approach

Ji and Zhao [62-64] simulated the acoustic attenuation of an orifice, showing how the shear layers affect the acoustic streaming and convert the acoustic energy into vorticity. The acoustic field was simulated under the influence of several harmonic signals that impacted the perforation. One hole with periodic boundaries was simulated, and the effect of the hole's geometry was discussed. The rounded edges generate less vorticity and, therefore, less absorption. With a similar approach, but using a *D3Q19* model, the absorption of a cylindrical hole in a perforated plate was studied; as in previous models, the periodic BC was used to define

a primitive repetitive cell of the perforated plate. An unsteady jet emerged from the orifice and converted the acoustic fluctuations into non-radiating vortices; periodic vortex shedding was also observed at the edges of the orifice. The spectral analysis confirmed the non-linearity present in the phenomena [65]. It was found that LBM can be an accurate tool for modeling sound absorption in a full-scale virtual impedance tube [66]. A standing wave tube terminated by a circular orifice was simulated in the presence of a mean flow. The absorption coefficient was determined for different frequencies from 380 Hz to 6 kHz and Mach numbers between 0.05-0.2, incrementing the frequency range from previous studies. This model implemented a turbulence VLES model for resolving the unsteady turbulent jet emerging from the perforation. A simple 2D model was implemented to predict the absorption properties of a rigid porous media by da Silva et al. [67], assuming tiny straight channels for the porous media with viscous absorption dominating the process (no slipping back BC), and a periodic primitive cell, see Fig. 6.8 as a reference (simulated using LBsim). Some macroscopic parameters of the sample, such as porosity and thickness, were studied and compared with an analytical model for a rigid porous material. Even though the heat transfer mechanism was not considered, the model was validated and can be implemented considering more complex geometries for the channels.

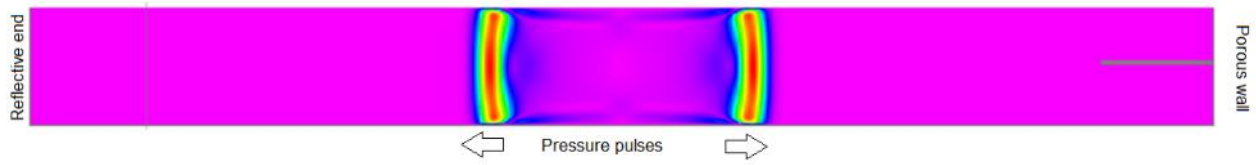

(a)

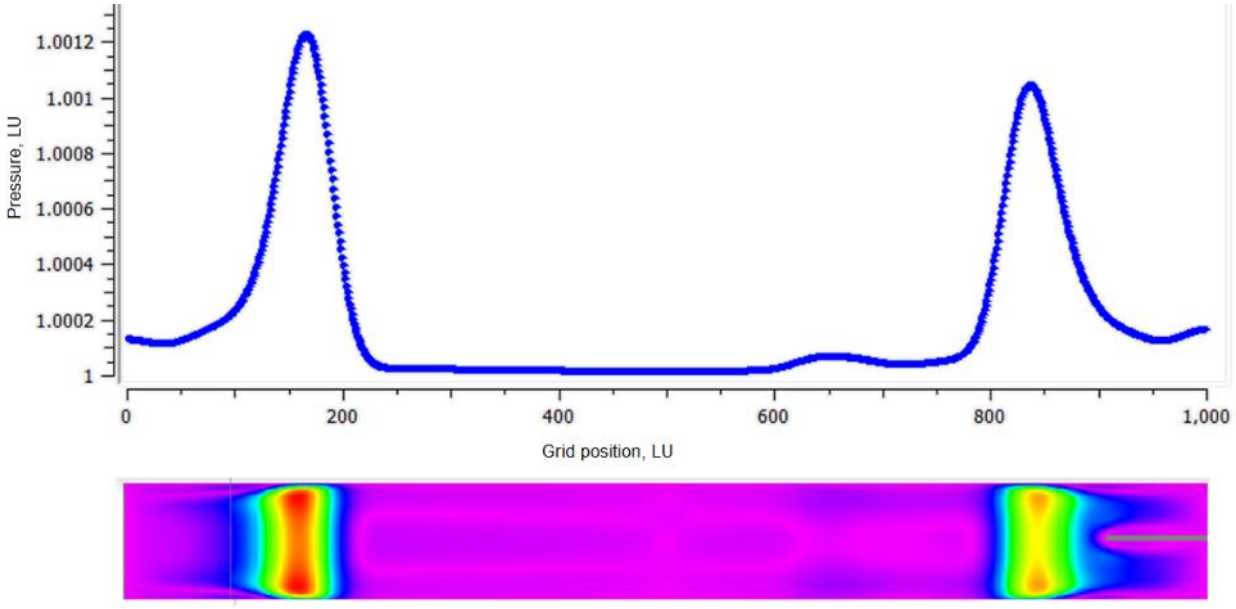

(b)

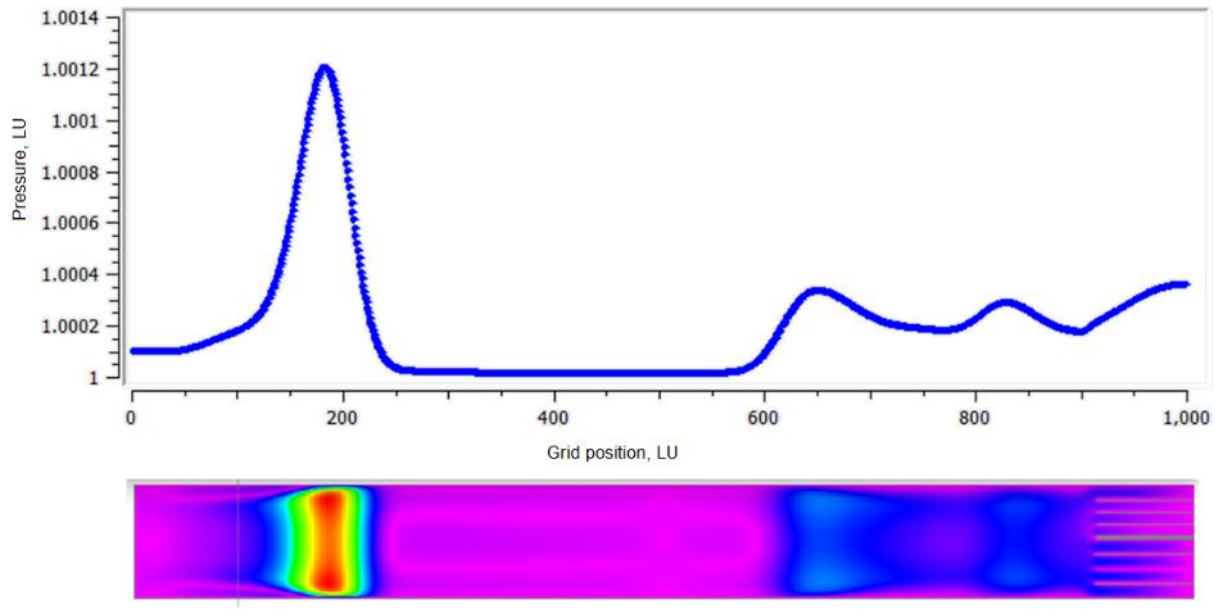

(c)

Figure 6.8 Sound absorption for simple straight channels using pressure pulses [67]. Two pulses travel in opposite directions toward different walls, at the left side a reflective wall and at the right two different porous walls (single straight channels), (a) propagating pulses before reflection (b) pressure after reflection wall 1 (c) pressure after reflection wall 2.

Previous works on perforated plates were expanded by Zhao et al. [68], comparing single and double layer *Perforated Plates* liners at low frequencies (200 Hz to 800 Hz). Experimental data were used to validate the results comparing measures from 12 different liners; the LBM was used to see the possible sound absorption mechanism involved on the double-layer liner. A more complex flux pattern and interaction between the layers emerged, and the gap between the layers played a relevant role in the absorption performance. Moreover, the interaction between the orifice thickness and porosity played a critical role in the noise-damping performance.

The effect of micro-perforated plates (unbacked) in attenuation of pressure fluctuation generated by flow passing over a shallow cavity (inducing flow noise) was researched experimentally and numerically with 2D simulations using LBM under a low-speed laminar boundary layer for a cavity in a transitional flow regime by Maury et al. [69]. The model showed that the energy dissipation mechanism occurs at the regions with maximum velocity fluctuations.

Surface approach/ Impedance BC

Adjustable impedance BC is of interest in acoustic simulations, for example, to simulate absorptive materials in a simplified way reducing the computational cost of simulating the entire absorptive material domain. In Toutant and Sagaut [70] an impedance BC was implemented using the regularized Skordos collision term, to modify the classical BC taking the collision as $f_i^{coll}(r,t) = f_i^{eq}(r,t) + f_i^{neq}(r,t)$ to calculate the unknown populations at the boundary, instead of $f_i^{coll}(r,t) = f_i^{eq}(r,t)$. The study uses the *D2Q9* BGK model but extends the impedance condition to *D3* lattices in the appendix. Simulations using single frequencies and broadband sources were presented. They match with direct aeroacoustics simulations and experimental data. Good results were found for different Mach numbers, tested until reaching Mach = 0.5.

In the work of Sun et al. [71], an impedance BC condition is implemented based on Özyörük's theory [72]. Normal slip and no-slip BC impose zero normal velocity, similar to these BC but taking into account a relationship between normal velocity and pressure in the wall and storing only a few data of previous pressure and velocity values, it is possible to implement this time-domain impedance BC. The strategy imposes a mass flux in the boundary to achieve the correct value of the normal velocity. This strategy does not alter the tangential momentum and can be added to friction or frictionless BC. The theory was tested with two virtual experiments: a normal impedance tube to test an acoustic liner CT73 and a NASA Langley grazing flow impedance tube with a tangential sound field.

Bulk approach- equivalent fluid

In the work of Perot and Freed [73], a porous media was simulated as an equivalent fluid and tested in a normal impedance tube, applying a regression method for a known impedance curve, it is possible to determine the parameters of the equivalent fluid. The model was compared with the predictions of Delany-Bazley and Johnson-Allard models. The strategy is to include a Darcy type (flow resistivity interacting with local velocity) force term as an external force that affects the local velocity distribution during the collision step. The impedance tube is simulated in 3D (100-4000 Hz tube), the LBM matches the analytical results, but for low resistivity, it tends to overestimate absorption to high frequency, perhaps due to viscous effects. Sun [74] implemented an equivalent fluid for porous media buffer. The alternative model in this paper uses the porosity and flow resistivity properties to describe the equivalent porous fluid. The lattice used was *D3Q19* single relaxation time, with a high order LBM (3^{rd} power expansion for the equilibrium function). In this strategy, the viscous force in NS is replaced by a Darcy force. The model is tested in 3 cases with a resistivity flow meter, a normal impedance tube, and a Nasa Langley grazing flow. Complex geometries of the porous material can be implemented in this way.

Indirect approach

Finally, LBM can be applied to determine sound absorption indirectly, calculating the non-acoustical response of the porous material and using an acoustical model to derive the sound absorption coefficient from the determined non-acoustical parameters. For example, Schladitz's [75] adopts this strategy. The model of a non-woven fiber material uses cylinders in a random structure. The direction of the fibers can change by applying pressure inducing anisotropy. The geometrical parameters were estimated using microscopy and then used to calculate the flow resistivity applying Darcy's law. Then the Delany-Bazley semi-empirical model was implemented to predict sound absorption. The indirect approach to simulate porous materials is illustrated in Fig. 6.9. The flow resistivity of the material is calculated using Darcy's law. It is only necessary to know the porosity, the velocity, and the pressure drop. All those parameters can be obtained by a fluid dynamic simulation of the material into an imposed flow. After that, the semiempirical model of Delany-Bazley (valid for fibrous materials, or some other empirical model) is used to calculate the absorption: this kind of model uses non-acoustical parameters, in this case the flow resistivity, as the input.

The use of LBM to study acoustic effects and porous materials is not limited to sound absorption. For example, the work of Hasert et al. [76] simulated the flow of air through porous media at high Re numbers in the limit of Darcy's theory. Their work points to the turbulent noise generated by a fluid that crosses a porous media.

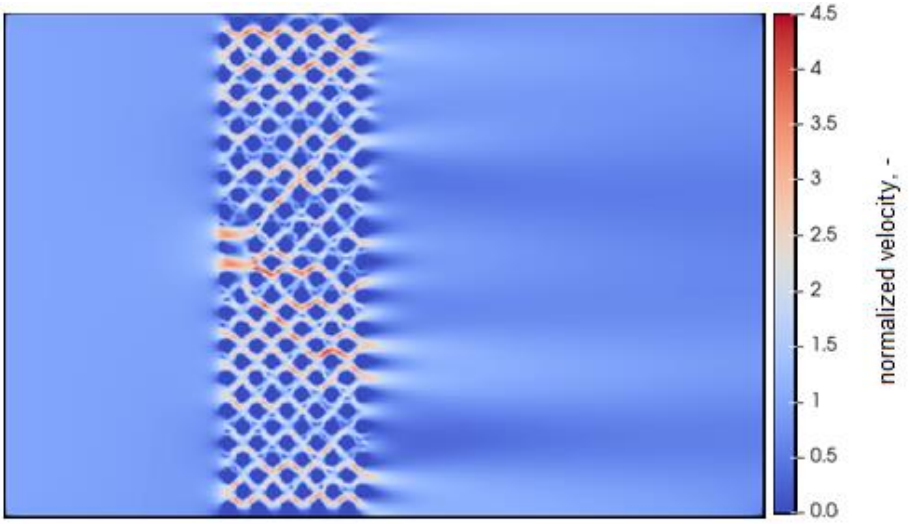

Figure 6.9 Velocity field simulation to calculate the flow resistivity of a porous material (Darcy's law). Velocity normalized to inlet value.

6.2.2 Application to aeroacoustics

Recent reviews in aeroacoustics show the community interest in the Lattice Boltzmann method [77-79]. A review of LBM in aeroacoustics can be found in Shao [2], remarking on the most recent advances in LBM to be applicable in aeroacoustics. A complete list of applications between 2005-2016 in aeroacoustics problems can be found in [80]. In this section, a sample of works related to aeroacoustics is presented and categorized as *Fans, Jets, Ducts, Frames, and low Reynolds number (or Musical Acoustics) applications*.

Fan noise

Fan noise is characterized by a broadband spectrum combined with tonal peaks; the complexity of the generation mechanism involves moving parts, mean flow, vortex shedding, and turbulence. Fans are present in several applications, from cooling systems and HVAC to implants and turbines.

Noise from a low-speed fan (automotive cooling fan) was simulated by Perot et al. [81]. To simulate the fan's rotation, a strategy called Local Reference Frame (LRF) is implemented in which the rotation body is attached to a fixed surrounding mesh, and a secondary mesh for the environment communicates by an interface with this inner rotating mesh. The role of the tip clearance in an axial fan was investigated with the LBM [82]. A complex vortex system emerged from the clearance generating variations on the pressure on the blade surface near the tip region, and these pressure variations generated sound. Compressible LBM combined with FWH analogy was used to simulate trailing-edge far-field noise of a wind turbine blade [83]. LBM was applied to predict the noise generated by large radial fans commonly used in ventilation systems by Sanjose and Moreau [84]. Different configurations were tested to diminish the noise with a modified hub, flux correctors at the inlet to reduce turbulence, and a rotating obstruction to reduce tonal noise. A study on the simulation of an axial fan used in an automotive engine cooling was presented in [85]. The time length of the simulation was relevant to obtain tonal noise results comparable with the experimental measures; using the FW-H analogy and wall pressure data, it was possible to locate the noise sources and their contribution to the far-field noise. The investigation on the noise generated by the tip clearance of an axial fan continued in work by Zhu et al. [86], where the broadband and narrowband sound spectra in the far-field were studied at a low-flow rate. Moreau et al. [87] tested different obstruction configurations to control the tonal noise from a low-speed axial fan. An Advanced Noise Control Fan was simulated for rotating blades in [88].

One of the noise generation mechanisms in an aero-engine is the rotor-stator interaction, which involves periodic impingement of the rotor wake on the stator. The process causes unsteady loading on the stator surface, followed by noise radiation with tonal and broadband components. The NASA/GE Source Diagnostic Test was simulated for this condition [89]. The hybrid LBM-FWH was implemented to compute the far-field noise through an integral extrapolation in a complete airplane model focused on broadband noise estimation and the perceived far-field Sound Pressure Level footprint in the ground area (predicted using the hybrid LBM-FWH analogy in a region of 5 km), Casalino and Hazir [90]. The benchmark case (NASA/GE Source Diagnostic Test) was simulated again, predicting the aeroacoustics of a rotating-blade configuration (fan-Outlet Guide Vane OGV) in near-field and far-field [91]. The main characteristics of the acoustic field were predicted and corroborated (by experimental data contrast), varying the rotor/stator configuration and the rotational speed (simulating an approach with different operative conditions, cutback, and sideline/takeoff). For the same benchmark, Casalino et al. [92] studied three different outlet-vane configurations; the effect of serrations in the vane was simulated, searching for a way to reduce the radiated noise. This simulation was done in the high subsonic Mach number flows with local Mach numbers greater than 0.5, solving the entropy equation E-LBM. To study rotator-stator noise, a rod cascade geometrical configuration (known as a rod-linear cascade - RLC - model) is possible. The generated vortex street was used to simulate the stator-rotor interaction; the rod was designed to match the fundamental frequency that equals the first frequency of the NASA-Glenn Source Diagnostic Test fan stage at approach condition [93]. On this configuration, two aeroacoustics phenomena interact: first, the leading edge generates noise by interaction with the oncoming turbulence from the rod, and second, the acoustics-blade interactions similar to the engine rotor-stator interaction. RLC presents the opportunity as a test rig to explore novel noise mitigation techniques for applications in future turbofans. Possible mechanisms to control the noise can be applied: dampening the surface pressure fluctuation at the leading edge, enhancing the decorrelation or phase interference effects of the turbulence impingement process (e.g., with leading-edge serrations), and reducing the cascade effects with acoustic treatment on the blade surface.

Jet noise

Jets are present in a great variety of systems, such as musical instruments or emergency cooling systems. Noise generated by jets involves turbulence and fluid-structure interaction. A jet is simulated in Fig. 6.10. From the left side, the fluid exit from a pipe, the jet velocity profile shows instabilities and oscillates, in Fig. 6.10(b) is also noticeable the presence of traveling vortices. The noise characteristics depend, among other parameters, on the fluid regime and the evolution of the jet velocity profile. A few relevant applications on jet noise are presented in this section.

Simulation of turbulent noise generation in a mixing layer (two layers with parallel velocities that form turbulence) was presented by Hiraishi et al. [94]. The preserving dispersion relation and LES Smagorinsky turbulence model were implemented in a thermal *D2Q21* model; the first vortex pairing seemed to be the main acoustical source. The simulation of a jet in subsonic flow speeds (Mach 03 to 0.4) was presented for near-field flow and far-field noise generation [95]. Special BC was implemented and the predicted far-field. Spurious waves (high-frequency tones) related to interfaces at variable resolution VR were detected, but they did not significantly affect the far-field broadband power spectra. A simulation of the noise generated by a subsonic highspeed jet (Mach around 0.9) was presented by Casalino and Hazir [96], where the LBM method was modified to simulate turbulent unsteady flows with the inclusion of the entropy equation E-LBM (extending the applicability of the traditional LBM from Mach 0.4 to near 1.0).

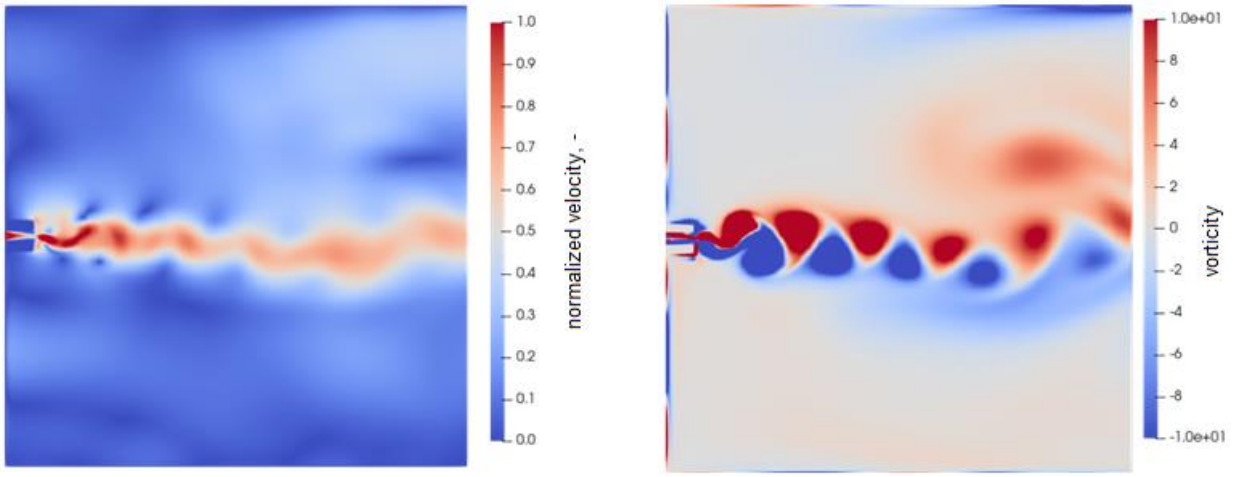

(a) (b)

Figure 6.10 Oscillating jet. (a) normalized velocity; (b) vorticity in lattice units.

Duct noise

Pipes and ducts are present in many industrial plants and, particularly, in HVAC system ducts. The mean flow into the ducts can generate noise at the openings, and often the duct noise is correlated with jet behavior. In this section, some research items concerning duct acoustic applications of the LBM are presented.

The radiation on a far-field from an unflagged cylindrical waveguide was simulated by da Silva and Scavone [97]; the acoustic field was strongly determined by the reflection coefficient of the open end (dependent on the wavelength), but also more complex phenomena were present such as vortex shedding. The previous study on unflagged pipes was extended, including a sinusoidal source and low subsonic mean flow, calculating the sound reflection at the open end of the duct, and testing the effect of circular horns. The vortex formation took place at the same point with and without horns. The horn reduced the end correction at low frequency and enhanced the vortex strength, according to da Silva et al. [98]. Acoustical energy losses from the interaction of an acoustical field and vortex formed at the opening of a duct were investigated in [99]. Two different regimes were found with vortex attached and detached from the opening of the duct; analytical and numerical models failed to predict the magnitude of the losses. The transition between these two regimes depended on the inner shape of the pipe. Extending previous models, in the work of Shi et al. [100], the LBM was used to simulate the sound directivity of the open end of a pipe with subsonic mean flow. The directivity results showed good agreement between theory and experiments in no flow condition (and with low Mach flow) for angles lower than 100. Discrepancies appeared for angles <30°.

In the same way, da Silva and Greco [101] studied this system under excitation by a lineal chirp signal. They continued the study of this kind of system, presenting results for plane wave reflection at open ends of intakes with subsonic mean flow, considering two geometries: cylindrical bell mouth (horn) and a sharp edge tube. In sharp geometries, the flow separation at the opening and the reflection are affected by the energy exchange between the fluid and the acoustic wave. The *"interplay between flow rotational kinetic energy and the acoustic field plays a major role on the behavior of both the magnitude of the reflection coefficient and the end correction."*

Adam et al. [102] presented a simulation of automotive ventilation outlets. The reflection coefficient of an open circular waveguide was calculated with an analytical expression, and the results validated the LBM method. Also, in the automotive industry, the vents in the outlet of an HVAC system were investigated for

several conditions of mass flow rate [103]. The mass flow rate controls the noise levels and frequency. The peaks on the SPL were related to duct modes.

Some other acoustical phenomena in ducts and pipes have been simulated with the LBM, for example, the acoustic flow over a flat plate in a pipe, by Habibi, et al. [104]: the model was linked with the non-linear physics of a thermoacoustic engine. They found the vortex formation at the edges of the plate with a possible implication for the heat transfer characteristics. The mean flow determines the behavior under two different regimes: 1. counter-rotating symmetric vortices were found; 2. at high pressure, asymmetry and vortex shedding could be observed. Vortex separation in some moments could cause additional tonal noise.

Frames

Solid frames in a mean flow can generate noise induced by the tridimensional geometry of the solid interacting with the flow pattern, vortex, and complex flow structures that emerge from this interaction generate a sound field. Normally frame noise is tested experimentally in a wind tunnel. The LBM found a wide field of application with several studies concerning this subject. Here is a sample of some applicative works in this field to understand how it has been implemented and to see some possibilities of this numerical method.

The noise generated by a mean flow interacting with a car frame focusing on the underbody interaction was presented by Crouse et al. [105]. A third-octave band analysis shows a strong peak for the 200Hz band and moves down to 160 Hz if the chin spoiler is removed. This analysis identified where strong pressure fluctuations were being generated: at the wheels, wheel-houses, and the exhaust system. Also, from the automotive field, Adam et al. [106] used the LBM to evaluate direct noise generated from an automobile frame in a virtual wind tunnel. They found a relevant noise source in the side mirrors that matched experimental data; the wheel noise was not estimated and could be due to low mesh resolution in this section. Again from the automotive industry, the noise generated by door gaps was addressed by a simplified model. The aero-acoustic resonance of partially covered cavities with a width much larger than their length was simulated by de Jong et al. [107].

An application example from the aeronautical field was presented by Avallone et al. [108]. They simulated the effect of trailing-edge serrations implemented in airfolds to mitigate noise and turbulent boundary layer; two types of serrations were tested on an airfold NACA 0018 at zero angle of attack.

Musical instruments

Early works of Skordos [109] showed the inner capacity of the LBM to simulate wind instruments and helped to understand the complex mechanism underlying the interaction between the mean flow and an acoustic field in a pipe. He used an extended BGK model in *D2Q9* to simulate jet labium interaction (open and closed pipe), vortex generation, and the acoustic field in the pipe as the feedback system involved. He used an artificial viscosity filter to handle the instabilities of the high-frequency range, attaining reasonable agreement with acoustic signals. He also introduced a regularized scheme for the BC. After this first approximation, he pointed out the need for an ABC, the limitations of the computational power (partially overcome by parallelization), and 3D models to correctly solve the vortex and turbulence. Kuhnelt [110] explored the sound generation mechanism in a small, closed organ pipe. He found the generation of a vortex of low energy and studied how geometric parameters affect the vortex generation. The formation of the oscillating jet showed how the viscosity effects were developed naturally in LBM; the velocity profiles showed a good fit with analytical prediction, known as the Bickley profile. The pressure (density) stories in the mouth and the resonator showed oscillations around the natural frequency of the pipe. In a successive work, Kuhnelt [111] performed simulations of recorders and flute-like instruments. 3D models were implemented, and the sound mechanism related to vortex shedding in the mouth was evaluated. He was showing that the vortices generated by the jet-lip interaction are the main source of the sound. Shi et al. [112] performed a simulation of whistles using the MRT to maintain low viscosity stable simulations (previous

works of Skordos and Kuhnelt used an artificial higher viscosity to maintain stability), the oscillations of the jet and vortex formation around the labium were qualitatively observed with the same features as previous experimental results around the obstacle and interact with the jet itself generating an oscillation of the jet.

An alternative approach was presented by Da Silva and Scavone [113] using a hybrid scheme to simulate wind instruments; the LBM was coupled to a Digital Wave Guide (DWG). The DWG was used to simulate lossless propagation in a 1D pipe model; meanwhile, the LBM was used to simulate the complex mechanism related to the labium and the oscillating reed. In order to couple the two methods, it was necessary to assume a planar-wave region and then use a buffer zone with an ABC. Additionally, a FD scheme was implemented to simulate the reed oscillations. Self-sustained oscillations were simulated (with and without DWG), and the reed oscillation was close to its natural frequency. Moreover, when the DWG was coupled to the model, the sound frequency was near the pipe resonance frequency.

Velasco et al. [114] showed the adaptation of the LBM to curvilinear coordinates for the propagation of scalar waves. They applied the method to determine vibrational modes in cylinders and trumpets bells expanding the LBM capabilities to represent complex geometries as helicoidal tubes. The main idea of the model was to maintain a cartesian array of cells to store the information, and each dimension in this array represented a generalized coordinate in the real curve space. The velocity vectors were the same as traditional cubic discretization, but the macroscopic quantities, equilibrium functions, and forcing terms were chosen to simulate the conservation laws in generalized coordinates. The coordinate system was transformed to simulate the trumpet bell (Bessel horn shape) and a coiled horn (helicoidal); the change in the normal modes with respect to the cylindrical waveguide was obtained. The deduction for the wave equation in this LBM with generalized coordinates was also presented.

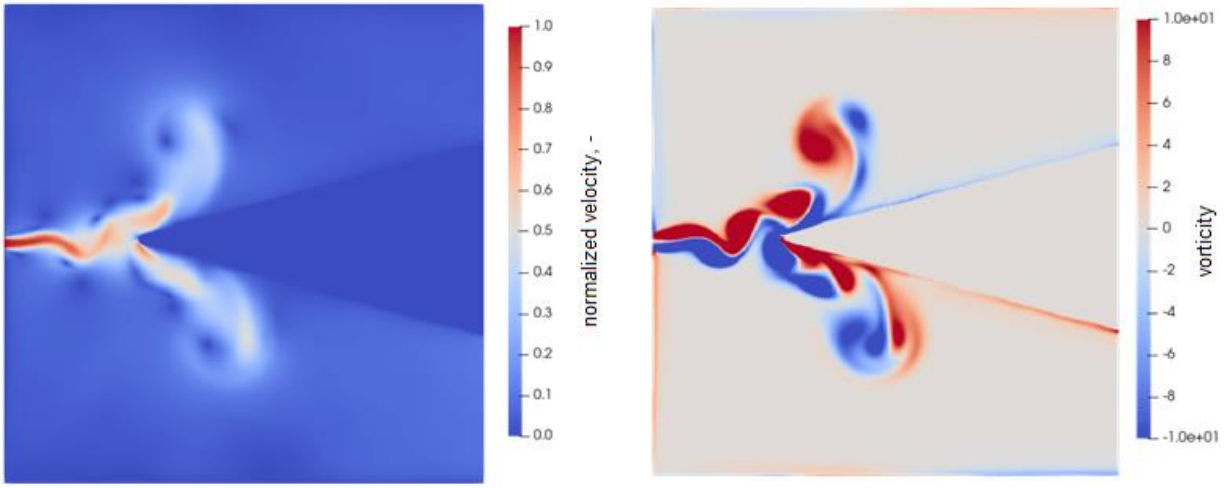

(a) (b)

(c)

Figure 6.11 Edge tone. Oscillating jet and vortex shedding. (a) velocity field (normalized to jet velocity at the outlet), (b) vorticity field in lattice units (c) vorticity field in lattice units (edge tone by a cylinder impacted by a jet).

In Fig. 6.11, an edge tone simulation is presented as a visual reference for this section. The oscillations of the jet are visible, as well as the vortex shedding.

6.2.3 Outdoor acoustics

A few researchers have used the LBM method for outdoor acoustics and large-scale simulations.

The most general work in this area is presented in the Salomons et al. paper [115]. They have used the LBM for outdoor sound propagation, testing the model with different cases (some of are presented in Fig. 6.12:

- propagation of a sound wave in the free-field,
- propagation of sound in the free-field plus a solid ground,
- propagation of sound in the free-field plus a porous ground (random solid-wall buffer),
- effects of a barrier on sound propagation,
- wind influence on the sound field.

At the outdoor scale, the dissipation in the LBM is greater than the physical values in the air. The LBM reproduced the analytical solution of a free-field propagation with high dissipation by an augmented viscosity. Salomons et al. [115] proposed using an excess sound level (with respect to free-field solution) to correct this increased dissipation instead of using the direct sound level of the simulations.

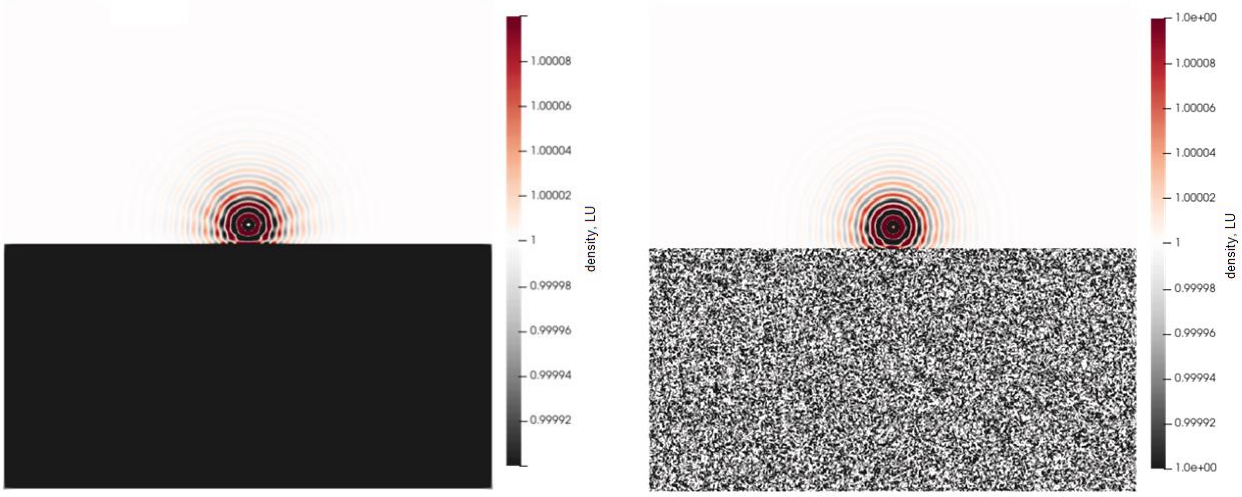

(a) (b)

Figure 6.12 (a) hard ground, (b) absorbent ground. Interference patterns by reflection are more intense on the hard ground [115].

Some other examples of outdoor acoustic problems are related to underwater acoustics or shockwaves in the air. For example, Prestininzi et al. [116] presented a large-scale LBM acoustic application for low-frequency waves in tsunamis; hydro-acoustic waves are useful for early warning of tsunamis as acoustic waves travel ten times faster than the tsunami. The interferences in the layers of water (with different sound speeds) and a semi-porous layer for the sediments are considered in their model. In the work of Ha et al. [117], the LBM was used to simulate underwater sound propagation in a hypothetical warfare scenario. The point source method was applied, and the simulation handled propagation loss, interaction with ground and sea interface layers, and interference with background noises. The sound production by a volumetric flow of magma into the air from a volcano was simulated in the paper by Brogi et al. [118]; a sonic explosion was simulated for different volume flow profiles at volcanos.

6.3 Conclusions

This chapter shows the applicability of the Lattice Boltzmann Method in the acoustical field. A comprehensive literature review concerning the application the Lattice Boltzmann Method in acoustical problems is accomplished, including more than one hundred research items from 1988 to 2021. A brief description of the literature items has been presented, and a summary of the items is included in Annex A.

Moreover, simulation results for different test cases were presented to illustrate the LBM capabilities in acoustics. The test cases includes:

1. Propagation of a sound wave using different collision models;
2. Interference between coherent sources;
3. Diffraction through one or two orifices;
4. Buffer zones for a non-reflective boundary condition;
5. Sound absorption by porous materials,
6. Aeolian noise by a cylinder into a mean flow;
7. Jet noise;
8. Edge noise with two type of edges sharp edge and cylinder.
9. Outdoor propagation, contrasting hard and porous floor.

A wide field of problems can be treated using this numerical model; these acoustical problems were categorized in main fields: porous media and absorption, aeroacoustics, musical acoustics, and outdoor acoustics.

In aeroacoustics, the Lattice Boltzmann Methods framework is gaining special attention by the complex and accurate geometry representation, the capability to handle turbulences, and especially the one-step approach to the aeroacoustics problem simulating at the same time the complex aerodynamic flow and the generated acoustic field.

The Lattice Boltzmann Method directly simulates the wave propagation thanks to the recovery of the Navier-Stokes equation in a semi-incompressible regime (small density variations, present in linear acoustic problems). Additional improvements of the method have been achieved in recent years that enhance the capabilities concerning acoustics applications:

- Simulation of different source conditions (monopole, dipole, quadrupole impulses, broadband noise and single frequencies).
- Non reflective Boundary Conditions of different types, to dissipate spurious waves and reflections, including perfect match layers.
- Impedance boundary conditions.
- Equivalent fluid to simplify a porous absorption domain.
- More stable methods to reduce the fluid viscosity as multiple relaxation time models (including cumulant model), regularized and entropic models.
- Thermal models to allow variable sound speed.
- Additional degrees of freedom to include rotation of molecules in the internal energy.
- Hybrid models for far-field acoustic calculations.
- Turbulence models to handle high Reynolds numbers.
- Advanced mesh techniques such as variable resolution mesh refinement technique, rotating bodies with rotating mesh, or generalized curvilinear lattices.

In early works, the validation of simulation results comes from analytical results, but in the most recent cases in which the method is applied in the industry, the experimental contrast (with wind tunnel and particle image velocimetry PIV techniques) becomes recurrent. Many other times, the simulation results were compared with other numerical method results.

Applications in the engineering field with precise geometrical models such as implants, vehicle frames, fans, and porous materials for sound absorption are possible and represent areas of great interest for researchers. However, the future development is not limited to those industrial applications. The theoretical research concerning this numerical method is an open field, particularly the development of more sophisticated variants of the LBM to ensure stability or include other physical interactions.

REFERENCES

[1] J. Latt, O. Malaspinas, D. Kontaxakis, A. Parmigiani, D. Lagrava, F. Brogi, M.B. Belgacem, Y. Thorimbert, S. Leclaire, S. Li, F. Marson, J. Lemus, C. Kotsalos, R. Conradin, C. Coreixas, R. Petkantchin, F. Raynaud, J. Beny, B. Chopard, Palabos: Parallel Lattice Boltzmann Solver, Computers & Mathematics with Applications. (2020) S0898122120301267. https://doi.org/10.1016/j.camwa.2020.03.022.

[2] W. Shao, J. Li, Review of Lattice Boltzmann Method Applied to Computational Aeroacoustics, Archives of Acoustics. 44 (2019) 215–238. https://doi.org/10.24425/AOA.2019.128486.

[3] B. Chopard, P.O. Luthi, Lattice Boltzmann computations and applications to physics, Theoretical Computer Science. 217 (1999) 115–130. https://doi.org/10.1016/S0304-3975(98)00153-4.

[4] N. Fraser, R. Hall, Simulating Acoustic Propagation Using A Lattice Boltzmann Model Of Incompressible Fluid Flow, in: Proceedings of the 7th WSEAS International Conference on Acoustics & Music: Theory & Applications, Cavtat, Croatia, 2006: pp. 42–47.

[5] M. Saidi, H.B. Tabrizi, R.S. Samian, Lattice Boltzmann Modeling of Wave Propagation and Reflection in the Presence of Walls and Blocks, in: Proceedings of the World Congress on Engineering 2013, London, U.K., 2013: p. 5.

[6] D. Haydock, J.M. Yeomans, Lattice Boltzmann simulations of acoustic streaming, Journal of Physics A: Mathematical and General. 34 (2001).

[7] J.M. Buick, D.M. Campbell, C.A. Greated, Lattice Boltzmann methods in acoustics, The Journal of the Acoustical Society of America. 103 (1998) 2975–2975. https://doi.org/10.1121/1.422412.

[8] J.M. Buick, C.A. Greated, D.M. Campbell, Lattice BGK simulation of sound waves, Europhysics Letters (EPL). 43 (1998) 235–240. https://doi.org/10.1209/epl/i1998-00346-7.

[9] J.M. Buick, C.L. Buckley, C.A. Greated, J. Gilbert, Lattice Boltzmann BGK Simulation of Non-Linear Sound Waves: The Development Of A Shock Front, Journal of Physics A: Mathematical and General. 33 (2000) 3917–3928.

[10] J.M. Buick, M.A. Neal, J.A. Cosgrove, D.M. Campbell, The Lattice Boltzmann Model and its Application to Acoustics, in: ICA 2001 Proceedings, Rome, Italy, 2001.

[11] G. Brès, F. Pérot, D. Freed, Properties of the Lattice Boltzmann Method for Acoustics, in: 15th AIAA/CEAS Aeroacoustics Conference (30th AIAA Aeroacoustics Conference), American Institute of Aeronautics and Astronautics, Miami, Florida, 2009. https://doi.org/10.2514/6.2009-3395.

[12] E.M. Viggen, The Lattice Boltzmann Method with Applications in Acoustics, Master Thesis, Norwegian University of Science and Technology, 2009.

[13] E.M. Viggen, The lattice Boltzmann method in acoustics, in: 33rd Scandinavian Symposium on Physical Acoustics, Norwey, 2010: p. 5.

[14] E.M. Viggen, Acoustic multipole sources for the lattice Boltzmann method, Physical Review E. 87 (2013). https://doi.org/10.1103/PhysRevE.87.023306.

[15] E.M. Viggen, The lattice Boltzmann method: Fundamentals and acoustics, Ph.D. Thesis, Norwegian University of Science and Technology, 2014.

[16] C. Zhuo, P. Sagaut, Acoustic multipole sources for the regularized lattice Boltzmann method: Comparison with multiple-relaxation-time models in the inviscid limit, Phys. Rev. E. 95 (2017) 063301. https://doi.org/10.1103/PhysRevE.95.063301.

[17] S. Marié, D. Ricot, P. Sagaut, Accuracy of Lattice Boltzmann Method for Aeroacoustic Simulations, in: 13th AIAA/CEAS Aeroacoustics Conference (28th AIAA Aeroacoustics Conference), American Institute of Aeronautics and Astronautics, Rome, Italy, 2007. https://doi.org/10.2514/6.2007-3515.

[18] X. Zhang, H. Feng, Application of the mesoscopic method to model nonlinear thermoacoustic oscillations, in: 1proceedings on 9th International Congress on Sound and Vibration 2012 (ICSV19), Vilnius, Lithuania, 2012: p. 2032.

[19] Y. Rafat, K. Habibi, L. Mongeau, Direct numerical simulations of acoustic streaming in standing wave tubes using the Lattice Boltzmann Method, The Journal of the Acoustical Society of America. 19 (2013) 3238. https://doi.org/10.1121/1.4805174.

[20] J.M. Buick, J.A. Cosgrove, Investigation of a lattice Boltzmann model with a variable speed of sound, Journal of Physics A: Mathematical and General. 39 (2006) 13807–13815. https://doi.org/10.1088/0305-4470/39/44/013.

[21] J.M. Buick, J.A. Cosgrove, R. Higham, Acoustic lattice Boltzmann model for immiscible binary fluids with a species-dependent impedance, Phys. Rev. E. 76 (2007) 036713. https://doi.org/10.1103/PhysRevE.76.036713.
[22] Y. Li, X. Shan, Lattice Boltzmann method for adiabatic acoustics, Philosophical Transactions of the Royal Society A: Mathematical, Physical and Engineering Sciences. 369 (2011) 2371–2380. https://doi.org/10.1098/rsta.2011.0109.
[23] P. Lallemand, L.-S. Luo, Theory of the lattice Boltzmann method: Acoustic and thermal properties in two and three dimensions, Phys. Rev. E. 68 (2003) 036706. https://doi.org/10.1103/PhysRevE.68.036706.
[24] E.W.S. Kam, R.M.C. So, S.C. Fu, One-step simulation of thermoacoustic waves in two-dimensional enclosures, Computers & Fluids. 140 (2016) 270–288. https://doi.org/10.1016/j.compfluid.2016.10.005.
[25] S. Mallick, R. Shock, V. Yakhot, Numerical simulation of the excitation of a Helmholtz resonator by a grazing flow, The Journal of the Acoustical Society of America. 114 (2003) 1833–1840. https://doi.org/10.1121/1.1606464.
[26] A. Wilde, Application of the Lattice-Boltzmann method in flow acoustics, in: Fourth SWING Aeroacoustic Workshop, Aachen, Germany, 2004: p. 1070.
[27] A. Wilde, Calculation of sound generation and radiation from instationary flows, Computers & Fluids. 35 (2006) 986–993. https://doi.org/10.1016/j.compfluid.2005.03.005.
[28] A. Wilde, Flow acoustic simulations using the Lattice-Boltzmann method, in: 22nd CAD-FEM User's Meeting 2004 International Congress on FEM Technology with ANSYS CFX & ICEM CFD Conference, November 10–12, 2004, Dresden, Germany, 2004: p. 9.
[29] B. Crouse, D. Freed, G. Balasubramanian, S. Senthooran, P.-T. Lew, L. Mongeau, Fundamental Aeroacoustics Capabilities of the Lattice-Boltzmann Method, in: 12th AIAA/CEAS Aeroacoustics Conference (27th AIAA Aeroacoustics Conference), American Institute of Aeronautics and Astronautics, Cambridge, Massachusetts, 2006. https://doi.org/10.2514/6.2006-2571.
[30] X.M. Li, R.C. K. Leung, R.M. C. So, One-Step Aeroacoustics Simulation Using Lattice Boltzmann Method, AIAA Journal. 44 (2006) 78–89. https://doi.org/10.2514/1.15993.
[31] X.M. Li, R.M. C. So, R.C. K. Leung, Propagation Speed, Internal Energy, and Direct Aeroacoustics Simulation Using Lattice Boltzmann Method, AIAA Journal. 44 (2006) 2896–2903. https://doi.org/10.2514/1.18933.
[32] M. Tsutahara, T. Kataoka, K. Shikata, N. Takada, New model and scheme for compressible fluids of the finite difference lattice Boltzmann method and direct simulations of aerodynamic sound, Computers & Fluids. 37 (2008) 79–89. https://doi.org/10.1016/j.compfluid.2005.12.002.
[33] M. Tsutahara, The finite-difference lattice Boltzmann method and its application in computational aero-acoustics, Fluid Dyn. Res. 44 (2012) .045507.
[34] S.C. Fu, R.M.C. So, R.C.K. Leung, Modeled Boltzmann Equation and Its Application to Direct Aeroacoustic Simulation, AIAA Journal. 46 (2008) 1651–1662. https://doi.org/10.2514/1.33250.
[35] S. Marié, D. Ricot, P. Sagaut, Comparison between lattice Boltzmann method and Navier–Stokes high order schemes for computational aeroacoustics, Journal of Computational Physics. 228 (2009) 1056–1070. https://doi.org/10.1016/j.jcp.2008.10.021.
[36] Y. Peng, W. Liao, L.-S. Luo, L.-P. Wang, Comparison of the lattice Boltzmann and pseudo-spectral methods for decaying turbulence: Low-order statistics, Computers & Fluids. 39 (2010) 568–591. https://doi.org/10.1016/j.compfluid.2009.10.002.
[37] M. Tsutahara, A. Tamura, K. Yasuno, Y. Komatsu, Direct simulation of sound emitted by a ra- pidly rotating elliptic cylinder by the finite difference lattice boltzmann method, in: 17th International Congress on Sound and Vibration (ICSV17), ICSV, Cairo, Egypt, 2010: p. 8.
[38] M. Hasert, J. Bernsdorf, S. Roller, Towards aeroacoustic sound generation by flow through porous media, Proc. R. Soc. A. 369 (2011) 2467–2475. https://doi.org/10.1098/rsta.2011.0089.
[39] H. Xu, P. Sagaut, Optimal low-dispersion low-dissipation LBM schemes for computational aeroacoustics, Journal of Computational Physics. 230 (2011) 5353–5382. https://doi.org/10.1016/j.jcp.2011.03.040.
[40] H. Machrouki, D. Ricot, O. Coste, Lattice Boltzmann aero-acoustics modelling of flow around obstacles, in: Proceedings of the Acoustics 2012 Nantes Conference, HAL-00811101ff, Nantes, France, 2012: pp. 1298–1301.

[41] E. Vergnault, O. Malaspinas, P. Sagaut, A lattice Boltzmann method for nonlinear disturbances around an arbitrary base flow, Journal of Computational Physics. 231 (2012) 8070–8082. https://doi.org/10.1016/j.jcp.2012.07.021.
[42] E. Vergnault, O. Malaspinas, P. Sagaut, Noise source identification with the lattice Boltzmann method, The Journal of the Acoustical Society of America. 133 (2013) 1293–1305. https://doi.org/10.1121/1.4776181.
[43] E. Vergnault, O. Malaspinas, P. Sagaut, A time-reversal lattice Boltzmann method, Journal of Computational Physics. 230 (2011) 8155–8167. https://doi.org/10.1016/j.jcp.2011.07.014.
[44] E. Vergnault, P. Sagaut, An adjoint-based lattice Boltzmann method for noise control problems, Journal of Computational Physics. 276 (2014) 39–61. https://doi.org/10.1016/j.jcp.2014.07.027.
[45] Y. Zhou, Y.-H. Dong, An investigation of the lattice Boltzmann equation-based hybrid approach for simulation of sound generated by isotropic turbulence, Computers & Fluids. 100 (2014) 267–277. https://doi.org/10.1016/j.compfluid.2014.05.015.
[46] R. Brionnaud, M. Chávez Modena, G. Trapani, D. M. Holman, Direct Noise Computation with a Lattice-Boltzmann Method and Application to Industrial Test Cases, in: 22nd AIAA/CEAS Aeroacoustics Conference, American Institute of Aeronautics and Astronautics, Lyon, France, 2016. https://doi.org/10.2514/6.2016-2969.
[47] R.-Q. Guo, X.-P. Chen, Sound generation by two dimensional vortex pair motion and the influence of viscosity, Computers & Mathematics with Applications. 78 (2019) 2761–2771. https://doi.org/10.1016/j.camwa.2019.04.022.
[48] M. Gorakifard, I. Cuesta, C. Salueña, E. Kian Far, Acoustic wave propagation and its application to fluid structure interaction using the Cumulant Lattice Boltzmann Method, Computers & Mathematics with Applications. 87 (2021) 91–106. https://doi.org/10.1016/j.camwa.2021.02.011.
[49] C. Feuchter, Direct aeroacoustic simulation with a cumulant Lattice-Boltzmann model, Computers & Fluids. 224 (2021) 104970. https://doi.org/10.1016/j.compfluid.2021.104970.
[50] M. Geier, M. Schönherr, A. Pasquali, M. Krafczyk, The cumulant lattice Boltzmann equation in three dimensions: Theory and validation, Computers & Mathematics with Applications. 70 (2015) 507–547. https://doi.org/10.1016/j.camwa.2015.05.001.
[51] H. Xu, P. Sagaut, Analysis of the absorbing layers for the weakly-compressible lattice Boltzmann methods, Journal of Computational Physics. 245 (2013) 14–42. https://doi.org/10.1016/j.jcp.2013.02.051.
[52] A. Najafi-Yazdi, L. Mongeau, An absorbing boundary condition for the lattice Boltzmann method based on the perfectly matched layer, Computers & Fluids. 68 (2012) 203–218. https://doi.org/10.1016/j.compfluid.2012.07.017.
[53] M.M. Tekitek, M. Bouzidi, F. Dubois, P. Lallemand, Towards perfectly matching layers for lattice Boltzmann equation, Computers & Mathematics with Applications. 58 (2009) 903–913. https://doi.org/10.1016/j.camwa.2009.02.013.
[54] E.W.S. Kam, R.M.C. So, R.C.K. Leung, Non-Reflecting Boundary Conditions for One-Step LBM Simulation of Aeroacoustics, in: 12th AIAA/CEAS Aeroacoustics Conference (27th AIAA Aeroacoustics Conference), American Institute of Aeronautics and Astronautics, Cambridge, Massachusetts, 2006. https://doi.org/10.2514/6.2006-2416.
[55] E.W.S. Kam, R.M.C. So, R.C.K. Leung, Lattice Boltzmann Method Simulation of Aeroacoustics and Nonreflecting Boundary Conditions, AIAA JOURNAL. 45 (2007) 1703–1712. https://doi.org/10.2514/1.27632.
[56] S. Izquierdo, N. Fueyo, Characteristic nonreflecting boundary conditions for open boundaries in lattice Boltzmann methods, Phys. Rev. E. 78 (2008) 046707. https://doi.org/10.1103/PhysRevE.78.046707.
[57] G. Wissocq, N. Gourdain, O. Malaspinas, A. Eyssartier, Regularized characteristic boundary conditions for the Lattice-Boltzmann methods at high Reynolds number flows, Journal of Computational Physics. 331 (2017) 1–18. https://doi.org/10.1016/j.jcp.2016.11.037.
[58] T. Inamuro, M. Yoshino, F. Ogino, Lattice Boltzmann simulation of flows in a three-dimensional porous structure, (1999) 12.
[59] M. Ayub, A.C. Zander, C.Q. Howard, B.S. Cazzolato, A Review of Acoustic Absorption Mechanisms of Nanoscopic Fibres, in: Proceedings of Acoustics 2011, Gold Coast, Australia, 2011: p. 9.
[60] M. Ayub, A.C. Zander, C.Q. Howard, B.S. Cazzolato, D.M. Huang, A Review of MD Simulations of Acoustic Absorption Mechanisms at the Nanoscale, in: Proceedings of Acoustics 2013–Victor Harbor, Victor Harbor, Australia, 2013: p. 8.

[61] F. Chevillotte, M. Martinez, F.-X. Bécot, L. Jaouen, Modeling of acoustical porous materials under flow, in: SIA Automotive NVH Comfort 2016, Le Mans, France, 2016: p. 7.
[62] C. Ji, D. Zhao, Numerical Investigation of Acoustically Excited Flow Through an Orifice Using Lattice Boltzmann Method, in: 19th AIAA/CEAS Aeroacoustics Conference, American Institute of Aeronautics and Astronautics, Berlin, Germany, 2013. https://doi.org/10.2514/6.2013-2127.
[63] C. Ji, D. Zhao, Lattice Boltzmann simulation of sound absorption of an in-duct orifice, in: Proc. Mtgs. Acoust. 19, Acoustical Society of America., Montreal, Canada, 2013: pp. 030015–030015. https://doi.org/10.1121/1.4799686.
[64] C. Ji, D. Zhao, Two-dimensional lattice Boltzmann investigation of sound absorption of perforated orifices with different geometric shapes, Aerospace Science and Technology. 39 (2014) 40–47. https://doi.org/10.1016/j.ast.2014.08.010.
[65] C. Ji, D. Zhao, Lattice Boltzmann investigation of acoustic damping mechanism and performance of an in-duct circular orifice, The Journal of the Acoustical Society of America. 135 (2014) 3243–3251. https://doi.org/10.1121/1.4876376.
[66] K. Habibi, L. Mongeau, Prediction of sound absorption by a circular orifice termination in a turbulent pipe flow using the Lattice-Boltzmann method, Applied Acoustics. 87 (2015) 153–161. https://doi.org/10.1016/j.apacoust.2014.07.008.
[67] A.R. da da Silva, P. Mareze, E. Brandão, Prediction of sound absorption in rigid porous media with the lattice Boltzmann method, Journal of Physics A: Mathematical and Theoretical. 49 (2016) 065501. https://doi.org/10.1088/1751-8113/49/6/065501.
[68] D. Zhao, C. Ji, J. Li, L. Ang, Experimental comparison of noise dissipation effects of single- and double-layer acoustic liners, Applied Acoustics. 141 (2018) 281–292. https://doi.org/10.1016/j.apacoust.2018.07.024.
[69] C. Maury, T. Bravo, D. Mazzoni, The use of microperforations to attenuate the cavity pressure fluctuations induced by a low-speed flow, Journal of Sound and Vibration. 439 (2019) 1–16. https://doi.org/10.1016/j.jsv.2018.09.045.
[70] A. Toutant, P. Sagaut, Lattice Boltzmann simulations of impedance tube flows, Computers & Fluids. 38 (2009) 458–465. https://doi.org/10.1016/j.compfluid.2008.05.006.
[71] C. Sun, F. Pérot, R. Zhang, D.M. Freed, H. Chen, Impedance Boundary Condition for Lattice Boltzmann Model, Commun. Comput. Phys. 13 (2013) 757–768. https://doi.org/10.4208/cicp.421011.260112s.
[72] Y. Özyörük, L.N. Long, M.G. Jones, Time-Domain Numerical Simulation of a Flow-Impedance Tube, Journal of Computational Physics. 146 (1998) 29–57. https://doi.org/10.1006/jcph.1998.5919.
[73] F. Perot, D. Freed, Acoustic absorption of porous materials using LBM, in: 19th AIAA/CEAS Aeroacoustics Conference, American Institute of Aeronautics and Astronautics, Berlin, Germany, 2013. https://doi.org/10.2514/6.2013-2070.
[74] C. Sun, F. Pérot, R. Zhang, P.-T. Lew, A. Mann, V. Gupta, D.M. Freed, I. Staroselsky, H. Chen, Lattice Boltzmann formulation for flows with acoustic porous media, Comptes Rendus Mécanique. 343 (2015) 533–544. https://doi.org/10.1016/j.crme.2015.07.013.
[75] K. Schladitz, S. Peters, D. Reinel-Bitzer, A. Wiegmann, J. Ohser, Design of acoustic trim based on geometric modeling and flow simulation for non-woven, Computational Materials Science. 38 (2006) 56–66. https://doi.org/10.1016/j.commatsci.2006.01.018.
[76] M. Hasert, J. Bernsdorf, S. Roller, Lattice Boltzmann Simulation of non-Darcy Flow in Porous Media, Procedia Computer Science. 4 (2011) 1048–1057. https://doi.org/10.1016/j.procs.2011.04.111.
[77] S. Caro, CEAS-ASC highlights 2006, Journal of Sound and Vibration. 304 (2007) 421–449. https://doi.org/10.1016/j.jsv.2007.03.029.
[78] G.J. Bennett, J. Kennedy, C. Meskell, M. Carley, P. Jordan, H. Rice, Aeroacoustics research in Europe: The CEAS-ASC report on 2013 highlights, Journal of Sound and Vibration. 340 (2015) 39–60. https://doi.org/10.1016/j.jsv.2014.12.005.
[79] A.G. Wilson, Aeroacoustics research in Europe: The CEAS-ASC report on 2016 highlights, Journal of Sound and Vibration. 427 (2018) 188–221. https://doi.org/10.1016/j.jsv.2017.10.016.
[80] Powerflow® Lbm Aeroacoustics Bibliography, (2016). www.exa.com (accessed June 21, 2019).
[81] F. Perot, S. Moreau, M.-S. Kim, M. Henner, D. Neal, Direct aeroacoustics predictions of a low speed axial fan, in: 16th AIAA/CEAS Aeroacoustics Conference, American Institute of Aeronautics and Astronautics, Stockholm, Sweden, 2010. https://doi.org/10.2514/6.2010-3887.

[82] T. Zhu, M. Sturm, T.H. Carolus, B. Neuhierl, Experimental and numerical investigation of tip clearance noise of an axial fan using a lattice boltzmann method, in: The 21st International Congress on Sound and Vibration (ICSV 21), ICSV, Beijing, China, 2014: p. 9.
[83] W.C.P. van der Velden, S. Pröbsting, A.H. van Zuijlen, A.T. de Jong, Y. Guan, S.C. Morris, Numerical and experimental investigation of a beveled trailing-edge flow field and noise emission, Journal of Sound and Vibration. 384 (2016) 113–129. https://doi.org/10.1016/j.jsv.2016.08.005.
[84] M. Sanjose, S. Moreau, Direct noise prediction and control of an installed large low-speed radial fan, European Journal of Mechanics - B/Fluids. 61 (2017) 235–243. https://doi.org/10.1016/j.euromechflu.2016.10.004.
[85] D. Lallier-Daniels, M. Piellard, B. Coutty, S. Moreau, Aeroacoustic study of an axial engine cooling module using lattice-Boltzmann simulations and the Ffowcs Williams and Hawkings' analogy, European Journal of Mechanics - B/Fluids. 61 (2017) 244–254. https://doi.org/10.1016/j.euromechflu.2016.10.008.
[86] T. Zhu, D. Lallier-Daniels, M. Sanjosé, S. Moreau, T. Carolus, Rotating coherent flow structures as a source for narrowband tip clearance noise from axial fans, Journal of Sound and Vibration. 417 (2018) 198–215. https://doi.org/10.1016/j.jsv.2017.11.014.
[87] S. Moreau, M. Sanjosé, S. Magne, Optimization of tonal noise control with flow obstruction, Journal of Sound and Vibration. 437 (2018) 264–275. https://doi.org/10.1016/j.jsv.2018.09.001.
[88] F. Pérot, A. Mann, M.-S. Kim, D. Casalino, E. Fares, Investigation of inflow condition effects on the ANCF aeroacoustics radiation using LBM, in: Inter-Noise 2012, Inter-noise, New York, USA, 2012: p. 14.
[89] D. Casalino, A. Hazir, A. Mann, Turbofan Broadband Noise Prediction using the Lattice Boltzmann Method, in: 22nd AIAA/CEAS Aeroacoustics Conference, American Institute of Aeronautics and Astronautics, Lyon, France, 2016. https://doi.org/10.2514/6.2016-2945.
[90] D. Casalino, A. Hazir, Lattice boltzmann based aeroacoustic simulation of turbofan noise installation effects, in: ICSV23, Athens, Greece, 2016: p. 8.
[91] I. Gonzalez-Martino, D. Casalino, Fan Tonal and Broadband Noise Simulations at Transonic Operating Conditions Using Lattice-Boltzmann Methods, in: 2018 AIAA/CEAS Aeroacoustics Conference, American Institute of Aeronautics and Astronautics, Atlanta, Georgia, 2018. https://doi.org/10.2514/6.2018-3919.
[92] D. Casalino, F. Avallone, I. Gonzalez-Martino, D. Ragni, Aeroacoustic study of a wavy stator leading edge in a realistic fan/OGV stage, Journal of Sound and Vibration. 442 (2019) 138–154. https://doi.org/10.1016/j.jsv.2018.10.057.
[93] C. Teruna, D. Ragni, F. Avallone, D. Casalino, A rod-linear cascade model for emulating rotor-stator interaction noise in turbofans: A numerical study, Aerospace Science and Technology. 90 (2019) 275–288. https://doi.org/10.1016/j.ast.2019.04.047.
[94] M. Hiraishi, M. Tsutahara, R.C.K. Leung, Numerical simulation of sound generation in a mixing layer by the finite difference lattice Boltzmann method, Computers & Mathematics with Applications. 59 (2010) 2403–2410. https://doi.org/10.1016/j.camwa.2009.08.073.
[95] P.-T. Lew, L. Mongeau, A. Lyrintzis, Noise prediction of a subsonic turbulent round jet using the lattice-Boltzmann method, J. Acoust. Soc. Am. 128 (2010) 1118. https://doi.org/10.1121/1.3458846.
[96] D. Casalino, A. Hazir, Computation of dual-stream unsteady jet flows and noise, in: Proceedings of ICSV22, Florence, Italy, 2015: p. 9.
[97] A.R. da Silva, G.P. Scavone, Lattice Boltzmann simulations of the acoustic radiation from waveguides, J. Phys. A: Math. Theor. 40 (2007) 397–408. https://doi.org/10.1088/1751-8113/40/3/004.
[98] A.R. da Silva, G.P. Scavone, A. Lefebvre, Sound reflection at the open end of axisymmetric ducts issuing a subsonic mean flow: A numerical study, Journal of Sound and Vibration. 327 (2009) 507–528. https://doi.org/10.1016/j.jsv.2009.06.027.
[99] J.M. Buick, M. Atig, D.J. Skulina, D.M. Campbell, J.P. Dalmont, J. Gilbert, Investigation of non-linear acoustic losses at the open end of a tube, The Journal of the Acoustical Society of America. 129 (2011) 1261–1272. https://doi.org/10.1121/1.3543987.
[100] Y. Shi, A.R. da Silva, G.P. Scavone, Lattice Boltzmann simulations of sound directivity of a cylindrical pipe with mean flow, Journal of Physics A: Mathematical and Theoretical. 46 (2013) 315501. https://doi.org/10.1088/1751-8113/46/31/315501.

[101] A.R. da Silva, G.F. Greco, Computational investigation of plane wave reflections at the open end of subsonic intakes, Journal of Sound and Vibration. 446 (2019) 412–428. https://doi.org/10.1016/j.jsv.2019.01.044.
[102] J. Adam, D. Ricot, F. Dubief, C. Guy, Aeroacoustic simulation of automotive ventilation outlets, The Journal of the Acoustical Society of America. 123 (2008) 3250–3250. https://doi.org/10.1121/1.2933531.
[103] F. Perot, M.-S. Kim, D. Freed, D. Lee, K.D. Ih, Direct Aeroacoustics Prediction of Ducts and Vents Noise, in: 16th AIAA/CEAS Aeroacoustics Conference, American Institute of Aeronautics and Astronautics, Stockholm, Sweden, 2010. https://doi.org/10.2514/6.2010-3724.
[104] K. Habibi, Y. Rafat, L. Mongeau, R. Taher, Numerical and experimental characterization of oscillatory flows over a flat spoiler in a duct, in: 2012: p. 11.
[105] B. Crouse, D. Freed, S. Senthooran, F. Ullrich, C. Fertl, Analysis of Underbody Windnoise Sources on a Production Vehicle using a Lattice Boltzmann Scheme, in: Sae Technical Paper Series, St. Charles, Illinois, 2007.
[106] J.-L. Adam, A. Menoret, D. Ricot, Direct Aeroacoustic Source Identification Based on Lattice Boltzmann Simulation and Beamforming Technique, in: 15th AIAA/CEAS Aeroacoustics Conference (30th AIAA Aeroacoustics Conference), American Institute of Aeronautics and Astronautics, Miami, Florida, 2009. https://doi.org/10.2514/6.2009-3182.
[107] A.T. de Jong, H. Bijl, A. Hazir, J. Wiedemann, Aeroacoustic simulation of slender partially covered cavities using a Lattice Boltzmann method, Journal of Soundand Vibration. 332 (2013) 1687–1703. http://dx.doi.org/10.1016/j.jsv.2012.09.040.
[108] F. Avallone, W.C.P. van der Velden, D. Ragni, D. Casalino, Noise reduction mechanisms of sawtooth and combed-sawtooth trailing-edge serrations, J. Fluid Mech. 848 (2018) 560–591. https://doi.org/10.1017/jfm.2018.377.
[109] P.A. Skordos, Modeling flue pipes: subsonic flow, lattice Boltzmann, and parallel distributed computers, Ph.D., Massachusetts Institute of Technology, 1995.
[110] H. Kuhnelt, Simulating the Mechanism of Sound Generation in Flutes Using the Lattice Boltzmann Method, in: Proceedings of the Stockholm Music Acoustics Conference, SMAC 03, Stockholm, Sweden, 2003: p. 5.
[111] H. Kuhnelt, Vortex sound in recorder and flute like instruments: Numerical simulation and analysis, in: ISMA 2007, International Symposium on Musical Acoustics, EITSEB, Barcelona, Spain, 2007: p. 8.
[112] Y. Shi, A. da Silva, G. Scavone, Numerical Simulation of Whistles Using Lattice Boltzmann Methods, in: Proceedings of the 2014 International Symposium on Musical Acoustics, Le Mans, France, 2014: pp. 615–621.
[113] A.R. da Silva, G. Scavone, Coupling Lattice Boltzmann Models to Digital Waveguides for Wind Instrument Simulations, in: Proceedings of the International Symposium on Musical Acoustics (ISMA), Barcelona, Spain., 2007.
[114] A.M. Velasco, J.D. Muñoz, M. Mendoza, Lattice Boltzmann model for the simulation of the wave equation in curvilinear coordinates, Journal of Computational Physics. 376 (2019) 76–97. https://doi.org/10.1016/j.jcp.2018.09.031.
[115] E.M. Salomons, W.J.A. Lohman, H. Zhou, Simulation of Sound Waves Using the Lattice Boltzmann Method for Fluid Flow: Benchmark Cases for Outdoor Sound Propagation, PLOS ONE. 11 (2016) e0147206. https://doi.org/10.1371/journal.pone.0147206.
[116] P. Prestininzi, A. Abdolali, A. Montessori, J.T. Kirby, M. La Rocca, Lattice Boltzmann approach for hydro-acoustic waves generated by tsunamigenic sea bottom displacement, Ocean Modelling. 107 (2016) 14–20. https://doi.org/10.1016/j.ocemod.2016.09.012.
[117] S. Ha, N. Ku, K.-Y. Lee, Lattice Boltzmann approach to acoustic propagation for underwater warfare simulation, in: Proceedings of the 2012 Symposium on Theory of Modeling and Simulation, Orlando, FL, USA, 2012: p. 27:1-27:9.
[118] F. Brogi, M. Ripepe, C. Bonadonna, Lattice Boltzmann modeling to explain volcano acoustic source, Scientific Reports. 8 (2018). https://doi.org/10.1038/s41598-018-27387-0.

7. FINAL REMARKS

In this work, the application of the Lattice Boltzmann Method to thermal fluid dynamics and energy systems was studied.

In the wide field of thermal fluid dynamics and energy systems, some specific topics were selected to develop this research: nuclear reactors, natural circulation loops, nanofluids, and acoustics. These topics have the following characteristics:

- are relevant in engineering applications and scientific research;
- cover several topics related to applied physics;
- the results are generalizable and extendible to other energy systems;
- experimental activity concerning those topics was developed in the DIME-UNIGE facilities.

The original contributions of this thesis are:

1. the systematic description of the current status of LBM applications to nuclear reactors problems and the testing of the main variants of the method in this field simulating test cases and benchmark problems;
2. the development and validation of a LBM model for a single-phase natural circulation loop;
3. the development and validation of a LBM model for gravitational sedimentation of nanoparticles, considering different sedimentation and diffusion models;
4. The systematic description of the current status of LBM applications to acoustics and the testing of the main algorithms in this field simulating several test cases.

Additionally, some other specific apports are resumed below:

- the applicability of the neutron transport LBM to study nuclear waste disposal using porous materials to store and handle radioactive fluids was shown. This possible application profits the simple representation of complex geometric domains as foams and other porous materials;
- changes in the thermophysical performance of the natural circulation loop were simulated when the loop reached a non-laminar (transition) regime. In particular, the transition between the laminar and turbulent regime occurs at a Reynolds number lower than the typical range;
- Experimental studies in parallel connected natural circulation loops of small inner diameter;
- Modeling the diffusion and sedimentation parameters dependent on local nanoparticle concentration was a simple way to consider agglomeration and cluster formation;
- a boundary condition based on Finite Differences was adapted for the sedimentation model. However, this boundary condition has presented an inferior performance compared with the common Bounce Back boundary condition.

The reputation of the LBM as an accurate Navier-Stokes solver is well established. Moreover, it is shown that the LBM is a versatile numerical method that can be applied in many other fields as:

- advection-diffusion problems (and consequently also for diffusive problems);
- thermo-fluid dynamics;
- neutral particles transport (and consequently radiation transport);
- one-step aeroacoustics.

Benefits and drawbacks

Resuming, some observed characteristics that show the versatility and power of the Lattice Boltzmann Method are:

I. it can handle complex boundaries by Boolean masks, reducing the meshing computational cost of other numerical methods;
II. the algorithm remains local and parallelizable. By applying *first neighbor lattices* (*D1Q3*, *D2Q9*, *D3Q19*, *D3Q27*);
III. the algorithm remains simple by applying the linear BGK collision operator;
IV. each specific application has required adaptation of the source terms, equilibrium distribution function, and boundary conditions. Nevertheless, the lattice and the collision operator were similar in all the cases;
V. isotropy of the fluid lattice ensures the conservation of angular momentum and vorticity;
VI. the LBM is not limited to steady-state simulations. By its nature, the algorithm generates transient simulations;
VII. turbulence models and advanced BGK collision operators (regularized and MRT) enhance the stability for low viscosity (and high Reynolds number) simulations.

The LBM results are accurate as those obtained by the standard numerical methods, but it must be considered that the LBM does not replace traditional numerical methods; instead, they can be adapted to work together in hybrid schemes. In fact, in some contexts (as far-field aeroacoustics calculations), the hybrid schemes overcome the micro-scale or mini-scale application limits of the LBM.

Some critical points that have limited the popularity of the LBM in some engineering fields are:

I. the necessary theoretical background differs from the classical macroscopic fluid dynamics equations;
II. the units conversion from lattice units to physical units is not straightforward;
III. having a programming culture to implement the code is almost a need.

However, all those critical points can be overcome. The LBM framework gives a very simplified approach to statistical mechanics. The use of non-dimensional groups to describe the physical problems could be the clear way to overcome the unit translation problem. The algorithms are easily implemented in different programming languages. Additionally, the programming culture in Science, Technology, Engineering, and Mathematics is growing every day. On the other hand, some recent commercial solutions are becoming popular.

Validation of numerical method results is the key point to gain acceptability in engineering applications. In the revised applications, the validation of the LBM was usually done by comparison with benchmark solutions obtained by other well-established numerical methods. Sometimes, the validation of the LBM comes from analytic or experimental data of generic problems and not necessarily from an experimental setup related to the problem simulated. In this sense, the explored possibility to validate the LBM with experimental data was very satisfactory because it clarifies that LBM represents a coherent physical model and not only a *computational automata*.

Future work

The application of the LBM in thermo-fluid dynamics and energy systems could have many more applications, such as the inclusion of phase change phenomena, two-phase flows, reactive flows, or magnetohydrodynamics.

This work shows that a multi-physics simulation framework can be developed based on the Lattice Boltzmann Method. This capability is enhanced by integrating hybrid models, such as the Finite Volume method, to adjust unstructured meshes or the Boundary Immersed Method to calculate fluid-solid interactions.

For example, a complete multi-physics simulation of a Nuclear Reactor including neutronics, heat transfer (with the integration of radiative, convective and conductive mechanisms), fluid dynamics, and transport-deposition mechanisms for secondary chemical species has not yet been done. However, the LBM is a candidate for a possible comprehensive framework to study a nuclear reactor as a whole. Using the LBM in a single framework could partially overcome the limitation related to *the use of several methods and several interfaces between physical domains that limit the credit of numerical methods in critical problems as nuclear plants safety analysis*[2].

Specific works that can be derived from the models developed and validated in this thesis are:

- Testing the performance of the NCL-LBM under different power steps.
- Adapting the NCL LBM model for parallel-coupled natural circulation loops.
- Developing an NCL-nanofluid-LBM model.
- Implementing the sedimentation model in three-dimensional lattices, adding a deposition model (i.e., changing fluid cells by solid or porous cells).
- Researching specific acoustical problems of interest in NCL implants as 1. sound absorption of perforated plates that can be used as flux correctors, 2. acoustic resonance in corrugated or irregular pipes.
- Developing a coupled interface that includes the four models: 1. flow field, 2. thermal field, 3. nanoparticle concentration, and 4. neutrons flux.

[2] *Validation of Computer Codes and Calculation Methods, Office for Nuclear Regulation, UK, 2019.*

ANNEX A

This annex presents resume tables concerning the references presented in chapter 6: application to acoustical problems.

Table A. 1 LBM applied to wave generation and propagation.

Author and year	**Grid**	***Collision operator***	***Special feature/ turbulence model***	***Acoustic problem***	***Validation***	***Highlights***
Buick et al. [7], [8]	D2Q7	*BGK*		*Damping of a standing wave in a pipe*	*Analytical*	*Acoustic streaming cells near the wall related to the dissipation of waves.*
Chopard and Luthi [3]	D2Q9	*BGK wave-model*		*Derive a wave-model that includes BC, source, adjustable sound speed*	*Analytical*	*Propagation of waves in outdoor spaces from a point source. The distribution can represent sound waves or other fields (such as EM for radio waves).*
Buick et al. [9]	D2Q7	*BGK*		*Development of shock plane wavefront in unbounded media. No thermal energy dissipation*	*Analytical*	*The BGK model can simulate non-linear acoustic effects with high-amplitude sound waves.*
Buick et al. [10]	D2Q7	*BGK*		*Shock waves, organ air supply, brass player lips*	*Not Specified*	*Two possible approaches to establishing sound speed. The simple-one (ideal gas state eq.) is enough to simulate shock wavefronts.*
Haydock and Yeomans [6]	D2Q7	*BGK*		*Acoustic streaming, the interaction of a wave and a solid boundary: cylinder plates linear limit standing wave*	*Analytical*	*Simulate accurately the acoustic streaming around solid objects. Exploration of streaming outside the analytical limits of channel width around wavelength.*
Lallemand and Luo [23]	D2Q13 D3Q13 D3Q15	*HTLBE (hybrid), MRT*		*Thermal and acoustic properties of the LBM*	*Analytical*	*Increment stability and decouple shear and thermal modes in thermal LBM.*
Buick and Cosgrove [20]	D2Q9	*BGK*	*Variable sound speed (body force).*	*One dimensional plane wave, measurement of sound speed by 2 methods: 2 points and impedance. Development of non-linearity concerning sound speed.*	*Analytical*	*A model with variable sound velocity. Fluid viscosity does not change varying sound speed. The nonlinearity of a pressure wave depends not only on its amplitude but also on the speed of sound in the medium.*
Fraser and Hall [4]	D2Q9	*BGK*		*Wave phenomena, reflection, and diffraction through an orifice*	*Analytical*	*Sound speed dependence of relaxation parameter. Standing wave and diffraction patterns.*
Marié et al. [17]	D3Q19	*BGK vs MRT*		*Gaussian pulse propagation, dispersion and dissipation relation*	*Numerical LBM Variants*	*MRT model. The bulk viscosity could be controlled independently but has effects on the acoustic waves. This stability study showed that the different propagation modes could interfere, involving unstable situations.*

ANNEX A

Buick et al. [21]	D2Q7	*BGK*	*Variable sound speed (body force*	*Acoustic propagation in a binary fluid. Pulse and plane wave through plane interfaces and bubbles*	*Analytical*	*Species-dependent impedance model can correctly simulate transmission and reflection of acoustic waves.*
Brès et al. [11]	D3	*BGK*	*LES*	*Dissipation and dispersion concerning resolution. i. temporal decay of a planar standing wave. ii. Spatial decay of a planar Gaussian pulse*	*Analytical*	*Low dispersive and dissipative capabilities applicable to the near field. The turbulence model introduces an additional dissipation, inverse to NPPW.*
Viggen [12] and [13]	D2Q9, D3Q19	*BGK*		*Punctual sound sources, pulse propagation, standing waves, diffraction through two orifices*	*Analytical*	*The point source method imposes a variable distribution in a cell, and it is extendable to a line source.*
Li and Shan [22]	D2Q9 D2Q17 D2Q21 D2Q37 D3Q15 D3Q19 D3Q39 D3Q121.	*BGK-MRT*	*Second distribution for energy*	*Adiabatic waves, energy conservation. Benchmark simulation*	*Analytical*	*Improvement of the method to include adiabatic acoustic using high order lattices.*
Zhang and Feng [18]	D2Q?	*BGK*		*Thermoacoustic waves in a tube resonator*	*Numerical, LG*	*Non-linear effects in temperature and pressure waves can be observed. Acoustic streaming.*
Saidi et al. [5]	D2Q9	*BGK*		*Wave propagation with solid obstacles*	*Numerical, Benchmark Lid Cavity*	*Effects on the wavefront. The ability of LBM to simulate acoustic reflections*
Viggen [14], [15]		*MRT*		*Multipole source*	*Analytical*	*Multipole source can be generated by adding a source term in the collision operator*
Rafat et al. [19]	D2	*BGK*	*isothermal*	*Thermoacoustic refrigerator, acoustic streaming over a flat stack*	*Analytical*	*Two kinds of streaming cells were found.*
Kam et al. [24]	D2	*FD-LBM*		*Thermoacoustic waves*	*Numerical DAS*	*FDLBM can be used to simulate the interaction between acoustic waves and thermal disturbances.*
Zhuo and Sagaut [16]	D3Q19	*RLBM*		*Acoustic Multipole Source in inviscid limit. Scattering around a cylinder.*	*Numerical RLBM vs MRT*	*Improves stability for monopoles; dipoles and quadrupoles are correctly simulated. Scattering is simulated better with slip BC*

Table A. 2 Non-reflective and impedance boundary conditions for the Lattice Boltzmann Method.

Author and year	***Grid***	***Collision model***	***Turbulence model/ special features***	***Acoustic problem***	***Validation***	***Highlights***
Kam et al. [54]; 2007 [55]	*D2Q13*	*BGK (improved with 3/2 RT) FDLBM*		*Test 3 NRBC with two aeroacoustics problems 1. propagation of a plane pressure pulse; case 2) propagation and interaction of acoustic, entropy and vortex pulses in a uniform stream*	*Numerical Contrast with DNS solution (larger domain)*	*EM/FM types and ABC are suitable for one-step LBM simulation of aeroacoustics problems*
Izquierdo and Fueyo [56]	*D2Q9*	*BGK-MRT*		*NRBC, Characteristic Boundary Condition (CBC)*	*Numerical CBC vs. BB*	*Adaptation of LODI CBC to MRT, no need for an extended domain*
Toutant and Sagaut [70]	*D2Q9*	*SRT-BGK*		*Impedance tube NASA Langley flow. Impedance BC. Tested with single and broadband frequencies.*	*Numerical, Experimental*	*Surface acoustic Impedance condition using extended collision operator. Validated with different Mach numbers.*
Tekitek et al. [53]	*D2Q9*	*MRT, BLB-LBM*		*PML boundary condition. Test cases: plane waves*	*Numerical*	*The sponge zone can generate reflected waves (BLB-LBM) if no damping term is included. New BC including damp via streaming step near the boundary.*
Najafi-Yazdi and Mongeau [52]	*2D and 3D*	*BGK*		*Perfectly Matched Layer: Test cases: Gaussian pulses and vortex dissipation in the buffer zone. Square vortex street*	*Numerical PML vs ZG*	*Absorptive BC based on PML with no need to know the direction of the wave. Exponential decay in the buffer zone.*
Xu and Sagaut [51]		*BGK, MRT*		*Theoretical analysis of absorbing layers. Test cases: Gaussian pulses, plane wave, vortex*	*Analytical/ Numerical*	*Optimal absorption profile for a sponge zone, performance similar to PML.*
Sun et al. [71]	*D3Q19*	*BGK SRT*	f_i^{eq} *expanded to 3rd power*	*Implementation of impedance BC Test cases: impedance tube and NASA Langley acoustic liner.*	*Experimental*	*Implement a time-domain BC based on the Ozyoruk theory for the impedance. Independence from BC of fluid model and geometry (mesh orientation of the channel)*
Sun et al. [74]	*D3Q19*	*BGK SRT*	f_i^{eq} *expanded to 3rd power*	*Implementation of impedance BC: equivalent fluid-porous media. Test cases: flow meter, normal impedance tube, and NASA Langley acoustic liner.*	*Experimental*	*Equivalent fluid from porosity and flow resistivity. Validated model. Useful with and without mean flow. Complex geometries of porous media.*
Wissocq et al. [57]	*D2Q*	*Regularized FDLBM*		*Characteristic Boundary Conditions adaptation to LBM Test cases: plane and spherical acoustic waves, vortices. NACA profile.*	*Numerical LBM (larger domain)*	*Adaptation to regularized LBM of 3 CBC, including transverse component*

ANNEX A

Table A. 3 LBM in aeroacoustics studies.

Author and year	***Grid***	***Collision model***	***Turbulence model***	***Mesh***	***Acoustic problem***	***Validation***	***Highlights***
Mallick et al. [25]	*D3*	*BGK*	*RNG*	*VR*	*Noise in Helmholtz resonator by grazing flow*	*Experimental*	*LBM correctly predict the resonance frequency of the system*
Wilde [26],[27], [28]	*D2Q9, D3Q19*	*BGK*	*Standard turbulence model LES*		*Helmholtz resonator Benchmark. D3* *Trailing edge generated noise.* *Acoustic propagation with mean flow.* *Acoustic propagation with a turbulent flow.*	*Numerical FD/ experimental*	*Phase error 1% for 12ppw, Isotropy.* *Use of LBM for turbulent low Mach flow.* *Capability of simulating advection of sound waves.*
Crouse et al. [29]	*2D,3D,*	*BGK*		*VR*	*Canonical problems:* *Planar propagating sound wave.* *Gaussian pulse dispersion 2D* *Driven standing-wave tube to absorb BC.* *Helmholtz* *Resonator.*	*Analytical/ experimental*	*Grid resolution minimizing numerical dispersion 5,6PPWL.* *White noise signal.*
Li et al. [30] [31]	*D2Q9 D2 Q13*	*BGK MRT modified collision term*			*1D acoustic pulse* *2D acoustic pulse* *Acoustic, vorticity and entropy waves with mean flow*		*Diatomic gas treatment with more degrees of freedom. MRT for a higher Mach spectrum than SRT. Accurate as DNS, more computationally effective.*
Tsutahara et al. [32]	*D2Q21, D3Q39,*	*FDLBM, BGK, f^{eq} equilibrium distribution expanded to 3rd order, Additional DOF*			*Extension of LBM to diatomic gases* *Test cases: pressure waves initial step distribution* *Aeolian tone by cylinder* *Edge tone box*	*DNS NS*	*Gamma can be adjusted with DOF for diatomic gases.*
Fu et al. [33]	*D2Q9*	*LBM, Feq (rotational polyatomic)*			*Extension of LBM to diatomic gases* *Test cases:* *Gaussian pulse* *Pulses in a stream MA 0.9* *Pressure, vorticity entropic*	*Numerical FD, LBM D2Q13*	*New Feq can recover the state equation for polyatomic gases, the scheme can go to high MA. Includes rotational DOF.*
Marie et al. [34]	*D3Q19*	*BGK, MRT*			*Dispersion dissipation analysis*	*Numerical NS high order*	*Low dissipation, higher dispersion of MRT.*
Peng et al. [35]	*D3Q19*	*MRT*			*Isotropic decaying turbulence dissipation*	*Numerical LBM vs. PS Method*	*Presence of acoustic waves not predicted by PS.*
Tsutahara et al. [36]	*D2Q21*	*BGK FDLBM*		*ALE rotating mesh*	*Rapidly rotating ellipse into a mean flow and different aspect ratios*		*Rotating adaptative mesh geometry. Sound generation mechanism.*
Hasert et al. [37]	*D3(Q19)?*	*BGK*	*LES*		*Sound generation for flow passing porous media.* *Test cases:* *Propagation standing wave.* *Generation rotating vortex pair*	*Analytical*	*The sound generated by the rotating vortex pair is correctly simulated. LDLD concerning NPPW min 6 corroborated.*

Xu and Sagaut [38]	*D2Q9*	*MRT modified*		*2D Gaussian pulse propagation and harmonic monochromatic source point*		*Improve the MRT to achieve optimal dissipation dispersion in acoustics. Stability at low viscosity. Annihilates spurious waves.*
Machrouki et al. [39]	*D3*	*BGK*	*LES*	*Jet flow and noise of a cube obstacle behind a fence. A jet impacts the fence and then the cube generating turbulence and noise.*	*Experimental*	*Compare results with anechoic wind tunnel measurements, correct flow pattern and dipolar nature of the source*
Tsutahara [40]	*D2Q9 isothermal D2Q21 Thermal*	*FDLBM*		*Aeolian tone by a circular obstacle Noise produced by a train in a tunnel Falling drop Scattering by a drop*	*Not specific, comparison between isothermal and thermal models*	*FDLBM can be applied to biphasic aeroacoustics problems, and also for high Reynolds number using Arbitrary Lagrangian-Eulerian (ALE) formulation*
Vergnault et al. [42]	*D2Q9*	*BGK*		*Source detection from pressure stories in boundaries, tested with Gaussian pulse and single frequency in waveguides, with the mean flow and Posseiule flow Mach 0.6. and also a source behind a wall.*	*Analytical*	*A backward propagation scheme coupled with a base flow split of LBM can be used in source detection also with 90% of information loss.*
Vergnault & Sagaut [44]	*D2Q9*	*BGK Adjoint LBM*		*Optimal parameters in active noise control. Examples with 1 and 2 noises and with mean flow.*	*Analytical*	*Possibilities of using ALBM in optimization schemes.*
Zhou and Dong [45]	*D3Q19*	*BGK, 2 forcing schemes, Hybrid (Lighthill's acoustic analogy)*		*A hybrid approach to noise generated by isotropic turbulence (statically stationary)*	*Numerical and analytical*	*LBM solves the aerodynamic fluctuations AAL solves the far-field noise. Stochastic and deterministic forcing terms to generate the turbulence.*
Brionnaud et al. [46]	*D3Q27*	*MRT*	*LES*	*1. duct flow passing through an orifice, 2. subsonic jet through a pipe and, 3. flow-through wheel gear.*	*Experimental*	*possibility of obtaining the noise spectrum (including broadband noise)*
Guo and Chen [47]	*D2Q9,*	*BGK, ABC*		*Noise generated by Vortex pair*	*Analytical*	*Initial conditions for Gaussian rotating vortices (velocity profile). Direct simulation of sound field for unsteady flows*

Table A. 4 LBM in porous media sound absorption studies.

Author and year	***Grid***	***Collision model***	***special features***	***Acoustic problem***	***Validation***	***Highlights***
Inamuro et al. [58]	*D3Q15*	*BGK*		*Flow through porous media, packed balls.*	*Analytical*	*Possibility of studying porous media with the LBM. Instabilities in the flow at high Re number. Fit with experimental data.*
Schladitz et al. [75]	*D3*			*Optimization of the absorption coefficient for a fibrous material of PET non-woven.*	*Experimental*	*Uses LBM to estimate flow resistivity from a 2D image of the geometry and then Delaney Bazley for the absorption coefficient.*
Ayub et al. [59], [60]	-	-	-	*Review "molecular dynamic methods" applied to the propagation of acoustic waves in nanotubes. Comparison between Monte Carlo method and LBM*	-	*Advantages for simulating acoustic waves for high* $\boldsymbol{K_n}$*<1.0 Limitations on heat conduction. Perhaps Monte Carlo method can work better*
Hasert et al. [76]	*D3Q19*	*BGK TRT*	*LES*	*Darcy and non-Darcy law through a generic, under resolved porous media. Vorticity aeroacoustics noise generation for high Re of flow through a porous media in a duct.*	-	*For a fine mesh BGK, TRT, TRT-LES converges in the estimation of friction factor; TRT-LES also converges for a coarse mesh. Allowing the use of LBM in aeroacoustics with lower effort.*
Perot and Freed [73]	*D3Q19*			*Porous media simulated in an impedance normal tube, with backing layer from resistivity parameter using equivalent fluid.*	*Experimental, Analytical*	*Inversion of parameters from experimental data to fit the absorption curve of equivalent fluid.*
Ji and Zhao [62] [63]	*D2Q9*	*BGK*		*Perforated plates, sound absorption*	*Analytical Howe model HM and MHM*	*Sound absorption curves and unsteady jet (vorticity) mechanism*
Ji and Zhao [64]	*D2Q9*	*BGK*	*ABC*	*Perforated plates (5mm diameter), sound absorption: effect of edge geometry*	*Experimental/ theoretical MHM*	*Sound absorption curves. Vorticity involved in sound absorption mechanism, rounded edges generate less vorticity and therefore less absorption.*
Ji and Zhao [65]	*D3Q19*	*BGK*	*ABC*	*Perforated plates (cylindrical hole)*	*Experimental, Analytical, Numerical*	*Non-linearity in the damping mechanism. Unsteady jet and vortex shedding downstream, the perforation causes dissipation below 1Khz*
Habibi and Mongeau [66]	*D3Q19*	*BGK*	*ABC/VLES*	*Standing wave tube one perforation absorption.*	*Experimental, Analytical*	*Corroborates the turbulent jet formation, increases the calculus to mid frequencies up to 6 kHz*
da Silva et al. [67]	*D2Q9*	*BGK*		*Viscous absorption of a rigid porous material. Straight channels.*	*Analytical*	*The model is validated for simplified channel geometry and can be used for more complex geometries. Up to 16kHz.*
Chevillotte et al. [61]	*D3Q19*	*TRT*	*LES*	*Porous absorption simulation. i. Macroscopic properties of porous media. ii. Surface impedance BC iii. Bulk representation of porous media.*	*Analytical, Numerical LBM*	*Compares 3 possible models for the absorption of porous materials, the equivalent fluid (bulk) works better: reproduces the absorption properties and allows flow through.*
Zhao et al. [68]	*D2Q9*	*BGK*	*ABC*	*Single- and double-layer perforated plates*	*Experimental*	*Influence of porosity and thickness. Turbulent jet dissipation. Optimization.*
Maury et al. [69]	*D2Q9*	*BGK*		*Unbacked microperforated plates to dissipate flow-induced noise.*	*Experimental*	*Energy dissipation mechanisms occur at the regions with maximum velocity fluctuations. Overestimation by using 2D geometry representation.*

Table A. 5 LBM in aeroacoustics studies, fan noise.

Author and year	**Grid**	**Collision model**	**Turbulence model**	**Mesh**	**Acoustic problem**	**Validation**	**Highlights**
Perot et al. [81]	*D3*	*BGK/compressible/*	*VLES*	*VR*	*Real automotive cooling fan (H380EC1) at low speeds*	*Experimental*	*LBM used to identify noise source, linking complex flow patterns and acoustic field*
Zhu et al. [82]	*D3Q19*	*BGK*	*VLES*	*VR/SLR*	*Clearance tip noise in axial fan*	*Experimental*	*Complex vortex structures emerge from the clearance tip asymmetrically and generate pressure variations on the blade surface producing noise.*
van der Velden et al. [83]	*D3Q19*	*BGK*	*VLES*	*VR*	*Trailing edge noise emission*	*Experimental*	*The relevance of the vortex shedding mechanism in tonal noise was assessed.*
Casalino et al. [89]	*D3*	*BGK/(subsonic)*	*VLES*	*VR*	*NASA/GE Source Diagnostic Test (SDT), fan-Outlet Guide Vane OGV with one operation condition*	*Experimental*	*Tonal and broadband noise correctly predicted. Simulation of the attenuation of a honeycomb liner.*
Casalino and Hazir [90]	*D3Q19*	*BGK*	*VLES*	*VR*	*Digital aircraft certification*	*Experimental*	*Using a realistic model of an aircraft and FWH analogy it is possible to obtain broadband sound levels in wider ground areas*
Sanjose & Moreau [84]	*D3*		*VLES*	*VR*	*Radial fan and possible strategies to reduce noise: filters, hub modifications, rotating obstacles*	*Experimental*	*Different strategies are tested to diminish the flow separation and the noise; a porous filter can be applied at the inlet but it induces an additional pressure loss.*
Lallier-Daniels et al. [85]	*D3Q19*	*BGK*	*VLES*	*VR*	*Noise source location on an axial fan for automotive engine cooling*	*Experimental*	*Use of FWH to predict the sources and contribution to tonal noise. Propagative nature of the sources*
Zhu et al. [86]	*D3Q19*	*BGK*	*VLES*	*VR*	*Noise from axial fan tip clearance*	*Experimental*	*Modal analysis to locate rotating coherent flow structures that generate narrowband hump*
Moreau et al. [87]	*D3Q19*	*BGK*	*VLES*	*VR*	*Tonal noise control of a low-speed axial fan*	*Experimental*	*Optimization strategy for the shape and position of the structure for a given fan geometry and operating conditions.*
Gonzalez-Martino and Casalino [91]	*D3*	*BGK transonic*	*VLES*	*VR*	*NASA/GE Source Diagnostic Test (SDT), fan-Outlet Guide Vane OGV with different operating conditions, rotation speeds*	*Experimental*	*Tonal noise is more sensitive to uncertainty than broadband noise.* *Buzz-saw noise emerges from a random variation angle of the blades*
Casalino et al. [92]	*D3*	*BGK-entropy (high subsonic)*	*VLES*	*VR*	*NASA/GE Source Diagnostic Test (SDT), fan-Outlet Guide Vane OGV effects of sinusoidal serrations on vanes*	*Experimental*	*The effect of serrations depends on the engine configuration (rotor-stator) and the proportion of the wavelength and amplitude serrations concerning turbulence.*
Teruna et al. [93]	*D3Q19*	*BGK/compressible*	*VLES*		*Rod linear blade cascade in a contraction duct (blades NASA/GE Source Diagnostic Test (SDT))*	*Experimental/Numerical*	*An alternative approach to test mitigation strategies with a duct, rod, cascade blade that emulates stator-rotor interaction.*
Pérot et al. [88]	*D3Q19*	*BGK*	*VLES*	*VR/SLR*	*Advanced Noise Control Fan (ANCF)*	*Experimental*	*Far-field, near field, tonal content, and broadband simulation for different configuration inlets*

Table A. 6 LBM in aeroacoustics studies – Jet noise.

Author and year	**Grid**	**Collision model**	**Turbulence model**	**Mesh**	**Acoustic problem**	**Validation**	**Highlights**
Hiraishi et al. [94]	*D2Q21*	*BGK DRP*	*LES Smagorosky*		*Sound generation in a turbulent mixing layer*	*Numerical DNS*	*Vortex pairing as the main source and sound directivity correctly simulated*
Lew et al. [95]	*D3Q19*	*BGK*	*VLES*	*VR*	*Jet in subsonic flow speeds (Mach 03 to 0.4) far-field noise generation is presented*	*Experimental/ Numerical LES Runge Kutta*	*Spurious waves related to interfaces at VR are detected but do not significantly affect the far-field broadband power spectra*
Casalino and Hazir [96]	*D3Q19*	*BGK-regularized (entropy)*	*VLES*	*VR*	*Noise generated by a subsonic highspeed jet, coaxial dual-stream*	*Experimental*	*Use of enhanced LBM (entropy) to high-speed flows simulation capture sound and flow characteristics*

Table A. 7 LBM in aeroacoustics studies- Duct noise.

Author and year	**Grid**	**Collision model**	**Turbulence model**	**Mesh**	**Acoustic problem**	**Validation**	**Highlights**
da Silva and Scavone [97]	*D2Q9 axisymmetric*	*BGK*			*Radiation of an open end of a circular duct*	*Analytical*	*End correction, reflection factor, and directivity of an open waveguide*
Adam et al. [102]	*D3*	*BGK*			*Radiation in automotive ventilation outlets by turbulent flow*	*Analytical (reflection coefficient of an open waveguide) /BEM/experimental*	*Aeroacoustic predictions up to 3kHz, mesh resolution. Industrial applications to test geometrical parameter*
da Silva et al. [98]	*D2Q9 axisymmetric*	*BGK*			*Radiation reflection of open circular duct, effects of horns*	*Analytical/experimental*	*The effect of the mean flow on the reflection coefficient is negligible (high frequencies). Vortex formation takes place at the same point with and without horns.*
Perot et al. [103]	*D3*		*VLES*	*VR*	*Noise in a duct end HVAC automotive with vents*	*Experimental*	*HVAC noise predictions for subsonic flows. Duct modes affect the spectrum*
Buick et al. [99]	*D2Q9*	*BGK*			*Non-linear losses at the open end of a duct*	*Experimental, analytical*	*Identifies two regimes for the vortex acoustic field interaction. The 2D model fails to predict the acoustic velocity.*
Habibi et al. [104]	*D3Q19*	*BGK*		*VR*	*Acoustic flow over a flat plate in a duct. Thermoacoustic engine*	*Experimental*	*Vortex separation in some moments causes an additional tone. Phase lag between drag force and acoustic flow*
Shi et al. [100]	*D2Q9 axisymmetric*	*BGK*		*ABC/Shrimp signal buffer*	*Sound radiation directivity of pipes issuing subsonic mean flows M0.15*	*Analytical/experimental*	*Agreement for low-frequency silence zones.*

da Silva and Greco, [101]c	*D3Q19*	*BGK*	*VLES*	*VR/SLR/sweep signal*	*Acoustic reflection at open ends of intakes with a subsonic flow effect of intake geometry*	*Analytical*	*For sharp geometries, the flow rotational kinetic energy and the acoustic field play a major role in the behavior of both the magnitude of the reflection coefficient and the end correction*

Table A. 8 LBM in aeroacoustics studies- Frame noise.

Author and year	***Grid***	***Collision model***	***Turbulence model***	***Mesh***	***Acoustic problem***	***Validation***	***Highlights***
Crouse et al. [105]	*D3Q19*	*BGK*	*VLES*		*Underbody wind noise for a car effect of a chin spoiler*	*Experimental*	*Strong pressure fluctuations being generated by the wheels, wheelhouses and the exhaust system, chin spoiler benefits from reducing the flow available*
Adam et al. [106]	*D3Q19*	*BGK*	*Turbulent model*		*Sound source identification in an automotive, virtual wind tunnel validated with experimental data. Validation test of a wideband monopole in a 3D space and 1.5m above a reflecting surface.*		*Possibility of integrating LBM with beamforming techniques to identify the noise source.*
de Jong et al. [107]	*D3Q19*	*BGK*	*LES*	*VR*	*Mean flow resonance of door gaps*	*Experimental*	*Influence of direct fluctuations on resonance, without an overestimation of the amplitude resonance flow. Simulations indicate that LBM in the current setup can simulate door gap cavity resonance behavior. Large spanwise widths and included boundary layer direct turbulent fluctuation*
Avallone et al.[108]	*D3Q19*	*BGK*	*VLES*	*VR/SLR/ sweep signal*	*Effect of trailing edge serrations in airfolds*	*Experimental*	*Serration with filaments-combs are more effective than sawtooth in low and mid frequencies*

Table A. 9 LBM in musical acoustics.

Author and year	***Grid***	***Collision model***	***Turbulence model***	***Acoustic problem***	***Validation***	***Highlights***
Skordos [109]	*D2Q7X, d2Q9X, D3Q15X*	*BGK extended equilibrium distribution,*	*Turbulence filter (LES type)*	*Mean flow and acoustic field in a 2D pipe. Organ, flute, recorder.*	*Analytical Numerical FD*	*Jet-labium interaction, traveling vortex generation, and feedback. Need for ABC*
Kuhnelt [110]	*D3Q19,*	*BGK,*		*Sound generation organ pipe, closed flue pipe*	*Analytical*	*Vortex of low energy, geometric parameters affect all the processes. Jet velocity Bickley profile recovery*
Kuhnelt [111]	*D3Q19,*	*BGK,*		*Flute-like instruments: recorder, transverse flute, stopped organ pipe*	*Experimental*	*The sound generation process is strongly related to vortex generation: sound generation is local and absorption spatially distributed. Sound generation in the recorder concentrates more at the labium (from the acute-angled labium). in the flute it is located upstream of the labium (obtuse-angled).*

da Silva and Scavone [113]	*D2Q9,*	*BGK-DWG, ABC for coupling*	*Coupled a digital waveguide (pipe) and LBM mouth for wind instruments. Test cases: Impulse response closed-closed pipe and single-reed "clarinet"*	*Numerical DWG vs LBM-DGW*	*Use the ABC to couple the LBM (2D) and the DWG (1D).*
Shi et al. [112]	*D2Q9,*	*MRT, ABC*	*Whistles. Interaction between edge tone and Helmholtz resonator*	*Numerical*	*Vortex and jet oscillation are visible and induce Helmholtz resonance. Vorticity implies the use of 3D models.*
Velasco et al. [114]	*3D*	*BGK-curvilinear coordinates*	*Vibrational modes of a cylinder, a horn, and a trumpet*	*Analytical*	*Curvilinear coordinates to implement complex geometries without interpolation schemes*

Table A. 10 LBM in outdoor acoustics.

Author and year	***Grid***	***Collision model***	***Turbulence model***	***source***	***Acoustic problem***	***Validation***	***Highlights***
Salomons et al. [115]	*D2*				*Propagation of sound waves in free field, with solid ground, porous ground, barrier, or wind.*	*Analytical*	*The sound level can be corrected by making the difference with the free-field solution, the dissipation effect disappears with this method.*
Prestininzi et al. [116]	*D2*				*Propagation of t. waves for a possible tsunami, the sea acts as a waveguide and the variable depth as a filter in the signal. A semi-porous condition is used for the sea bottom.*	*Numerical FEM*	*Capabilities of LBM to simulate underwater sound wave propagation with interface effects.*
Brogi et al. [118]	*D3*				*Propagation of shock wave by magma expulsion n a volcano*		*Possibilities of using LBM in sonic propagation in outdoor conditions.*
Ha et al. [117]	*D2Q9*	*BGK*		*Point sources*	*Simulation of an acoustic underwater space to be applied in warfare scenarios. Prediction of the best angle to shoot a torpedo.*		*Capabilities of LBM to simulate underwater sound propagation*